STEADY-STATE NONLINEAR INTERACTIONS OF SURFACE ACOUSTIC WAVES

by

NICKOLAS PEPPINO VLANNES

S.B., ELECTRICAL ENGINEERING AND COMPUTER SCIENCE,
MASSACHUSETTS INSTITUTE OF TECHNOLOGY
(1975)

S.B., PHYSICS, MASSACHUSETTS INSTITUTE OF TECHNOLOGY
(1975)

SUBMITTED IN PARTIAL FULFILLMENT

OF THE REQUIREMENTS FOR THE

DEGREE OF (MASTER OF SCIENCE)
ELECTRICAL ENGINEER

at the

MASSACHUSETTS INSTITUTE OF TECHNOLOGY

September 1977

Signature of Author....
Department of Electrical Engineering and Computer Science, August 1977

Certified by....
Thesis Supervisor

Accepted by..
Chairman, Departmental Committee on Graduate Students

STEADY-STATE NONLINEAR INTERACTIONS OF SURFACE ACOUSTIC WAVES

by

NICKOLAS PEPPINO VLANNES

Submitted to the Department of Electrical Engineering and Computer Science, September 1977, in partial fulfillment of the requirements for the Degree of Master of Science.

ABSTRACT

A general coupled amplitude equation is derived for surface acoustic waves. This equation accounts for the full three-dimensional characteristics of the uncoupled waves. The equation is applied to interactions arising from the nonlinear properties of materials that support surface waves. It is shown how the coupling constants can be calculated from a knowledge of the nonlinear material properties; and the normalized electric field and strain of the linear normal modes. For conservative interactions, any nonlinear three-wave interaction is described by a single coupling constant.

Application of the nonlinear theory to experiments of harmonic generation reveals that the coupling constants scale as fundamental frequency squared. With the coupled amplitudes of the modes normalized to action density, the magnitude of coupling constants at a fundamental frequency of 50 MHz are found to be:

a. for YZ-$LiNbO_3$; $1.1\times10^{9}\ \frac{m}{sec^2 W^{1/2}}$

b. for $(1\bar{1}0)$-(001) $Bi_{12}GeO_{20}$: $1.4\times10^{8}\ \frac{m}{sec^2 W^{1/2}}$

The nonlinear coupled mode theory is then applied to noncollinear three-wave interactions. From this an experiment is designed to measure the magnitude of the coupling constant. With pump frequencies of 36 MHz and 214 MHz, and phase propagation directions of $\theta_{36} = 90°$ and $\theta_{214} = 100°$, on y-cut $LiNbO_3$, a coupling constant of

$$7.9\times10^{8}\ \frac{m}{sec^2 W^{1/2}} \pm 4.0\times10^{8}\ \frac{m}{sec^2 W^{1/2}}$$

is determined.

Thesis Supervisor: Abraham Bers
Title: Professor of Electrical Engineering and Computer Science

ACKNOWLEDGEMENTS

It is with great appreciation I express my thanks to the people who have contributed to my completion of this thesis.

First to Professor Abraham Bers, I express my gratitude for his guidance and patience in supervising the thesis work. Through my undergraduate and graduate acquaintance with him, my background in electrical engineering has been enhanced and Professor Bers provided my introduction to surface acoustic wave technology.

Dr. John Cafarella has been a friend who has shared his office with me for two years. His expert knowledge on circuit theory and electronic systems was instrumental in the design of the detection network used with the experiments. It is with great thanks that I acknowledge his many hours of discussion and assistance. In addition to his professional assistance, John Cafarella's wry humor and unorthodox antics balanced the rigors of the day with comedy.

For my research assistantship at Lincoln Laboratory, and his interest in my work, I thank Mr. Ernest Stern, leader of Group 86, Surface Acoustic Wave Technology.

Dr. Richard Williamson, associate leader of Group 86, I thank for his interest, and many discussions and suggestions.

The other staff members of the Surface Acoustic Wave Technology Group:

Dr. John Melngailis

Dr. Stanley Reible

Dr. Victor Dolat

Dr. Robert Li

Dr. Richard Ralston

Dr. Henry Smith

Dr. Douglas Hurlburt, and

Dr. Manfred Shulz

are greatly appreciated for discussions, suggestions, and equipment during my time with them.

The computer support from Lincoln Laboratory was by way of the excellent programming of Mr. Jon Holtham.

To the instrument lab technicians and the fabrication people, I thank for their skills in fabricating the transducers and construction of the packaging of $LiNbO_3$ crystals. They have been of superb assistance in my understanding of the techniques of fabrication and crystal care, and the use of the electronic equipment. Particular thanks to Mr. Steve Cupoli for the time he spent with the electrostatic probe and me.

Thanks also goes to the Plasma Dynamics Group, Department of Electrical Engineering and Computer Science, for their tolerance of a non-plasma person among their midst, and for the use of the Mathlab Consortium computer system MACSYMA.

Typing of the thesis manuscript was done by Debi Lauricella.

Lastly, I must express my indebtedness and thanks to my parents and sister for the love and encouragement they have shown me. Their

moral and financial support during the two years I have pursued this thesis were instrumental in its completion.

TABLE OF CONTENTS

TABLE OF CONTENTS (cont).

TABLE OF CONTENTS (cont.)

CHAPTER 1

INTRODUCTION

A. Background

Nonlinear properties of materials that support acoustic waves have been explored for the development of new devices in signal processing. Investigations have resulted in theoretical and experimental techniques to examine the nonlinear material properties and interactions of acoustic waves. Previous work has involved bulk acoustic wave and surface acoustic wave (SAW) effects.

The development of a set of equations by R.N. Thurston and K. Brugger led to the first method of determining nonlinear elastic constants [1] [2]. The third-order elastic constants were found to be determinable from the velocity of small amplitude waves in homogeneously stressed media. However, B.E. Powell and M.J. Skove [3] [4] demonstrated that the method developed by Thurston and Brugger determined constants that were not adiabatic or isothermal, but a mix of thermodynamic relations, and do not possess the symmetry of the nonlinear elastic constants under constant thermodynamic equilibrium. Powell and Skove developed a relationship between isothermal constants and those found by the Thurston-Brugger equations. Application of the corrected Thurston-Brugger work to cubic crystals was performed by S.S. Sekoyan [5], [6] and elastic constants of other non-piezoelectric materials have also been examined [32].

The investigation of nonlinear material constants has been extended to piezoelectric materials. Nonlinear acoustic parameters of piezoelectric crystals have been discussed with device application [7], [17], [19], and elaborated upon by V.E. Lyamov [8]. Extension of the Thurston-Brugger work by Y. Nakagawa et al., [9] and A.I. Korobov and V.E. Lyamov [10] has resulted in theoretical and experimental determination of the nonlinear elastic and nonlinear piezoelectric constants with particular application to lithium niobate. The theoretical work retains the thermodynamic mix of the Thurston-Brugger equations as discussed by Powell and Skove. Further, the method for finding nonlinear acoustic constants developed by Y. Nakagawa et al., determines a mixture of nonlinear elastic and nonlinear piezoelectric constants. Hence the knowledge of nonlinear elastic and nonlinear piezoelectric constants are clouded by error of theory and experiment. To avoid the problems encountered by use of the Thurston-Brugger work, R.A. Graham has developed an impact loading technique which applies well-defined states of uniaxial strain to a crystal [11]. The resulting piezoelectric polarization due to the strain is determined from measurements of "time-resolved, short-circuit current during the first wave transit of the shock wave" [11], [12]. Linear and nonlinear hydrostatic piezoelectric constants can be found from this method. The materials examined have been quartz, lithium niobate and lithium tantalate. Unfortunately, a determination of all the nonlinear piezoelectric constants has not been made. Though work has been done to investigate the nonlinear

material constants of piezoelectric materials, the field has opportunities for correcting previous work and experimentally determining the constants.

Concurrent with the studies of the nonlinear material constants of crystalline materials, investigations of various wave interactions that the nonlinear properties cause have been pursued. Among the applications of the nonlinear properties have been parametric interactions, harmonic generation, convolution and correlation devices, and stearing and switching devices. The work has examined bulk wave and surface wave interactions independently, and interactions between bulk and surface waves.

Acoustic bulk wave work has explored all but beam stearing and switching systems. Traveling wave parametric amplification was examined by N.S. Shiren [13]. Experiments and early coupled mode theory have been discussed by Shiren. Convolution and correlation devices with bulk waves were investigated by R.B. Thompson and C.F. Quate [14],[15]. Frequencies near 3 GHz were used with the devices discussed by Thompson and Quate. Bulk wave interactions have usually been done at frequencies higher than surface waves. However, because surface waves can have high power densities with smaller total power than bulk waves, nonlinear phenomenon are generated with less power than for bulk waves. Further the accessability and planar nature of SAW make them attractive for practical devices.

The first investigation into the application of nonlinear properties of piezoelectric materials to convolution and correlation

devices was made by L.O. Svaasand [16],[17]. M. Luukkala and G.S. Kino [18] extended Svaasand's work with surface waves and explored correlation, convolution, and time inversion signal processing capabilities of the nonlinear properties of $LiNbO_3$. Frequencies as high as 220 MHz were used. Later work by M. Luukkala and J. Surakka examine the associated parameters of convolution, correlation, and idler generation for $LiNbO_3$ [19]. Because the nonlinearities of the surface wave materials are weak, these so called elastic convolvers have been superceded by electro-acoustic devices using the nonlinearities of semiconductors [20],[21]. Techniques to increase the efficiency of the elastic convolvers have resulted in beam compression systems pursued by Ph. Defranould and C. Maerfeld [22].

Several surface acoustic wave materials have been used with elastic convolvers. T.C. Lim, E.A. Kraut and R.B. Thompson have examined the nonlinear effects for convolution in the basal plane of PZT-8; y-cut, z-propagating $LiNbO_3$; basal plane of ZnO; y-cut, x-propagating quartz; and (001)-cut, (110)-propagating Bi_{12} Ge O_{20} [23]. Though PZT-8 has the highest nonlinear properties of these materials, trade-offs due to propagation loss and ease of fabrication have resulted in YZ-$LiNbO_3$ being the most popular material for the devices.

Besides convolution and correlation type devices, harmonic generation and other parametric interactions of surface acoustic waves have been experimentally and theoretically investigated. Harmonic generation has been discussed for collinear propagating

waves [24]-[35], and has been more thoroughly investigated than noncollinear work. Nonlinear interactions of noncollinear waves have been pursued with particular applications to switching, beam stearing and parametric amplification devices [36]-[41].

Besides bulk wave interactions and surface wave interactions, in which, respectively, either bulk or surface waves are present, nonlinear interactions between bulk and surface waves have also been investigated. Work has been carried out by T.C. Padmore and G.I. Stegeman [42], and J.M. Rouvaen et al. [43].

With power densities of 1 MW/m^2, the nonlinear acoustic stress and electric displacement fields can be five orders of magnitude smaller than the linear fields, when computed from the nonlinear constants [9]-[10] and linear fields. This has led to coupled mode theory becoming the most prominent technique in modeling the nonlinear interactions. However, the development of coupled amplitude equations describing the interactions has been incomplete or inconsistent. with coupled mode theory.

This discussion has been primarily intended to convey the range of work in nonlinear acoustic wave interactions and devices. Other work has been done, but only the general areas of study are reviewed here.

B. Outline of Thesis

The thesis is divided into the five following chapters. Chapter 2 discusses general theory in regard to the development of a general

coupled amplitude equation, and application to nonlinear interactions and the coupling constants of nonlinear interactions. Chapter 3 examines collinear harmonic generation from the coupled mode theory discussed in Chapter 2. Chapter 4 is a study of non-collinear three-wave theory, and an experiment to determine the magnitude of the coupling constants. Chapter 5 gives the results of one set of experiments and Chapter 6 is a concluding discussion reviewing Chapters 2 through 5, and suggesting future work.

CHAPTER 2

THEORY

A. Chapter Outline

This chapter is composed of five ensuing sections. It begins with a review and critique of previous theories that model nonlinear interactions of surface acoustic waves due to the nonlinearities of the materials that can support surface waves. Because of the problems and inconsistencies of these theories, a general coupled amplitude equation is developed from coupled mode theory, and this is presented in the second section. The third section discusses the application of the equation from section B to the nonlinear case. Section D discusses the coupling constants found from the nonlinear theory, and the last section summarizes the chapter.

B. Previous Work and Critique

Nonlinear properties of materials used with surface acoustic wave technology have been utilized in theoretical investigations on the potential applications and problems of nonlinear interactions. Several approaches have been taken to theoretically model collinear and noncollinear interactions. These methods include a one-dimensional, single-nonlinear parameter theory [28]-[29], "nonlinear cross sections-energy approach" [30]-[32], numerical evaluation of a nonlinear wave equation [32], and a "general perturbation formula" developed for nonlinear interactions in piezoelectric media [41]. A brief review

of these approaches shall be presented.

The one-dimensional, single-nonlinear parameter theory is illustrated through the work done by E.L. Adler et al. [28]. This method derives a system of coupled differential equations from a one-dimensional wave equation that phenomenologically introduces a single nonlinear parameter into the wave equation:

$$\frac{\partial^2 s}{\partial t^2} - v_s^2 \frac{\partial^2 s}{\partial z^2} = \beta v_s^2 \frac{\partial^2 s^2}{\partial z^2} \qquad (2.B.1)$$

where s could be any displacement, strain, or other combination of surface wave variables, and z is the direction of propagation. The fact that a surface wave decays exponentially into the supporting material is assumed to be contained in v_s. The term β is the single phenomenological nonlinear parameter. This approach has been used to model phase matched harmonic generation [28], and harmonic generation with dispersion [29]. For the dispersive cases, it is assumed that the phase velocity is linearly porportional to frequency or equivalently the dispersion relation of k vs. ω can be approximated by a quadratic of the form of ω^2. Therefore a single-dispersion parameter can be used to describe dispersive effects [29]. The single-nonlinear parameter has been successful in modeling both the non-dispersive and dispersive interactions, and single-dispersion parameter calculations have agreed with experimental results [28], [29]. The effectiveness of the single nonlinear parameter theory is highly fortuitous, and little physical insight has been gained. There

is no understanding as to how the decay of a surface wave is contained in v_s, or if it is contained in v_s, particularly when one considers steady-state interactions in which the v_s^2 term drops from the single parameter equations. Further no information is obtained as to how the surface wave variables interact to drive the nonlinearities, or why the single nonlinear parameter is successful.

A "nonlinear cross sections-energy approach" is used by E.G. Lean and C.C. Tsang [30]-[31], and P.J. Vella et al. [32] to derive a system of nonlinearly coupled amplitude equations. This technique equates the work done on a surface wave by nonlinear forces to the change in energy of the surface acoustic wave [30]-[32]. To compute energy storage and power flow an integration over decay depth of surface waves must be done, thereby accounting for the decay properties of surface waves. However, to derive the coupled mode equations from the conservation equation that is obtained from energy-power arguments, it is assumed the phase of the slowly varying amplitude of each wave is a constant. As is presented in [30]-[32], this assumption is presumed a general one for nonlinear interactions, but this is not consistent with coupled mode theory. A coupled interaction could produce slowly varying changes in phase as well as magnitude of the amplitude functions, and to a priori consider a slowly varying nonlinear interaction to have constant phase is to misinterpret the meaning of slowly varying. The phase of the amplitude may be slowly varying in comparison to the rapid oscillations of the propagation vector, or frequency of the normal mode, but the

change in phase of the slowly varying amplitude could be comparable with the change in magnitude. Special cases exist in which the phase is constant, but these special cases are not considered nor specified in [30]-[32]. One of these special cases is discussed in detail in Chapter 4, and it is applicable to the experiments that are described in [24]-[35]. This special case accounts for the success this method has for modeling the experimental results.

A numerical analysis of a nonlinear wave equation is also discussed by P.J. Vella et al. The analysis considers the nonlinear volume forces and the nonlinear surface boundary conditions. The results of the calculations indicate that a SAW growing from zero and being generated by two nonlinearly interacting surface waves rapidly approaches the normal-mode SAW for the frequency of the wave being produced. For most materials only a few wavelengths are needed for the generated wave to become a normal-mode [32]. Since the generated wave rapidly approaches a normal-mode, coupled mode theory is the most tractable means of modeling the nonlinear interactions.

Noncollinear work using the results of the "energy cross section" analysis by Lean and Tsang [30]-[31] have been discussed by K.L. Davis, V.L. Newhouse, and C.L. Chen [37]-[40]. Besides the inconsistency of energy-analysis for collinear interactions of [30]-[31], a further problem occurs in that the two-dimensional character of the collision of noncollinear SAW's is not fully accounted for. A set of equations [38]-[39]

$$\frac{\partial A_1}{\partial x_1} = \frac{-i\lambda_1}{2} A_2^* A_3 \exp(-i\bar{q}_+\bar{r}) \tag{2.B.2}$$

$$\frac{\partial A_2^*}{\partial x_2} = \frac{i\lambda_2}{2} A_1 A_3^* \exp(+i\bar{q}_+\bar{r}) \tag{2.B.3}$$

$$\frac{\partial A_3}{\partial x_3} = \frac{-i\lambda_3}{2} A_1 A_2 \exp(+i\bar{q}_+\bar{r}) \tag{2.B.4}$$

are derived, in which

$\bar{q}_+ = \bar{k}_3 - (\bar{k}_1 + \bar{k}_2)$, and $\bar{k}_i$'s are propagation vectors,

A_i = slowly varying magnitude of the mechanical displacement of i^{th} wave,

λ_i = phenomenological coupling constants,

x_i = a coordinate axis specified by $\vec{k}_i$.

Given, y_i is perpendicular to x_i, and z_i is the direction of surface wave decay and perpendicular to y_i and x_i, the derivation of the above equations specifically states that for noncollinear interactions, the coupled mode description is still valid provided $\left|\frac{\partial A_i}{\partial x_i}\right|$ and $\left|\frac{\partial A_i}{\partial z_i}\right|$ are negligible [38]-[39]. To the contrary, the coupled mode description is valid even if $\left|\frac{\partial A_i}{\partial x_i}\right|$ and $\left|\frac{\partial A_i}{\partial z_i}\right|$ are not negligible. $\frac{\partial A_i}{\partial z_i}$ does not appear in coupled mode theory for SAW due to the decay nature of the normal modes of surface waves and propagation in two dimensions. Further, because of the anisotropy encountered with surface acoustic

wave materials, the phenomenon of beam steering occurs [52] and the propagation of the surface waves are not in the direction of $\vec{k}_i$, and a $\frac{\partial A_i}{\partial y_i}$ term must be introduced. Another difficulty arises due to the introduction of three sets of coordinates for each wave which makes calculation and analysis clumsy. These problems are avoided by a "general perturbation formula" developed by R.C. Ho and C.L. Chen [41].

Later work done by R.C. Ho and C.L. Chen [41] by-passes the energy cross-section approach, and develops a coupled mode equation from Maxwell's equations and the acoustic field equations. As presented, the "general perturbation formula", which is a coupled amplitude equation, is derived only for steady-state interactions and the derivation considers only one mode. An integration over decay depth is performed which accounts for this SAW characteristic, and there are no assumptions regarding phase. However, the theoretical development is not complete and an appreciation for the integration over depth is missing. As stated, only one mode is considered in the interaction, but when working with the electromagnetic and acoustic field equations, the total fields must be considered which are sums over all modes present, and this is not accounted for in [41]. The integration over decay depth is a necessity in finding the coupled amplitude equation that describes the evolution of each mode separately. The "general perturbation formula" method given in [41] almost presents a consistent derivation of the nonlinear interactions of surface waves; however, the derivation does not consider the existence of multiple-mode cases particularly since the "general

formula" is applied to nonlinear interactions where at least three modes are interacting. Further the discussion does not include time varying problems.

The primary method employed to model weak nonlinear interactions of acoustic surface waves has been to apply coupled mode theory to derive coupled amplitude equations. To date, each approach taken to derive such a theory has not been complete or consistent with coupled mode theory or the qualities of surface acoustic waves. As an alternative to these methods, a general coupled mode theory will be derived that allows for the decay characteristics of SAW's into the supporting material and the simultaneous existence of many modes. The coupled mode theory that will be developed is applicable to surface waves on anisotropic and/or piezoelectric materials. Once the general coupled mode theory has been derived, it will be used to model nonlinear interactions. From the derivations, it will be seen how the decay characteristics of surface waves enter coupled mode theory, and what material properties contribute to the nonlinear interactions.

C. General Coupled Mode Theory

A detailed discussion of the derivation of the general coupled amplitude equation is given in Appendix I. The basic arguments are presented here. Fig. 2.1 illustrates the Cartesian coordinate system to be used in this discussion.

The acoustic field equations and Maxwell's equations for a

Fig. 2.1

Cartesian Coordinate System

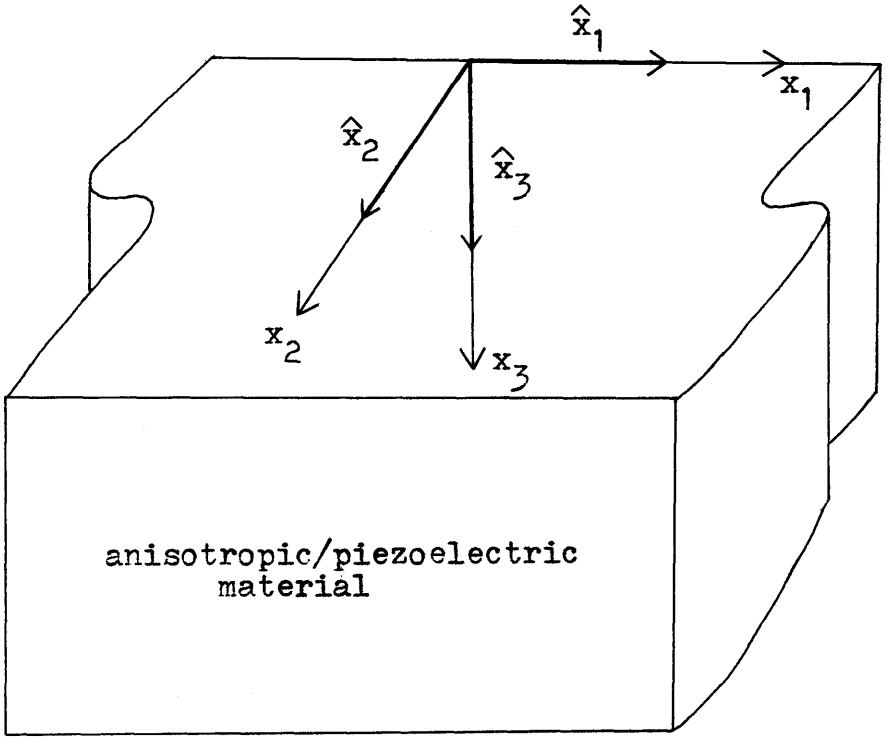

$\hat{x}_i$: unit vector in i^{th} direction

lossless-charge free medium can be written [47] as

$$\bar{\nabla} \cdot \bar{\bar{T}} = \rho \frac{\partial \bar{v}}{\partial t} - \bar{F}_e \tag{2.C.1}$$

$$\frac{\partial \bar{\bar{S}}}{\partial t} = \nabla_s \bar{v} \tag{2.C.2}$$

$$\bar{\nabla} \times \bar{E} = \frac{-\partial \bar{B}}{\partial t} \tag{2.C.3}$$

$$\bar{\nabla} \times \bar{H} = \frac{\partial \bar{D}}{\partial t} + \bar{J}_e \tag{2.C.4}$$

$$\nabla \cdot \bar{B} = 0 \tag{2.C.5}$$

$$\bar{\nabla} \cdot \bar{D} = \rho_e \tag{2.C.6}$$

where $\bar{J}_e$, $\bar{F}_e$, ρ_e are external perturbations of current density, force denisty, and charge density respectively. The other variables can be identified as stress ($\bar{\bar{T}}$), strain ($\bar{\bar{S}}$), particle velocity ($\bar{v}$), electric field ($\bar{E}$), magnetic flux ($\bar{B}$), magnetic field ($\bar{H}$), electric displacement ($\bar{D}$), and mass density (ρ). The expression $\nabla_s \bar{v}$ in equation (2.C.2) is the matrix form of the tensor

$$\frac{\partial S_{ij}}{\partial t} = \frac{1}{2}\left[\frac{\partial v_i}{\partial x_j} + \frac{\partial v_j}{\partial x_i}\right] .$$

The total of each field quantity is the sum of the contribution from each mode that is propagating. The total of each field is given by the following expressions:

$$\bar{v} = \sum_{\beta=1}^{\infty} \left[\underline{v}_\beta(x_3) a_\beta(t,x_1,x_2) e^{i(\omega_\beta t - \bar{k}_\beta \cdot \bar{r}')} \right] \tag{2.C.7}$$

$$\bar{\bar{T}} = \sum_{\beta=1}^{\infty} \left[\underline{\underline{t}}_\beta(x_3) a_\beta(t,x_1,x_2) e^{i(\omega_\beta t - \bar{k}_\beta \cdot \bar{r}')} \right] \tag{2.C.8}$$

$$\bar{\bar{S}} = \sum_{\beta=1}^{\infty} \left[\underline{\underline{s}}_\beta(x_3) a_\beta(t,x_1,x_2) e^{i(\omega_\beta t - \bar{k}_\beta \cdot \bar{r}')} \right] \tag{2.C.9}$$

$$\bar{E} = \sum_{\beta=1}^{\infty} \left[\underline{e}_\beta(x_3) a_\beta(t,x_1,x_2) e^{i(\omega_\beta t - \bar{k}_\beta \cdot \bar{r}')} \right] \tag{2.C.10}$$

$$\bar{B} = \sum_{\beta=1}^{\infty} \left[\underline{b}_\beta(x_3) a_\beta(t,x_1,x_2) e^{i(\omega_\beta t - \bar{k}_\beta \cdot \bar{r}')} \right] \tag{2.C.11}$$

$$\bar{H} = \sum_{\beta=1}^{\infty} \left[\underline{h}_\beta(x_3) a_\beta(t,x_1,x_2) e^{i(\omega_\beta t - \bar{k}_\beta \cdot \bar{r}')} \right] \tag{2.C.12}$$

$$\bar{D} = \sum_{\beta=1}^{\infty} \left[\underline{d}_\beta(x_3) a_\beta(t,x_1,x_2) e^{i(\omega_\beta t - \bar{k}_\beta \cdot \bar{r}')} \right] \tag{2.C.13}$$

where

$$\bar{k}_\beta = k_1^{(\beta)} \hat{x}_1 + k_2^{(\beta)} \hat{x}_2$$

$$\overline{r}' = x_1\hat{x}_1 + x_2\hat{x}_2,$$

the subscript β indicates the β^{th} mode. The terms $\underline{v}_\beta(x_3)$, $\underline{\underline{t}}_\beta(x_3)$, $\underline{\underline{s}}_\beta(x_3)$, $\underline{e}_\beta(x_3)$, $\underline{b}_\beta(x_3)$, $\underline{h}_\beta(x_3)$, and $\underline{d}_\beta(x_3)$ are unperturbed polarization amplitudes of the field quantities of the β^{th} mode. $\underline{v}_\beta(x_3)$, $\underline{e}_\beta(x_3)$, $\underline{d}_\beta(x_3)$, $\underline{h}_\beta(x_3)$, and $\underline{b}_\beta(x_3)$ are vector quantities and functions of x_3 only. $\underline{\underline{t}}_\beta(x_3)$ and $\underline{\underline{s}}_\beta(x_3)$ are tensors and also functions of x_3 only. The amplitude terms $a_\beta(t,x_1,x_2)$ are dimensionless, slowly varying functions of position and time, that is:

$$\left|\frac{\partial a_\beta(t,x_1,x_2)}{\partial t}\right| << \left|\omega_\beta a_\beta(t,x_1,x_2)\right|$$

$$\left|\frac{\partial a_\beta(t,x_1,x_2)}{\partial x_1}\right| << \left|k_1^{(\beta)} a_\beta(t,x_1,x_2)\right|$$

$$\left|\frac{\partial a_\beta(t,x_1,x_2)}{\partial x_2}\right| << \left|k_2^{(\beta)} a_\beta(t,x_1,x_2)\right|$$

To facilitate the derivation of the coupled amplitude equation, the following identities are made:

$$a_\beta = a_\beta(t,x_1,x_2) \qquad \underline{v}_\beta = \underline{v}_\beta(x_3) \qquad \underline{\underline{t}}_\beta = \underline{\underline{t}}_\beta(x_3)$$

$$\underline{\underline{s}}_\beta = \underline{\underline{s}}_\beta(x_3) \qquad \underline{e}_\beta = \underline{e}_\beta(x_3) \qquad \underline{b}_\beta = \underline{b}_\beta(x_3)$$

$$\underline{h}_\beta = \underline{h}_\beta(x_3) \qquad \underline{d}_\beta = \underline{d}_\beta(x_3)$$

With the definitions of the field quantities given in (2.C.7) - (2.C.13), $\overline{F}_e$, $\overline{J}_e$, and ρ_e are the complex external perturbations.

The next step in the derivation is to substitute (2.C.7) - (2.C.13) into equations (2.C.1) - (2.C.6) and expand the results. The expressions derived consist of slowly varying and fast varying terms as described above. The fast terms determine the dispersion relation of the normal modes, and the slow ones are used to find the coupled mode equations. The perturbations $\overline{F}_e$, $\overline{J}_e$, and ρ_e are assumed slowly varying and are grouped with the slow terms. Fast varying terms are not given here, but can be found in Appendix I. Slow terms used to derive the coupled mode equations:

$$\sum_\beta \left[(\underline{\underline{t}}_\beta \cdot \overline{\nabla} a_\beta) e^{i(\omega_\beta t - \overline{k}_\beta \cdot \overline{r}')} \right] = \rho \sum_\beta \left[\left(\underline{v}_\beta \frac{\partial a_\beta}{\partial t} \right) e^{i(\omega_\beta t - \overline{k}_\beta \cdot \overline{r}')} \right] - \overline{F}_e \quad (2.C.14)$$

$$\sum_\beta \left[\left(\underline{\underline{s}}_\beta \frac{\partial a_\beta}{\partial t} \right) e^{i(\omega_\beta t - \overline{k}_\beta \cdot \overline{r}')} \right] = \sum_\beta \left[\frac{1}{2} (\underline{v}_\beta \overline{\nabla} a_\beta + (\overline{\nabla} a_\beta) \underline{v}_\beta) e^{i(\omega_\beta t - \overline{k}_\beta \cdot \overline{r}')} \right] \quad (2.C.15)$$

$$\sum_\beta \left[(\overline{\nabla} a_\beta \times \underline{e}_\beta) e^{i(\omega_\beta t - \overline{k}_\beta \cdot \overline{r}')} \right] = -\sum_\beta \left[\left(\underline{b}_\beta \frac{\partial a_\beta}{\partial t} \right) e^{i(\omega_\beta t - \overline{k}_\beta \cdot \overline{r}')} \right] \quad (2.C.16)$$

$$\sum_\beta \left[(\overline{\nabla} a_\beta \times \underline{h}_\beta) e^{i(\omega_\beta t - \overline{k}_\beta \cdot \overline{r}')} \right] = \sum_\beta \left[\left(\underline{d}_\beta \frac{\partial a_\beta}{\partial t} \right) e^{i(\omega_\beta t - \overline{k}_\beta \cdot \overline{r}')} \right] + \overline{J}_e \quad (2.C.17)$$

The expressions $\underline{v}_\beta \bar{\nabla} a_\beta$, $(\bar{\nabla} a_\beta)\underline{v}_\beta$ are diadic products.

Equations (2.C.14) - (2.C.17) describe the coupled mode interaction, as a sum over all the modes. However, one is interested in examining the effects of the coupling on each mode alone, and what contributes to the evolution of each mode. To obtain the equations that give the behavior of each mode, one works through the orthogonality relation of surface waves. This orthogonality relation is derived in Appendix II, and shall only be applied here.

The coupled amplitude equation is developed after performing the following operations on equations (2.C.14) - (2.C.17) with field quantities of mode α:

$$\frac{\underline{v}_\alpha^*}{4} e^{-i(\omega_\alpha t - \bar{k}_\alpha \cdot \bar{r}')} \cdot \quad (2.C.14)$$

$$\frac{\underline{t}_\alpha^*}{4} e^{-i(\omega_\alpha t - \bar{k}_\alpha \cdot \bar{r}')} : \quad (2.C.15)$$

$$\frac{\underline{h}_\alpha^*}{4} e^{-i(\omega_\alpha t - \bar{k}_\alpha \cdot \bar{r}')} \cdot \quad (2.C.16)$$

$$\frac{-\underline{e}_\alpha^*}{4} e^{-i(\omega_\alpha t - \bar{k}_\alpha \cdot \bar{r}')} \cdot \quad (2.C.17)$$

and letting $\Delta\omega = \omega_\beta - \omega_\alpha$, $\Delta\bar{k} = \bar{k}_\beta - \bar{k}_\alpha$. One has:

$$\frac{1}{4}\sum_{\beta}\left[(\underline{v}^*_{\alpha}\cdot\underline{\underline{t}}_{\beta}\cdot\bar{\nabla}a_{\beta})e^{i(\Delta\omega t-\Delta\bar{k}\cdot\bar{r}')}\right] = \frac{1}{4}\sum_{\beta}\left[\rho\underline{v}^*_{\alpha}\cdot\underline{v}_{\beta}\frac{\partial a_{\beta}}{\partial t}e^{i(\Delta\omega t-\Delta\bar{k}\cdot\bar{r}')}\right]$$

$$-\frac{1}{4}\underline{v}^*_{\alpha}\cdot\bar{F}_e\, e^{-i(\omega_{\alpha}t-\bar{k}_{\alpha}\cdot\bar{r}')} \qquad (2.C.18)$$

$$\frac{1}{4}\sum_{\beta}\left[\left(\underline{\underline{t}}^*_{\alpha}:\underline{\underline{s}}_{\beta}\frac{\partial a_{\beta}}{\partial t}\right)e^{i(\Delta\omega t-\Delta\bar{k}\cdot\bar{r}')}\right] = \frac{1}{4}\sum_{\beta}\left[\frac{1}{2}\,\underline{\underline{t}}^*_{\alpha}:(\underline{v}_{\beta}\bar{\nabla}\alpha_{\beta}+(\bar{\nabla}a_{\beta})\underline{v}_{\beta})e^{i(\Delta\omega t-\Delta\bar{k}\cdot\bar{r}')}\right] \qquad (2.C.19)$$

$$\frac{1}{4}\sum_{\beta}\left[\underline{h}^*_{\alpha}\cdot(\bar{\nabla}a_{\beta}\times\underline{e}_{\beta})e^{i(\Delta\omega t-\Delta\bar{k}\cdot\bar{r}')}\right] = \frac{1}{4}\sum_{\beta}\left[\left(\underline{h}^*_{\alpha}\cdot\underline{b}_{\beta}\frac{\partial a_{\beta}}{\partial t}\right)e^{i(\Delta\omega t-\Delta\bar{k}\cdot\bar{r}')}\right] \qquad (2.C.20)$$

$$\frac{1}{4}\sum_{\beta}\left[-\underline{e}^*_{\alpha}\cdot(\bar{\nabla}a_{\beta}\times\underline{h}_{\beta})e^{i(\Delta\omega t-\Delta\bar{k}\cdot\bar{r}')}\right] = -\frac{1}{4}\sum_{\beta}\left[\left(\underline{e}^*_{\alpha}\cdot\underline{d}_{\beta}\frac{\partial a_{\beta}}{\partial t}\right)e^{i(\Delta\omega t-\Delta\bar{k}\cdot\bar{r}')}\right]$$

$$-\frac{1}{4}e^*_{\alpha}\bar{J}_e\, e^{-i(\omega_{\alpha}t-\bar{k}_{\alpha}\cdot\bar{r}')} \qquad (2.C.21)$$

By regrouping terms and using appropriate vector and tensor identities, equations (2.C.18) - (2.C.21) can be rewritten as

$$\frac{1}{4}\sum_{\beta}\left[\left(\rho\underline{v}^*_{\alpha}\cdot\underline{v}_{\beta}\frac{\partial a_{\beta}}{\partial t}-\underline{v}^*_{\alpha}\cdot\underline{\underline{t}}_{\beta}\cdot\bar{\nabla}a_{\beta}\right)e^{i(\Delta\omega t-\Delta\bar{k}\cdot\bar{r}')}\right] = \frac{1}{4}\underline{v}^*_{\alpha}\cdot\bar{F}_e\, e^{-i(\omega_{\alpha}t-k_{\alpha}\cdot\bar{r}')} \qquad (2.C.22)$$

$$\frac{1}{4}\sum_{\beta}\left(\left(\underline{\underline{t}}^*_{\alpha}:\underline{\underline{s}}_{\beta}\frac{\partial a_{\beta}}{\partial t} - v_{\beta}\underline{\underline{t}}^*_{\alpha}\bar{\nabla}a_{\beta}\right)e^{i(\Delta\omega t-\Delta\bar{k}\cdot\bar{r}')}\right) = 0 \qquad (2.C.23)$$

$$\frac{1}{4}\sum_{\beta}\left(\left(\underline{h}^*_{\alpha}\underline{b}_{\beta}\frac{\partial a_{\beta}}{\partial t} + (\underline{e}_{\beta}\times\underline{h}^*_{\alpha})\cdot\bar{\nabla}a_{\beta}\right)e^{i(\Delta\omega t-\Delta\bar{k}\cdot\bar{r}')}\right) = 0 \qquad (2.C.24)$$

$$\frac{1}{4}\sum_{\beta}\left(\left(\underline{e}^*_{\alpha}\underline{d}_{\beta}\frac{\partial a_{\beta}}{\partial t} + (\underline{e}^*_{\alpha}\times\underline{h}_{\beta})\cdot\bar{\nabla}a_{\beta}\right)e^{i(\Delta\omega t-\Delta\bar{k}\cdot\bar{r}')}\right) = \frac{1}{4}\underline{e}^*_{\alpha}\bar{J}_e\, e^{-i(\omega_{\alpha}t-\bar{k}_{\alpha}\cdot\bar{r}')} \qquad (2.C.25)$$

By adding (2.C.22) - (2.C.25) one can reduce these equations to a single equation which contains the perturbing terms $\bar{J}_e$ and $\bar{F}_e$.

$$\sum_{\beta}\left[\left[\frac{1}{4}(\rho\underline{v}^*_{\alpha}\underline{v}_{\beta}+\underline{\underline{t}}^*_{\alpha}:\underline{\underline{s}}_{\beta}+\underline{h}^*_{\alpha}\underline{b}_{\beta}+\underline{e}^*_{\alpha}\underline{d}_{\beta})\frac{\partial a_{\beta}}{\partial t} + \frac{1}{4}(-\underline{v}^*_{\alpha}\underline{\underline{t}}_{\beta}-\underline{v}_{\beta}\underline{\underline{t}}^*_{\alpha}+(\underline{e}_{\beta}\times\underline{h}^*_{\alpha})+(\underline{e}^*_{\alpha}\times\underline{h}_{\beta}))\cdot\bar{\nabla}a_{\beta}\right]\right]$$

$$e^{i(\Delta\omega t-\Delta\bar{k}\cdot\bar{r}')} = \frac{1}{4}[\underline{v}^*_{\alpha}\bar{F}_e - \underline{e}^*_{\alpha}\bar{J}_e]e^{-i(\omega_{\alpha}t-\bar{k}_{\alpha}\cdot\bar{r}')} \qquad (2.C.26)$$

Equation (2.C.26) is still a sum over all modes of terms that are products of operators on the unperturbed amplitudes $\underline{v}_{\alpha}$, $\underline{\underline{t}}_{\alpha}$, $\underline{b}_{\alpha}$, $\underline{d}_{\alpha}$, $\underline{h}_{\alpha}$, $\underline{\underline{s}}_{\alpha}$, $\underline{e}_{\alpha}$, and slowly varying amplitudes a_{β}. However this equation is in a form from which an equation for a specific mode can be found.

Integrating equation (2.C.26) with respect to x_3, $-\infty \leq x_3 \leq \infty$; defining the identities:

$$\langle W_{\alpha\beta} \rangle = \frac{1}{4} \int_{-\infty}^{\infty} (\rho \underline{v}^*_\alpha \cdot \underline{v}_\beta + \underline{\underline{t}}^*_\alpha : \underline{\underline{s}}_\beta + \underline{h}^*_\alpha \cdot \underline{b}_\beta + \underline{e}^*_\alpha \cdot \underline{d}_\beta) dx_3 \qquad (2.C.27)$$

$$\langle \overline{S}_{\alpha\beta} \rangle = \frac{1}{4} \int_{-\infty}^{\infty} (-\underline{v}^*_\alpha \cdot \underline{\underline{t}}_\beta - \underline{v}_\beta \cdot \underline{\underline{t}}^*_\alpha + \underline{e}_\beta \times \underline{h}^*_\alpha + \underline{e}^*_\alpha \times \underline{h}_\beta) dx_3 \qquad (2.C.28)$$

and rewriting the results of the integration of (2.C.26) by substituting (2.C.27) and (2.C.28) one has:

$$\sum_\beta \left(\left[\langle W_{\alpha\beta} \rangle \frac{\partial a_\beta}{\partial t} + \langle \overline{S}_{\alpha\beta} \rangle \overline{\nabla} a_\beta \right] e^{i(\Delta\omega t - \Delta\overline{k} \cdot \overline{r}')} \right) = \int_{-\infty}^{\infty} \frac{1}{4} [\underline{v}^*_\alpha \cdot \overline{F}_e - \underline{e}^*_\alpha \cdot \overline{J}_e] e^{-i(\omega_\alpha t - \overline{k}_\alpha \cdot \overline{r}')} dx_3 \qquad (2.C.29)$$

From the orthogonality relations for surface acoustic waves derived in Appendix II,

$$(\overline{k}_\alpha - \overline{k}_\beta) \cdot \langle \overline{S}_{\alpha\beta} \rangle = 0$$

$$(\omega_\alpha - \omega_\beta) \langle W_{\alpha\beta} \rangle = 0$$

If $\alpha \neq \beta$, then $\langle \overline{S}_{\alpha\beta} \rangle = 0$ and $\langle W_{\alpha\beta} \rangle = 0$, and thus the only non-zero term of the $\sum_\beta$ expression in (2.C.29) is $\beta = \alpha$, and (2.C.29) becomes:

$$\langle W_{\alpha\alpha} \rangle \frac{\partial a_\alpha}{\partial t} + \langle \overline{S}_{\alpha\alpha} \rangle \overline{\nabla} a_\alpha = \int_{-\infty}^{\infty} \frac{1}{4} [\underline{v}^*_\alpha \cdot \overline{F}_e - \underline{e}^*_\alpha \cdot \overline{J}_e] e^{-i(\omega_\alpha t - \overline{k}_\alpha \cdot \overline{r}')} dx_3 \qquad (2.C.30)$$

$\langle W_{\alpha\alpha} \rangle$ and $\langle \bar{S}_{\alpha\alpha} \rangle$ are the time average energy density and power density respectively of the α^{th} mode. The units of the energy density and power density are

$$[\langle W_{\alpha\alpha} \rangle] = \frac{\text{(unit energy)}}{\text{(unit propagation length)(unit beam width)}}$$

$$[\langle \bar{S}_{\alpha\alpha} \rangle] = \frac{\text{(unit power)}}{\text{(unit beam width)}}$$

For notation,

$$\langle W_{\alpha} \rangle = \langle W_{\alpha\alpha} \rangle$$

$$\langle \bar{S}_{\alpha} \rangle = \langle \bar{S}_{\alpha\alpha} \rangle$$

The ratio

$$\frac{\langle \bar{S}_{\alpha\alpha} \rangle}{\langle W_{\alpha\alpha} \rangle} = \bar{v}_{g\alpha} \tag{2.C.31}$$

is the group velocity of the α^{th} mode. Dividing equation (2.C.30) by $\langle W_{\alpha\alpha} \rangle$ and using the identity (2.C.31) the coupled amplitude equation for mode α can be written as:

$$\frac{\partial a_{\alpha}}{\partial t} + \bar{v}_{g\alpha} \cdot \bar{\nabla} a = \int_{\infty}^{\infty} \frac{\frac{1}{4}[\underline{v}_{\alpha}^{*} \bar{F}_e - \underline{e}_{\alpha}^{*} \bar{J}_e] e^{-i(\omega_{\alpha} t - \bar{k}_{\alpha} \cdot \bar{r}')}}{\langle W_{\alpha} \rangle} dx_3 \tag{2.C.32}$$

Equation (2.C.32) is the general form of a coupled mode equation for surface acoustic waves on a lossless medium. For a material that is weakly lossy, a term of the form $\nu_\alpha a_\alpha$, where ν_α is a constant, can be added to the left side of (2.C.32) to account for small perturbations due to loss. Therefore:

$$\frac{\partial a_\alpha}{\partial t} + \bar{v}_{g\alpha}\cdot\bar{\nabla}a + \nu_\alpha a_\alpha = \frac{\int_{-\infty}^{\infty} \frac{1}{4}[\underline{v}_\alpha\cdot\bar{F}_e - \underline{e}_\alpha\cdot\bar{J}_e]e^{-i(\omega_\alpha t - \bar{k}_\alpha\cdot\bar{r}')}\,dx_3}{\langle W_\alpha\rangle} \qquad (2.C.33)$$

This is the coupled mode equation that is sought and can be used to describe linear and nonlinear interactions.

It should be noted that no assumptions regarding the phase of a_α have been made, the decay effects of surface waves are accounted for by an integral over x_3, and multi-mode existence and interactions are contained in the derivation and resultant formalism. Further, no assumptions regarding anisotropy or piezoelectricity have been made on the material supporting the surface waves, and thus the coupled amplitude equation describes interactions in anisotropic and/or piezoelectric media.

With the development of equation (2.C.33), a specific application is made to nonlinear interactions of surface acoustic waves due to the nonlinear properties of the material the waves are propagating through.

D. Nonlinear Theory

Materials used with surface acoustic wave devices have exhibited weak nonlinear properties that perturb the linear normal mode propagation. Since the nonlinear properties are weak, the nonlinear interactions that result can be viewed as an external perturbation on the normal modes that are travelling through a given material. Therefore the nonlinearities enter the coupled mode equation (2.C.33), through the external current density $\overline{J}_e$ and the external force density $\overline{F}_e$. Hence, one must determine $\overline{J}_e$ and $\overline{F}_e$, two complex quantities, from the nonlinear properties of a given material. The resultant expressions for $\overline{J}_e$ and $\overline{F}_e$ are then substituted into equation (2.C.33) to give a nonlinearly coupled equation. Appendix IV contains a detailed discussion of the derivation. A basic discussion is presented here.

The nonlinearities that contribute to the interactions are defined from the electric Gibbs function (G) [48], [9]:

$$G = \frac{1}{2} c_{ijk\ell} S_{ij} S_{k\ell} - e_{ijk} E_i S_{jk} - \frac{1}{2} e_{ij} E_i E_j +$$

$$\frac{1}{6} \theta_{ijk\ell mn} S_{ij} S_{k\ell} S_{mn} - \frac{1}{2} \eta_{ijk\ell m} E_i S_{jk} S_{\ell m} -$$

$$\frac{1}{2} Q_{ijk\ell} E_i E_j S_{k\ell} - \frac{1}{6} O_{ijk} E_i E_j E_k - \sigma T \qquad (2.D.1)$$

Here sum over repeated indices is assumed, and magnetic effects are not considered. The terms in the above expression are:

S_{ij} = strain components

E_i = electric field components

$c_{ijk\ell}$ = elastic stiffness constants

e_{ijk} = piezoelectric constants

e_{ij} = dielectric constants

$\theta_{ijk\ell mn}$ = nonlinear elastic constants

$\eta_{ijk\ell m}$ = nonlinear piezoelectric constants

$Q_{ijk\ell}$ = electrostriction constants

O_{ijk} = electro-optic constants

σ = entropy

T = temperature

From the electric Gibbs function, the stress (T_{ij}) components, and electric displacement (D_i) components, can be determined:

$$T_{ij} = \left(\frac{\partial G}{\partial S_{ij}}\right)_{E_k,T} \tag{2.D.2}$$

$$D_i = -\left(\frac{\partial G}{\partial E_i}\right)_{S_{ij},T} \tag{2.D.3}$$

Upon substituting the expression for G in equation (2.D.1) into

(2.D.2) and (2.D.3) one finds that T_{ij} and D_i are composed of a linear and nonlinear part

$$T_{ij} = T^{L}_{ij} + T^{NL}_{ij} \tag{2.D.4}$$

$$D_i = D^{L}_{i} + D^{NL}_{i} \tag{2.D.5}$$

The T^{NL}_{ij} and D^{NL}_{i} are assumed weak perturbations on the linear stress (T^{L}_{ij}) and linear electric displacement (D^{L}_{i}). D^{NL}_{i} and T^{NL}_{ij} are responsible for the coupling of modes for this situation. In terms of the electric field and strain T^{NL}_{ij} and D^{NL}_{i} are:

$$T^{NL}_{ij} = -\eta_{kij\ell m}E_k S_{\ell m} + \frac{1}{2}\theta_{ijk\ell mn}S_{k\ell}S_{mn} - \frac{1}{2}Q_{k\ell ij}E_k E_\ell \tag{2.D.6}$$

$$D^{NL}_{i} = Q_{ijk\ell}E_j S_{k\ell} + \frac{1}{2}\eta_{ijk\ell m}S_{jk}S_{\ell m} + \frac{1}{2}O_{ijk}E_j E_k \tag{2.D.7}$$

Following coupled mode theory, T^{NL}_{ij} and D^{NL}_{i} are determined from the unperturbed linear strain and linear electric field. The total unperturbed electric and strain fields are a sum of the contributions from each normal mode. Further, the field quantities in equation (2.D.1) are real, but can be represented as a sum of a complex term and its complex conjugate:

$$E_i = \frac{1}{2}\left[\sum_{\beta=1}^{\infty} e_i^{(\beta)}(x_3)a_\beta(t,x_1,x_2)e^{i(\omega_\beta t - \bar{k}_\beta\cdot\bar{r}')} + c.c.\right] \tag{2.D.8}$$

$$S_{ij} = \frac{1}{2}\left[\sum_{\beta=1}^{\infty} s_{ij}^{(\beta)}(x_3)a_\beta(t,x_1,x_2)e^{i(\omega_\beta t-\bar{k}_\beta\cdot\bar{r}')} + c.c.\right] \qquad (2.D.9)$$

The real external current density ($\bar{J}_e^{\,r}$) and real external force density ($\bar{F}_e^{\,r}$) are found from T_{ij}^{NL} and D_i^{NL} through the relations:

$$\bar{F}_e^{\,r} = \bar{\nabla}\cdot\bar{\bar{T}}^{NL} \qquad (2.D.10)$$

$$\bar{J}_e^{\,r} = \frac{\partial\bar{D}^{NL}}{\partial t} \qquad (2.D.11)$$

In tensor notation, one has

$$F_{ei}^{\,r} = \frac{\partial T_{ij}^{NL}}{\partial x_j} \qquad (2.D.12)$$

$$J_{ei}^{\,r} = \frac{\partial D_i^{NL}}{\partial t} \qquad (2.D.13)$$

By substituting the expressions for E_i and S_{ij} given in equations (2.D.8) and (2.D.9) into the expressions of (2.D.6) and (2.D.7) and carrying out the operations of equations (2.D.12) and (2.D.13), F_{ei}^{r} and J_{ei}^{r} are determined from the normal mode fields. However, the coupled mode equation needs $\bar{F}_e$ and $\bar{J}_e$, which are two complex terms. Because of the form of E_i and S_{ij} of (2.D.8) and (2.D.9) F_{ei}^{r} and J_{ei}^{r} can be used to determine F_{ei} and J_{ei}, where F_{ei} and J_{ei} are the components of $\bar{F}_e$ and $\bar{J}_e$. F_{ei}^{r} and J_{ei}^{r} consist of sums of complex terms and the complex conjugates of these terms. Hence, J_{ei}^{r} and F_{ei}^{r}

can be represented as:

$$F^r_{ei} = \frac{F_{ei} + F^*_{ei}}{2} \tag{2.D.14}$$

$$J^r_{ei} = \frac{J_{ei} + J^r_{ei}}{2} \tag{2.D.15}$$

By writing the results of equations (2.D.12) and (2.D.13) in a form as given in (2.D.14) and (2.D.15), J_{ei} and F_{ei} can be identified. Appendix IV gives a detailed derivation of F_{ei} and J_{ei}. Equations (2.D.16) and (2.D.17) give the outcome of that discussion

$$F_{ei} = -\eta_{kij\ell m}\Bigg\{\frac{1}{2}\sum_{\beta\gamma}\Bigg[a_\beta a_\gamma\Bigg[\frac{\partial}{\partial x_j}\left(e_k^{(\beta)}s_{\ell m}^{(\gamma)}+(1-\delta_{\beta\gamma})e_k^{(\gamma)}s_{\ell m}^{(\beta)}\right)-i\left(k_j^{(\beta)}+k_j^{(\gamma)}\right)$$
$$\left(e_k^{(\beta)}s_{\ell m}^{(\gamma)}+(1-\delta_{\beta\gamma})e_k^{(\gamma)}s_{\ell m}^{(\beta)}\right)\Bigg]e^{i[(\omega_\beta+\omega_\gamma)t-(\bar{k}_\beta+\bar{k}_\gamma)\cdot\bar{r}]}\Bigg]$$
$$+\frac{1}{2}\sum_{\beta\gamma}\Bigg[a_\beta a^*_\gamma\Bigg[\frac{\partial}{\partial x_j}\left(e_k^{(\beta)}s_{\ell m}^{(\gamma)*}+(1-\delta_{\beta\gamma})e_k^{(\gamma)*}s_{\ell m}^{(\beta)}\right)-i\left(k_j^{(\beta)}-k_j^{(\gamma)}\right)$$
$$\left(e_k^{(\beta)}s_{\ell m}^{(\gamma)*}+(1-\gamma_{\beta\gamma})e_k^{(\gamma)*}s_{\ell m}^{(\beta)}\right)\Bigg]e^{i[(\omega_\beta-\omega_\gamma)t-(\bar{k}_\beta-\bar{k}_\gamma)\cdot\bar{r}]}\Bigg]$$
$$+\frac{1}{2}\theta_{ijk\ell mn}\Bigg\{\frac{1}{2}\sum_{\beta\gamma}\Bigg[a_\beta a_\gamma\Bigg[\frac{\partial}{\partial x_j}\left(s_{k\ell}^{(\beta)}s_{mn}^{(\gamma)}+(1-\delta_{\beta\gamma})s_{k\ell}^{(\gamma)}s_{mn}^{(\beta)}\right)-i\left(k_j^{(\beta)}+k_j^{(\gamma)}\right)$$
$$\left(s_{k\ell}^{(\beta)}s_{mn}^{(\gamma)}+(1-\delta_{\beta\gamma})s_{k\ell}^{(\gamma)}s_{mn}^{(\beta)}\right)\Bigg]e^{i[(\omega_\beta+\omega_\gamma)t-(\bar{k}_\beta+\bar{k}_\gamma)\cdot\bar{r}]}\Bigg]$$

$$+\frac{1}{2}\sum_{\beta\gamma}\Bigg[a_\beta a_\gamma^*\Bigg[\frac{\partial}{\partial x_j}\left(s_{k\ell}^{(\beta)}s_{mn}^{(\gamma)*}+(1-\delta_{\beta\gamma})s_{k\ell}^{(\gamma)*}s_{mn}^{(\beta)}\right)-i\left(k_j^{(\beta)}-k_j^{(\gamma)}\right)$$

$$\left(s_{k\ell}^{(\beta)}s_{mn}^{(\gamma)*}+(1-\delta_{\beta\gamma})s_{k\ell}^{(\gamma)*}s_{mn}^{(\beta)}\right)\Bigg]e^{i[(\omega_\beta-\omega_\gamma)t-(\bar{k}_\beta-\bar{k}_\gamma)\cdot\bar{r}']}\Bigg]\Bigg)$$

$$+\frac{1}{2}\theta_{k\ell ij}\Bigg(\frac{1}{2}\sum_{\beta\gamma}\Bigg[a_\beta a_\gamma\Bigg[\frac{\partial}{\partial x_j}\left(e_k^{(\beta)}e_\ell^{(\gamma)}+(1-\delta_{\beta\gamma})e_k^{(\gamma)}e_\ell^{(\beta)}\right)-i\left(k_j^{(\beta)}+k_j^{(\gamma)}\right)$$

$$\left(e_k^{(\beta)}e_\ell^{(\gamma)}+(1-\delta_{\beta\gamma})e_k^{(\gamma)}e_\ell^{(\beta)}\right)\Bigg]e^{i[(\omega_\beta+\omega_\gamma)t-(\bar{k}_\beta+\bar{k}_\gamma)\cdot\bar{r}']}\Bigg]$$

$$+\frac{1}{2}\sum_{\beta\gamma}\Bigg[a_\beta a_\gamma^*\Bigg[\frac{\partial}{\partial x_j}\left(e_k^{(\beta)}e_\ell^{(\gamma)*}+(1-\delta_{\beta\gamma})e_k^{(\gamma)*}e_\ell^{(\beta)}\right)-i\left(k_j^{(\beta)}-k_j^{(\gamma)}\right)$$

$$\left(e_k^{(\beta)}e_\ell^{(\gamma)*}+(1-\delta_{\beta\gamma})e_k^{(\gamma)*}e_\ell^{(\beta)}\right)\Bigg]e^{i[(\omega_\beta-\omega_\gamma)t-(\bar{k}_\beta-\bar{k}_\gamma)\cdot\bar{r}']}\Bigg]\Bigg)$$

(2.D.16)

$$J_{ei}=Q_{ijk\ell}\Bigg(\frac{1}{2}\sum_{\beta\gamma}\Bigg[i\,a_\beta a_\gamma(\omega_\beta+\omega_\gamma)\left(e_j^{(\beta)}s_{k\ell}^{(\gamma)}+(1-\delta_{\beta\gamma})e_j^{(\gamma)}s_{k\ell}^{(\beta)}\right)$$

$$e^{i[(\omega_\beta+\omega_\gamma)t-(\bar{k}_\beta+\bar{k}_\gamma)\bar{r}']}\Bigg]$$

$$+\frac{1}{2}\sum_{\beta\gamma}\Bigg[i\,a_\beta a_\gamma^*(\omega_\beta-\omega_\gamma)\left(e_j^{(\beta)}s_{k\ell}^{(\gamma)*}+(1-\delta_{\beta\gamma})e_j^{(\gamma)*}s_{k\ell}^{(\beta)}\right)$$

$$e^{i[(\omega_\beta-\omega_\gamma)t-(\bar{k}_\beta-\bar{k}_\gamma)\cdot\bar{r}']}\Bigg]\Bigg)$$

$$+\frac{1}{2}\eta_{ijk\ell m}\left\{\frac{1}{2}\sum_{\beta\gamma}\left[i\ a_\beta a_\gamma(\omega_\beta+\omega_\gamma)\left\{s_{k\ell}^{(\beta)}s_{mn}^{(\gamma)}+(1-\delta_{\beta\gamma})s_{k\ell}^{(\gamma)}s_{mn}^{(\beta)}\right\}\right.\right.$$

$$\left.e^{i[(\omega_\beta+\omega_\gamma)t-(\bar{k}_\beta+\bar{k}_\gamma)\cdot\bar{r}]}\right]$$

$$+\frac{1}{2}\sum_{\beta\gamma}\left[i\ a_\beta a_\gamma^*(\omega_\beta-\omega_\gamma)\left\{s_{k\ell}^{(\beta)}s_{mn}^{(\gamma)*}+(1-\delta_{\beta\gamma})s_{k\ell}^{(\gamma)*}s_{mn}^{(\beta)}\right\}\right.$$

$$\left.\left.e^{i[(\omega_\beta-\omega_\gamma)t-(\bar{k}_\beta-\bar{k}_\gamma)\cdot\bar{r}]}\right]\right\}$$

$$+\frac{1}{2}O_{ijk}\left\{\frac{1}{2}\sum_{\beta\gamma}\left[i\ a_\beta a_\gamma(\omega_\beta+\omega_\gamma)\left\{e_j^{(\beta)}e_k^{(\gamma)}+(1-\delta_{\beta\gamma})e_j^{(\gamma)}e_k^{(\beta)}\right\}\right.\right.$$

$$\left.e^{i[(\omega_\beta+\omega_\gamma)t-(\bar{k}_\beta+\bar{k}_\gamma)\cdot\bar{r}]}\right]$$

$$+\frac{1}{2}\sum_{\beta\gamma}\left[i\ a_\beta a_\gamma^*(\omega_\beta-\omega_\gamma)\left\{e_j^{(\beta)}e_k^{(\gamma)*}+(1-\delta_{\beta\gamma})e_j^{(\gamma)*}e_k^{(\beta)}\right\}\right.$$

$$\left.\left.e^{i[(\omega_\beta-\omega_\gamma)t-(\bar{k}_\beta-\bar{k}_\gamma)\cdot\bar{r}]}\right]\right\} \qquad (2.D.17)$$

with, $\beta \geq \gamma$, and

$$\delta_{\beta\gamma} = \begin{cases} 1, & \beta = \gamma \\ 0, & \beta \neq \gamma \end{cases}$$

The complex external perturbations $\bar{F}_e$ and $\bar{J}_e$ are given by

$$\overline{J}_e = J_{ei}\,\hat{x}_i \tag{2.D.18}$$

$$\overline{F}_e = F_{ei}\,\hat{x}_i \tag{2.D.19}$$

Substituting the results of (2.D.16) - (2.D.19) into equation (2.C.33) and regrouping terms, one has:

$$\frac{\partial a_\alpha}{\partial t} + \overline{v}_{g\alpha}\overline{\nabla} a_\alpha + \nu_\alpha a_\alpha = \frac{1}{8<w_\alpha>}\int_0^\infty dx_3 \Bigg\{ \sum_{\beta\gamma}\sum \Big\{ a_\beta a_\gamma e^{i(\delta\omega^+ t - \delta\overline{k}^+\cdot\overline{r}')}$$

$$\Bigg(v_i^{(\alpha)*}\Bigg[-i\Big(k_j^{(\beta)} + k_j^{(\gamma)}\Big) + \frac{\partial}{\partial x_j}\Bigg]\Bigg[-\eta_{kij\ell m}\Big(e_k^{(\beta)} s_{\ell m}^{(\gamma)} + (1-\delta_{\beta\gamma}) e_k^{(\gamma)} s_{\ell m}^{(\beta)}\Big)$$

$$+\tfrac{1}{2}\theta_{ijk\ell mn}\Big(s_{k\ell}^{(\beta)} s_{mn}^{(\gamma)} + (1-\delta_{\beta\gamma}) s_{k\ell}^{(\gamma)} s_{mn}^{(\beta)}\Big)$$

$$-\tfrac{1}{2}Q_{k\ell ij}\Big(e_k^{(\beta)} e_\ell^{(\gamma)} + (1-\delta_{\beta\gamma}) e_k^{(\gamma)} e_\ell^{(\beta)}\Big)\Bigg]$$

$$-ie_i^{(\alpha)*}(\omega_\beta + \omega_\gamma)\Bigg[Q_{ijk\ell}\Big(e_j^{(\beta)} s_{k\ell}^{(\gamma)} + (1-\delta_{\beta\gamma}) e_j^{(\gamma)} s_{k\ell}^{(\beta)}\Big)$$

$$+\tfrac{1}{2}\eta_{ijk\ell m}\Big(s_{jk}^{(\beta)} s_{\ell m}^{(\gamma)} + (1-\delta_{\beta\gamma}) s_{jk}^{(\gamma)} s_{\ell m}^{(\beta)}\Big)$$

$$+\tfrac{1}{2}\theta_{ijk}\Big(e_j^{(\beta)} e_k^{(\gamma)} + (1-\delta_{\beta\gamma}) e_j^{(\gamma)} e_k^{(\beta)}\Big)\Bigg]\Bigg)$$

$$+a_\beta a_\gamma^* e^{i(\delta\overline{\omega}t - \delta\overline{k}^-\cdot\overline{r}')}$$

$$\Bigg\{ v_i^{(\alpha)*} \Big[-i\Big(k_j^{(\beta)} - k_j^{(\gamma)}\Big) + \frac{\partial}{\partial x_j} \Big] \Big[-\eta_{kij\ell m} \Big(e_k^{(\beta)} s_{\ell m}^{(\gamma)*} + (1-\delta_{\beta\gamma}) e_k^{(\gamma)*} s_{\ell m}^{(\beta)} \Big)$$

$$+\tfrac{1}{2}\theta_{ijk\ell mn} \Big(s_{k\ell}^{(\beta)} s_{mn}^{(\gamma)*} + (1-\delta_{\beta\gamma}) s_{k\ell}^{(\gamma)*} s_{mn}^{(\beta)} \Big)$$

$$-\tfrac{1}{2} Q_{k\ell ij} \Big(e_k^{(\beta)} e_\ell^{(\gamma)*} + (1-\delta_{\beta\gamma}) e_k^{(\gamma)*} e_\ell^{(\beta)} \Big) \Big]$$

$$-ie_i^{(\alpha)*} (\omega_\beta - \omega_\gamma) \Big[Q_{ijk\ell} \Big(e_j^{(\beta)} s_{k\ell}^{(\gamma)*} + (1-\delta_{\beta\gamma}) e_j^{(\gamma)*} s_{k\ell}^{(\beta)} \Big)$$

$$+\tfrac{1}{2}\eta_{ijk\ell m} \Big(s_{jk}^{(\beta)} s_{\ell m}^{(\gamma)*} + (1-\delta_{\beta\gamma}) s_{jk}^{(\gamma)*} s_{\ell m}^{(\beta)} \Big)$$

$$+\tfrac{1}{2} O_{ijk} \Big(e_j^{(\beta)} e_k^{(\gamma)*} + (1-\delta_{\beta\gamma}) e_j^{(\gamma)*} e_k^{(\beta)} \Big) \Big] \Big) \Bigg\} \qquad (2.D.20)$$

with

$$\delta\omega^+ = \omega_\beta + \omega_\gamma - \omega_\alpha, \qquad \overline{\delta k}^+ = \overline{k}_\beta + \overline{k}_\gamma - \overline{k}_\alpha,$$

$$\delta\omega^- = \omega_\beta - \omega_\gamma - \omega_\alpha, \qquad \overline{\delta k}^- = \overline{k}_\beta - \overline{k}_\gamma - \overline{k}_\alpha,$$

and

$$\Big[-i\Big(k_j^{(\beta)} + k_j^{(\gamma)}\Big) + \frac{\partial}{\partial x_j} \Big] ;$$

$$\Big[-i\Big(k_j^{(\beta)} - k_j^{(\gamma)}\Big) + \frac{\partial}{\partial x_j} \Big] ;$$

are operators applied prior to multiplication by $v_i^{(\alpha)*}$ and integration over x_3. Because the nonlinearities exist only for $0 \leq x_3 \leq \infty$, the integration is only over this region.

Equation (2.D.20) is the nonlinearly coupled amplitude equation that models coupled mode interactions in materials that are weakly nonlinear. This equation illustrates the manner in which different nonlinearities contribute to the coupling and how the decay characteristic of surface waves enters a coupled mode description of an interaction.

For later discussion, it is convenient to normalize the field amplitudes, a_α's, to action density (n_α) [46],

$$n_\alpha = \frac{<W_\alpha>}{\omega_\alpha} \tag{2.D.21}$$

Defining a new amplitude $q_\alpha(t,x_1,x_2)$,

$$q_\alpha(t,x_1,x_2) \triangleq q_{\alpha o}\, a_\alpha(t,x_1,x_2) \tag{2.D.22}$$

in which

$$p_\alpha q_{\alpha o}^2 = n_\alpha, \tag{2.D.23}$$

p_α = +1 or -1, which is the energy parity of mode α,

and

$$<W_\alpha> = p_\alpha |<W_\alpha>| .$$

Further

$$n_\alpha = p_\alpha |q_\alpha|^2, \tag{2.D.24}$$

or

$$q_{\alpha o} = \left| \frac{<W_\alpha>}{\omega_\alpha} \right| \tag{2.D.25}$$

After defining the following:

$$C^+_{\alpha\beta\gamma} \triangleq \int_0^\infty \Bigg(v_i^{(\alpha)*} \left[-i\left(k_j^{(\beta)} + k_j^{(\gamma)}\right) + \frac{\partial}{\partial x_j} \right] \Bigg[-\eta_{kij\ell m} \left(e_k^{(\beta)} s_{\ell m}^{(\gamma)} + (1-\delta_{\beta\gamma}) e_k^{(\gamma)} s_{\ell m}^{(\beta)} \right)$$

$$+ \frac{1}{2}\theta_{ijk\ell mn} \left(s_{k\ell}^{(\beta)} s_{mn}^{(\gamma)} + (1-\delta_{\beta\gamma}) s_{k\ell}^{(\gamma)} s_{mn}^{(\beta)} \right)$$

$$- \frac{1}{2} Q_{k\ell ij} \left(e_k^{(\beta)} e_\ell^{(\gamma)} + (1-\delta_{\beta\gamma}) e_k^{(\gamma)} e_\ell^{(\beta)} \right) \Bigg]$$

$$- i e_i^{(\alpha)*} (\omega_\beta + \omega_\gamma) \Bigg[Q_{ijk\ell} \left(e_j^{(\beta)} s_{k\ell}^{(\gamma)} + (1-\delta_{\beta\gamma}) e_j^{(\gamma)} s_{k\ell}^{(\beta)} \right)$$

$$+ \frac{1}{2}\eta_{ijk\ell m} \left(s_{jk}^{(\beta)} s_{\ell m}^{(\gamma)} + (1-\delta_{\beta\gamma}) s_{jk}^{(\gamma)} s_{\ell m}^{(\beta)} \right)$$

$$+ \frac{1}{2} O_{ijk} \left(e_j^{(\beta)} e_k^{(\gamma)} + (1-\delta_{\beta\gamma}) e_j^{(\gamma)} e_k^{(\beta)} \right) \Bigg] \Bigg) dx_3 \tag{2.D.26}$$

$$C^{-}_{\alpha\beta\gamma} = \int_0^{\infty}\Bigg\{ v_i^{(\alpha)*}\Bigg[-i\left(k_j^{(\beta)}-k_j^{(\gamma)}\right) + \frac{\partial}{\partial x_j}\Bigg]\Bigg[-\eta_{kij\ell m}\left(e_k^{(\beta)}s_{\ell m}^{(\gamma)*}+(1-\delta_{\beta\gamma})e_k^{(\gamma)*}s_{\ell m}^{(\beta)}\right)$$

$$+\tfrac{1}{2}\theta_{ijk\ell mn}\left(s_{k\ell}^{(\beta)}s_{\ell m}^{(\gamma)*}+(1-\delta_{\beta\gamma})s_{k\ell}^{(\gamma)*}s_{mn}^{(\beta)}\right)$$

$$-\tfrac{1}{2}Q_{k\ell ij}\left(e_k^{(\beta)}e_\ell^{(\gamma)*}+(1-\delta_{\beta\gamma})e_k^{(\gamma)*}e_\ell^{(\beta)}\right)\Bigg]$$

$$-ie_i^{(\alpha)*}(\omega_\beta-\omega_\gamma)\Bigg[Q_{ijk\ell}\left(e_j^{(\beta)}s_{k\ell}^{(\gamma)*}+(1-\delta_{\beta\gamma})e_j^{(\gamma)*}s_{k\ell}^{(\beta)}\right)$$

$$+\tfrac{1}{2}\eta_{ijk\ell m}\left(s_{jk}^{(\beta)}s_{\ell m}^{(\gamma)*}+(1-\delta_{\beta\gamma})s_{jk}^{(\gamma)*}s_{\ell m}^{(\beta)}\right)$$

$$+\tfrac{1}{2}O_{ijk}\left(e_j^{(\beta)}e_k^{(\gamma)*}+(1-\delta_{\beta\gamma})e_j^{(\gamma)*}e_k^{(\beta)}\right)\Bigg]\Bigg\}dx_3 \qquad (2.D.27)$$

and substituting the results of (2.D.21)-(2.D.27) into (2.D.20) one has:

$$\frac{\partial q_\alpha}{\partial t} + \bar{v}_{g\alpha}\bar{\nabla}q_\alpha + \nu_\alpha q_\alpha = \frac{p_\alpha}{8}\sum_{\beta\gamma}\sum\frac{(\omega_\beta\omega_\gamma/\omega_\alpha)^{1/2}}{|<W_\alpha><W_\beta><W_\gamma>|^{1/2}}$$

$$\left(C^{+}_{\alpha\beta\gamma}a_\beta a_\gamma e^{i(\delta\omega^{+}t-\delta\bar{k}^{+}\bar{r}')}+C^{-}_{\alpha\beta\gamma}a_\beta a^{*}_\gamma e^{i(\delta\omega^{-}t-\delta\bar{k}^{-}\bar{r}')}\right) \qquad (2.D.28)$$

Defining the terms $K^{+}_{\alpha\beta\gamma}$ and $K^{-}_{\alpha\beta\gamma}$:

$$K^{+}_{\alpha\beta\gamma} \triangleq \frac{C^{+}_{\alpha\beta\gamma}(\omega_\beta\omega_\gamma/\omega_\alpha)^{1/2}}{8|\langle W_\alpha\rangle\langle W_\beta\rangle\langle W_\gamma\rangle|^{1/2}} \tag{2.D.29}$$

$$K^{-}_{\alpha\beta\gamma} \triangleq \frac{C^{-}_{\alpha\beta\gamma}(\omega_\beta\omega_\gamma/\omega_\alpha)^{1/2}}{8|\langle W_\alpha\rangle\langle W_\beta\rangle\langle W_\gamma\rangle|^{1/2}} \tag{2.D.30}$$

The $K^{+}_{\alpha\beta\gamma}$ and $K^{-}_{\alpha\beta\gamma}$ are to be known as coupling constants. These terms substituted into equation (2.D.28) give

$$\frac{\partial q_\alpha}{\partial t} + \bar{v}_{g\alpha}\nabla q_\alpha + \nu_\alpha q_\alpha = p_\alpha \sum_{\beta\gamma}\sum\Big(K^{+}_{\alpha\beta\gamma}q_\beta q_\gamma e^{i(\delta\omega^{+}t-\delta\bar{k}^{+}\bar{r}')} + K^{-}_{\alpha\beta\gamma}q_\beta q^{*}_\gamma e^{i(\delta\omega^{-}t-\delta\bar{k}^{-}\bar{r}')}\Big) \tag{2.D.31}$$

Equation (2.D.31) is the nonlinearly-coupled amplitude equation that describes the evolution of a given mode due to the nonlinear properties of surface wave materials. It is the equation that is the basis for the discussions of harmonic generation and parametric interactions.

This section has presented a discussion of the nonlinearly-coupled amplitude equation and what contributes to the nonlinear interactions. The nonlinear properties of surface wave materials involved with the interactions are embodied in the coupling constants. Coupling constants are terms that are characteristic of the nonlinear interactions and their properties are important in understanding how coupled mode theory has been able to model experiments, and in using

coupled mode theory to predict the results of nonlinear interactions. The fifth section is devoted to a presentation of the properties of the coupling constants.

E. Coupling Constants

Equations (2.D.29) and (2.D.30) define the coupling constants $K^{+}_{\alpha\beta\gamma}$ and $K^{-}_{\alpha\beta\gamma}$ respectively, and from these equations the coupling constants can be calculated from the nonlinear material constants and the field amplitudes. However, without numerical calculation, several important properties can be determined. These properties include relationships among the coupling constants, and the frequency dependence and power independence of $K^{\pm}_{\alpha\beta\gamma}$. The characteristics just listed are determined from a normalization of the unperturbed field quantities as given in [49],[50], and the conservation of energy and momentum.

In general the coupling constants are independent, but by considering conservative interactions, it can be shown that a single coupling constant is sufficient to describe a given three wave coupling. When $\delta\omega^{+}$, $\delta\omega^{-}$, $\bar{\delta}k^{+}$, $\bar{\delta}k^{-}$ are zero, or on the order or smaller than the slow variation of $\frac{\partial}{\partial t} + \bar{v}_{g\alpha}\cdot\bar{\nabla} + \nu_{\alpha}$, one can define a conservative nonlinear perturbation to be such that the perturbed waves satisfy conservation of energy:

$$\sum_{\alpha=1}^{\infty}\left[p_{\alpha}\omega_{\alpha}\left[\left(\frac{\partial}{\partial t}+\nu_{\alpha}\right)\int_{-\infty}^{\infty}|q_{\alpha}|^{2}d\bar{r}+\int_{-\infty}^{\infty}(\bar{v}_{g\alpha}\cdot\bar{\nabla}|q_{\alpha}|^{2})d\bar{r}'\right]\right]=0 \quad (2.E.1)$$

and conservation of momentum

$$\sum_{\alpha=1}^{\infty}\left[p_\alpha \bar{k}_\alpha\left[\left(\frac{\partial}{\partial t}+\nu_\alpha\right)\int_{-\infty}^{\infty}|q_\alpha|^2 d\bar{r}' + \int_{-\infty}^{\infty}(\bar{v}_{g_\alpha}\cdot\bar{\nabla}|q_\alpha|^2)d\bar{r}'\right]\right] = 0 \quad (2.E.2)$$

From (2.D.31), (2.E.1) and (2.E.2), one can find the relationships among the $K^{\pm}_{\alpha\beta\gamma}$'s. The results are:

1. if $\omega_\alpha > \omega_\beta \neq \omega_\gamma$

$$K^{+}_{\alpha\beta\gamma} = -K^{-*}_{\beta\alpha\gamma} = -K^{-*}_{\gamma\alpha\beta} \quad (2.E.3)$$

2. if $\omega_\alpha > \omega_\beta = \omega_\gamma$

$$-2K^{+}_{\alpha\beta\beta} = K^{-*}_{\beta\alpha\beta} \quad (2.E.4)$$

Therefore, one finds that a single constant is sufficient to describe the coupling of three given modes.

To determine the frequency and power dependence of $K^{\pm}_{\alpha\beta\gamma}$, one works through equations (2.D.29) and (2.D.30). The coupling constants $K^{\pm}_{\alpha\beta\gamma}$ given by equations (2.D.29) and (2.D.30) are composed of the products of components of the unperturbed field amplitudes $\underline{e}$, $\underline{v}$, and $\underline{s}$ of the interacting modes. The products are contained in $C^{\pm}_{\alpha\beta\gamma}$. It is these field quantities which are normalized in [49] and [50] to give terms that are constants for a given material

cut and propagation vector, and characterize $K^{\pm}_{\alpha\beta\gamma}$ as power independent.

Each component of particle velocity, strain, and electric field is composed of a sum of partial waves for a given surface acoustic wave [49]. In general four partial waves exist, but for non-piezoelectric materials and degenerate piezoelectric cases, less than four partial waves contribute. The field components of mode p can be represented by

$$v_i^{(p)} = \sum_{r=1}^{4} V_i^{(p)(r)} e^{-\alpha_p^{(r)} \omega_p x_3 / v_{sp}} \qquad (2.E.5)$$

$$s_{k\ell}^{(p)} = \sum_{r=1}^{4} S_{k\ell}^{(p)(r)} e^{-\alpha_p^{(r)} \omega_p x_3 / v_{sp}} \qquad (2.E.6)$$

$$e_i^{(p)} = \sum_{r=1}^{4} E_i^{(p)(r)} e^{-\alpha_p^{(r)} \omega_p x_3 / v_{sp}} \qquad (2.E.7)$$

where

v_{sp} = phase velocity of mode p

i,k,ℓ = component subscripts

$\alpha_p^{(r)}$ = r^{th} partial wave decay constant and is a constant for any mode p propagating in the same direction on a given material cut. It is independent of power and frequency.

The terms $V_i^{(p)(r)}$, $S_{k\ell}^{(p)(r)}$, and $E_i^{(p)(r)}$ are dependent upon the frequency and power density of mode p. However by dividing (2.E.5)-

(2.E.7) by $\omega_p \left[\frac{R_e P_{im}^{(p)}}{\omega_p} \right]^{1/2}$ where

$R_e P_{im}^{(p)}$ = real part of complex mechanical power flow [49] in the phase velocity direction,

one finds the components of the field quantities become terms independent of power, and frequency, and dependent only on the decay characteristics.

$$\hat{v}_i^{(p)} = \frac{v_i^{(p)}}{\omega_p \left[\frac{R_e P_{im}^{(p)}}{\omega_p} \right]^{1/2}} = \sum_{r=1}^{4} \hat{V}_i^{(p)}(r) e^{-\alpha_p^{(r)} \omega_p x_3 / v_{sp}} \qquad (2.E.8)$$

$$\hat{s}_{k\ell}^{(p)} = \frac{s_{k\ell}^{(p)}}{\omega_p \left[\frac{R_e P_{im}^{(p)}}{\omega_p} \right]^{1/2}} = \sum_{r=1}^{4} \hat{S}_{k\ell}^{(p)}(r) e^{-\alpha_p^{(r)} \omega_p x_3 / v_{sp}} \qquad (2.E.9)$$

$$\hat{e}_i^{(p)} = \frac{e_i^{(p)}}{\omega_p \left[\frac{R_e P_{im}^{(p)}}{\omega_p} \right]^{1/2}} = \sum_{r=1}^{4} \hat{E}_i^{(p)}(r) e^{-\alpha_p^{(r)} \omega_p x_3 / v_{sp}} \qquad (2.E.10)$$

$$\hat{S}_{k\ell}^{(p)(r)} = \frac{S_{k\ell}^{(p)(r)}}{\omega_p \left[\frac{R_e P_{lm}^{(p)}}{\omega_p}\right]^{1/2}} \qquad (2.E.11)$$

$$\hat{V}_i^{(p)(r)} = \frac{V_i^{(p)(r)}}{\omega_p \left[\frac{R_e P_{lm}^{(p)}}{\omega_p}\right]^{1/2}} \qquad (2.E.12)$$

$$\hat{E}_i^{(p)(r)} = \frac{E_i^{(p)(r)}}{\omega_p \left[\frac{R_e P_{lm}}{\omega_p}\right]^{1/2}} \qquad (2.E.13)$$

The terms $\hat{E}_i^{(p)(r)}$, $\hat{V}_i^{(p)(r)}$, $\hat{S}_{k\ell}^{(p)(r)}$ are constants for a given material cut and propagation direction. A further discussion of this normalization procedure and the method of finding the constants is given in Appendix V.

Therefore it becomes only a matter of variable manipulation to cast $K_{\alpha\beta\gamma}^{\pm}$ into a form in which one works with constants that are characteristics of the normal modes which are propagating in a given direction and material cut. By working with these constants one can determined the behavior of $K_{\alpha\beta\gamma}^{\pm}$ on frequency and power density.

$K^{\pm}_{\alpha\beta\gamma}$ are dependent upon $|<W_\alpha>|$, $|<W_\beta>|$ and $|<W_\gamma>|$. Equation (2.C.31) gives a relationship between $<W_\alpha>$ and $<\overline{S}_\alpha>$. Thus:

$$|\overline{v}_{g\alpha}<W_\alpha>| = |<\overline{S}_\alpha>| \tag{2.E.14}$$

and

$$|<W_\alpha>| = \frac{|<\overline{S}_\alpha>|}{v_{g\alpha}} \tag{2.E.15}$$

with $|\overline{v}_{g\alpha}| = v_{g\alpha}$.

Substituting for $|<W_\alpha>|$ the result of (2.E.15) into (2.D.29) and (2.D.30), one has

$$K^{\pm}_{\alpha\beta\gamma} = \frac{p_\alpha C^{\pm}_{\alpha\beta\gamma}(\omega_\beta\omega_\gamma/\omega_\alpha)^{1/2}(v_{g\alpha}v_{g\beta}v_{g\gamma})^{1/2}}{(|<\overline{S}_\alpha>||<\overline{S}_\beta>||<\overline{S}_\gamma>|)^{1/2}} \tag{2.E.16}$$

The complex power density is

$$<\overline{S}_{\alpha c}> = \int_{-\infty}^{\infty}\left[-\frac{1}{2}(\underline{v}^*_\alpha\cdot\underline{\underline{t}}_\alpha) + \frac{1}{2}(\underline{e}_\alpha x\underline{h}^*_\alpha)\right]dx_3 \tag{2.E.17}$$

This is composed of the complex mechanical power density, $\overline{P}^{(\alpha)}_m$ and complex electromagnetic power density $\overline{P}^{(\alpha)}_E$. Therefore

$$\overline{P}^{(\alpha)}_M = \int_{-\infty}^{\infty} -\frac{1}{2}(\underline{v}^*_\alpha\cdot\underline{\underline{t}}_\alpha) \tag{2.E.18}$$

$$\overline{P}^{(\alpha)}_E = \int_{-\infty}^{\infty}\frac{1}{2}(\underline{e}_\alpha x\underline{h}^*_\alpha)dx_3 \tag{2.E.19}$$

and for quasistatics,

$$\overline{P}_E^{(\alpha)} = \int_{-\infty}^{\infty} \frac{1}{2}(\phi_\alpha \underline{d}^*_{-\alpha}) dx_3$$

with ϕ_α = unperturbed amplitude of electric potential.

The real power flow is then

$$<\overline{S}_\alpha> = R_e P_m^{(\alpha)} + R_e P_E^{(\alpha)} \qquad (2.E.20)$$

Breaking this into components $<\overline{S}_i^{(\alpha)}> = R_e P_{im}^{(\alpha)} + R_e P_{iE}^{(\alpha)}$, and for surface waves i = 1,2. Let i=1, or x_1 be the direction of the phase velocity and i=2, or x_2 be the direction perpendicular to the phase velocity (Fig. 2.1). The $|<\overline{S}_\alpha>|$ can be written as:

$$|<\overline{S}_\alpha>| = \left[(R_e P_{1m}^{(\alpha)} + R_e P_{1E}^{(\alpha)})^2 + (R_e P_{2m}^{(\alpha)} + P_{2E}^{(\alpha)})^2 \right]^{1/2}$$

$$|<\overline{S}_\alpha>| = \omega_\alpha \frac{R_e P_{im}^{(\alpha)}}{\omega_\alpha} \left[\left(1 + \frac{R_e P_{1E}^{(\alpha)}/\omega_\alpha}{R_e P_{1m}/\omega_\alpha} \right)^2 + \left(\frac{R_e P_{2m}^{(\alpha)}/\omega_\alpha}{R_e P_{1m}^{(\alpha)}/\omega_\alpha} + \frac{R_e P_{2E}^{(\alpha)}/\omega_\alpha}{R_e P_{1m}^{(\alpha)}/\omega_\alpha} \right)^2 \right]^{1/2}$$

(2.E.21)

The ratios $\frac{R_e P_{1E}^{(\alpha)}/\omega_\alpha}{R_e P_{1m}^{(\alpha)}/\omega_\alpha}$, $\frac{R_e P_{2m}^{(\alpha)}/\omega_\alpha}{R_e P_{1m}^{(\alpha)}/\omega_\alpha}$, $\frac{R_e P_{2E}^{(\alpha)}/\omega_\alpha}{R_e P_{1m}^{(\alpha)}/\omega_\alpha}$ are constants of

mode α for a given material cut and propagation direction.

For simplicity,

$$\langle \hat{S}_\alpha \rangle = \left[\left[1 + \frac{R_e P_{1E}^{(\alpha)}/\omega_\alpha}{R_e P_{1m}^{(\alpha)}/\omega_\alpha} \right]^2 + \left[\frac{R_e P_{2m}^{(\alpha)}/\omega_\alpha}{R_e P_{1m}^{(\alpha)}/\omega_\alpha} + \frac{R_e P_{2E}^{(\alpha)}/\omega_\alpha}{R_e P_{1m}/\omega_\alpha} \right]^2 \right]^{1/2} \qquad (2.E.22)$$

which is also constant for a material cut and propagation direction, and (2.E.21) is reduced to:

$$|\langle \bar{S}_\alpha \rangle| = \omega_\alpha \left[\frac{R_e P_{1m}^{(\alpha)}}{\omega_\alpha} \right] \langle \hat{S}_\alpha \rangle \qquad (2.E.23)$$

Given equation (2.E.23), $K^{\pm}_{\alpha\beta\gamma}$ can be written as

$$K^{\pm}_{\alpha\beta\gamma} = \frac{C^{\pm}_{\alpha\beta\gamma} (v_{g\alpha} v_{g\beta} v_{g\gamma})^{1/2}}{8\omega_\alpha \left[\frac{R_e P_{1m}^{(\alpha)}}{\omega_\alpha} \; \frac{R_e P_{1m}^{(\beta)}}{\omega_\beta} \; \frac{R_e P_{1m}^{(\gamma)}}{\omega_\gamma} \right]^{1/2} (\langle \hat{S}_\alpha \rangle \langle \hat{S}_\beta \rangle \langle \hat{S}_\gamma \rangle)^{1/2}} \qquad (2.E.24)$$

To normalize the field quantities of $K^{\pm}_{\alpha\beta\gamma}$, one needs $\omega_p \left[\frac{R_e P_{1m}^{(p)}}{\omega_p} \right]^{1/2}$ in the denominator of (2.E.24). Hence multiplying and dividing (2.E.24) by $(\omega_\alpha \omega_\beta \omega_\gamma)$,

$$K^{\pm}_{\alpha\beta\gamma} = \frac{\omega_\beta \omega_\gamma \hat{C}^{\pm}_{\alpha\beta\gamma} (v_{g\alpha} v_{g\beta} v_{g\gamma})^{1/2}}{8(<\hat{S}_\alpha><\hat{S}_\beta><\hat{S}_\gamma>)^{1/2}} \qquad (2.E.25)$$

where

$$\hat{C}^{\pm}_{\alpha\beta\gamma} = \frac{C^{\pm}_{\alpha\beta\gamma}}{\left[\frac{R_e P^{(\alpha)}_{lm}}{\omega_\alpha} \frac{R_e P^{(\beta)}_{lm}}{\omega_\beta} \frac{R_e P^{(\gamma)}_{lm}}{\omega_\gamma}\right]^{1/2} (\omega_\alpha \omega_\beta \omega_\gamma)} \qquad (2.E.26)$$

$\hat{C}^{\pm}_{\alpha\beta\gamma}$ are the terms that contain the normalized field quantities derived by dividing the appropriate field quantities in $C^{\pm}_{\alpha\beta\gamma}$ by the its corresponding $\left[\frac{R_e P_{lm}}{\omega}\right]^{1/2} \omega$. Thus $K^{\pm}_{\alpha\beta\gamma}$ can be written in terms of normalized field quantities as given in (2.E.8)-(2.E.13).

Taking the term in $\hat{C}^{\pm}_{\alpha\beta\gamma}$ that contains the elastic nonlinearities, $\theta_{ijk\ell mn}$, one can illustrate the results of this procedure on $K^{\pm}_{\alpha\beta\gamma}$ and learn something of the qualities of the coupling constants. Letting

$$\frac{\omega_\beta}{\omega_\gamma} = f_{\beta\gamma}, \quad \omega_\beta \geq \omega_\gamma ,$$

and

$$k_j = \frac{\omega v_{sj}}{v_s^2}$$

and performing the indicated operations in $C^{\pm}_{\alpha\beta\gamma}$, one has

$$C^{+\theta}_{\alpha\beta\gamma} = \left\{ \sum_{j=1}^{2} \frac{1}{2}\theta_{ijk\ell mn} \left[-i\hat{V}_i^{(\alpha)(r)*} \left(\hat{S}_{k\ell}^{(\beta)(t)} \hat{S}_{mn}^{(\gamma)(w)} + (1-\delta_{\beta\gamma}) \hat{S}_{k\ell}^{(\gamma)(w)} \hat{S}_{mn}^{(\beta)(t)} \right) \right.\right.$$

$$\left[\frac{f_{\beta\gamma} v_j^{(\beta)}}{v_{s\beta}^2} + \frac{v_{sj}^{(\gamma)}}{v_{s\gamma}^2} \right] \left[\frac{\alpha_\alpha^{(r)*}}{v_{s\alpha}} \left(1 + f_{\beta\gamma} - \frac{\delta_\omega^+}{\omega_\gamma} \right) + \frac{f_{\beta\gamma} \alpha_\beta^{(w)}}{v_{s\beta}} + \frac{\alpha_\gamma^{(t)}}{v_{s\gamma}} \right]^{-1} \Bigg]$$

$$- \frac{1}{2}\theta_{i3k\ell mn} \left[\hat{V}_i^{(\alpha)(r)*} \left(\hat{S}_{k\ell}^{(\beta)(t)} \hat{S}_{mn}^{(\gamma)(w)} + (1-\delta_{\beta\gamma}) \hat{S}_{k\ell}^{(\gamma)(w)} S_{mn}^{(\beta)(t)} \right) \right.$$

$$\left[\frac{f_{\beta\gamma} \alpha_\beta^{(w)}}{v_{s\beta}} + \frac{\alpha_\gamma^{(t)}}{v_{s\gamma}} \right] \left[\frac{\alpha_\alpha^{(r)*}}{v_{s\alpha}} \left(1 + f_{\beta\gamma} - \frac{\delta_\omega^+}{\omega_\gamma} \right) + \frac{f_{\beta\gamma} \alpha_\beta^{(w)}}{v_{s\beta}} \right.$$

$$\left.\left.\left. + \frac{\alpha_\alpha^{(t)}}{v_{s\gamma}} \right]^{-1} \right] \right\}$$

(2.E.27)

$$C^{-\theta}_{\alpha\beta\gamma} = \left\{ \sum_{j=1}^{2} \frac{1}{2}\theta_{ijk\ell mn} \left[-i\hat{V}_i^{(\alpha)(r)*} \left(\hat{S}_{jk}^{(\beta)(t)} \hat{S}_{\ell m}^{(\gamma)(w)*} + (1-\delta_{\beta\gamma}) \hat{S}_{jk}^{(\gamma)(w)*} \hat{S}_{\ell m}^{(\beta)(t)} \right) \right.\right.$$

$$\left[\frac{f_{\beta\gamma} v_j^{(\beta)}}{v_{s\beta}^2} - \frac{v_{sj}^{(\gamma)}}{v_{sj}^2} \right] \left[\frac{\alpha_\alpha^{(r)*}}{v_{s\alpha}} \left(f_{\beta\gamma} - 1 - \frac{\delta_\omega^-}{\omega_\gamma} \right) + \frac{f_{\beta\gamma} \alpha_\beta^{(t)}}{v_{s\beta}} \right.$$

$$\left.\left.\left. + \frac{\alpha_\gamma^{(w)*}}{v_{s\gamma}} \right]^{-1} \right] \right\}$$

$$- \frac{1}{2}\theta i3k\ell mn \left[\hat{V}_i^{(\alpha)(r)*} \left\{ \hat{S}_{3k}^{(\beta)(t)} \hat{S}_{\ell m}^{(\gamma)(w)*} + (1-\delta_{\beta\gamma}) \hat{S}_{3k}^{(\gamma)(w)*} \hat{S}_{m}^{(\beta)(t)} \right\} \right.$$

$$\left[\frac{f_{\beta\gamma}\alpha_\beta^{(t)}}{v_{s\beta}} + \frac{\alpha_\gamma^{(w)*}}{v_{s\gamma}} \right] \left[\frac{\alpha_\alpha^{(r)*}}{v_{s\alpha}} \left(f_{\beta\gamma} - 1 - \frac{\delta_\omega^-}{\omega_\gamma} \right) + \frac{f_{\beta\gamma}\alpha_\beta^{(t)}}{v_{s\beta}} \right.$$

$$\left. \left. \left. \frac{\alpha_\gamma^{(w)*}}{v_{s\gamma}} \right]^{-1} \right] \right]$$

Sum over repeated indices is assumed with i,k,ℓ,m,n = 1,2,3 and r,t,w = 1,2,3,4. The rest of $C^+_{\alpha\beta\gamma}$ and $C^-_{\alpha\beta\gamma}$, can be found by substituting the appropriate nonlinear material constants and normalized field terms, and performing the indicated operations. The results for $C^\pm_{\alpha\beta\gamma}$ give sums of constants with the variable term being $\frac{\delta\omega^\pm}{\omega_\gamma}$.

From equations (2.E.26) and (2.E.27), one can see that $C^\pm_{\alpha\beta\gamma}$ are independent of power and depend on frequency through $\frac{\delta\omega^\pm}{\omega_\gamma}$. Therefore $K^\pm_{\alpha\beta\gamma}$ is also independent of power and dependent only upon frequency.

Under the conditions described for conservative coupling in which a resonant interaction ($\delta\omega^\pm=0$, $\delta k^\pm=0$) occurs, $\hat{C}_{\alpha\beta\gamma}$ is independent of frequency. With the conditions of $\delta\omega^\pm$, $\delta k^\pm$ comparable or slower than $\frac{\partial}{\partial t} + vg_i\cdot\nabla + \nu_i$, the term $\frac{\delta\omega^\pm}{\omega_\gamma} << 1$, and $\frac{\delta\omega^\pm}{\omega_\gamma}$ can be dropped

from $\hat{C}_{\alpha\beta\gamma}$, thus approximating $\hat{C}^{\pm}_{\alpha\beta\gamma}$ as frequency independent. When $\hat{C}^{\pm}_{\alpha\beta\gamma}$ are frequency independent, the $K^{\pm}_{\alpha\beta\gamma}$ are functions of the $\omega_\beta\omega_\gamma = f_{\beta\gamma}\omega^2_\gamma$. Therefore

$$K^{\pm}_{\alpha\beta\gamma} = \frac{f_{\beta\gamma}\omega^2_\gamma \hat{C}^{\pm}_{\alpha\beta\gamma}(v_{g\alpha}v_{g\beta}v_{g\gamma})^{1/2}}{8(<\hat{S}_\alpha><\hat{S}_\beta><\hat{S}_\gamma>)^{1/2}} \qquad (2.E.28)$$

and dependent only on ω^2_γ.

Equation (2.E.25) is the general form of the coupling constants. The coupling constants are power independent and functions of frequency. With the conditions of conservative coupling and small $\delta k^{\pm}$, $\delta\omega^{\pm}$, relationships among the coupling constants exist, and $K^{\pm}_{\alpha\beta\gamma}$ are dependent on frequency squared.

F. Summary

This chapter has presented a discussion of the current theoretical models that have been used to describe nonlinear interactions of surface acoustic waves. Each of the coupled mode theories that have been developed have deficiencies in the manner of their derivations, but they have been successful in modeling the nonlinear interactions. However, because of inconsistent or incomplete theoretical development, little insight has been achieved in regard to the characteristics of the nonlinear coupling.

Alternatively, a coupled amplitude equation is formulated here that avoids the problems and failings of previous work. It is

consistent with coupled mode theory and the characteristics of surface acoustic waves, and is applicable to linear and nonlinear interactions. With the development of the coupled amplitude equation, a nonlinearly coupled equation is determined and the characteristic of the coupling constants discussed. By way of this nonlinear equation, coupled mode theory can be used to explore collinear harmonic generation and noncollinear parametric interactions.

CHAPTER 3

COLLINEAR HARMONIC GENERATION

A. Introduction and Outline

One of the strongest nonlinear phenomena observed has been steady-state collinear harmonic generation on a free-surface [24]-[35]. A fundamental frequency evolves harmonics of itself which propagate in the same direction as the fundamental. The first wave to evolve from the fundamental is the second harmonic. This interacts with the fundamental and itself to produce the third and fourth harmonics. The mixing of the harmonics continues and conceivably an unlimited number of harmonics can be produced. Because of its relative simplicity, collinear harmonic generation has been one of earliest nonlinear interactions to be modeled by coupled mode theory [28]-[32], and the harmonic that has received the most attention is the second harmonic.

Second harmonic generation can be used to illustrate the basic coupled mode concepts that can be applied to harmonic generation, and to experimentally verify these concepts. The discussion that follows will cover:

1. coupled mode equations,
2. theoretical properties of coupling constants,
3. phase-locking,
4. experimental verification of properties of coupling constants and determination of the coupling constants,

5. numerical calculation of theoretical coupling constants.

The arguments presented in this case can be extended to higher harmonic generation, and four waves interacting is considered.

Following the discussion presented for the second harmonic, the more complicated fourth harmonic case is reviewed. Generation of the fourth harmonic is accompanied by the growth of the third harmonic [26], [28]-[31] and thus the nonlinear interactions result in at least four waves present. From the second harmonic discussion the issues raised are:

1. coupled mode equations,
2. coupling constants,
3. phase-locking and,
4. a dispersive case.

To facilitate the following discourse, several assumptions are made:

1. no beam steering and thus group and phase velocities are in the same direction, and all group velocities are equal,
2. the x_1 direction (Fig. 1.1) is chosen as the direction of propagation,
3. steady-state conditions,
4. lossless propagation.

As stated the limitations are primarily for ease of discussion, and do not detract from the general coupled mode approach.

B. Second Harmonic Generation

With the assumptions given above, two equations, derived from equation (2.D.31), describe the coupled interaction between the fundamental and second harmonic. These equations are

$$v_g \frac{\partial q_1}{\partial x_1} = K^-_{121}\, q_2 q_1^* \tag{3.B.1}$$

$$v_g \frac{\partial q_2}{\partial x_1} = K^+_{211}\, q_1^2 \tag{3.B.2}$$

where q_1 = amplitude of fundamental

q_2 = amplitude of second harmonic.

Because q_1 and q_2 are slowly varying, the strongest coupling occurs when $\delta\bar{k}^{\pm} = 0$ and $\delta\omega^{\pm} = 0$. Hence resonant coupling is assumed.

From equations (2.D.29) and (2.D.30)

$$K^+_{211} = \frac{(\omega_1^2/\omega_2)^{\frac{1}{2}} C^+_{211}}{8|\langle W_2\rangle\langle W_1\rangle\langle W_1\rangle|^{1/2}} \tag{3.B.3}$$

$$K^-_{121} = \frac{(\omega_2\omega_1/\omega_1)^{\frac{1}{2}} C^-_{121}}{8|\langle W_2\rangle\langle W_1\rangle\langle W_1\rangle|^{1/2}} \tag{3.B.4}$$

and from equations (2.D.26) and (2.D.21)

$$C^{-}_{121} = \int_0^\infty dx_3 \Bigg\{ v_i^{(1)*} \Big[-ik_j^{(1)} + \frac{\partial}{\partial x_j} \Big] \Big[-\eta_{kij\ell m} \Big(e_k^{(2)} s_{\ell m}^{(1)*} + e_k^{(1)} s_{\ell m}^{(2)} \Big)$$

$$+ \tfrac{1}{2}\theta_{ijk\ell mn} \Big(s_{k\ell}^{(2)} s_{mn}^{(1)*} + s_{k\ell}^{(1)*} s_{mn}^{(2)} \Big)$$

$$- \tfrac{1}{2} Q_{k\ell ij} \Big(e_k^{(2)} e_\ell^{(1)*} + e_k^{(1)*} e_\ell^{(2)} \Big) \Big]$$

$$- ie_i^{(1)} \omega_1 \Big[Q_{ijk\ell} \Big(e_j^{(2)} s_{k\ell}^{(1)*} + e_j^{(1)*} s_{k\ell}^{(2)} \Big)$$

$$+ \tfrac{1}{2}\eta_{ijk\ell m} \Big(s_{jk}^{(2)} s_{\ell m}^{(1)*} + s_{jk}^{(1)*} s_{\ell m}^{(2)} \Big)$$

$$- \tfrac{1}{2} O_{ijk} \Big(e_j^{(2)} e_k^{(1)*} + e_j^{(1)*} e_k^{(2)} \Big) \Big] \Bigg\} \qquad (3.B.5)$$

$$C^{+}_{211} = \int_0^\infty dx_3 \Bigg\{ v_i^{(2)*} \Big[-ik_j^{(2)} + \frac{\partial}{\partial x_j} \Big] \Big[-\eta_{kij\ell m} \Big(e_k^{(1)} s_{\ell m}^{(1)} \Big)$$

$$+ \tfrac{1}{2}\theta_{ijk\ell mn} \Big(s_{k\ell}^{(1)} s_{mn}^{(1)} \Big)$$

$$- \tfrac{1}{2} Q_{k\ell ij} \Big(e_k^{(1)} e_\ell^{(1)} \Big) \Big]$$

$$- ie_i^{(2)*} \omega_2 \Big[Q_{ijk\ell} \Big(e_j^{(1)} s_{k\ell}^{(1)} \Big)$$

$$+ \tfrac{1}{2}\eta_{ijk\ell m} \Big(s_{jk}^{(1)} s_{\ell m}^{(1)} \Big)$$

$$- \tfrac{1}{2} O_{ijk} \Big(e_j^{(1)} e_k^{(1)} \Big) \Big] \Bigg\} \qquad (3.B.6)$$

From the discussion of the coupling constants in Chapter 2, one has:

$$-2K^{+*}_{211} = K^{-}_{121} \tag{3.B.7}$$

and thus (3.B.1) and (3.B.2) can be written with a single coupling constant K^{+}_{211}. Letting $K = K^{+}_{211}$, one has

$$v_g \frac{\partial q_1}{\partial x_1} = -2K^* \, q_2 q_1^* \tag{3.B.8}$$

$$v_g \frac{\partial q_2}{\partial x_1} = K \, q_1^2 \tag{3.B.9}$$

Hence the problem of determining coupling constants reduces to finding a single constant which can be represented with normalized terms as:

$$K = \frac{\omega_1^2 \, \hat{C}^{+}_{211} (v_{g2} v_{g1} v_{g1})^{1/2}}{8(\langle \hat{S}_2 \rangle \langle \hat{S}_1 \rangle \langle \hat{S}_1 \rangle)^{1/2}} \tag{3.B.10}$$

Because the modes are collinear,

$$\langle \hat{S}_2 \rangle = \langle \hat{S}_1 \rangle = \langle \hat{S} \rangle \tag{3.B.11}$$

$$v_{g2} = v_{g1} = v_g \tag{3.B.12}$$

and

$$K = \frac{\omega_1^2 \hat{C}^+_{211} v_g^{3/2}}{8(<S>)^{3/2}} \qquad (3.B.13)$$

Because of the resonant conditions $\delta\omega^{\pm} = 0$, $\delta k^{\pm} = 0$, $\hat{C}^+_{211}$ is frequency independent. Thus K is dependent upon the fundamental frequency squared and independent of power. A verification of these characteristics can be made from experiments. Most experiments can determine only $|K|$, [24]-[33], but a few have been done to find both magnitude and phase [34],[35]. However, because of (3.B.13), it is sufficient to determine the frequency dependence and power dependence of K from $|K|$ since both K and $|K|$ have the same dependencies of frequency and power.

In using the experimental results, one must work with $|q_2|$ and $|q_1|$, but $|q_2|$ and $|q_1|$ do not appear in (3.B.8) and (3.B.9), and in general (3.B.8) and (3.B.9) cannot be manipulated to derive equations in which $|q_2|$ and $|q_1|$ are the variables. However, special cases exist for which one may work with $|q_2|$ and $|q_1|$, and one of these special cases is characteristic of all the harmonic generation experiments.

This special case is known as phase-locking [45], and is a result of the boundary conditions of the experiments. Typically, a fundamental wave is launched at $x_1=0$ from which the second harmonic grows from noise and $q_2(x_1=0) \tilde{=} 0$. To see how this affects the phases of q_1 and q_2 for $x_1 > 0$, one can substitute

$$q_1(x_1) = |q_1(x_1)|\, e^{i\phi_1(x_1)} \tag{3.B.14}$$

$$q_2(x_1) = |q_2(x_1)|\, e^{i\phi_2(x_1)} \tag{3.B.15}$$

$$K = |K|\, e^{i\theta} \tag{3.B.16}$$

into equations (3.B.8) and (3.B.9) and find equations that describe the evolution of the magnitude and phase of q_1 and q_2. These equations are:

$$\frac{\partial|q_1|}{\partial x_1} = \frac{-2|K|}{v_g}\,|q_2||q_1|\,\cos(\phi_2 - 2\phi_1 - \theta) \tag{3.B.17}$$

$$\frac{\partial|q_2|}{\partial x_1} = \frac{|K|}{v_g}\,|q_1|^2\,\cos(2\phi_1 - \phi_2 + \theta) \tag{3.B.18}$$

$$\frac{\partial\phi_1}{\partial x_1} = \frac{-2|K|}{v_g}\,|q_2|\,\sin(\phi_2 - 2\phi_1 - \theta) \tag{3.B.19}$$

$$\frac{\partial\phi_2}{\partial x_1} = \frac{|K||q_1|^2}{v_g|q_2|}\,\sin(2\phi_1 - \phi_2 + \theta) \tag{3.B.20}$$

When q_2 is initially zero, the phase of q_2 is undefined at $x_1=0$. Examining equations (3.B.8) and (3.B.9) in a neighborhood around $x_1=0$ to find the inital ϕ_2, one has for $q_2(x_1=\Delta x)$:

$$q_2(x_1=\Delta x) \simeq \frac{K}{v_g}\, q_1(x_1=0)\,\Delta x \tag{3.B.21}$$

and

$$\phi_2(x_1=\Delta x) = \theta + 2\phi_2(x_1=0), \quad \text{or} \tag{3.B.22}$$

$$2\phi_2(x_1=0) - \phi_2(x_1=0) + \theta = 0 \tag{3.B.23}$$

(3.B.19) and (3.B.20) become

$$\frac{\partial \phi_1}{\partial x_1} = 0$$

$$\frac{\partial \phi_2}{\partial x_1} = 0, \quad [45].$$

Thus ϕ_1 and ϕ_2 are constants, and the nonlinear interaction can be described by

$$\frac{\partial |q_1|}{\partial x} = \frac{-2|K||q_2||q_1|}{v_g} \tag{3.B.24}$$

$$\frac{\partial |q_2|}{\partial x} = \frac{|K||q_1|^2}{v_g} \tag{3.B.25}$$

With phase locking and one of the wave amplitudes zero at $x_1=0$, one can choose K and q_α's to be real at $x_1=0$, and they will remain real [45]. For this discussion $|K|$ and $|q_\alpha|$'s will be retained because of the manner in which $|K|$ can be calculated from the normal mode field quantities.

As discussed in Chapter 2, the energy cross section analysis assumes constant phase. It is only because the experiments gave phase-locking that the theoretical methods used in [30]-[32] apply and are successful.

An illustrative example of the experiments for second harmonic generation is the work done by Adler et al to verify the single-nonlinear parameter model [28]. These same experiments can be used to confirm the predicted characteristics of $|K|$. The experiments were done with y-cut, z-propagating lithium niobate (YZ-$LiNbO_3$) and $(1\bar{1}0)$-cut, (001)-propagating bismuth germanium oxide ($(1\bar{1}0)$-(001) $Bi_{12}GeO_{20}$), and from this work a value of $|K|$ can be found for these cases. Second harmonic experiments done here have the fundamental frequency wave essentially undepleted. The power of the second harmonic is at least 20 dB lower than the fundamental. Hence $|q_1|$ can be treated as a constant undepleted pump, and only equation (3.B.25) is needed to describe the interaction. Equation (3.B.25) can be rewritten as:

$$\frac{\partial}{\partial x_1}\left[\frac{v_g|q_2|}{|q_1|^2}\right] = |K| \qquad (3.B.26)$$

This states that the expression $\dfrac{|q_2|}{v_g|q_1|^2}$ should have a linear behavior for the undepleted pump case.

The second harmonic experiments for YZ-$LiNbO_3$ were conducted at the same frequency, but with different input power levels, and can thus be used to determine if $|K|$ is independent of power. For the

experiments on $(1\bar{1}0)$-(001) $Bi_{12}GeO_{20}$, experiments at two different frequencies and the same input power were conducted and the square law dependence on frequency of $|K|$ can be checked. The parameters for the experiments are:

1. YZ-$LiNbO_3$

   Pac(fundamental acoustic power, x_1=0) = 31 dBm

   = 28 dBm

   f_1(fundamental frequency) = 50 MHz

   b(beam width) = 2mm

   v_g(group velocity) = 3487 m/sec

2. $Bi_{12}GeO_{20}$

   Pac: 28 dBm

   f_1: 100 MHz

   50 MHz

   b = 2 mm

   v_g = 1624 m/sec

It is assumed that diffraction does not contribute to the results of the experiments and that both the fundamental and second harmonic waves have rectangular cross-sections.

After converting the experimental data from [28] to the formalism here, the results are graphed in Fig. 3.1 and Fig. 3.2. Fig. 3.1 is a plot of $v_g \frac{|q_2(x_1)|}{|q_1(0)|^2}$ versus propagation distance x_1, and Fig. 3.2 is a plot of $\frac{v_g|q_2(x_1)|}{\omega^2|q_1(0)|^2}$.

Fig. 3.1

2nd Harmonic with Varying Power

[YZ-$LiNbO_3$]

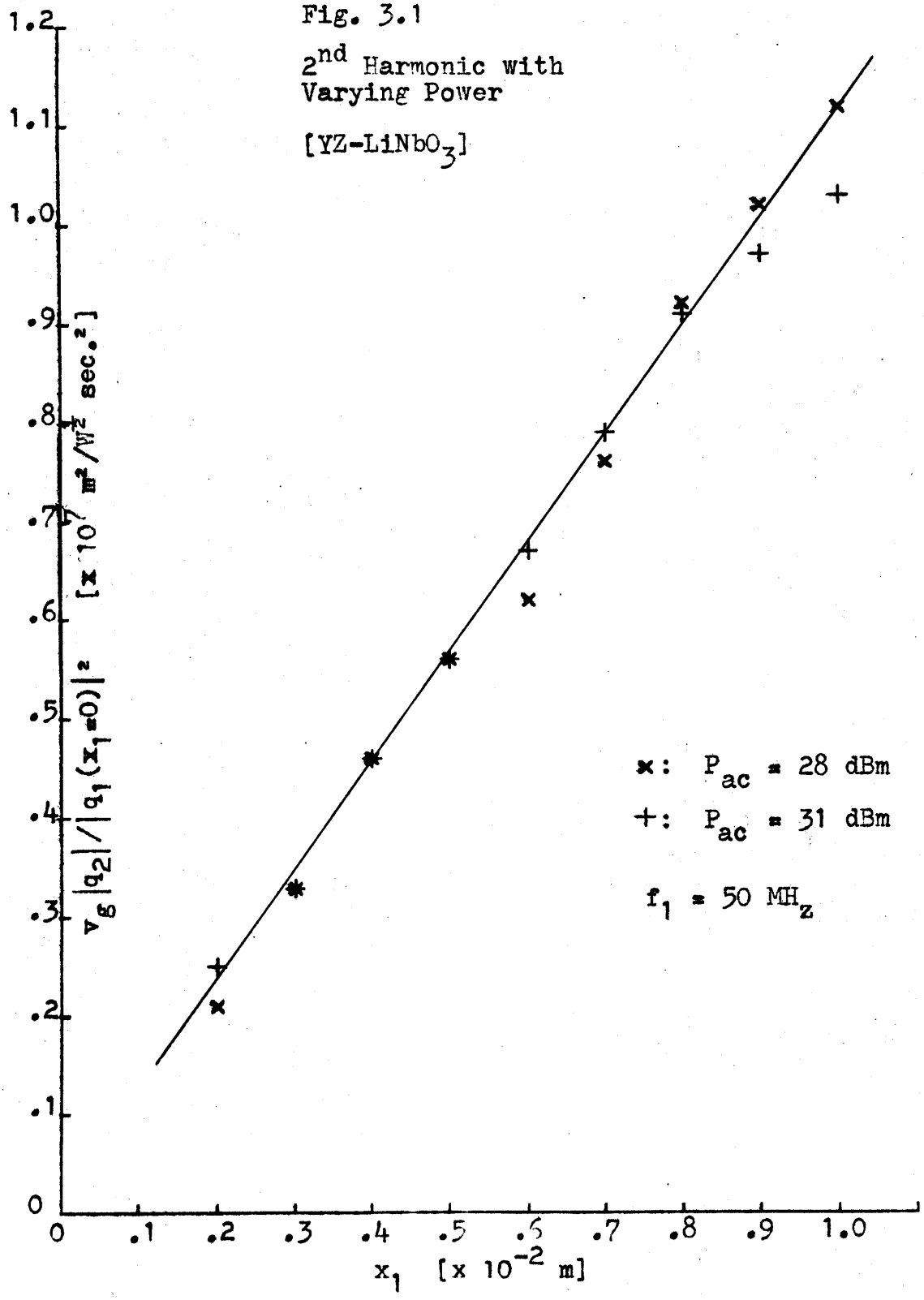

Fig. 3.2

2^{nd} Harmonic with Varying Frequency

[$(1\bar{1}0)$-(001) $Bi_{12}GeO_{20}$]

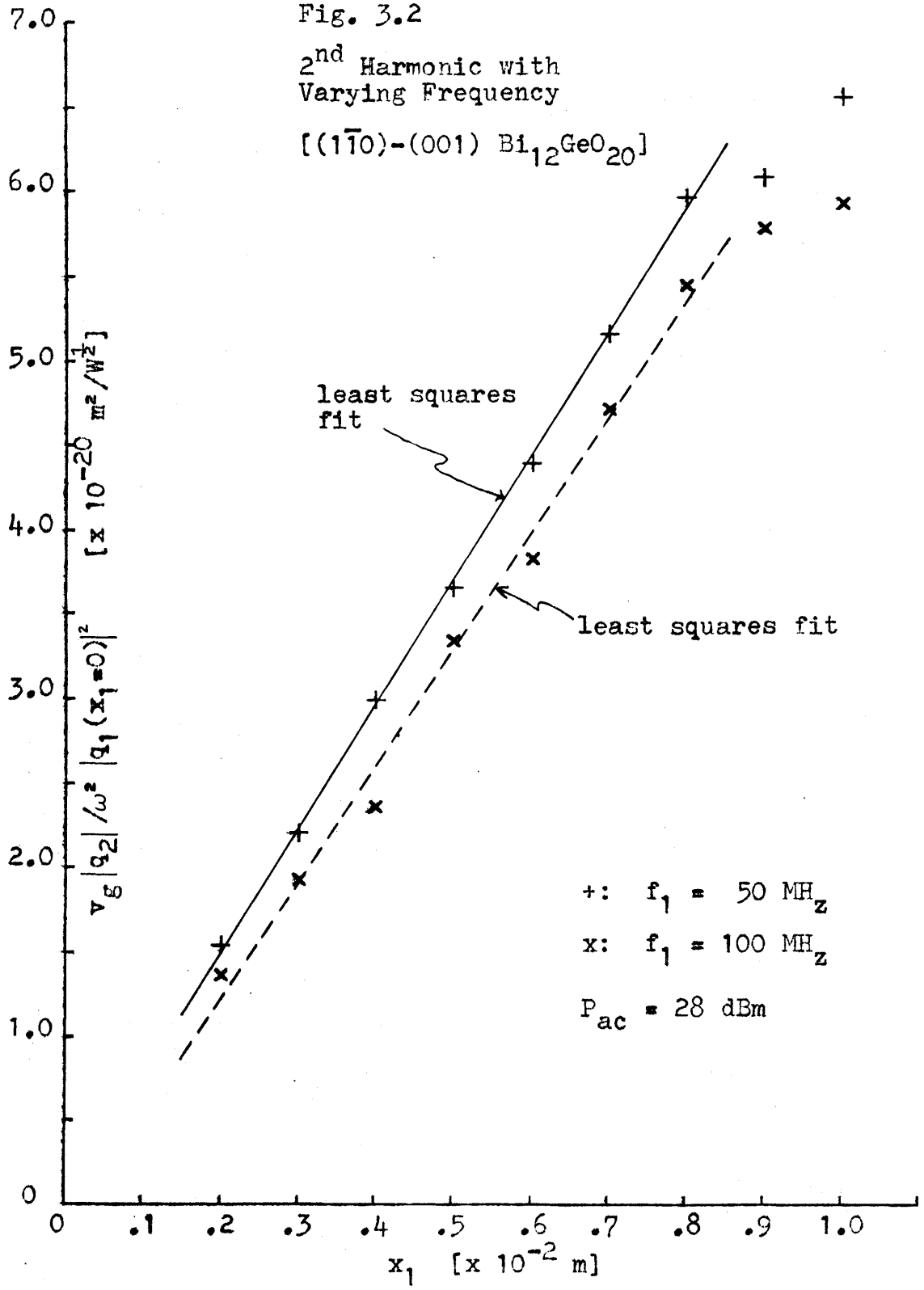

The results of Fig. 3.1 clearly indicate that the growth of the second harmonic is linear. A single line characterizes the data points of Fig. 3.1, and thus $|K|$ is independent of power. The slope of the line gives the magnitude of the coupling constant for YZ-$LiNbO_3$, with the result.

$$|K| = 1.1 \times 10^9 \frac{m}{\sec^2 W^{1/2}} \tag{3.B.27}$$

With the case of $(1\bar{1}0)$-(001) $Bi_{12}GeO_{20}$, the points from the 100 MHz and 50 MHz experiments should coincide. As indicated in the graph the points do not fall on each other. However, considering the accuracy of the experiments and converting the data from graphs of [28], an error of at least ten percent is justified. The slope of the two lines, which are least squares fitted for the data from 2 mm $\leq x \leq$ 8 mm, give $\frac{|K|}{\omega^2}$. The ratio of the slopes for the 100 MHz to the 50 MHz data points gives:

$$\frac{\frac{|K_{100}|}{\omega_{100}^2}}{\frac{|K_{50}|}{\omega_{50}^2}} = .95 \tag{3.B.28}$$

and the ratio of $|K_{100}|$ to $|K_{50}|$ is:

$$\frac{|K_{100}|}{|K_{50}|} = 3.8 \tag{3.B.29}$$

It would be expected that $\frac{|K_{100}|}{|K_{50}|} = 4$. However, the results fall well within experimental error, and justify the claim that $|K|$ is dependent upon frequency squared. The values of $|K|$ found for $(1\bar{1}0)$-(001) $Bi_{12}GeO_{20}$ are:

$$|K_{100}| = 5.3 \times 10^8 \frac{m}{sec^2 W^{1/2}} \tag{3.B.30}$$

$$|K_{50}| = 1.4 \times 10^8 \frac{m}{sec^2 W^{1/2}} \tag{3.B.31}$$

From the results on YZ-$LiNbO_3$ and $(1\bar{1}0)$-(001) $Bi_{12}GeO_{20}$, the characteristics of power independence of K, and a frequency squared dependence are experimentally verified. With these characteristics established, the coupling constants for other frequencies can be calculated, and in these two examples the $|K|$ has been determined.

As an estimate of the coupling constant K for YZ-$LiNbO_3$, one can perform numerical calculations from the results of the previous chapter and the computer work of [49]. Since surface acoustic wave power is primarily elastic, one can approximate K by calculating the contributions to K of the nonlinear elastic terms. Attempts to find the nonlinear elastic material constants $LiNbO_3$ have resulted in terms that contain the nonlinear piezoelectric constants [9] and are thermodynamically mixed [3], so that symmetries [4] of the actual nonlinear elastic constants are not present. However the nonlinear terms found in [9] are of the correct order of magnitude as the

nonlinear elastic constants defined in equation (2.D.1).

With equation $\hat{C}^{+}_{211} \simeq \hat{C}^{+\theta}_{211}$, from equation (2.E.27) one has

$$\hat{C}^{+}_{211} = -i\theta_{ijk\ell mn}\hat{V}^{(r)}_{i}\hat{S}^{(t)}_{k\ell}\hat{S}^{(w)}_{mn}\left[\alpha^{(t)} + \alpha^{(w)} + 2\alpha^{(r)*}\right]^{-1}$$

$$-\frac{1}{2}\theta_{ijk\ell mn}\hat{V}^{(r)}_{i}\hat{S}^{(t)}_{k\ell}\hat{S}^{(w)}_{mn}\left[\frac{\alpha^{(t)} + \alpha^{(w)}}{\alpha^{(t)} + \alpha^{(w)} + 2\alpha^{(r)*}}\right] \quad (3.B.32)$$

The superscripts for each mode have been dropped since the terms $\hat{V}^{(r)}_{i}$, $\hat{S}^{(t)}_{k\ell}$, $\hat{S}^{(w)}_{mn}$, and $\alpha^{(t)}$, $\alpha^{(w)}$, $\alpha^{(r)}$ are constants for all modes propagating collinearly. By choosing x_1 as the phase propagation direction, there is no contribution for j=2. Sum over repeated indices is assumed with

$$i,k,\ell,m,n = 1,2,3;$$

$$t,w,r = 1,2,3,4.$$

Appendix V discusses how $\hat{V}^{(r)}_{i}$, $\hat{S}^{(t)}_{k\ell}$, $\hat{S}^{(w)}_{mn}$ are calculated from [49]. Because of the degeneracies of YZ-$LiNbO_3$, whenever i,k,ℓ,m, or n equals two $\hat{S}_{k\ell} = \hat{S}_{mn} = 0$, and $\hat{V}_{i} = 0$. Therefore the only terms that contribute are those with subscripts of one and three. Thus only ten of the independent non-zero nonlinear elastic constants effect the harmonic generation of YZ-$LiNbO_3$ (see Appendix VI). Upon substituting the numbers found in [49] and [9], into (3.B.32) and $\hat{C}^{+}_{211}$ into the expression for K with $\omega_1 = 2\pi \cdot 50$ MHz, one finds:

$$K = 5.4 \times 10^{8}\, e^{.021i}\, \frac{m}{\sec^2 W^{1/2}} \qquad (3.B.33)$$

$$|K| = 5.4 \times 10^{8}\, \frac{m}{\sec^2 W^{1/2}} \qquad (3.B.34)$$

A more detailed discussion of the calculation of K is given in Appendix VI.

The result of this calculation is not in particularly good agreement with the experimentally determined value for YZ-$LiNbO_3$. The ratio of (3.B.34) to (3.B.27) is approximately $\frac{1}{2}$. P.J. Vella et al [33] also calculate a coupling parameter with the energy cross-section model, and the ratio of theoretical to experimental values is 3.4. Thus it appears that the terms used for $\theta_{ijk\ell mn}$ from [9] are badly contaminated by the nonlinear piezoelectric terms and the thermodynamic mix in the definitions of those terms and/or the other nonlinear terms produce important contributions to the interaction. It should be noted that the orders of magnitude of (3.B.34) and (3.B.27) are similar.

This section has discussed the theoretical coupled mode model for second harmonic generation and some of the properties of the coupling constants. It has been shown that a single nonlinear coupling constant can be used to describe the interactions and that the dependence of K on frequency squared and independence of power is experimentally verified. Experimental values of |K| for YZ-$LiNbO_3$ and $(1\bar{1}0)$-(001) $Bi_{12}GeO_{20}$ have been found, and because of the boundary

conditions of the interaction, phase-locking occurs. Hence, an understanding of the success of the single-nonlinear parameter model [28], and the "nonlinear cross sections-energy approach" has been achieved. From the arguments of phase-locking and relations among the coupling constants, one can extend the results of this section to the case of fourth harmonic generation.

C. Four Harmonics

With the generation of the fourth harmonic, the first through the third harmonics are also present, thus one has four waves interacting. This case can be modeled by four coupled amplitude equations. Again assuming resonant interactions the four equations are (see 2.D.31):

$$v_g \frac{\partial q_1}{\partial x_1} = K^-_{121}\, q_2 q_1^* + K^-_{132}\, q_3 q_2^* + K^-_{143}\, q_4 q_3^* \qquad (3.C.1)$$

$$v_g \frac{\partial q_2}{\partial x_1} = K^+_{211}\, q_1^2 + K^-_{231}\, q_3 q_1^* + K^-_{242}\, q_4 q_2^* \qquad (3.C.2)$$

$$v_g \frac{\partial q_3}{\partial x_1} = K^+_{321}\, q_2 q_1 + K^-_{341}\, q_4 q_1^* \qquad (3.C.3)$$

$$v_g \frac{\partial q_4}{\partial x_1} = K^+_{422}\, q_2^2 + K^+_{431}\, q_3 q_1 \qquad (3.C.4)$$

From the results of Chapter 2, the K's have specific relations, and from equations (2.E.3) and (2.E.4):

$$-2K^{+}_{211} = K^{-*}_{121} = -2K_1 \tag{3.C.5}$$

$$K^{+}_{321} = -K^{-*}_{132} = -K^{*}_{231} = K_2 \tag{3.C.6}$$

$$K^{+}_{431} = -K^{-*}_{341} = -K^{-*}_{143} = K_3 \tag{3.C.7}$$

$$-2K^{+}_{422} = K^{-*}_{242} = -2K_4 \tag{3.C.8}$$

Because K^{+}_{422} is the coupling constant for second harmonic generation for q_2 to give q_4, it is four times larger than K^{+}_{211} since ω_2 is twice ω_1, and the coupling constant for second harmonic generation scales as frequency squared. Therefore (3.C.5) and (3.C.8) combine to give

$$K_4 = 4K_1 \tag{3.C.9}$$

and the four coupling constants of (3.C.5) and (3.C.8) reduce to a single independent constant K_1. Thus the original ten coupling constants of (3.C.1)-(3.C.4) can be represented in terms of K_1, K_2, and K_3.

In general K_1, K_2, and K_3 are independent and not equal. This would initially indicate that a contradiction has occurred between this model, and the single-nonlinear parameter (β) discussed in [28] for multiharmonic generation. In the formalism developed here, the

term that is analogous to β is $C^{\pm}_{\alpha\beta\gamma}$. From equation (2.E.27), $C^{+\theta}_{\alpha\beta\gamma}$ can be written for resonant collinear harmonic generation on YZ-$LiNbO_3$ as:

$$C^{+\theta}_{\alpha\beta\gamma} = \sum_{\alpha\beta}\sum \frac{1}{2}\theta_{ilk\ell mn}\left[-i\hat{V}_i^{(r)*}\left\{\hat{S}_{k\ell}^{(t)}\hat{S}_{mn}^{(w)} + (1-\delta_{\beta\gamma})\hat{S}_{k\ell}^{(w)}\hat{S}_{mn}^{(t)}\right\}\right.$$

$$\left.(f_{\beta\gamma}+1)\left\{\alpha^{(r)*}(1+f_{\beta\gamma}) + f_{\beta\gamma}\,\alpha^{(w)} + \alpha^{(t)}\right\}^{-1}\right]$$

$$-\frac{1}{2}\theta_{i3jk\ell mn}\left[\hat{V}_i^{(r)*}\left\{\hat{S}_{k\ell}^{(t)}\hat{S}_{mn}^{(w)} + (1-\delta_{\beta\gamma})\hat{S}_{k\ell}^{(w)}\hat{S}_{mn}^{(t)}\right\}\right.$$

$$\left.\left\{f_{\beta\gamma}\alpha^{(w)}+\alpha^{(t)}\right\}\left\{\alpha^{(r)*}(1+f_{\beta\gamma}) + f_{\beta\gamma}\,\alpha^{(w)} + \alpha^{(t)}\right\}^{-1}\right] \qquad (3.C.10)$$

The superscripts of (α), (β), (γ) for each mode have been dropped, since the parameters $\hat{V}_i^{(r)}$, $\hat{S}_{k\ell}^{(t)}$, $\hat{S}_{mn}^{(w)}$, $\hat{S}_{k\ell}^{(w)}$, $\hat{S}_{mn}^{(t)}$, and $\alpha^{(t)}$, $\alpha^{(w)}$, $\alpha^{(r)}$ are constants for all modes propagating collinearly. The only terms in (3.C.10) that are dependent on given modes, α, β, and γ, are those terms that contain the frequency ratio $f_{\beta\gamma}$. The expressions that contain $f_{\beta\gamma}$ are:

$$R^{(1)(r)(w)(t)}_{\beta\gamma} = \frac{(f_{\beta\gamma}+1)}{\left\{\alpha^{(r)*}(1+f_{\beta\gamma}) + f_{\beta\gamma}\alpha^{(w)} + \alpha^{(t)}\right\}} \qquad (3.C.11)$$

$$R_{\beta\gamma}^{(3)(r)(w)(t)} = \frac{f_{\beta\gamma}{}^{\alpha(w)} + \alpha^{(t)}}{\left[\alpha^{(r)*}(1+f_{\beta\gamma}) + f_{\beta\gamma}{}^{\alpha(w)} + \alpha^{(t)}\right]} \qquad (3.C.12)$$

YZ-$LiNbO_3$ has four α's from which 64 possible values for $R_{\beta\gamma}^{(1)}$ and $R_{\beta\gamma}^{(3)}$ can respectively be calculated for a given $f_{\beta\gamma}$. However, because of the degeneracy [49] of YZ-$LiNbO_3$, only 27 values of $R_{\beta\gamma}^{(1)}$ and $R_{\beta\gamma}^{(3)}$ respectively contribute to $C_{\alpha\beta\gamma}^{+\theta}$.

The coupling constants K_1, K_2, K_3 correspond to interacting modes with frequency ratios of $f_{11} = 1$, $f_{21} = 2$, and $f_{31} = 3$ respectively. $R_{\beta\gamma}^{(1)}$ and $R_{\beta\gamma}^{(3)}$ can then be calculated from the α's for YZ-$LiNbO_3$ and the frequency ratios. Values of $R_{\beta\gamma}^{(1)(r)(w)(t)}$ and $R_{\beta\gamma}^{(3)(r)(w)(t)}$ were computed for f_{21} and f_{31}, and compared to the values of $R_{\beta\gamma}^{(1)(r)(w)(t)}$ and $R_{\beta\gamma}^{(3)(r)(w)(t)}$ with the same superscript, determined with f_{11}.

Examining $R_{21}^{(1)(r)(w)(t)}$ against $R_{11}^{(1)(r)(w)(t)}$, one finds that only six of the twenty-seven terms of $R_{21}^{(1)(r)(w)(t)}$ differ by more than ten percent in magnitude of $R_{11}^{(1)(r)(w)(t)}$. The maximum percentage difference was twenty-two percent, and the maximum phase difference was .13 radian. For $R_{21}^{(3)(r)(w)(t)}$ and $R_{11}^{(3)(r)(w)(t)}$, nine out of twenty-seven values of $R_{21}^{(3)(r)(w)(t)}$ differed in magnitude by greater than ten percent of $R_{11}^{(3)(r)(w)(t)}$, but only four were greater than fifteen percent. The maximum percentage difference in magnitude was twenty-six percent, and maximum phase difference was .08 radians. Considering the comparison of $R_{31}^{(1)(r)(w)(t)}$ against

$R_{11}^{(1)(r)(w)(t)}$, twelve of the twenty-seven terms differed in magnitude more than ten percent, while six were greater than fifteen percent. The largest percentage difference between $R_{31}^{(1)(r)(w)(t)}$ and $R_{11}^{(1)(r)(w)(t)}$ in magnitude was thirty-three percent with a maximum phase difference of .20 radian. A comparison of $R_{31}^{(3)(r)(w)(t)}$ and $R_{11}^{(3)(r)(w)(t)}$ yielded a maximum difference of forty-seven percent and phase difference of .14 radian. Nine of the twenty-seven comparisons showed magnitude differences between $R_{31}^{(3)(r)(w)(t)}$ and $R_{11}^{(3)(r)(w)(t)}$ to be greater than ten percent and eight greater than fifteen percent.

Therefore, one finds that with so many of the contributing terms to $C_{\alpha\beta\gamma}^{+\theta}$ for f_{11}, f_{21}, f_{31} to be approximately equal, one has

$$\hat{C}_{211} \simeq \hat{C}_{321} \simeq \hat{C}_{431} \cdot \tag{3.C.13}$$

Hence the result that Adler et al [28] obtain in using a single nonlinear parameter β for YZ-$LiNbO_3$, are consistent with the formalism here. Given (3.C.13), one finds

$$K_1 \simeq \frac{1}{2} K_2 \simeq \frac{1}{3} K_3 \tag{3.C.14}$$

and by determining one coupling constant one can exactly or approximately find the other nine coupling constants. Since $|K_{211}^{+}| = |K_1|$ is known for second harmonics on YZ-$LiNbO_3$, one can use this term in fitting the results of multiharmonic experiments with coupled mode theory. The value of β quoted in [28] is for second

harmonic and was used to fit coupled mode theory to the other harmonics. Thus an understanding of the results of [28] for YZ-$LiNbO_3$ can be found by the nonlinear theory developed here.

Except for the single coupling constant comments, this discussion is general and easily extended to higher harmonics. No calculations of $R_{\beta\gamma}^{(1)(t)(u)(w)}$ and $R_{\beta\gamma}^{(3)(t)(u)(w)}$ have been made for higher harmonics, but it is conceivable that only small variations of a large number of these terms could occur, permitting one to model experiments of harmonics greater than four with coupled mode theory using only one K.

Multiharmonic generation is also discussed by [30]-[31] in which the "nonlinear cross section-energy" analysis is used. This approach is used to model the interactions at large power densities of $7x10^7$ Watts/m^2, and the coupling is stronger than in [28]. Again one finds that the multiharmonic case can be shown to be phased-locked thereby permitting this approach to be applied. Because at $x_1=0$ the harmonics are equal to zero, the phase of each harmonic is undefined. Following the procedure given in the last one can define

$$q_\alpha = |q_\alpha| \, e^{i\phi_\alpha} \tag{3.C.15}$$

$$K_i = |K_i| \, e^{i\phi_i} \tag{3.C.16}$$

and find four equations describing the phase change

$$\frac{\partial\phi_1}{\partial x_1} = \frac{-2|K_1||q_2||q_1|}{|q_1|}\sin(\phi_2-2\phi_1-\theta_1) - \frac{|K_2||q_3||q_2|}{|q_1|}\sin(\phi_3-\phi_2-\phi_1-\theta_2)$$

$$- \frac{|K_3||q_4||q_3|}{|q_1|}\sin(\phi_4-\phi_3-\phi_1-\theta_3) \qquad (3.C.17)$$

$$\frac{\partial\phi_2}{\partial x_1} = \frac{|K_1||q_1|^2}{|q_2|}\sin(2\phi_2+\theta_1-\phi_2) - \frac{|K_2||q_3||q_1|}{|q_2|}\sin(\phi_3-\phi_1-\phi_2-\theta_2)$$

$$- 8|K_1||q_4||q_2|\sin(\phi_4-2\phi_2-\theta_1) \qquad (3.C.18)$$

$$\frac{\partial\phi_3}{\partial x_1} = \frac{|K_2||q_2||q_1|}{|q_3|}\sin(\phi_1+\phi_2+\theta_2-\phi_3) - \frac{|K_3||q_4||q_1|}{|q_3|}\sin(\phi_4-\phi_1-\phi_3-\theta_3) \qquad (3.C.19)$$

$$\frac{\partial\phi_4}{\partial x_1} = \frac{4|K_1||q_2|^2}{|q_4|}\sin(2\phi_2+\theta_1-\phi_4) + \frac{|K_3||q_3||q_1|}{|q_4|}\sin(\phi_3+\phi_1+\theta_3-\phi_4) \qquad (3.C.20)$$

With q_2, q_3, q_4 initially zero, the phase of these amplitudes are undefined at $x_1=0$. Starting with the second harmonic, one finds from (3.C.2) that in a neighborhood around $x_1=0$, that for $q_2(x_1=\Delta x)$ with

$$q_1 >> q_3 \simeq 0$$

$$q_1 >> q_4 \simeq 0,$$

$$q_2(x_1=\Delta x) \simeq \frac{K_1}{v_g} q_1^2(x_1=0)\ \Delta x, \qquad \text{therefore} \tag{3.C.21}$$

$$2\phi_1(x_1=0) + \theta_1 - \phi_2\ (x_1=0) = 0 \tag{3.C.22}$$

From (3.C.3), $q_2 >> q_4 \simeq 0$, and

$$q_3(x_1=\Delta x) \simeq \frac{K_2}{v_g} q_2(x_1=\Delta x)\ q_1(x_1=0)\ \Delta x,$$

one has

$$q_3(x_1=\Delta x) \simeq \frac{K_1 K_2}{v_g} q_1^3(x_1=0)\ (\Delta x)^2 \tag{3.C.23}$$

and,

$$3\phi_1(x_1=0) + \theta_1 + \theta_2 - \phi_3(x_1=0) = 0 \tag{3.C.24}$$

Equation (3.C.4) gives

$$q_4(x_1=\Delta x) \simeq \frac{4K_1^2}{v_g} q_2^2(x_1=\Delta x)\Delta x + \frac{K_2 q_3(x_1=\Delta x)}{v_g} q_1(x_1=0)\Delta x$$

$$q_4(x_1=\Delta x) \simeq \frac{4K_1^2 q_1^4(x_1=0)(\Delta x)^3}{v_g} + \frac{K_2 q_1^4(x_1=0)(\Delta x)^3}{v_g}$$

because $4K_1^2 >> K_2$, one has

$$q_4(x_1=\Delta x) \simeq \frac{4K_1^2 q_1^4(x_1=0)(\Delta x)^3}{v_g}\ , \tag{3.C.25}$$

and

$$4\phi_1(x_1=0) + 2\theta_1 + \phi_4(x_1=0) = 0 \qquad (3.C.26)$$

Substituting (3.C.22), (3.C.24), and (3.C.26) into (3.C.17) - (3.C.20) gives

$$\frac{\partial \phi_\alpha}{\partial x_1} = 0$$

and thus all the phases are constant and phase-locking occurs. Hence the "nonlinear cross section-energy approach" is applicable.

The discussion up to here has examined only resonant coupling; however, dispersive effects have been reported [26] and theoretically examined [29]. E.L. Adler et al. have used a single nonlinear parameter approximately equal to the parameter for resonant interactions, and a single dispersive parameter to model the results of [26]. The single dispersive parameter is applicable because of the apparent linear behavior of velocity with frequency, or the dispersion relation is quadratic in frequency [29]. If the dispersion is small as given by the conditions as discussed in Chapter 2, one finds that (3.C.5)-(3.C.8) still hold and the discussion of using a single K given above is also valid. The δk^+ found from

$$\delta k^+ = k_2 - 2k_1$$

is the single dispersion parameter used in [29] and determined to be 500 times smaller than k_1. Hence, the nonlinear theory given here predicts that a single-nonlinear parameter can be used in calculating the results of small dispersive effects, and the single nonlinear parameter for dispersive cases should be approximately equal to the K for resonant interactions.

D. Summary

From the discussion of the second and fourth harmonic generation several characteristics of coupled mode theory have been examined. It is found that the frequency dependence and power independence of the coupling constants is experimentally verified. Because of boundary condition of $q_\alpha(x_1=0) = 0$, $\alpha > 1$, phase-locking occurs thus permitting one to work with $|q_\alpha|$ to find $|K|$, and explaining the success of the "nonlinear cross section-energy approach". Further it is seen that a single nonlinear parameter can be used to model multiharmonic interactions for resonant and dispersive cases, and is an expected result from examining the coupling constants for special cases. From the experiments conducted by Adler et al., values of $|K|$ are determined for YZ-$LiNbO_3$ and $(1\bar{1}0)$-(001) $Bi_{12}GeO_{20}$. It should be noted that $|K|$ is found in a rather simple manner without resorting to solving systems of simultaneous nonlinear equations by computer as has been done by [24]-[35]. The discussions presented here have had limitations placed on them, but the arguments given, especially for phase-locking, relations among coupling constants, and small

dispersive effects, are more general and can be applied to other cases.

Harmonic generation has been extensively studied with the result that coupled mode theory is an apt description; however, noncollinear interactions have not had this attention and no measure of the coupling constants have been performed. The next two chapters specifically discuss theory and experiments of steady-state noncollinear interactions.

CHAPTER 4

NONCOLLINEAR INTERACTIONS - THEORY AND EXPERIMENT

A. Introduction

Steady-state nonlinear interactions of noncollinear surface acoustic waves were first experimentally examined by P.H. Carr [36] and several characteristics of noncollinear interactions have resulted in beam stearing and switching devices [37]-[41], with potential use in logic and gating systems. The experimental work has been modeled by a "nonlinear cross section-energy approach" [37]-[40], and a "general perturbation formula" [41]. However, the theoretical approaches as discussed in Chapter 2, have not been complete [41], or correct [37]-[40] in deriving coupled amplitude equations for noncollinear interactions.

This chapter discusses a consistent method of modeling the nonlinear interactions of noncollinear SAW beams by use of equation (2.D.31). The coupled amplitude equations are then discussed in a specific coordinate system, and from phase-locking and undepleted pumps an equation is derived from which the magnitude of the coupling constants can be found. The simplest noncollinear interaction is a three-wave resonant interaction, and this shall be used for discussion.

Based on the three-wave theory an experiment was devised to find $|K|$ for a noncollinear interaction. This chapter briefly discusses in sections C and D the general experiment, and several parameters evaluated to specify the experimental design. The three-wave

collision scheme (section E) and the two pump-wave transducers (section F) are then reviewed and a discussion of the generation and detection schemes follows in section G. Section H considers several pre-experiment tests. After this, section I examines experimental procedure and this chapter concludes with the detection network calibration method (section J).

B. Noncollinear Three-Wave Theory

From equation (2.D.31), three coupled amplitude equations that model a steady-state noncollinear three-wave interaction can be derived. These equations

$$v_{g1}^{(3)} \frac{\partial q_3}{\partial x_1} + v_{g2}^{(3)} \frac{\partial q_3}{\partial x_2} = K_{321}^{+} \, q_2 q_1 \tag{4.B.1}$$

$$v_{g1}^{(2)} \frac{\partial q_2}{\partial x_1} + v_{g2}^{(2)} \frac{\partial q_2}{\partial x_2} = K_{231}^{-} \, q_3 q_1^{*} \tag{4.B.2}$$

$$v_{g1}^{(1)} \frac{\partial q_1}{\partial x_1} + v_{g2}^{(1)} \frac{\partial q_1}{\partial x_2} = K_{132}^{-} \, q_3 q_2^{*} \tag{4.B.3}$$

The coordinate system here is the same as Fig. 1.1, with $v_{gi}^{(\alpha)}$ the component of the group velocity of mode α in the i^{th} direction. Resonant conditions imply

$$\omega_3 = \omega_1 + \omega_2$$

$$\bar{k}_3 = \bar{k}_1 + \bar{k}_2$$

If the coordinate system is chosen so that the x_1 direction is parallel to the direction of the group velocity of mode 3, or equivalently $\hat{x}_1$ is parallel to $\bar{v}_{g3}$, then $v_{g2}^{(3)}$ is zero and equation (4.B.1) reduces to

$$v_{g1}^{(3)} \frac{\partial q_3}{\partial x_1} = K_{321}^{+} q_2 q_1 \tag{4.B.4}$$

Equations (4.B.2)-(4.B.4) are the equations to be used to describe the three-wave interaction and have been solved for a homogeneous medium [44].

The coupling constants are again related from equation (2.E.3) and thus

$$K_{321}^{+} = -K_{132}^{-*} = -K_{231}^{-*}. \tag{4.B.5}$$

For convenience,

$$K = K_{321}^{+}. \tag{4.B.6}$$

Therefore a single coupling constant describes the noncollinear interaction, and it is necessary to only find the value of K.

As in the case of harmonic generation, the simplest interaction is to launch two pump waves from which the third evolves. With this condition, the interaction could produce an up-converted wave of higher frequency than the two pumps or a down-converted wave of lower

frequency. From equations (4.B.1)-(4.B.3), and conservation of energy and momentum, the equivalent Manley-Rowe relations for steady-state interactions can be found. The results are:

$$\frac{\bar{v}_{g3}\cdot\bar{\nabla}\langle w_3\rangle}{\omega_3} = \frac{-\bar{v}_{g2}\cdot\bar{\nabla}\langle w_2\rangle}{\omega_2} = \frac{-v_{g1}\cdot\bar{\nabla}\langle w_1\rangle}{\omega_1} \tag{4.B.7}$$

$$\frac{\bar{\nabla}\cdot\langle\bar{S}_3\rangle}{\omega_3} = \frac{-\bar{\nabla}\cdot\langle\bar{S}_2\rangle}{\omega_2} = \frac{-\bar{\nabla}\cdot\langle\bar{S}_1\rangle}{\omega_1} \tag{4.B.8}$$

If two frequencies ω_a and ω_b ($\omega_a > \omega_b$) are launched, then two possible interactions can occur. One of these is an up-conversion interaction in which the up-converted frequency (ω_+) is the sum of two initial frequencies;

$$\omega_+ = \omega_a + \omega_b$$

The other case is a down-conversion interaction in which a difference frequency (ω_-) is produced:

$$\omega_- = \omega_a - \omega_b$$

For the up-conversion interaction, equation (4.B.8) gives,

$$\frac{\bar{\nabla}\cdot\langle\bar{S}_+\rangle}{\omega_+} = \frac{-\nabla\cdot\langle\bar{S}_a\rangle}{\omega_a} = \frac{-\nabla\cdot\langle\bar{S}_b\rangle}{\omega_b} \tag{4.B.9}$$

and the down-conversion case gives

$$\frac{\nabla\cdot\langle\bar{S}_a\rangle}{\omega_a} = \frac{-\nabla\cdot\langle\bar{S}_-\rangle}{\omega_-} = \frac{-\nabla\cdot\langle\bar{S}_b\rangle}{\omega_b} \tag{4.B.10}$$

If the powers in the pump waves are identical for the up- and down-conversion interactions, one has:

$$\frac{\bar{\nabla}\cdot\langle\bar{S}_+\rangle}{\omega_+} = \frac{\nabla\cdot\langle\bar{S}_-\rangle}{\omega_-} \tag{4.B.11}$$

and with $\omega_+ > \omega_-$,

$$\nabla\cdot\langle\bar{S}_+\rangle \; > \; \nabla\cdot\langle\bar{S}_-\rangle \tag{4.B.12}$$

Hence $\langle\bar{S}_+\rangle$ is greater than $\langle\bar{S}_-\rangle$ and $\langle\bar{S}_+\rangle$ will be favored in the interaction. This phenomenon is confirmed by Carr [36] for $LiNbO_3$. The following discussion will consider only the up-conversion interaction.

With the two-pump experiment in which ω_1 and ω_2 combine to produce ω_3 ($\omega_3 = \omega_1 + \omega_2$), one can again show that phase-locking occurs. Equations for the magnitude and phase of each q can be written. For q_3, one has

$$v_{g1}^{(3)} \frac{\partial|q_3|}{\partial x_1} = |K||q_2||q_1| \cos(\phi_2 + \phi_1 + \theta - \phi_3) \tag{4.B.13}$$

$$v_{g1}^{(3)} \frac{\partial\phi_3}{\partial x_1} = \frac{|K||q_2||q_1|}{|q_3|} \sin(\phi_2 + \phi_1 + \theta - \phi_3) \tag{4.B.14}$$

where,

$$q_\alpha = |q_\alpha| e^{i\phi_\alpha} , \qquad \alpha = 1,2,3$$

$$K = |K| e^{i\theta}$$

As with the other discussions on phase-locking, the phase of q_3 is undefined at $x_1=0$ because q_3 is initially zero. Investigating q_3 in a neighborhood of $x_1=0$, one finds from (4.B.4),

$$q_3(x_1=\Delta x, x_2) \simeq K q_2(x_1=0,x_2)\, q_1(x_1=0,x_2)\Delta x_1, \qquad (4.B.15)$$

thus

$$\phi_3(x_1=\Delta x) = \theta + \phi_1(x_1=0,x_2) + \phi_2(x_1=0,x_2) \qquad (4.B.16)$$

and from (4.B.14) the change in phase is zero. Hence ϕ_3 is a constant and phase-locking results. Therefore the equation that can be used to determine $|K|$ is:

$$v_{g1}^{(3)} \frac{\partial |q_3|}{\partial x_1} = |K||q_2||q_1| \qquad (4.B.17)$$

This discussion has specifically examined only phase-matched interactions. However, experiments [37]-[40] have been performed in which phase mismatching occurred. The arguments for slightly dispersive cases of collinear interactions discussed in Chapter 3, section C can be applied to noncollinear problems, but shall not be pursued here.

To illustrate the up-conversion process, two examples shall be reviewed. In both cases the pump waves are considered undepleted. The first example considers two initial waves of rectangular cross-section, and the second the pumps are ramps.

Example 1. By integrating equation (4.B.13) one has:

$$|q_3(x_1,x_2)| = \frac{|K|}{v_{g3}} \int_{-\infty}^{\infty} |q_1(x_1,x_2)||q_2(x_1,x_2)|dx_1 \qquad (4.B.18)$$

Fig. 4.1(a-e) show the overlapping pumps and the cross-hatched region is the overlapping sections. Fig. 4.2(a-d) show the profile of $|q_3|$ at the equivalent point along x_1. From Fig. 4.1a, one can see the initial conditions and paths that $q_1(x_1,x_2)$ and $q_2(x_1,x_2)$ will follow. This gives a relationship between x_1 and x_2 for the integral in (4.B.18). Therefore equation (4.B.18) becomes for $x_2 \geq 0$,

$$|q_3(x_1,x_2)| = |K| \int_{x_2}^{x_1} |q_1(\zeta,x_2)||q_2(\zeta,x_2)|d\zeta \qquad (4.B.19)$$

$x_2 \leq 0$

$$|q_3(x_1,x_2)| = |K| \int_{x_2}^{x_1} |q_1(\zeta,x_2)||q_2(\zeta,x_2)|d\zeta \qquad (4.B.20)$$

Following Figures 4.1(a-e) and 4.2(a-e) it should be noted that the profiles of $|q_3|$ have a peak along the line x_2=0. This example has the special arrangement that the group velocity vectors

Fig. 4.1
Overlapping Pumps

Fig. 4.1a

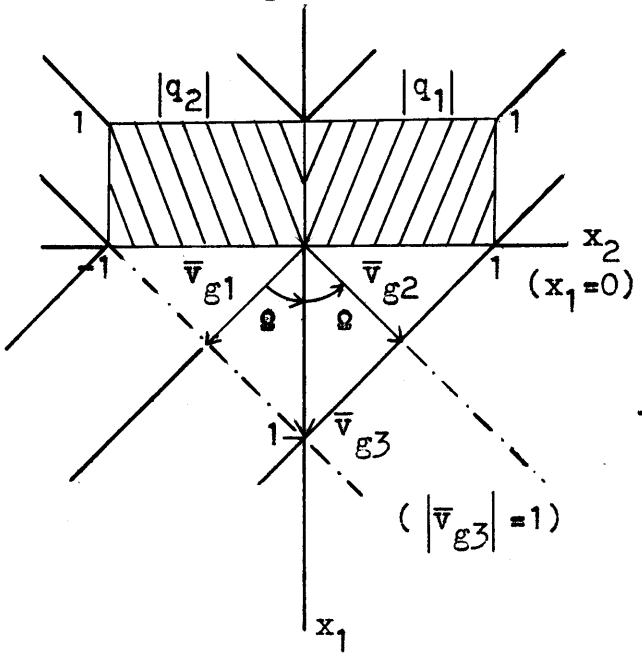

Fig. 4.1b

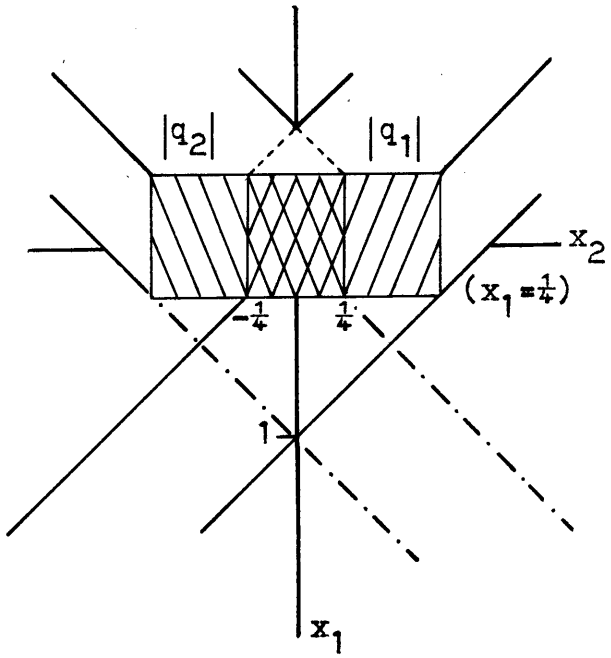

Fig. 4.2
Profile of $|q_3|$

Fig. 4.2a

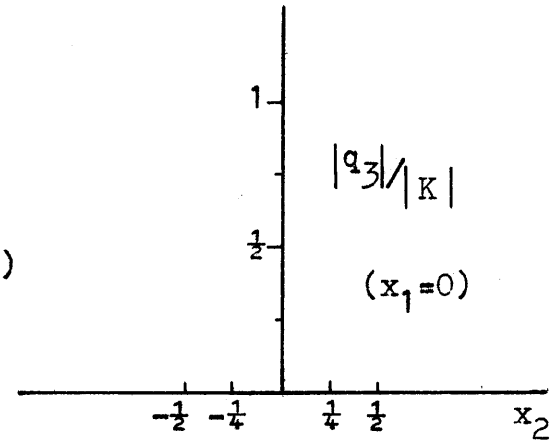

Fig. 4.2b

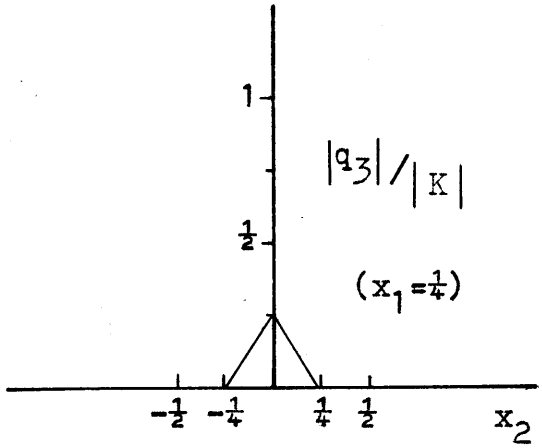

Fig. 4.1c

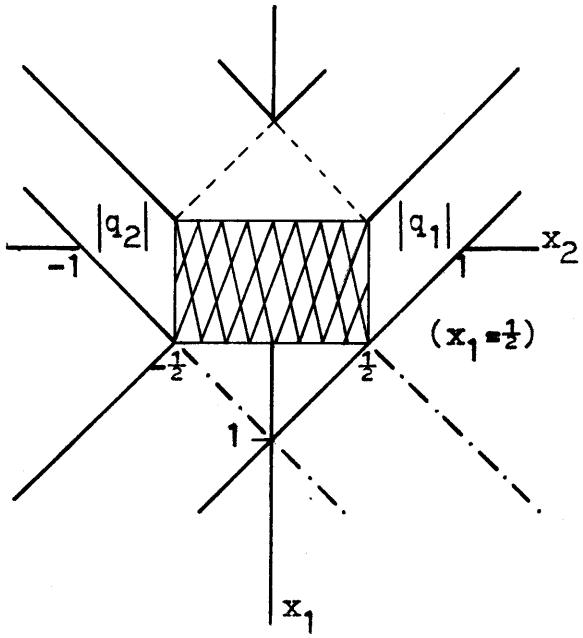

Fig. 4.2c

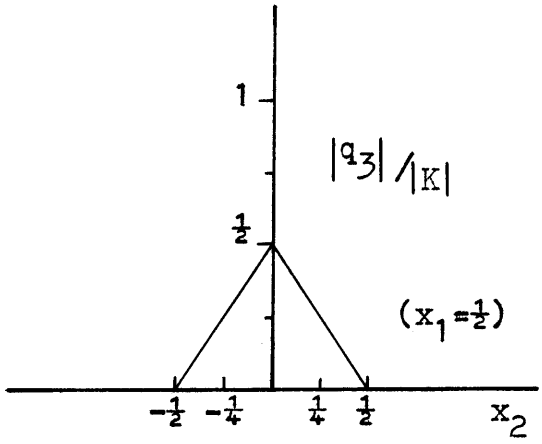

Fig. 4.1d

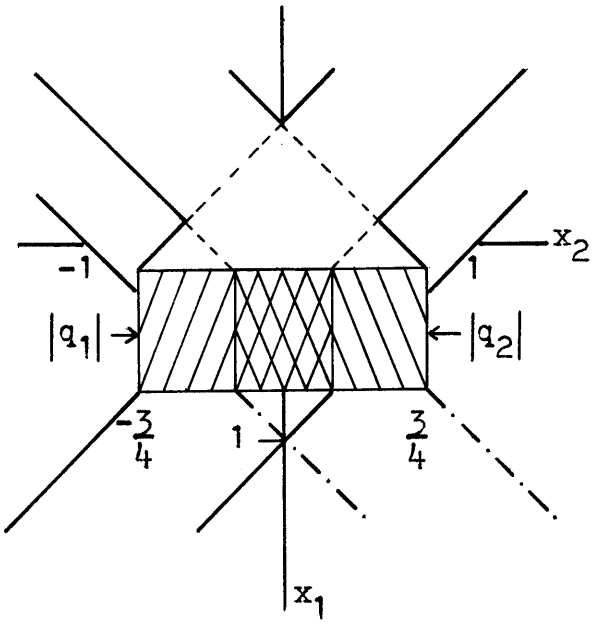

Fig. 4.2d

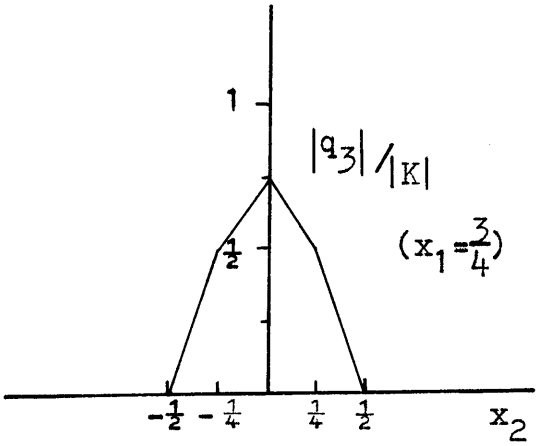

Fig. 4.1e

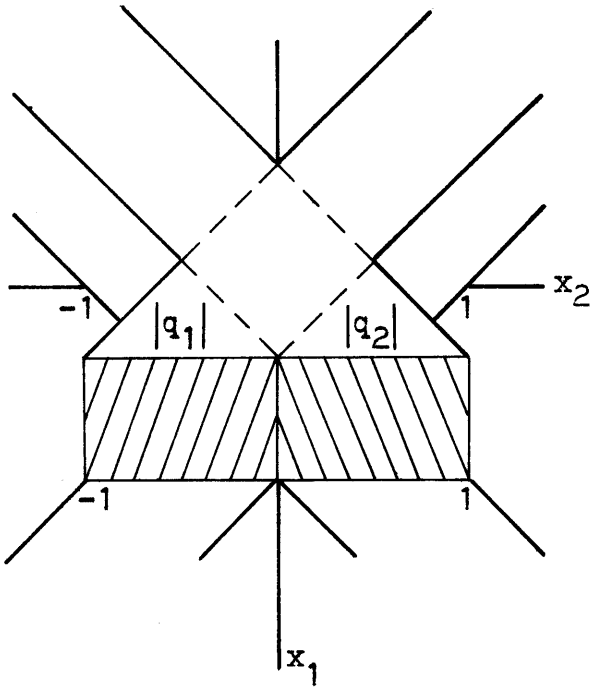

Fig. 4.2e

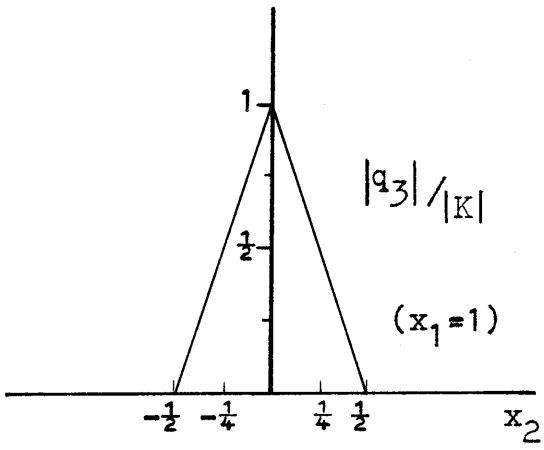

of the pump waves are at the same angular distance from $\vec{v}_{g3}$ as seen in Fig. 4.1a and the same magnitudes. If one follows $|q_3(x_1,x_2=0)|$, one finds that it increases linearly and the slope of the line of $|q_3(x_1,x_2=0)|$ vs. x_1 is $|K|$. Further, the peak of the profile follows the group velocity direction of $|q_3(x_1,x_2)|$. The next example considers the cases of equal and nonequal angles.

Example 2. With this case the interacting profiles are ramps as shown in Fig. 4.3. $|q_2|$ and $|q_1|$ are represented as

$$|q_2(x_1,x_2)| = -\delta(x_2 - \alpha x_1) \tag{4.B.21}$$

$$|q_1(x_1,x_2)| = \gamma(x_2 + \beta x_1) \tag{4.B.22}$$

Substituting equations (4.B.21) and (4.B.22) into (4.B.18), one has

1. $x_2 \geq 0$

$$|q_3(x_1,x_2)| = |K| \int_{\frac{x_2}{\alpha}}^{x_1} -\gamma\delta[x_2 - \alpha\zeta_1][x_2 + \beta\zeta_1]d\zeta_1 \tag{4.B.23}$$

2. $x_2 \leq 0$

$$|q_3(x_1,x_2)| = |K| \int_{-\frac{x_2}{\beta}}^{x_1} -\gamma\delta[x_2 - \alpha\zeta_1][x_2 + \beta\zeta_1]d\zeta_1 \tag{4.B.24}$$

Fig. 4.3

Ramp Profiles
($\alpha>0$, $\beta>0$, $\gamma>0$, $\delta>0$)

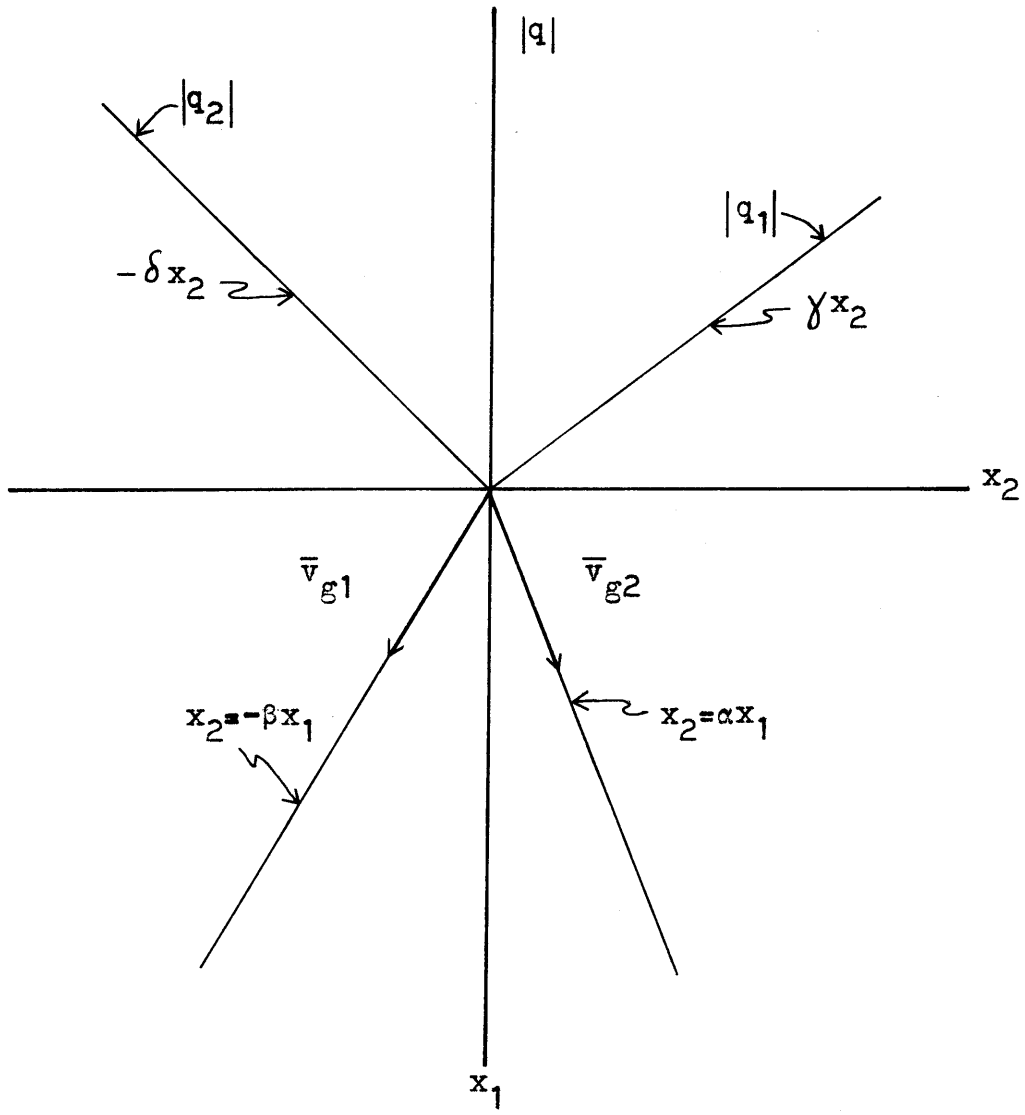

The result of the integration gives:

1. $x_2 \geq 0$

$$|q_3(x_1,x_2)| = |K|\left[\gamma\delta\left(\frac{3\alpha+\beta}{6\alpha^2}\right)x_2^3 - \gamma\delta x_1 x_2^2 + \gamma\delta\left(\frac{\alpha-\beta}{2}\right)x_1^2 x_2 + \frac{\gamma\delta\alpha\beta x_1^3}{3}\right] \tag{4.B.25}$$

2. $x_2 \leq 0$

$$|q_3(x_1,x_2)| = |K|\left[-\gamma\delta\left[\frac{3\beta+\alpha}{6\beta^2}\right]x_2^3 - \gamma\delta x_2 x_1^2 + \gamma\delta\left(\frac{\alpha-\beta}{2}\right)x_1^2 x_2 + \frac{\gamma\delta\alpha\beta x_1^3}{3}\right] \tag{4.B.26}$$

With the special case $\alpha=\beta=1$, then (4.B.25) and (4.B.26) reduce to:

$$|q_3(x_1,x_2)| = |K|\ \gamma\delta\left[\frac{2x_2^3}{3} - x_1 x_2^2 + \frac{x_1^3}{3}\right]; \quad x_2 \geq 0 \tag{4.B.27}$$

$$|q_3(x_1,x_2)| = |K|\ \gamma\delta\left[\frac{-2x_2^3}{3} - x_1 x_2^2 + \frac{x_1^3}{3}\right]; \quad x_2 \leq 0 \tag{4.B.28}$$

Fig. 4.4 is a graph of (4.B.27) and (4.B.28). Again, for all values of x_1, the peak appears at $x_2=0$. This is a result of setting $\alpha=\beta$, and the group velocity of q_3 bisects the angle formed by the group velocity vectors of q_1 and q_2. Therefore one can find the group

Fig. 4.4

Profile $|q_3|/|K|$

($\alpha=\beta=1$; $\gamma\delta=1$)

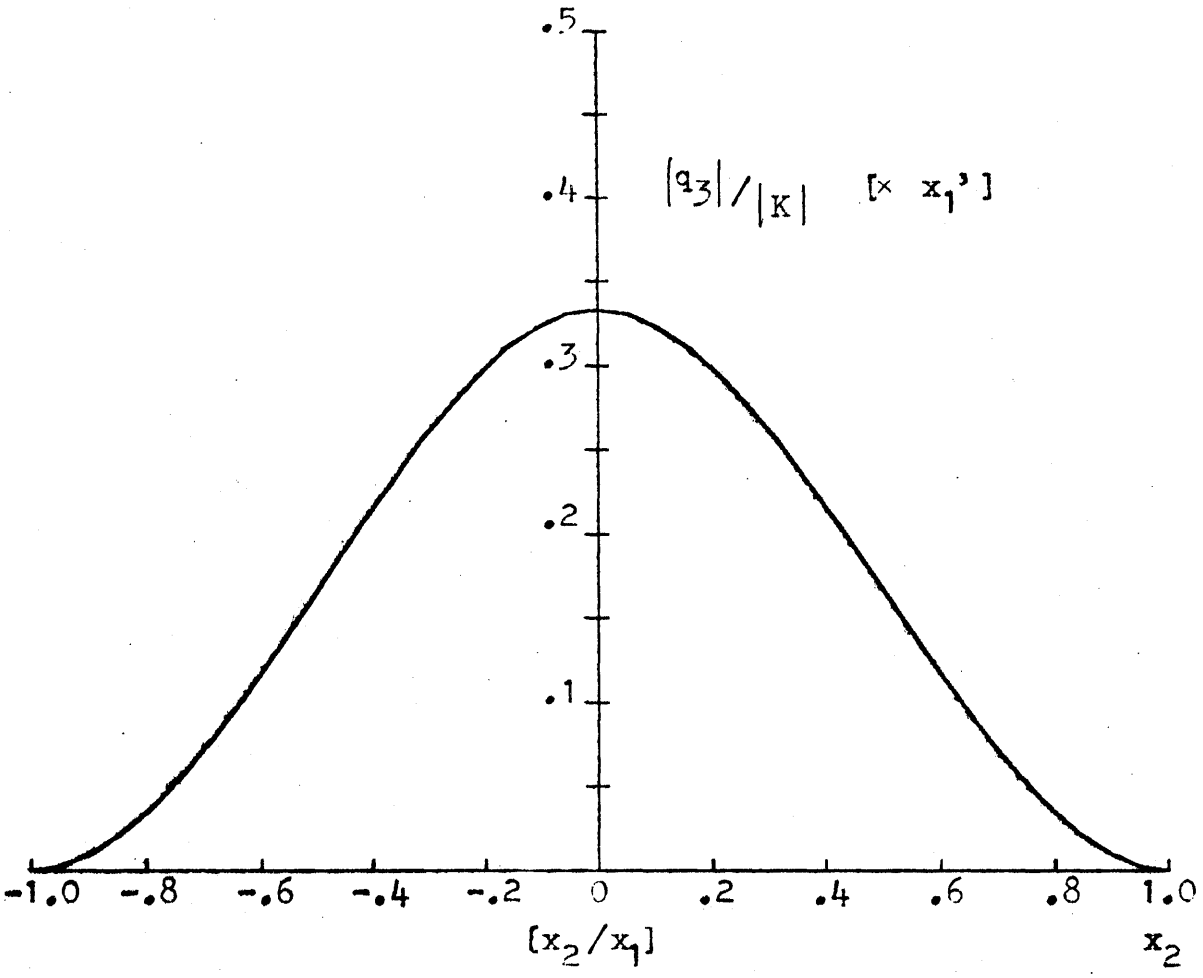

velocity direction of q_3 by locating the peak of the profile. However, if $\alpha \neq \beta$, the peak cannot be used to find the group velocity direction. Fig. 4.5 shows for $\alpha=2\beta$ a case in which the peak does not fall on $x_2=0$, and thus the peaks cannot be used to specify the group velocity direction of q_3.

The two examples just discussed were done so as a preview of the experiments. The experiments were predicated on example 1. The assumption was made that the two pump waves would remain essentially undepleted rectangular profiled waves. However it was found that diffraction distorted the pumps with the result that the profiles in the region in which data was taken more nearly resembled two ramps. Results of the experiments are given in the next chapter.

C. General Experiment

The experiment conducted basically consists of colliding two strong pump waves, q_1 and q_2, and examining the evolution of the up-converted wave q_3. From the measurements on the profile of the up-converted wave with an electrostatic probe as discussed by R.C. Williamson [51], the magnitude of q_3 can be determined. By setting the experiment so that the two initial beams remain essentially undepleted during the interaction one can find $|K|$ from the measurements of $|q_3|$, and initial values of $|q_1|$ and $|q_2|$ through equation (4.B.18). In addition to finding $|K|$, one can examine the general shape of the evolving $|q_3|$ as the interaction proceeds. Prior to initiating the experiment several parameters were reviewed to determine the

Fig. 4.5

Profile $|q_3| / |K|$

($\alpha = 2\beta = 1$; $\gamma\delta = 1$)

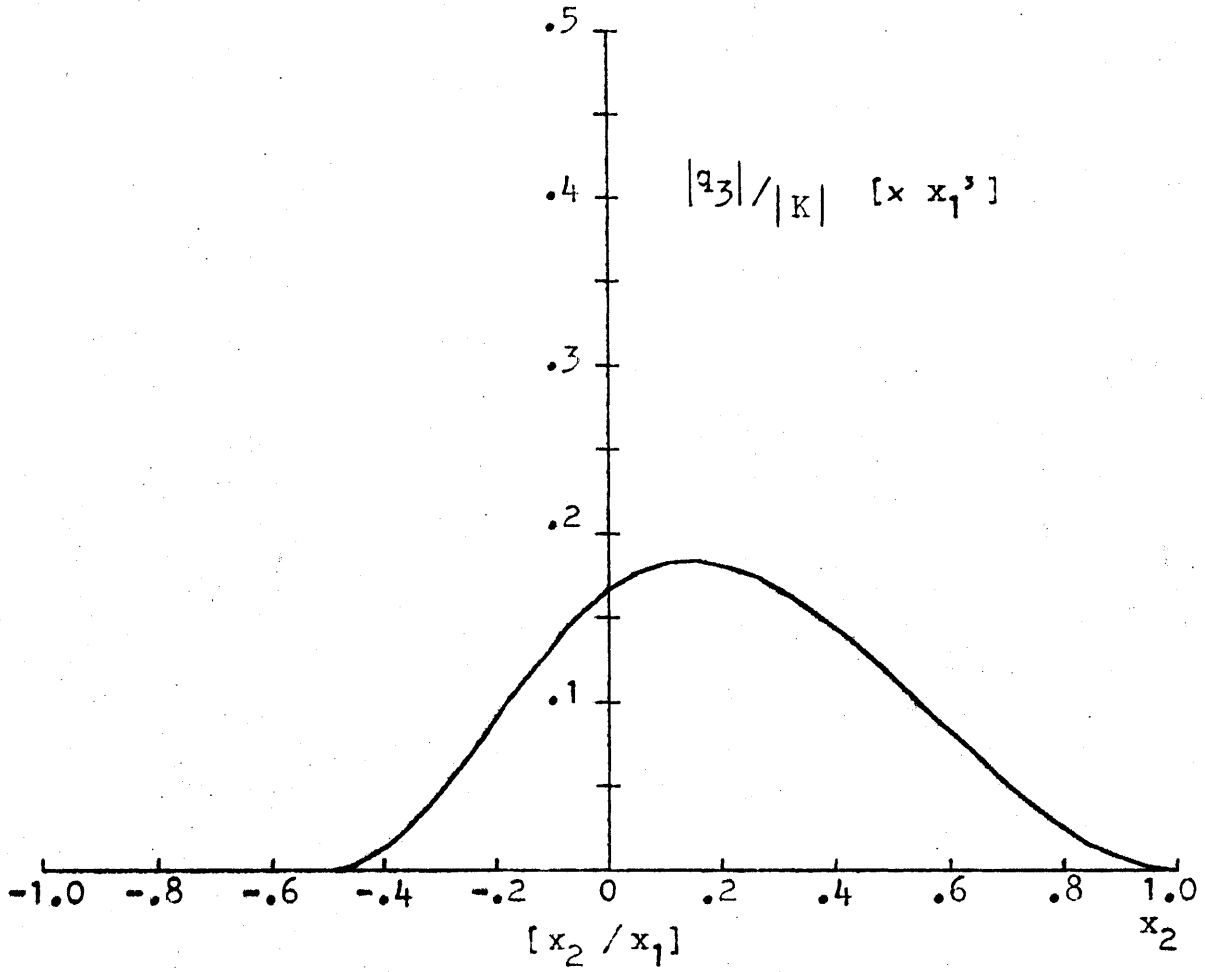

experimental scheme.

D. Parameter Evaluation

In order to configure the experiment, several factors were investigated. The variables examined included

a. a suitable nonlinear surface acoustic wave crystal

b. phase matching conditions

c. diffraction effects

d. harmonic contamination

e. electrostatic probe limitations

and how they would affect the experiments.

The material and its crystal cut must be chosen so that it is nonlinear, lossless, and will permit phase matching. A suitable material is y-cut $LiNbO_3$. y-cut $LiNbO_3$ is relatively lossless with a loss of 1.07 dB/μsec at 1 GHz. It is known to be nonlinear and noncollinear phase matching is possible [36]-[41]

Resonant conditions of

$$\omega_3 = \omega_1 + \omega_2,$$

$$\bar{k}_3 = \bar{k}_1 + \bar{k}_2$$

determine the direction of propagation for each beam. Material parameters to find phase matching for y-cut $LiNbO_3$ can be found in [52]. For the experiment, one must specify the angles for the

direction of phase propagation as defined in [50]. This determines the phase velocity of each wave on the material surface, and a frequency (f) ratio of the two initial interacting beams can be found. By varying the frequency ratio of the two initial SAW's the direction of propagation for the resultant wave is changed. The frequency ratio of the two initial beams for an up-conversion interaction is determined from:

$$\frac{f_2}{f_1} = \frac{\omega_2}{\omega_1} = \frac{-\left[\frac{\cos\psi_3}{v_{p_3}v_{p_2}} + \frac{1}{v_{p_3}^2}\right] + \left[\left[\frac{\cos\psi_3}{v_{p_1}v_{p_2}} + \frac{1}{v_{p_3}^2}\right]^2 - \left[\frac{1}{v_{p_3}^2} - \frac{1}{v_{p_1}^2}\right]\left[\frac{1}{v_{p_3}^2} - \frac{1}{v_{p_2}^2}\right]\right]^{1/2}}{\left[\frac{1}{v_{p_3}^2} - \frac{1}{v_{p_2}^2}\right]} \qquad (4.D.1)$$

Fig. 4.6 gives the geometry of the propagation vectors for this equation. It should be noted that ϕ_1, ϕ_2, ϕ_3 and θ_1, θ_2, θ_3 do not correspond to $\phi_i(x_1,x_2)$ and θ of the phase-locking discussions. v_{p_α} is the magnitude of the phase velocity for mode α. Equation (4.D.1) is derived in Appendix VII.

Because of the relatively high value of $\Delta v/v$ for the z-direction of y-cut $LiNbO_3$ [52], at least one of the initial waves is launched along this direction ($\bar{k}_1$) and thus $\theta_1 = 90°$. The other wave ($\bar{k}_2$) was chosen so that $\theta_2 = 100°$ as defined in [50]. The direction of the third wave is dependent on the frequency ratio of f_2/f_1.

Rough estimates of the coupling constants for noncollinear interactions near YZ-$LiNbO_3$ were made by assuming that the coupling

Fig. 4.6

$\bar{k}$-matching on
Y-Cut $LiNbO_3$ Coordinate System

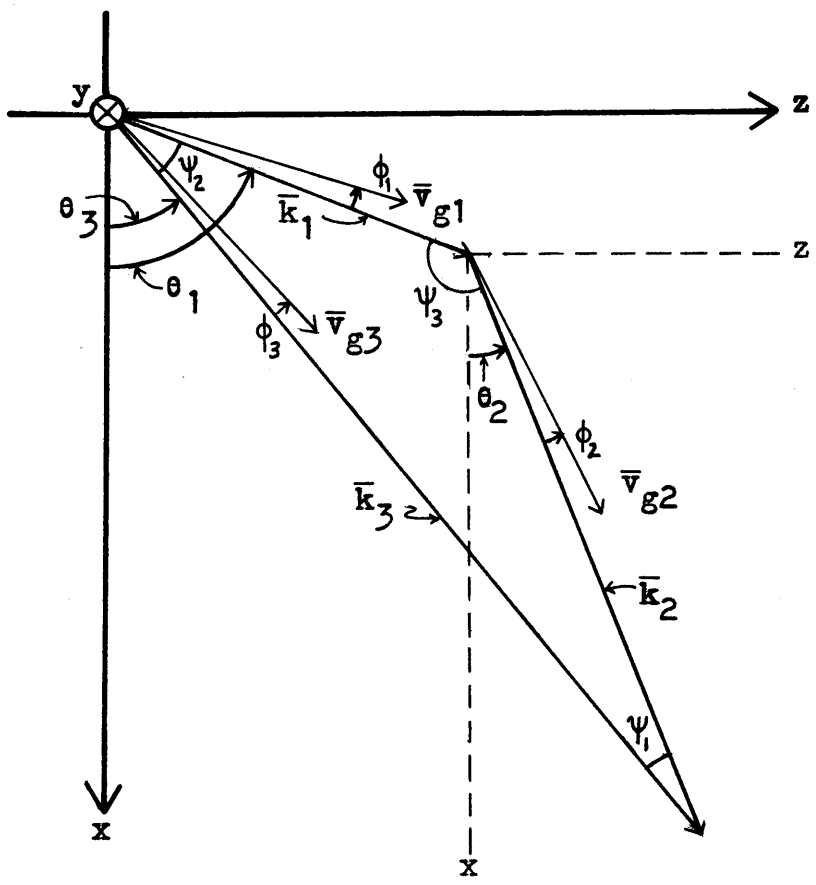

constants for harmonic generation on YZ-$LiNbO_3$ were applicable. These coupling constants were used in computer simulations of the nonlinear interactions. Because only order of magnitude could be assessed, crystals of maximum length and width were sought. Crystals of y-cut $LiNbO_3$ were available in the size .100" x 6.000" x .750", and designed for SAW propagation along and near the z-direction. The crystal cut corresponds to the Euler angle rotation from crystallographic axes of 0°, 90°, 90° as discussed in [49]. Growth, cut and polish of the crystals were to the standards of:

1. Material Specification:
   a. Lithium Niobate is clear, colorless, uniform, single domain, single crystal, free of cracks, cores and visible inclusions.
   b. No visible scattering centers when illuminated with a high intensity microscope lamp in normal room temperature.
2. Orientation Specification:
   a. Surfaces parallel to z axis are parallel to within 6 minutes of arc.
   b. Surfaces perpendicular to x and y axes are perpendicular to within 30 minutes of arc.
3. Dimension Specification:
   a. 0.100" ± .002 (y) thickness
   b. 6.000" ± .010 (z) length
   c. 0.750" ± .005 (x) width

4. Polish Specification:
   a. Optical polish
   b. Surface flat to within $\frac{1}{4}$ wave over any $\frac{1}{2}$ inch segment of length while mounted on polishing block.
   c. One micro-inch finish free of pits and scratches when inspected at 100 power magnification using dark field illumination.
   d. Optically polished surface has camferred edges.
   e. Back surface is a fine ground (frosted) finish.
   f. Minimum subsurface work damage, and adequate for optical contacting.

The $LiNbO_3$ crystals were obtained from Crystal Technology, Mountain Vale, California.

Because of the long interaction regions permitted by this crystal, propagation distances of over 8000 wavelengths are possible and diffraction effects could become prominent. Studies indicate that diffraction of surface waves on or near the z-direction of y-cut $LiNbO_3$ is poorly understood [53], and this effect could interfere with measurements of the nonlinear interaction. The Fresnel zone of diffraction is specified by the relation:

$$l > \frac{\lambda R}{b^2} \qquad (4.D.2)$$

where b = apeture width of launching transducer

λ = wavelength of SAW

R = propagation distance

If $\frac{\lambda R}{b^2}$ is larger than one, then Fraunhoeffer diffraction is approached. Equation (4.D.2) indicates that the further a SAW has propagated from its launching transducer the greater the diffraction. Further, the longer the wavelength of a SAW the more pronounced is diffraction for a given propagation distance. However, diffraction effects are reduced quadradically with beam width. Therefore to reduce diffraction, interdigital transducers to launch the pump waves were chosen to be as wide as fabrication would allow. Fabrication limits interdigital transducer size to 240 wavelengths of the center frequency of the transducer or one centimeter, whichever is smaller. With an apeture width of 240 wavelengths, and R equals 8000 wavelengths, (4.D.2) gives:

$$1 > \frac{\lambda R_{max}}{b^2} = \frac{8000\ \lambda^2}{(240\ \lambda)^2} \simeq .14 \qquad (4.D.3)$$

Thus with transducers of 240 λ, one is still in the Fresnel diffraction region even with propagation lengths of 8000 λ.

To minimally contaminate the noncollinear interaction with harmonic generation from the pumps, and to avoid pump depletion, power densities P_λ, defined as:

$$P_\lambda = \frac{(\text{SAW power})}{(\text{transducer beam width})(\text{wavelength})} \qquad (4.D.4)$$

had to be examined. R.C. Williamson has investigated power densities required for deviation from linearity for a propagating surface wave [54]. A power density of $3x10^6$ Watts/m^2 or less will have a deviation from linearity less than or equal to 1 dB. Power densities of 7.5×10^5 Watts/m^2 have been used in harmonic generation studies [33], but the second harmonic was lower by 20 dB, and thus the launched fundamental wave was barely depleted. However power densities above $3x10^6$ Watts/m^2 produce strong pump depletion [30], [26], and this could interfere with the parametric interaction and deplete the pumps. Therefore, power densities under $3x10^6$ Watts/m^2 were used with the experiments, and tests were conducted to examine the power levels of harmonics.

As stated, an electrostatic probe is used to measure the magnitude of the generated wave amplitude q_3. It is a useful tool in examining SAW propagation qualities of magnitude and phase. The characteristics of the probe are discussed in [51]. It has been found that the maximum useful frequency is 250 MHz. Thus 250 MHz was chosen as the maximum frequency for the experiments. One unfortunate feature of the electrostatic probe is the difficulty in obtaining calibrated measurements due to the flattening and thus changing of the tungsten probe tip. This proved to be a variable of concern, and thus special consideration is given in a later section on the calibration procedure used with the experiments.

This section has reviewed some of the parameters considered in determining the geometry of the experiment and transducer design.

The next two sections discuss the collision scheme and the transducers of the experiments in more detail.

E. Collision Scheme

Fig. 4.7 illustrates the geometry of the noncollinear interaction. Two beams are launched and collide from which the third wave evolves, and for an up-conversion interaction, the third wave propagates between the other two. From Fig. 4.7, two distinct areas are indicated. The overlap region is defined as the parallelogram area over which the two initial beams would overlap and separate in normal-mode propagation, and the interaction region is that area from where mode 1 and mode 2 initially collide to the line where all three modes would separate in normal-mode collision.

In order to have as much of the interaction region and all of overlap region on the crystal, with maximum transducer width to reduce diffraction, $\theta_2 = 100°$ (Fig. 4.6) was chosen. $\theta_1 = 90°$ was set by having $\bar{k}_1$ along the z-direction of y-cut $LiNbO_3$. With $\theta_1 = 90°$ and $\theta_2 = 100°$, the power flow angle (ϕ) for each initial wave is $\phi_1 = 0°$ and $\phi_2 = -3.902$ [52]. To have the third beam to propagate about halfway between the other two, θ_3 was chosen as 97.45° with $\phi_3 = -4.14°$. With the phase velocities included, the above is summarized as:

$$\theta_1 = 90°$$

$$\phi_1 = 0°$$

$$v_{p_1} = 3487 \text{ m/sec}$$

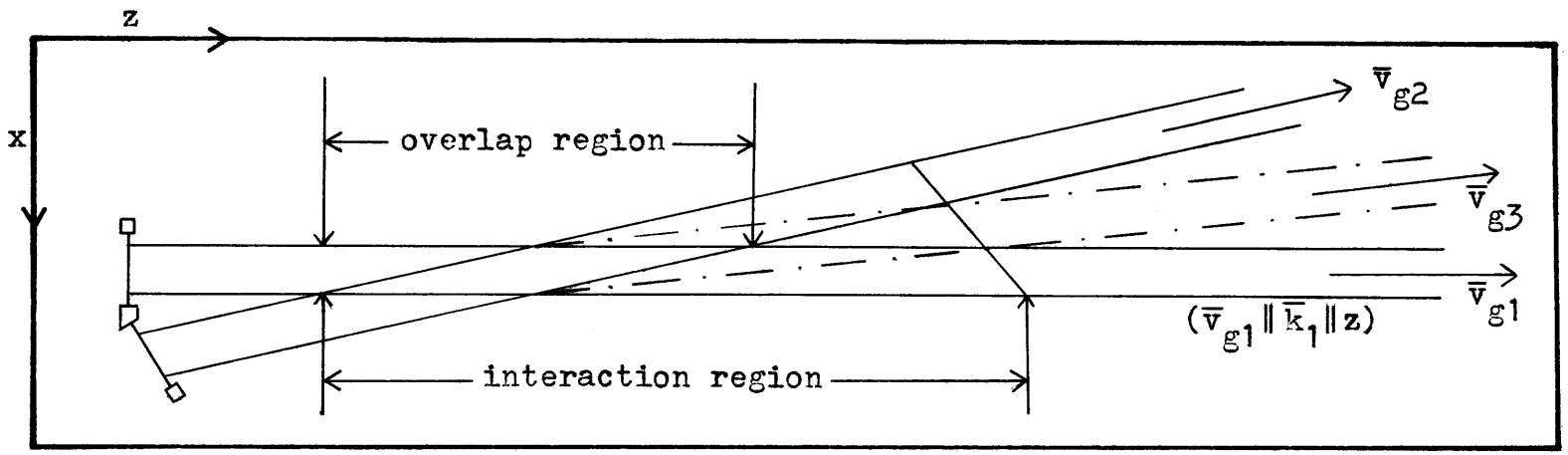

Fig. 4.7

Collision Scheme

$\theta_2 = 100°$

$\phi_2 = -3.902°$

$v_{p2} = 3454$ m/sec

$\theta_3 = 97.45°$

$\phi_3 = -4.14°$

$v_{p_3} = 3465$ m/sec

From this data ψ_3 can be determined, and thus the frequency ratio f_2/f_1 found. For these propagation angles

$$\frac{f_2}{f_1} = 6.09 \qquad (4.E.1)$$

However, to work with the highest energy density for each initial mode, and still have a maximum frequency of 250 MHz. It was decided that

$f_2 = 214$ MHz

$f_1 = 36$ MHz

which gives

$$\frac{f_2}{f_1} = 5.94 \qquad (4.E.2)$$

With the errors encountered with the experiment, the difference between (4.E.1) and (4.E.2) is insignificant.

The choice of angles and frequencies sets the transducer configuration which is given in section F.

F. Transducers

The basic transducer pattern is illustrated in Fig. 4.8. The figure shows three of the nine fingers of each transducer respectively. Transducers were designed with the XDUCER program written by the Surface Wave Technology Group, Lincoln Laboratory, M.I.T.. Five fingers emerge from the center or ground pad, with the other four fingers from the two end pads. Fig. 4.8 shows the interdigital nature of the transducers with the pattern of positive and ground polarities of the fingers. The pattern is continued for nine fingers for the experiment's transducers.

Because of the system used to generate the masks for transducer fabrication, the center frequency of transducer A is 209.23 MHz rather than 214 MHz. However, 214 MHz falls well within the theoretical and measured 3dB bandwidth for insertion loss. Transducer B has a center frequency of 36 MHz. Each transducer has finger width and spacing between fingers of 1/4 wavelength of its center frequency.

Masks for the photolithography process used to make the transducers were produced with a Mann 1600 A Pattern Generator and a Mann 1795 Photorepeater. The interdigital transducers were sputter deposited on the $LiNbO_3$ substrate with 200 Å-Cr as a base and 3000 Å

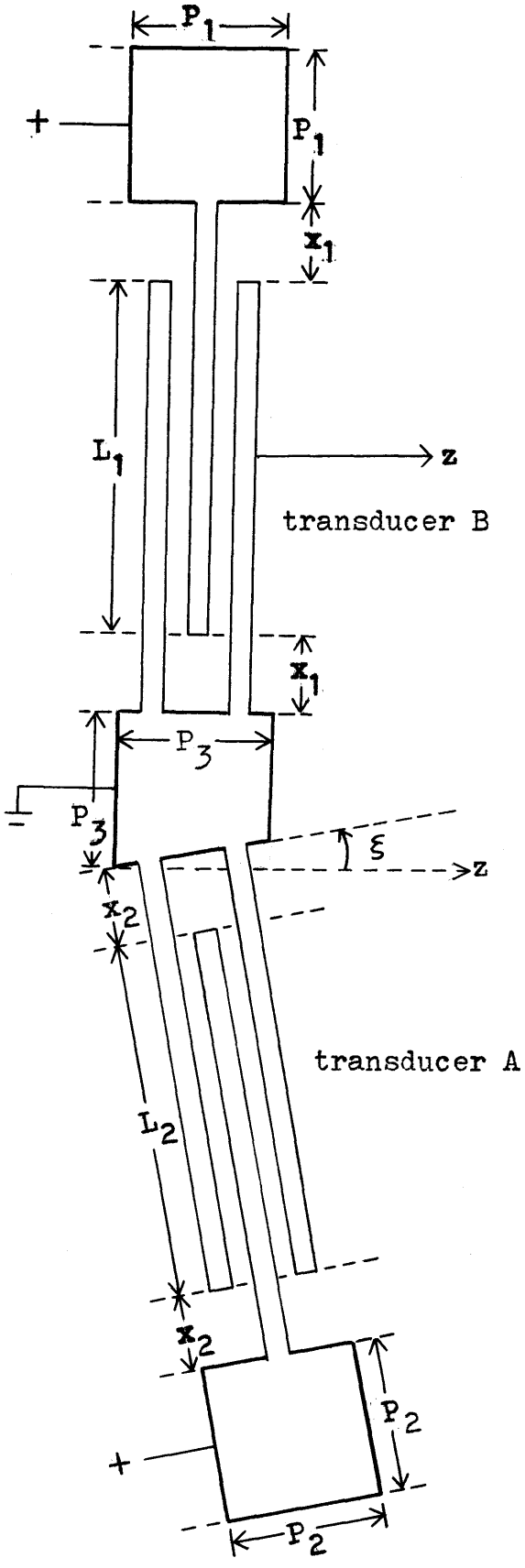

Fig. 4.8

Transducer Design

P_1 = 30 mils

P_2 = 40 mils

P_3 = 40 mils

x_2 = 5 mils

x_1 = 20 mils

L_1 = 152.6 mils
40 λ_1

L_2 = 152.5 mils
240 λ_2

λ_1 = 3.8 mils

λ_2 = .65 mils

ξ = 10°

Al as the top layer. Alignment with the edges of the crystal is given in Fig. 4.9. Fabrication alignment accuracy to the z parallel edge is within a 2.5×10^{-4} inch error over the 6.000" length of the crystal.

After the transducers were fabricated, the crystal was mounted and tuning inductors attached. The transducers were tuned so that at the center frequency, reflection and loss was purely resistive for a 50 Ω load.

G. Experimental Apparatus - Generation and Detection System

Figures 4.10-4.14 give the schematic of the principal components of the input signal generation system and the detection scheme used with the experiments. A brief discussion of Fig. 4.10-4.14 follow.

1. Generation System:

The input signal generation scheme illustrated in Fig. 4.10 is the source of the 214 MHz and 36 MHz signals used in the parametric interaction on the crystal and the heterodyne detection system for the up-converted wave. Part of the signal from each generator is removed from the line and used to mix with the 250 MHz signal from the crystal in the heterodyne detection system of Fig. 4.11. These split-off signals appear as (B) and (C) in Fig. 4.10a and Fig. 4.10b, and correspond to (B) and (C) of Fig. 4.11.

Because the electrostatic probe is sensitive to electromagnetic signals broadcast by the interdigital transducers, the cw signals from the generators are passed through switches to form a RF burst.

Fig. 4.9

Transducer Position on Crystal

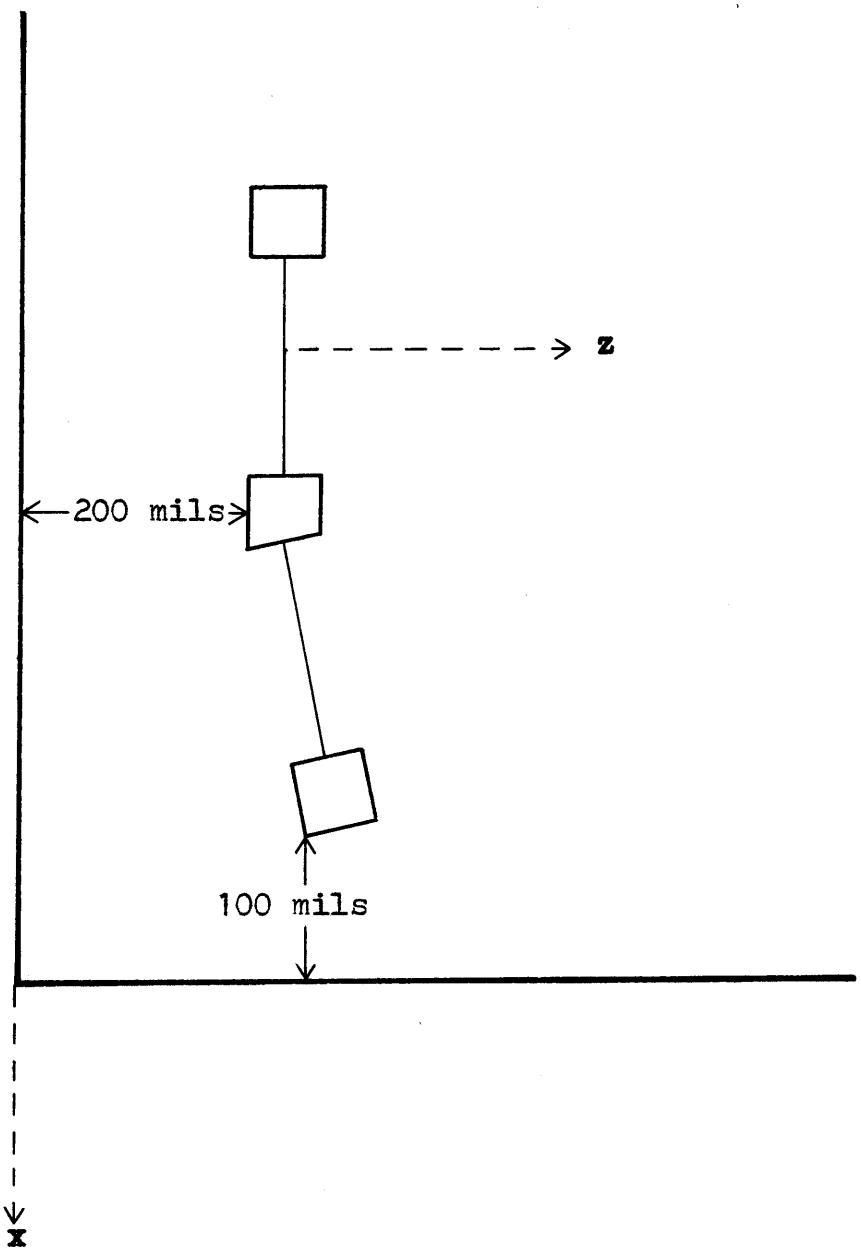

Fig. 4.10

Input Signal Generation

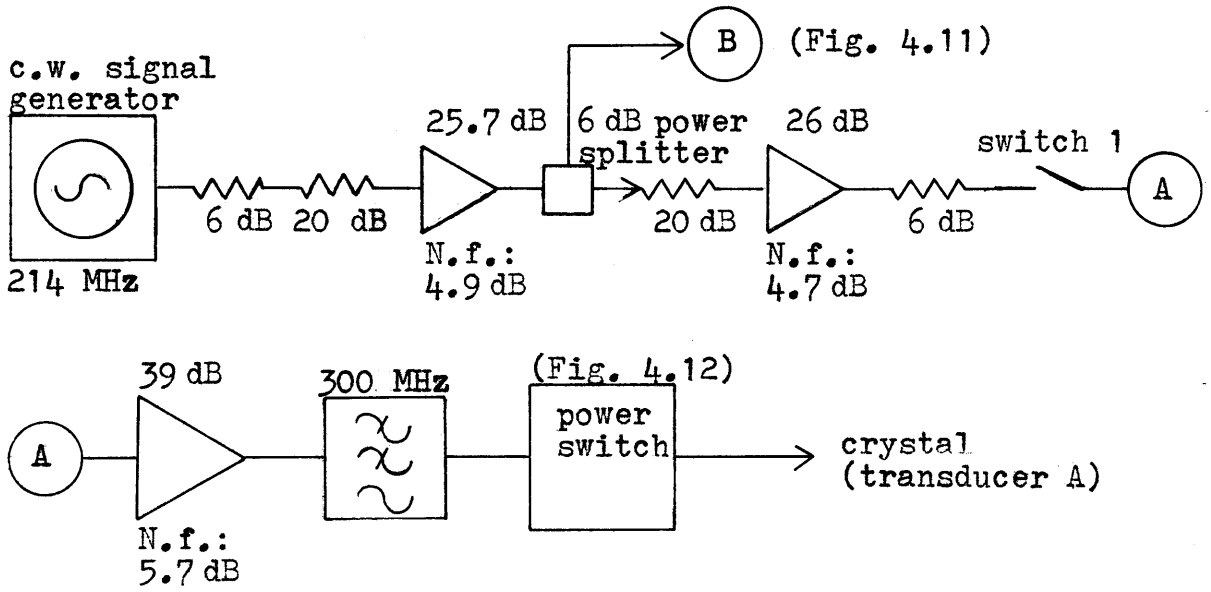

Fig. 4.10a

214 MHz Signal

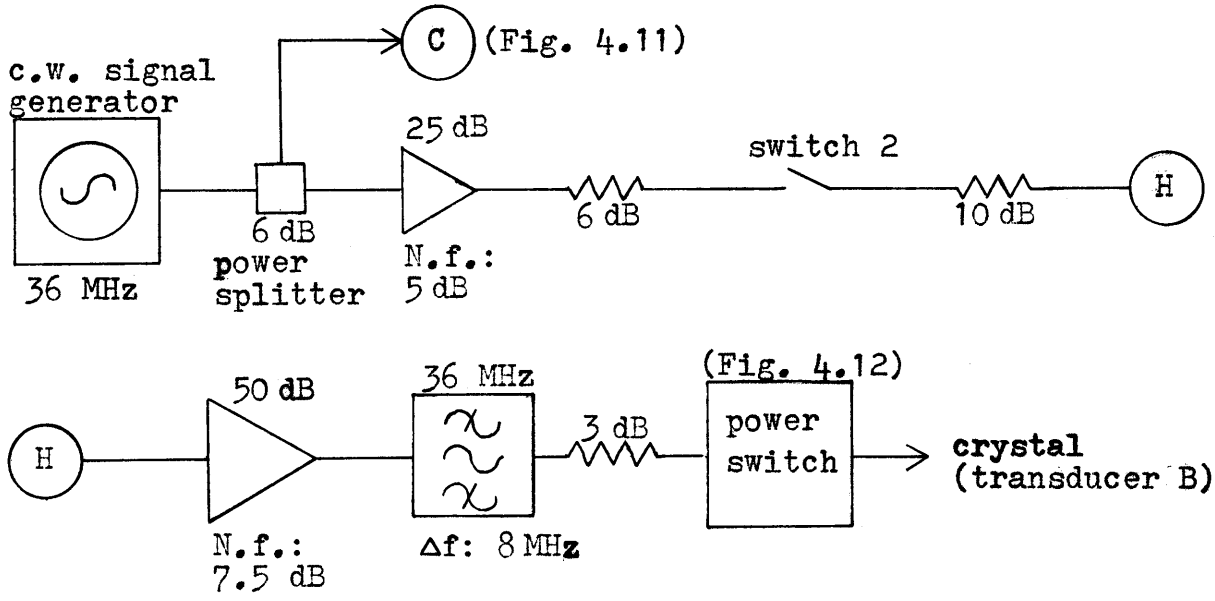

Fig. 4.10b

36 MHz Signal

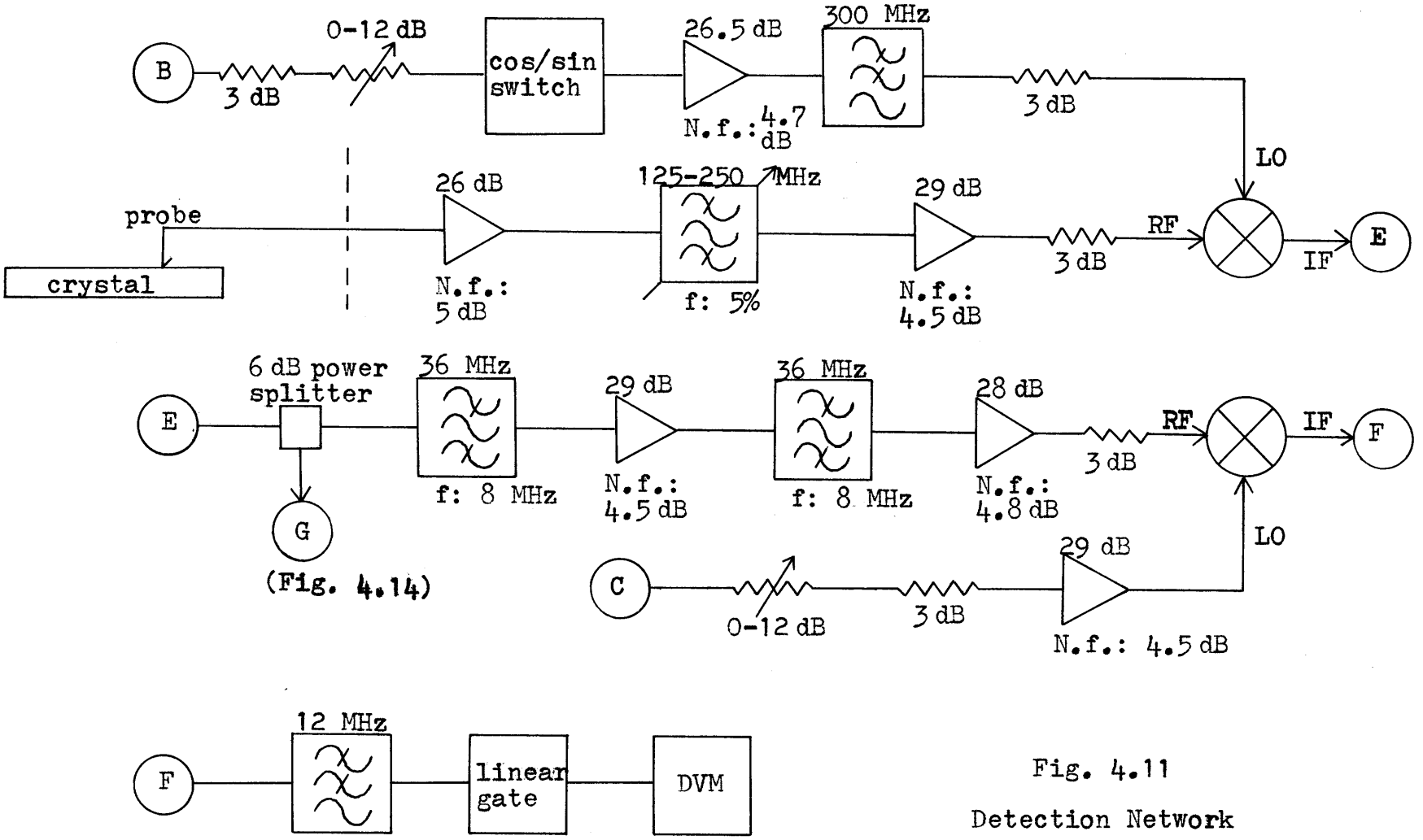

Fig. 4.11

Detection Network

Fig. 4.12

Power-Switch

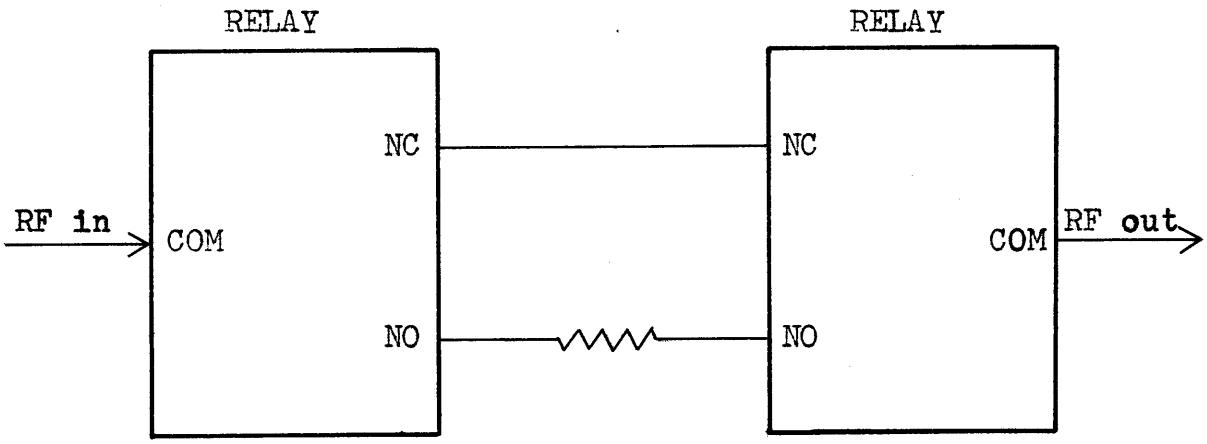

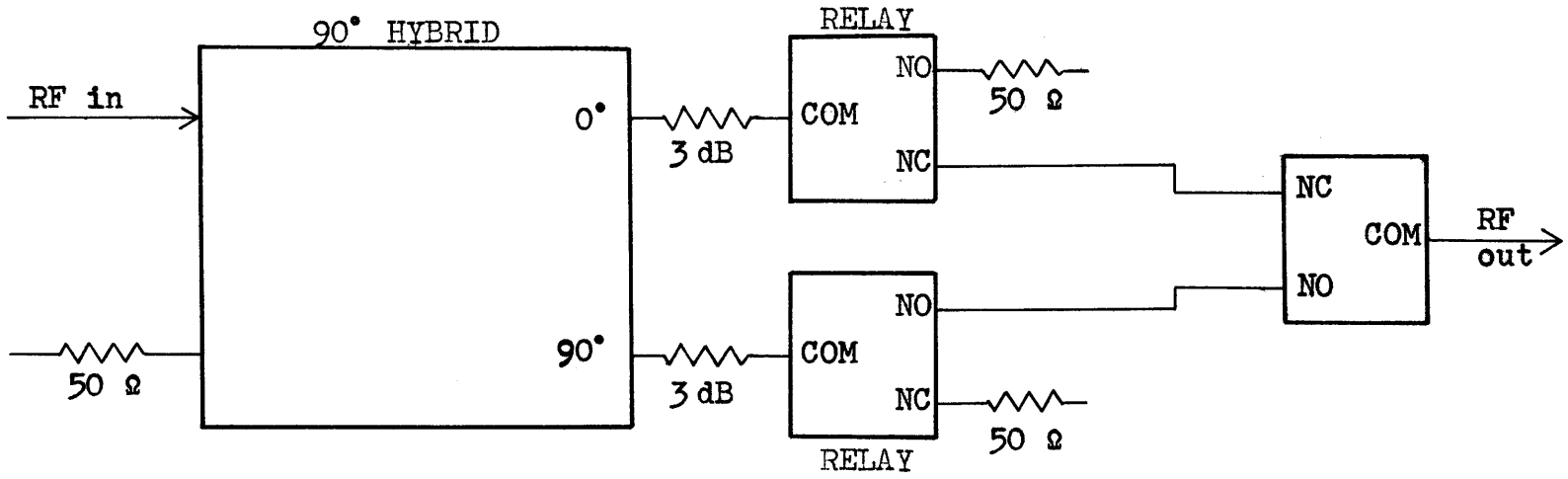

Fig. 4.13

COS/SIN Switch

Fig. 4.14

Synchronizing System

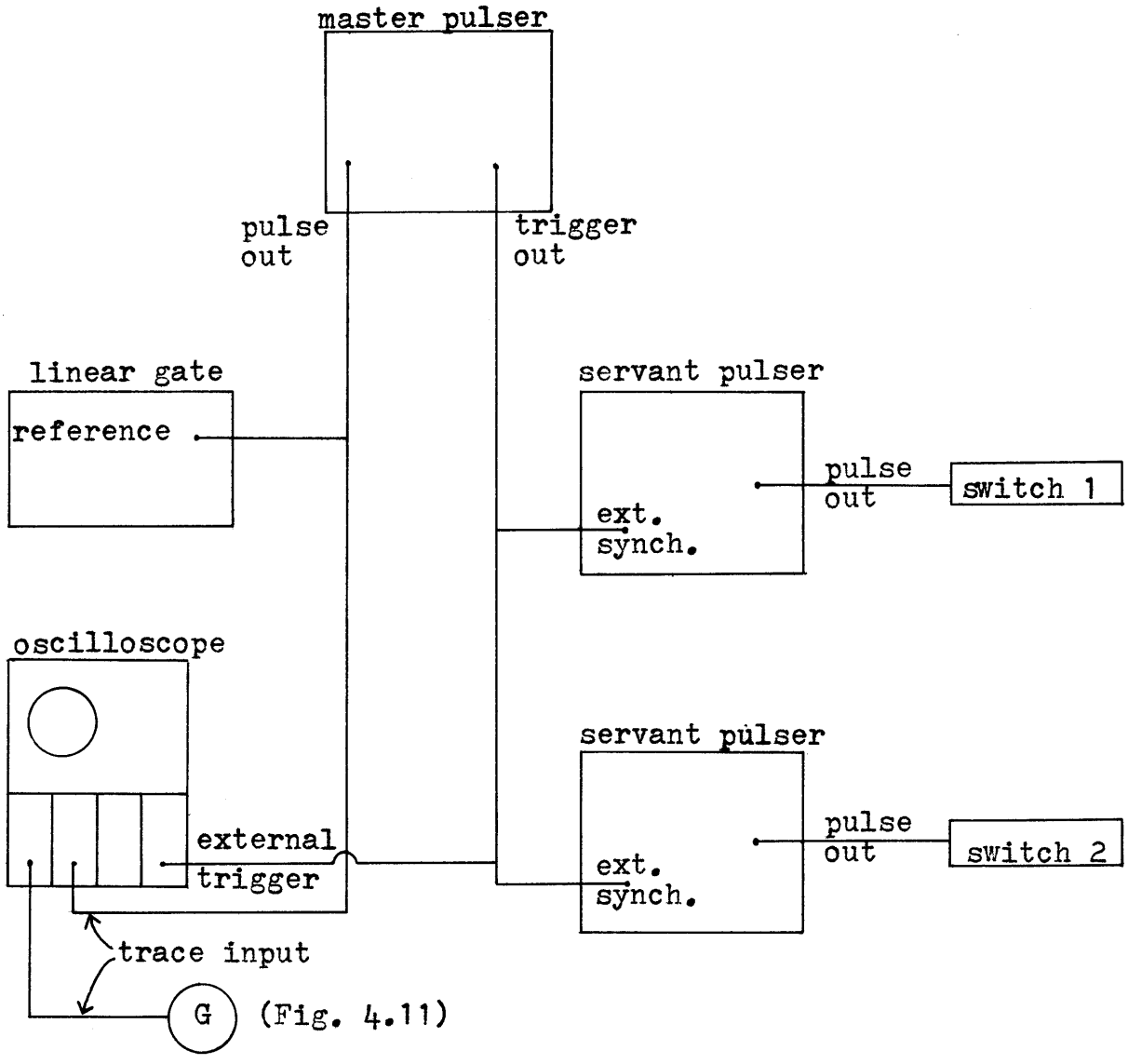

Since the velocity of the SAW's on the crystal are about 10^5 times smaller, one can time resolve to distinguish between electromagnetic feedthrough from the transducers and SAW signals. This necessitates the use of the RF burst, and the experiments used a pulse length of 2 μsec.

Harmonics of the 36 MHz and 214 MHz are produced by the signal generator and amplifiers, and thus filters are added after the last amplifier before the transducers.

Due to the interest in determining power dependency of the coupling constant, a network was added just prior to the crystal to vary the input power to the transducers. This network is referred as the power-switch and is illustrated in Fig. 4.12. With the power-switch off, the signal passes through the switch unimpeded, but with the switch on, the signal is diverted through an attenuator. The power-switch facilitates measurements of the nonlinear interactions with different power levels without physically altering the chain of electronics. The attenuators used in the power-switches were calibrated prior to insertion in the switch. For the experimental results of Chapter 5, the attenuator was a 3 dB pad.

2. Detection Network:

The detection scheme given in Fig. 4.11 consists of the electrostatic probe and a heterodyne detection system. The heterodyne detection system mixes the 250 MHz signal of the up-converted wave detected by the probe with the 214 MHz and 36 MHz signals from the cw signal generators to produce a video pulse used by the linear gate.

The processing from the linear gate is then displayed by a digital volt meter (DVM). The signal from the probe consists of all frequencies that exist on the crystal, therefore a filter centered on 250 MHz is required to eliminate the spurious frequencies. This is then mixed with the 214 MHz signal from the cw generator which is depicted starting at (B).

In the line of (B) the variable attenuator is used to control the power to the mixer to prevent saturation of the mixer. The cos/sin switch is discussed later, and to again eliminate harmonics and parametric signals produced by the generator and amplifiers a low pass filter is in the line. The 214 MHz signal is mixed with the 250 MHz signal which produces a 36 MHz and 464 MHz signal, and these are emitted by the IF port of the mixer.

From the IF-port of the first mixer part of the signal is split-off and sent to an oscilloscope (G). The signal to the oscilloscope is used in aligning the reference of the linear gate with SAW signal. The rest of the signal is passed through 36 MHz-bandpass filters to reduce the levels of the 464 MHz signal and any spurious signals from other sources. The 36 MHz signal enters another mixer and after mixing with the cw 36 MHz signal from the generator (C) results in a video and 72 MHz signal. The video and 72 MHz signal enter a 12 MHz lowpass filter and only the video signal enters the linear gate.

The linear gate is used to improve the signal to noise ratio of the system. The internal circuitry of the linear gate has a rise

time of 1 μsec. Therefore, with a reference signal of 1.5 μsec centered on the middle of the 2 μsec video pulse, the internal time constant of the linear gate will not affect the correlation gain of the linear gate. Hence, correlation gain of signal to noise at the ouput of the linear gate is dependent only on the number of video pulses that occur during the integration time. The integration time was set at one second for the experiment with the video pulses at a repetition rate of 25,000 pulses per second.

Because of the noncoherent properties of noise and the coherent character of the signals sought, the linear gate acts differently upon noise-power from the signal-power of the video pulse. Due to the qualities of the linear gate, a signal to noise correlation gain occurs, improving the signal to noise ratio. Therefore, the noise level output from the linear gate gives the minimum level a signal can be distinguished from the noise at the output. This noise level can be translated back to the input giving the minimum signal that can be detected from thermal noise. This translation can be viewed as either a device by device procedure, or the detection system can be considered a black box with a specified gain, noise-figure and bandwidth for the noise, and a different gain and bandwidth for coherent signals because of the linear gate. From the specifications of noise-bandwidth and noise-figure, the effective thermal noise or minimum detectable signal can be calculated from the expression:

$$N = kTB(N.f.) \qquad (4.G.1)$$

where

N = effective thermal noise power

k = Boltzmann's constant

T = temperature

B = noise-bandwidth

N.f. = noise-figure

Thus one needs to determine B and N.f. to find the effective thermal noise.

Noise-figure and noise-bandwidth are found from the devices that comprise the detection system. Because of the gain of the first amplifier (+26 dB) and the following amplifiers, the noise-figure of the black-box detection system is given by the noise-figure of the first amplifier. Thus the noise-figure is 5 dB. The effective noise-bandwidth is determined from the bandwidth of the devices in the detection chain. Amplifiers and mixers are wide band, with 5-1500 MHz dynamic range for the amplifiers and 3000 MHz for the mixers. The bandwidth of 36 MHz filters is 8 MHz, and at 250 MHz center frequency, the bandwidth of the tunable filter is 12.5 MHz. The linear gate can also be viewed as having a bandwidth. When the linear gate is considered as an averaging device, the output of the 25,000 pulses, each 1.5 μsec long, are processed and averaged every second. This can be viewed as a chain of back-to-back pulses which produces a single output pulse 37.5 milliseconds long. Thus the input noise-power contributes to the output noise for an equivalent

continuous duration of 37.5 milliseconds, which corresponds to a bandwidth of 1/(37.5 milliseconds) or 26 Hz. Hence the bandwidth of the linear gate is 26 Hz. Because the bandwidth of the linear gate is 300,000 times smaller than the next smallest bandwidth of 8 MHz for the 36 MHz filters, the effective bandwidth seen by the noise is 26 Hz. Substituting the values of 5 dB noise-figure and 26 Hz noise-bandwidth into (4.E.1) gives a minimum detectable signal for the heterodyne detection system of -160 dBm.

To determine the sensitivity and linearity of the detection system, a test was conducted. A 220 MHz signal with varying power levels was sent through the system. The noise level from the linear gate was removed by using the zeroing knob of the linear gate. Thus the output voltage of the linear gate is representative of the input signal to the detection system. As can be seen, (Fig. 4.15) the input to output characteristics are linear. The minimum input signal used was -130 dBm, and it was found that below this the output signal was on the same order as drift of the linear gate.

Because the amplifiers of the detection system will saturate above certain power levels, and generate harmonics and intermods of the signals to be amplified, it was necessary to set a threshold that would prevent saturations. This was done with the output of the linear gate. The maximum voltage output from the linear gate is ±10 volts, and above this the linear gate saturates. The voltage output of the linear gate can be easily monitored, therefore by setting signal levels so that the linear gate would output ±10 volts

Fig. 4.15

Detection Network Characterization

(220 MH_z)

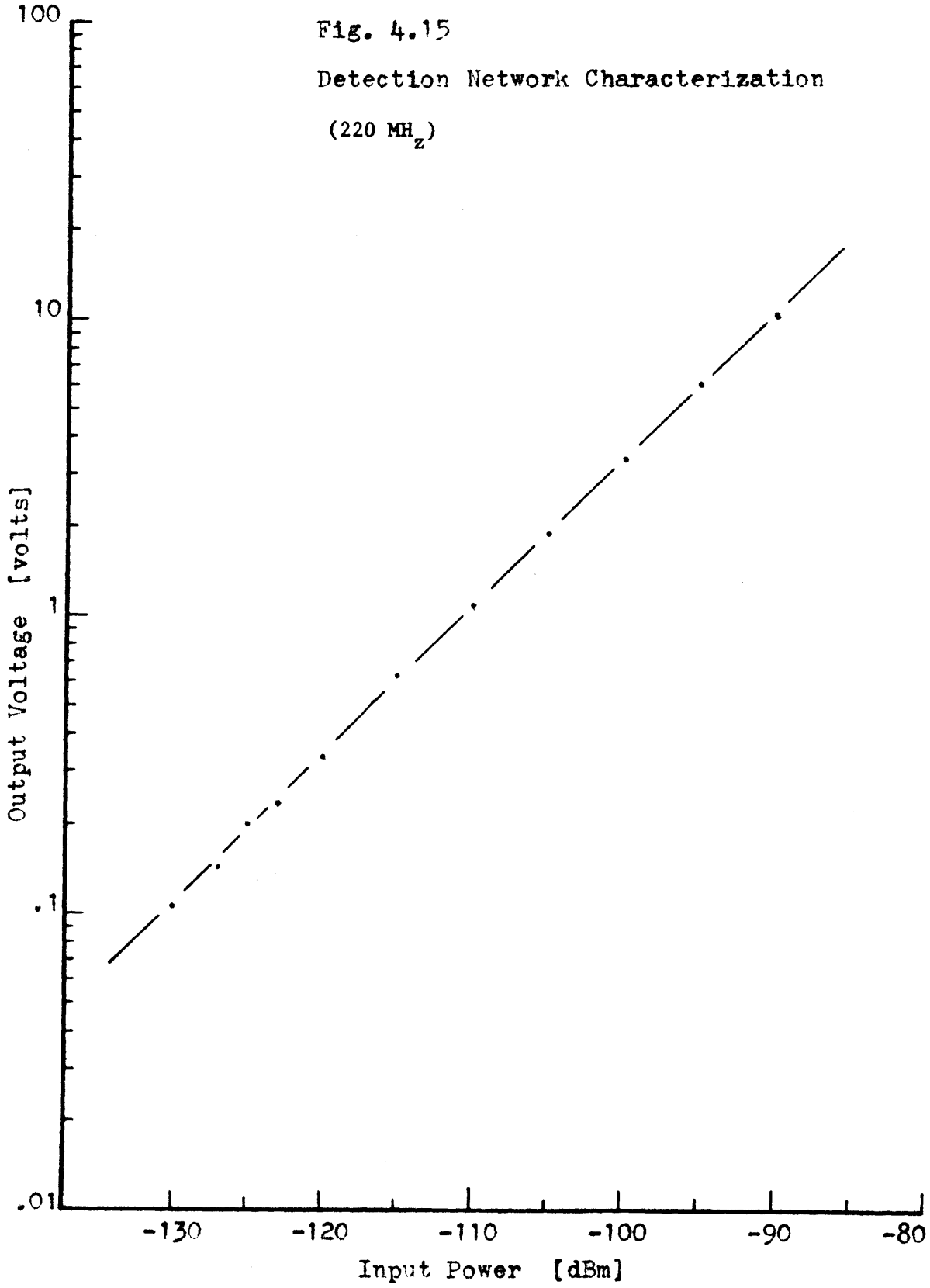

before the amplifiers saturate. One could therefore prevent nonlinear effects of the devices that comprise the detection system, contaminating the signal detected from the crystal nonlinearities.

The detection system as used for experiments can at best determine magnitudes of the signals sensed by the probe. However, from the probe to the digital volt meter, the detection scheme has a phase (ϕ_s). If V is the voltage associated with $|q_3|$, the DVM will register $V_{cs} = V \cos \phi_s$ and not V. One can find V using the detection network providing $V_{sn} = V \sin \phi_s$ can also be determined from the detection network. This can be done by introducing a shift in ϕ_s of 90°. The 90° phase shift is introduced in the 214 MHz LO line of the first mixer from the probe, with the cos/sin switch. A schematic of the cos/sin switch is given in Fig. 4.13. With no DC voltage applied to the relays, only the 0°-path (cos) is closed, the 90° path is opened, and V_{cs} is read on the DVM. When DC voltage is on, the 90°-path is closed and 0°-path is open, and ϕ_s becomes $\phi_s + 90°$. Thus V_{sn} is found from the DVM. V can then be determined by

$$V = \sqrt{V_{cs}^2 + V_{sn}^2} \qquad (4.G.2)$$

The V found from the above equation corresponds to $|q_3|$.

Saturation of power amplifiers and mixers, 50 Ω matching, and poor VSWR were problems that could affect the generation and detection system. Therefore microwave attenuators were added throughout both

systems as illustrated in Figures 4.10 and 4.11.

3. Synchronizing:

Because of the pulse nature of the experiment, the generation and detection systems must be properly synchronized. Fig. 4.14 illustrates the synchronizing scheme.

A master-pulser triggers two servant-pulsers, the linear gate, and an oscilloscope. The two servant-pulsers are externally triggered by the master-pulser which is thus controlling only the repetition rate of these two pulsers. The oscilloscope used in aligning signals is also externally triggered by the master-pulser. The master-pulser controls both repetition rate and pulse width of the reference signal to the linear gate and an alignment signal on the oscilloscope. Repetition rate was chosen to be 25,000 pulses/second.

The two-servant pulsers control switch 1 and switch 2 of Fig. 4.10a and Fig. 4.10b. The two pulses are synchronized with equal pulse width and delay by overlapping the pulses from each pulser on a dual trace oscilloscope. Pulse width was chosen to be 2 μsec.

Due to the slower propagation of a SAW signal compared to the electromagnetic feedthrough from the transducers to the probe, the SAW and feedthrough are separated in time and are thus time resolvable. To synchronize the linear gate with the SAW signal, part of the signal from the detection system, Fig. 4.11 (G), is split-off and displayed on a multi-trace oscilloscope. The displayed pulse on the oscilloscope from the master-pulser can then be aligned with the display of the SAW signal by adjusting the output-pulse

delay from the master-pulser. When the oscilloscope alignment pulse is centered on the oscilloscope SAW pulse, the reference signal to the linear gate synchronizes the linear gate with the detected signal from the nonlinear interaction on the crystal. The reference and alignment pulses are 1.5 μsec long. This pulse width centered on the 2 μsec detected signal avoids the transients of the rise and fall times of the pulse that is finally used by the linear gate.

4. 36 MHz Filter:

36 MHz, commerical, bandpass filters were not available and were thus made. Fig. 4.16 gives the circuit diagram of the filter. With the components used, it had a 8 MHz - 3 dB bandwidth and a 4 dB loss at center frequency.

H. Pre-Experiment Tests

Prior to performing the experiment, several measurements were conducted. These measurements include transducer insertion loss, nonlinearities of amplifiers and mixers, detection system linearity and sensitivity, harmonic contamination on the crystal, diffraction profiles, and phase fronts.

1. Transducer Insertion Loss:

Insertion loss of the transducers was needed to determine the amount of input power to the transducers converted to surface wave used in the nonlinear interaction. These tests were conducted with the TBRIDGE computer program and transmission bridge measurement system developed by the Surface Acoustic Wave Technology Group. The

Fig. 4.16

36 MH_z Filter

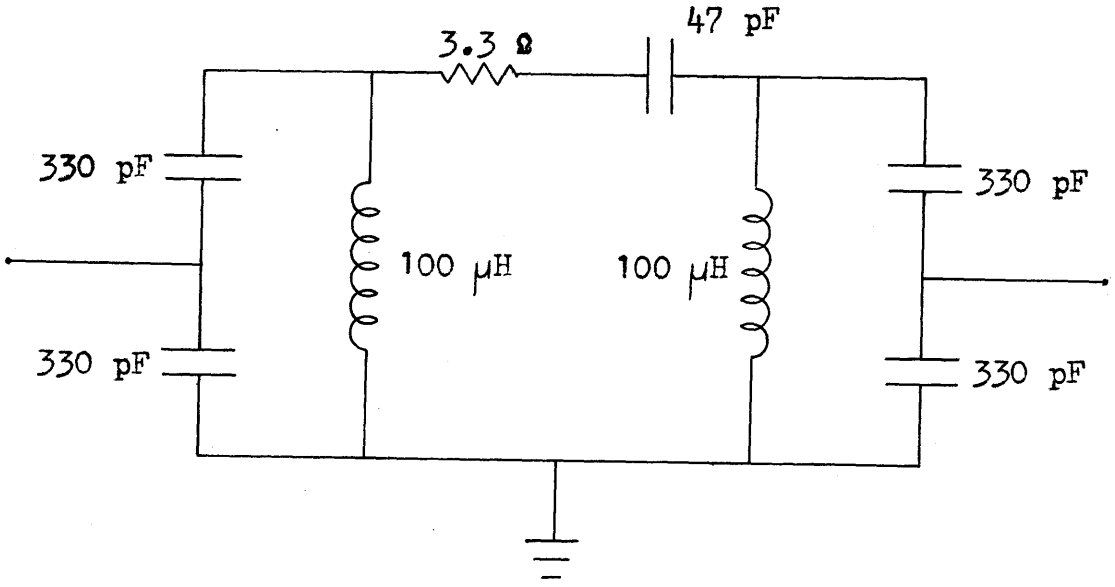

transducer scheme for these measurements is illustrated in Fig. 4.17. After fabrication, tuning inductors were attached and the transducers tuned for maximum transmission at the center frequency of the transducers.

Figures 4.18 and 4.19 illustrate the results of the measurements. Accuracy of the measurements are within ±.5dB. It was assumed that propagation loss over the distance the SAW travelled between transducers was negligible compared to the loss of the transducers. Besides the propagation loss assumption, it was assumed that the transducers were identical and properly aligned within the tolerances of fabrication.

Because of the necessity of calibrating the detection network, insertion loss was also performed at 250 MHz on the A transducers. The method used here to determine the loss was to find the output signal level of a specified input with the device of Fig. 4.17, then remove the device and insert calibrated pads until the input used with the delay line was attenuated to the level of the output of the delay device.

From the curves given in Figures 4.18 and 4.19, insertion loss for a single transducer is found at a given frequency by taking the results on the curves and dividing by two. The same is done for the 250 MHz signal with an insertion loss of a single transducer found to be -22.4 dB.

2. Diffraction-Phase Fronts

Diffraction profiles and phase front measurements on the 214 MHz

Fig. 4.17

Insertion Loss Test Transducers

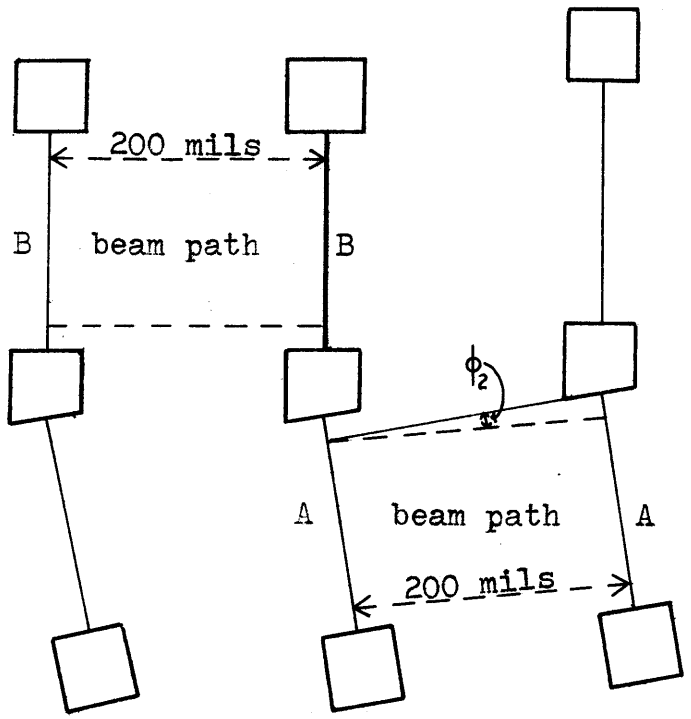

Fig. 4.18 Insertion Loss Curve
Transducer A

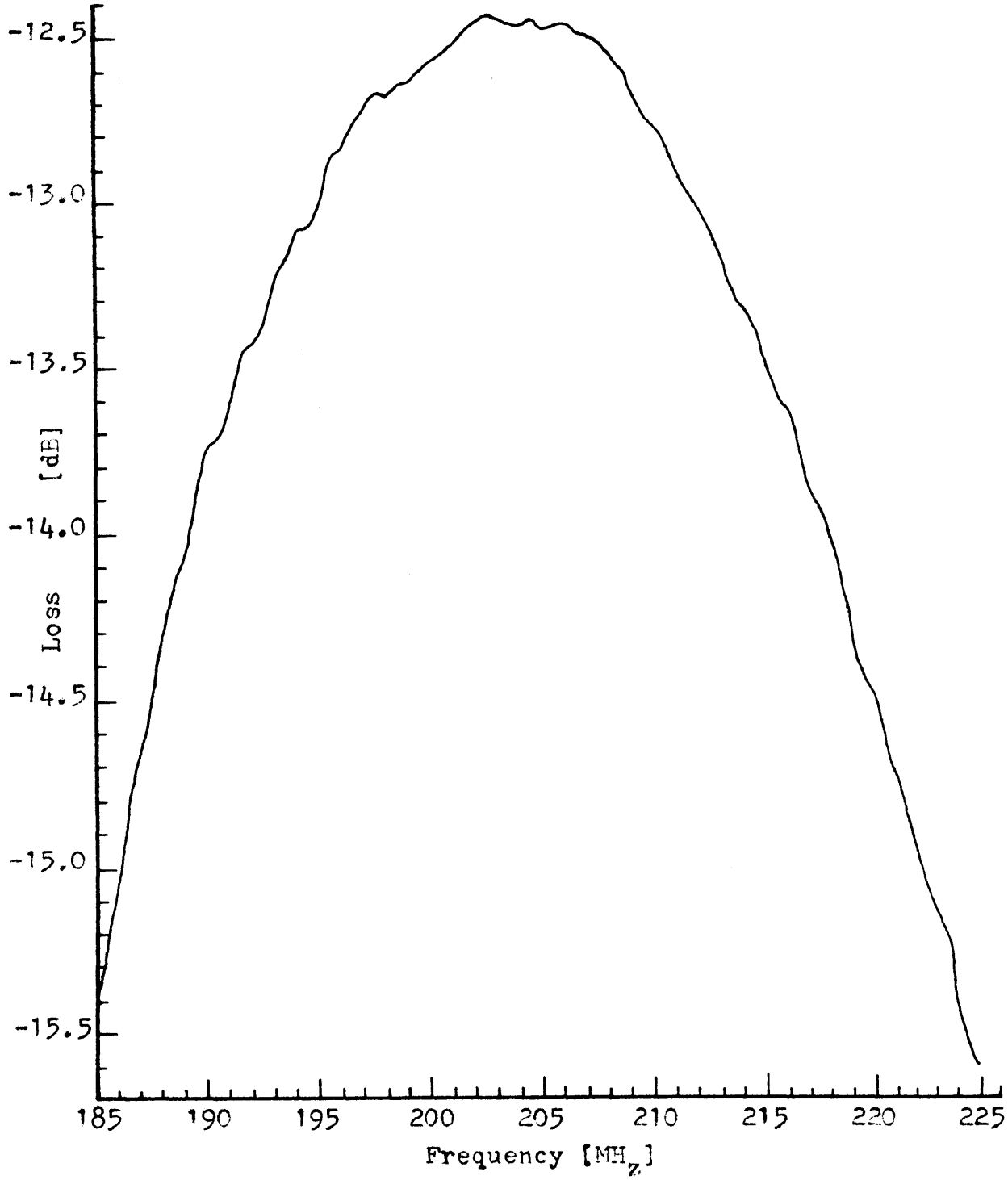

Fig. 4.19 Insertion Loss Curve
Transducer B

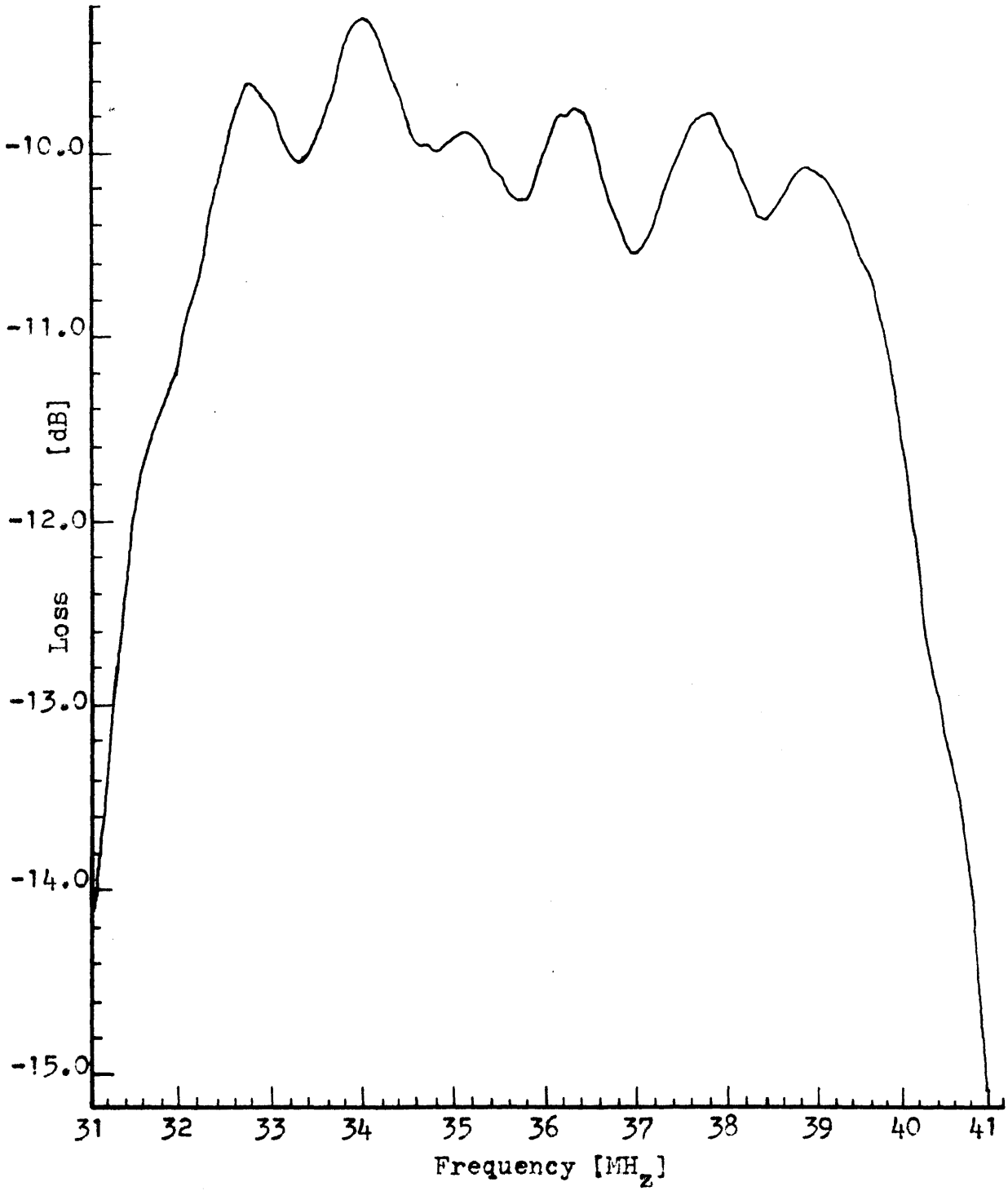

and 36 MHz surface acoustic waves were performed as described in [51]. Measurements were taken of each beam propagating with and without the other present. Results indicated that profiles and phase fronts did not have any unusual characteristics, and that the nonlinear interaction did not produce a measurable change in either phase or profile of the pump waves.

3. Harmonic and Parametric Contamination

The nonlinear interactions on the crystal are not the only potential source of harmonics and parametric interactions. Nonlinearities exist in the mixers and amplifiers which could be a source of the nonlinear signals. Further, harmonic generation on the crystal could interfere with the parametric interaction of up-conversion by depleting the pumps. Therefore contamination of the experiment from other nonlinear sources was explored.

As discussed earlier, harmonics of the pump waves could deplete the pumps and interfere with the parametric interaction. Thus, it was necessary to ascertain if the power levels used for the pumps would produce strong nonlinear interactions. Harmonic power levels and parametric levels were determined by amplifying the signal from the probe and sending it into a spectrum analyzer. The spectrum analyzer was a TEKTRONIX 7L13 in a 7613 CHASIS.

Fig. 4.20 shows the basic circuit used to determine the relative powers of the waves on the crystal. The probe was placed at randomly selected points within the interaction region, and it was found that the second harmonics generated acoustically were at least

Fig. 4.20

Relative Signal Level
Detection System

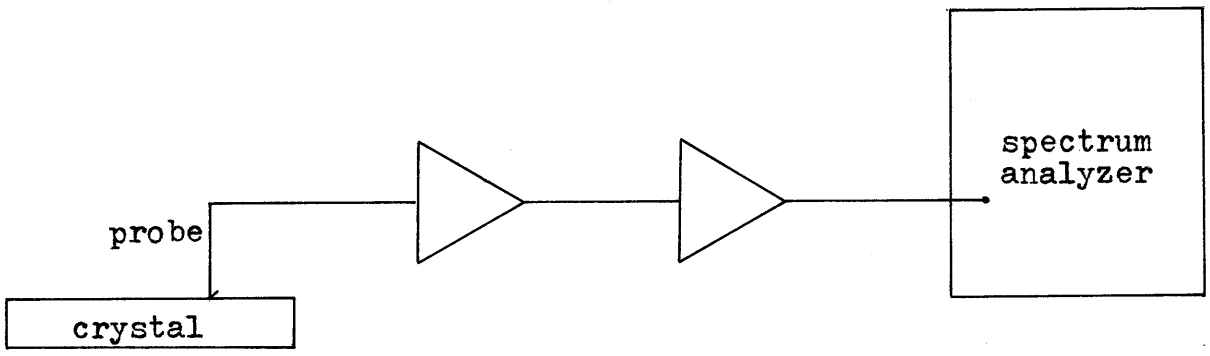

20 dB lower in power than the fundamental waves. Higher harmonics could not be measured. The down-converted, 178 MHz, wave was -5 dB of the up-converted wave which was at least 10 dB in power lower than either second harmonic. Thus it could be concluded that the pumps could be considered undepleted for the given interaction length.

Because it is possible for the amplifiers and spectrum analyzer used with the above tests to saturate and become nonlinear, and thus produce harmonics, intermods, and other parametric signals which would invalidate the measurements of the nonlinear signals from the crystal interactions, it was necessary to check the linearity of these devices. This was done by inserting a 6 dB pad before each device. First the pad was inserted immediately in front of the spectrum analyzer, and then removed and inserted before each amplifier in turn. With the 6 dB in the circuit all readings on the spectrum analyzer dropped by 6 dB indicating the active devices were operating linearly on the signals from the probe tip, and thus the second harmonics and parametric signals were generated by the crystal and not the devices.

The amplifiers and mixers used in the detection and generation systems can be driven nonlinear producing parametric and harmonic signals of the input. With the signal levels encountered by the detection system, any extraneous nonlinear signals produced by the mixers and amplifiers were at least 50 dB lower than the input signals to these devices. With the commercial filters used, any

signals 10 MHz beyond the 3 dB point are attenuated by 40 dB, and with the inhouse 36 MHz filters, between 20 dB and 40 dB depending on frequency. Therefore, the video signal used by the linear gate is representative of the up-converted wave from the crystal and not nonlinearities of any of the devices used in the detection system. The numbers discussed were direct measurements of the characteristics of the mixers and amplifiers. The frequency response of the filters was measured with a TEKTRONIX TR502 tracking generator. The problems of device nonlinearities are also encountered with the generation scheme. In this case not only do the filters reject signals outside of their bandwidth, but the transducers also reject harmonics with at least a 40 dB rejection of the second harmonic. Further the amplifier of the 36 MHz input, prior to transducer B (Fig. 4.5b) was operating 20 dB lower than its 1 dB gain compression point, and the 214 MHz amplifier of transducer A (Fig. 4.5a) was 7 dB lower than the 1 dB gain compression. Thus the interacting waves on the crystal are the 214 MHz and 36 MHz pump waves and the harmonics and parametrically generated signals detected are due to the nonlinearities of the crystal and not from the nonlinearities of the amplifiers, mixers, or generators of the generation system. Hence only the nonlinearities of the crystal contribute to the generation of a 250 MHz signal and not any power device of the experiment.

I. Experimental Procedure

The YZ-$LiNbO_3$ crystal and its mount sit on a rotatable and translatable support shown in Fig. 4.21. Translation is in two orthogonal directions, and a full 360° rotation is possible. Scaled micrometers determine translational movement, and the rotatable stage had degree markings. Rotational accuracy is to within .05° and translational accuracy is .1 mil. This system permitted several degrees of freedom in properly aligning the electrostatic probe with the crystal.

As an initial reference, the crystal was aligned so that the probe could be scanned perpendicular to the z-direction of the crystal or parallel to the phase-fronts of the 36 MHz wave and the crystallographic x-direction. Power was then added to the 214 MHz and 36 MHz transducers and the 250 MHz signal was sought. The 250 MHz signal was found by dragging the probe parallel to the x-direction. Once it was ascertained that the 250 MHz signal existed, the crystal was rotated and "fringe" measurements were made of the 250 MHz signal until the "fringes" were parallel [51]. This indicates the probe is aligned so that one can scan parallel to the phase fronts of the 250 MHz wave. The angle through which the rotation is made gives the angular variation between $\bar{k}_3$ and $\bar{k}_1$ as shown in Fig. 4.6.

The next step was to scan the 250 MHz SAW beam profile to determine the point at which the pump beams collided and determine if diffraction was altering the shape of the 250 MHz beam directly or if diffraction of the pump waves was affecting the interaction.

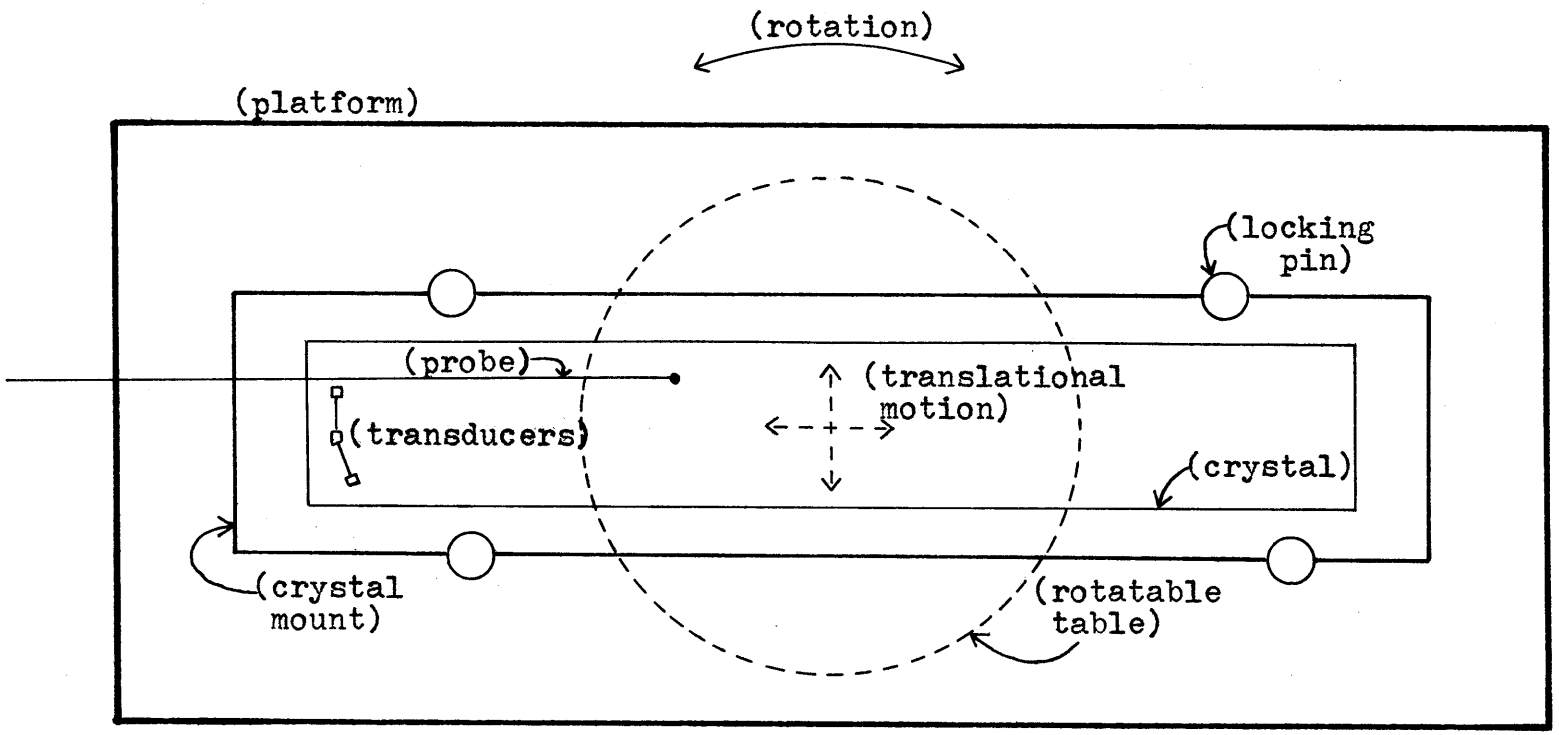

Fig. 4.21

Crystal and Mounting Assembly

The probe was again dragged across the crystal. At this point it was discovered that the 250 MHz SAW signal was too weak to be seen on the oscilloscope as discussed in the previous section. This posed difficulties in matching the alignment signal with the SAW signal on the oscilloscope to synchronize the linear gate. To correlate a time delay on the oscilloscope with the position of the probe, the variable filter was set at a center frequency of 214 MHz. The 214 MHz signal was displayed on the oscilloscope and was used to determine time delay to position. It was found that 1 μsec of delay time corresponded to 138 mils. This gives a group velocity of 3500 meters/sec for the velocity of the 214 MHz signal. However, the theoretical group velocity of this wave [52] is smaller than for the 36 MHz, z-directed wave and the 250 MHz signal. All three group velocities are within one percent of each other, and since the accuracy of any measurement of the group velocities as done here would only be significant to two places, the value of 3500 m/sec is used for all the waves. Hence the 138 mil/1 μsec relationship is used for the 250 MHz signal as well.

Sufficient electromagnetic feedthrough from the transducers to the probe passes through the variable filter to be seen on the oscilloscope. This is the zero-reference of time-delay. The zero for the longitudinal position along the beam was set on the longitudinal micrometer, when the time-distance ratio was determined. Thus by knowing the longitudinal position of the probe, the time delay for the alignment signal could be set on the oscilloscope without

the necessity of seeing the 250 MHz SAW pulse.

After the diffraction distortion was determined, a region for data taking was set and profiles of the up-converted were taken again. This time instead of dragging the probe another procedure was used. The procedure was the following:

1. set probe down;
2. V_{cs} taken from DVM;
3. cos/sin switch turned on and V_{sn} taken;
4. cos/sin switch turned off;
5. probe lifted and moved 5 mils;
6. lower probe and above process repeated.

Once sufficient data was taken to estimate the profile of $|q_3|$ for a given longitudinal position, the probe was moved down the beam and the profile measurements again taken. The detection network was not calibrated during these runs because only an estimate of the profile and the location of its peak was sought.

The probe was not dragged over the crystal for experimental data because of the damage done to the probe tips. It was found that lifting the probe and setting it down for data caused less damage to the tip and calibration was more accurate. Whenever the probe was to be moved for calibrated data and calibration, the probe tip was raised off of the crystal.

Once the region to be scanned and the general shape of the up-converted wave was determined, calibrated data was taken. The profile data for the calibrated-runs was centered on the peak of the

profiles. Data was taken transversely at 1 mil intervals because it has been found that the probe tip wears to the point that useful data could only be taken up to a probe tip diameter of 1 mil. New probe tips could have a diameter as small as .1 mil. Thus resolution of profile features is limited to 1 mil intervals.

The procedure for taking calibrated data is given below:

1. calibration (discussed next section);
2. input power to both transducers measured;
3. probe longitudinally and transversely positioned;
4. probe tip lowered;
5. V_{cs} taken from DVM;
6. cos/sin switch turned on and V_{sn} obtained from DVM;
7. cos/sin switch turned off;
8. power-switch turned on;
9. steps 5 through 7 repeated;
10. power-switch turned off;
11. probe lifted and moved 1 mil transversely;
12. checked DVM for drift of linear gate and if linear gate drifted, rezeroed the linear gate;
13. steps 4-9 repeated for 11-15 data points taken around the peak of the profile;
14. input power to transducers remeasured;
15. after data points taken, probe recalibrated.

The probe was calibrated after each data-run, so that the procedure for a set of data-runs was calibration, data, calibration, data, ...,

calibration.

The above describes the basic procedure used with the experiments. To find a relation between output voltage of the detection network with the amplitude of the up-converted SAW, and because of the varying characteristics of the probe due to the changing probe tip, a calibration method was devised. The next section describes this procedure.

J. Detection Network Calibration

The output of the detection network is a voltage displayed on the digital volt meter from which the V can be found that corresponds to $|q_3|$. To find $|q_3|$, V must be related to a power density ($|\langle\bar{S}_3\rangle|$) of the 250 MHz surface wave at the point the probe tip is sensing. Therefore to establish the voltage to power density relation; the probe must be calibrated from a surface wave of known power density. This then establishes a system response, G.

Because the up-converted 250 MHz wave is evolving from the two pump waves, and its power density characteristics are unknown, this wave cannot be used for calibration purposes. However, because transducer A (Fig. 4.8) launches a wave in approximately the same direction as the q_3 wave the power density characteristics are about equal. Further the $\Delta v/v$ value for $\theta = 100°$ is 9 percent of $\Delta v/v$ for $\theta = 97°$. Thus the probe response to at 250 MHz wave with a phase velocity defined by $\theta = 100°$ should be within 10 percent of the response for the 250 MHz up-converted wave. Therefore the probe can

be calibrated by launching a 250 MHz wave of known power density from transducer A.

A profile of a 250 MHz signal launched from transducer A revealed that diffraction had created Fresnel ripples on the profile of the amplitude. The profile was taken with the probe scanning parallel to the phase-fronts of the 250 MHz up-converted wave and not the phase fronts of a wave launched from transducer A. The probe was 2 μsecs of propagation time or 276 mils from transducer A. Because of the Fresnel ripples one could not calibrate the detection network at only one point. Therefore a portion of the profile was scanned. The part of the profile scanned for calibration was the center one-fifth, with data points taken every 3 mils for a total of 11 points. By transversing over the one-fifth portion of the beam, several Fresnel ripples were scanned from which an average value of the amplitude of the wave could be found.

The procedure for taking the calibration data was similar to the process for taking the experimental data. This consisted of:

1. transverse and longitudinal positioning,
2. lowering probe,
3. reading voltage from DVM for V_{cs},
4. turning cos/sin switch on,
5. reading V_{sn},
6. turning cos/sin switch off,
7. raising probe,
8. checking drift of linear gate,

9. repositioning of probe.

This method gave the center one-fifth portion of the profile. An average of the V's computed from V_{cs} and V_{sn} for each transverse position was taken and this average used as the calibration voltage (V_{cal}) for the power density of the SAW when launched from transducer A. This established G as

$$G = \frac{V_{cal}}{\sqrt{|\overline{\langle S \rangle}|}} \qquad (4.J.1)$$

The calibration input signal to transducer A was formed by mixing the 214 MHz and 36 MHz signal from the cw generators as discussed in section G and shown in Fig. 4.10a and Fig. 4.10b. Instead of going to the crystal, the RF bursts were attenuated for a mixer and then mixed. The output of the mixer was filtered with a variable bandpass filter centered on 250 MHz with a 12.5 MHz bandwidth, and then the filtered 250 MHz signal was applied to transducer A. Measuring the power of the input signal, subtracting for insertion loss, and dividing the beamwidth of transducer A gave the power density of the SAW launched. The power to transducer A was measured before and after each calibration run of 11 calibration points.

In contact with the crystal is a tungsten wire chemically etched to produce a contact point with diameters as small as .1 mil. Etching is an uncontrolled process which produces varying diameters and this alone requires a calibration of the probe for each probe

tip. However, the major problem is the unpredictable wearing or flattening of the contact tip when it is raised and lowered from, or dragged across, the crystal. The changing diameter caused by the mechanical wearing or flattening varies the pick-up characteristics of the probe. Fig. 4.22a - 4.22c show the changing nature of one probe tip. With a magnification of x200, Fig. 4.22a is the tip when new, and as can be seen, it is rounded. Fig. 4.22b and 4.22c illustrate the flattening of the tip after 90 contacts and 378 contacts with the crystal respectively. Because of this random feature of the tip a varying response of the probe to a surface wave occurs, and the voltage output of the detection network is equally variable.

Due to this unpredictable nature a statistical calibration procedure was devised based on the assumption that the probe sensitivity did not change by more than one or two percent between any two consecutive contacts the tip had with the crystal. During the course of the experiment it was found that for approximately 80 percent of the time this was true. The statistical method used for calibration was the following. A calibration-run was made with probe contact points as described above. A data-run was taken usually with 11 contact points, but with wider up-converted profiles, as many as 15 data points. Then another calibration-run was performed. This process was continued for a given set of profiles fo the 250 MHz up-converted SAW. The system response (G) of the calibration-run was then taken as a function of the number of contacts

Fig. 4.22

PROBE TIP

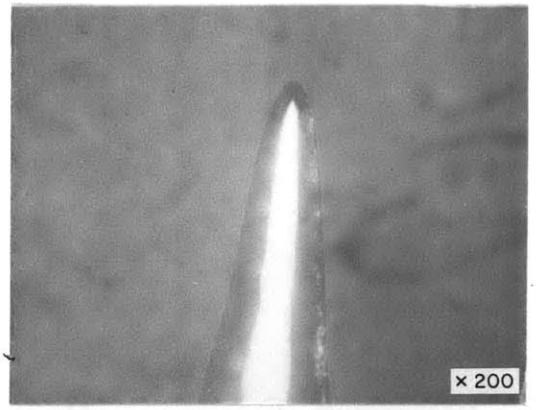

Fig. 4.22 a
NEW TIP

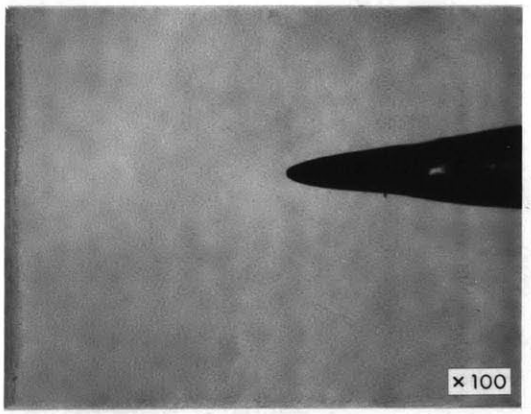

Fig. 4.22 b
90 CONTACTS WITH CRYSTAL
TIP DIAMETER: 0.5 mils

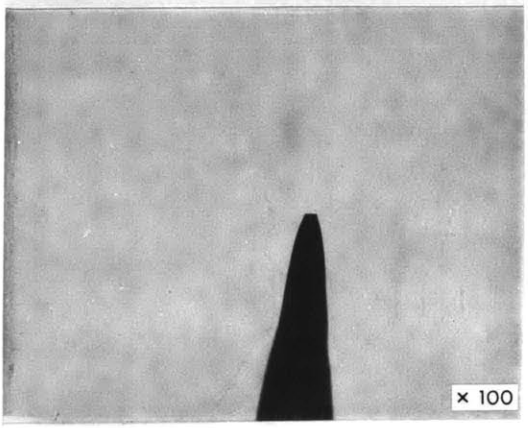

Fig. 4.22
378 CONTACTS WITH CRYSTAL
TIP DIAMETER: 1 mil

between the end of the first calibration run and the end of the last calibration. G for each data-run was the linear interpolation between its preceding and following calibration-runs. As an example, the voltage-power relation of the first calibration-run corresponded to 11 contacts, then 11 data points were taken and then another calibration-run. The G relation of this calibration-run corresponded to 33 contacts. The total number of contacts with the crystal at the end of the data run was 22. By linearly interpolating the voltage-power relation of the two calibration-runs for 22 contacts, the voltage-power relation for the data-run was found. The next data-run produced 44 contacts and the following calibration-run gives 55 contacts. Thus the voltage-power relation for the data-run giving 44 contacts is the linear interpolation of the calibration-run of 33 contacts and 55 contacts. This process continued for all data-runs.

This section has described the calibration procedure used for the experiments. The methods chosen were designed to reduce error due to probe tip changes and diffraction of the calibration SAW waves. The next chapter describes the results of this process and the variations between calibration-runs encountered.

CHAPTER 5

EXPERIMENTAL RESULTS AND ANALYSIS

A. Chapter Outline

This chapter covers five areas important to the analysis of the experimental results and the coupling constant. Section B discusses the determination of the area of the crystal from which calibrated data was taken and the propagation direction of the up-converted wave. The next section (C) examines the pump waves within the data region. Calibration results are reviewed in section D and with the evaluations of sections B-D, a determination of the magnitude of the coupling constant is made. The last section (F) is a brief look at some of the profiles of the up-converted wave within the interaction region.

B. Data Region and Propagation Direction

If the two pump waves have rectangular profiles, the collision of the two waves would begin 4.4 μsec or 604 mils from the transducers (see Fig. 4.7). However, because of diffraction, the pump waves spread and it was found that a nonlinear interaction occurred as early as 3 μsecs. At 3 μsecs, the up-converted wave had an erratic profile and detection of the wave was difficult. Therefore, the first calibrated data was taken at 4.5 μsec. Profiles of the 250 MHz wave were made up to 6 μsec, at intervals of .25 μsec of delay time or every 34.5 mils of longitudinal distance. Calibrated data was not taken beyond 6 μsec because diffraction of the pump waves and

self-diffraction distort the profile of the 250 MHz wave.

When the data for the calibrated runs were taken, it was found that the profile had a fine structure of several peaks. Fig. 5.1 and Fig. 5.2 are graphs of the position of the peaks versus longitudinal distance for two sets of data runs. The error on the transverse peak position is ± 2 mils. This error is due to probe tip variations and not micrometer error. The zeroes of the graphs are arbitrary and thus the graphs depict relative positions. Fig. 5.3 illustrates the reproducibility of the peak positions for two different data-runs.

Fig. 5.1 shows a line which is the least squares fit of the peaks of maximum value for the longitudinal positions 0-103.5 mils (4.5 μsec-5.25 μsec). The line is then extrapolated through the other three longitudinal positions (5.5 μsec-6 μsec), and this provided the positions of the data points used to find $|K|$. From the slope of this lines one can find the power-flow angle of the group velocity. The dashed line gives longitudinal and transverse position of the profile data to be used in evaluating $|K|$ with transverse position.

Fig. 5.2 is a graph similar to Fig. 5.1 but for a separate set of data runs. Only four profiles' data are shown because it was found that the probe tip used in the last three profiles was out of position compared to the first four profiles.

From Fig. 5.1 and Fig. 5.2, the slope of the line is the tangent of the power flow angle ϕ_3 (Fig. 4.6). Therefore:

$$\phi_3 = \tan^{-1}(\text{slope}) \qquad (5.B.1)$$

Fig. 5.1

Position of Peaks: Experiment-A

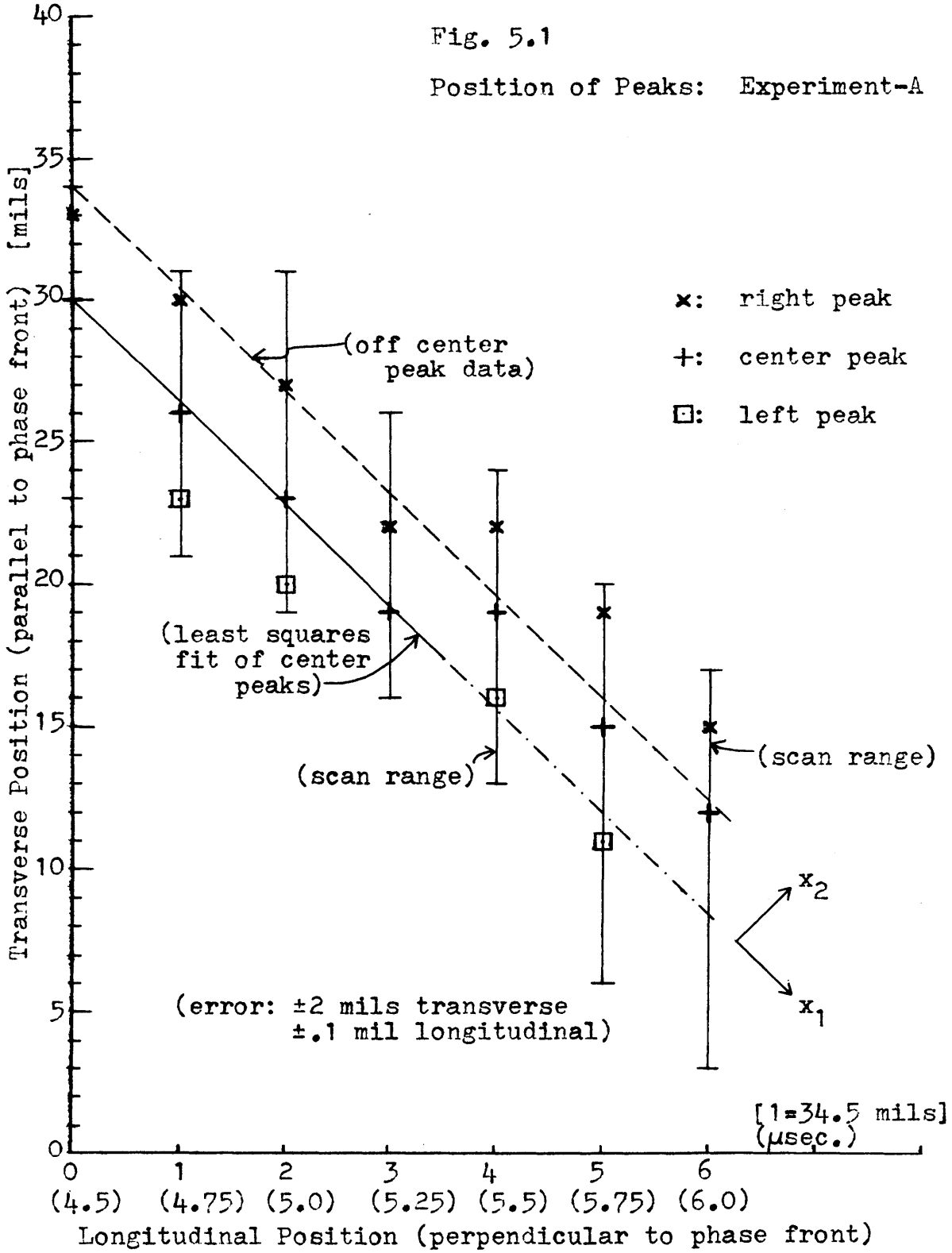

Fig. 5.2

Position of Peaks: Experiment-B

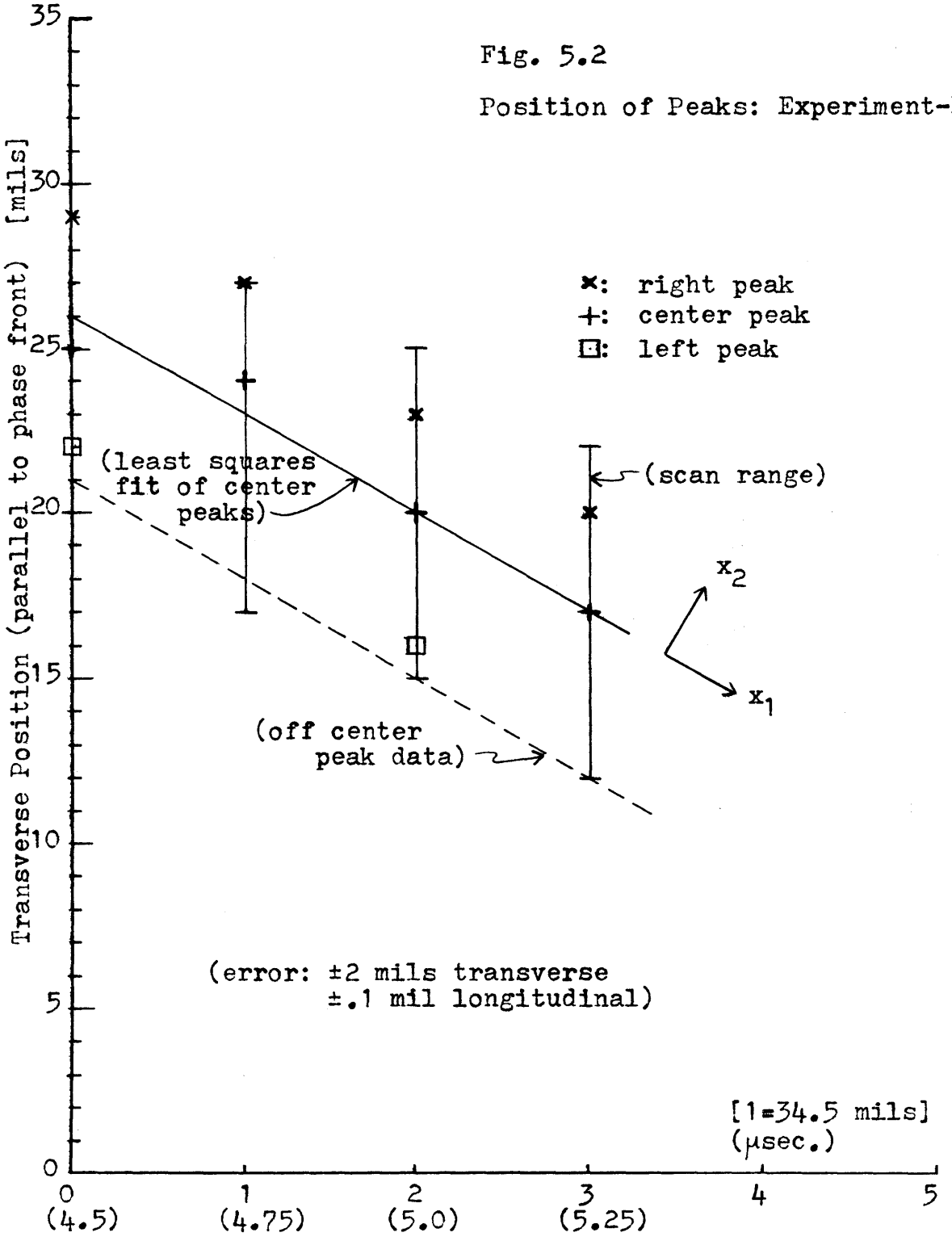

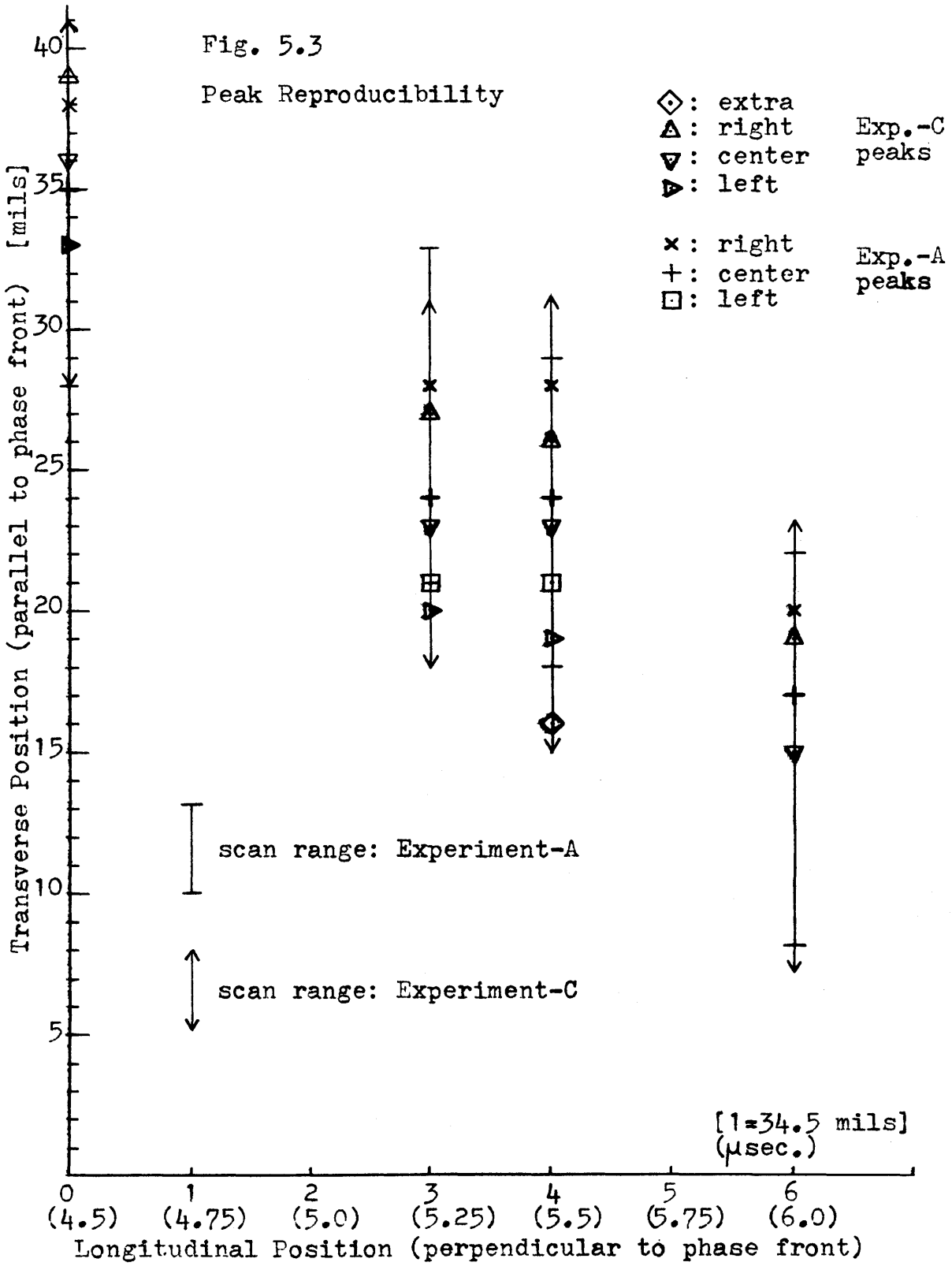
Fig. 5.3
Peak Reproducibility
◇: extra
△: right
▽: center
▷: left
Exp.-C peaks
×: right
+: center
□: left
Exp.-A peaks
scan range: Experiment-A
scan range: Experiment-C
Transverse Position (parallel to phase front) [mils]
40
35
30
25
20
15
10
5
[1=34.5 mils]
(μsec.)
0 (4.5)
1 (4.75)
2 (5.0)
3 (5.25)
4 (5.5)
5 (5.75)
6 (6.0)
Longitudinal Position (perpendicular to phase front)

For experiment-A of Fig. 5.1, ϕ_3 = -6° and for experiment-B of Fig. 5.2, ϕ_3 = -5°. With the error of ±2 mils for the transverse position due to probe variation, the two angles are within the error of each other. Therefore a ϕ_3 = -5.5° is used to specify the power flow angle.

As discussed in Chapter 4, section I, by aligning the probe so that the transverse scan was parallel to the phase fronts of the 250 MHz wave, the angle from the Z-direction could be determined. The angle was found to be 8.45°. This gives a θ_3 of 98.45°.

The ϕ_3 = -5.5° and θ_3 = 98.45° do not correspond to the predicted values of θ_3 = 97.45° and ϕ_3 = -4.14°. There could be several possible causes of this discrepancy. As stated before, propagation on and near the z-direction of y-cut $LiNbO_3$ is poorly understood as evidenced by the inability to predict diffraction features [53]. Thus the theoretical values calculated for the phase velocities v_{p1}, v_{p2}, and v_{p3}, and the power flow angles ϕ_1, ϕ_2 and ϕ_3 may not be correct. If the phase velocities are not properly known, then the frequency ratio f_2/f_1 used with this experiment becomes doubtful. If the power-flow angles used to construct the collision scheme are incorrect, then the direction of the up-converted wave may not correspond to the peaks of the amplitudes, and thus one has no indication as to the direction the SAW is propagating. Another problem could be that no phase matching exists and the up-converted wave is the result of a slightly mismatched interaction. If this were true then a sinusoidal variation of the amplitude of the

up-converted wave would be evident, and this was not found. Hence this case could be dismissed, and a phase-matched interaction is indicated.

Considering the phase-matched case again, and examining the profiles of the up-converted wave at 4.5 μsec, 5 μsec and 6 μsec, as shown in Figures 5.19, 5.20, and 5.21 of section F, one finds the profiles relatively symmetric, and not skewed as in Fig. 4.5. Hence one can conclude that even if the 250 MHz SAW is not propagating half-way between the other two waves, it is relatively close and since the angles one is working with are small, the peaks give an approximate indication of the direction of the group velocity. Even with the disagreement with theory, the θ_3 and ϕ_3 angles found here are used in determining the direction of the 250 MHz wave. For the 36 MHz and the 214 MHz wave, the theoretical values of θ and ϕ specify the direction of these waves.

With the group velocities of the waves specified by the angles discussed above, the x_1-x_2 coordinate system can be specified by v_{g3}. Fig. 5.4 illustrates the x_1-x_2 coordinate system determined by the experiment, its relation to the X-Z coordinate of the $LiNbO_3$, and the direction of the group velocity of each wave. The angular difference between each group velocity is also given and it is found that v_{g3} almost bisects the angle between v_{g1} and v_{g2} as was originally intended.

Fig. 5.4

$x_1 - x_2$ Coordinate System

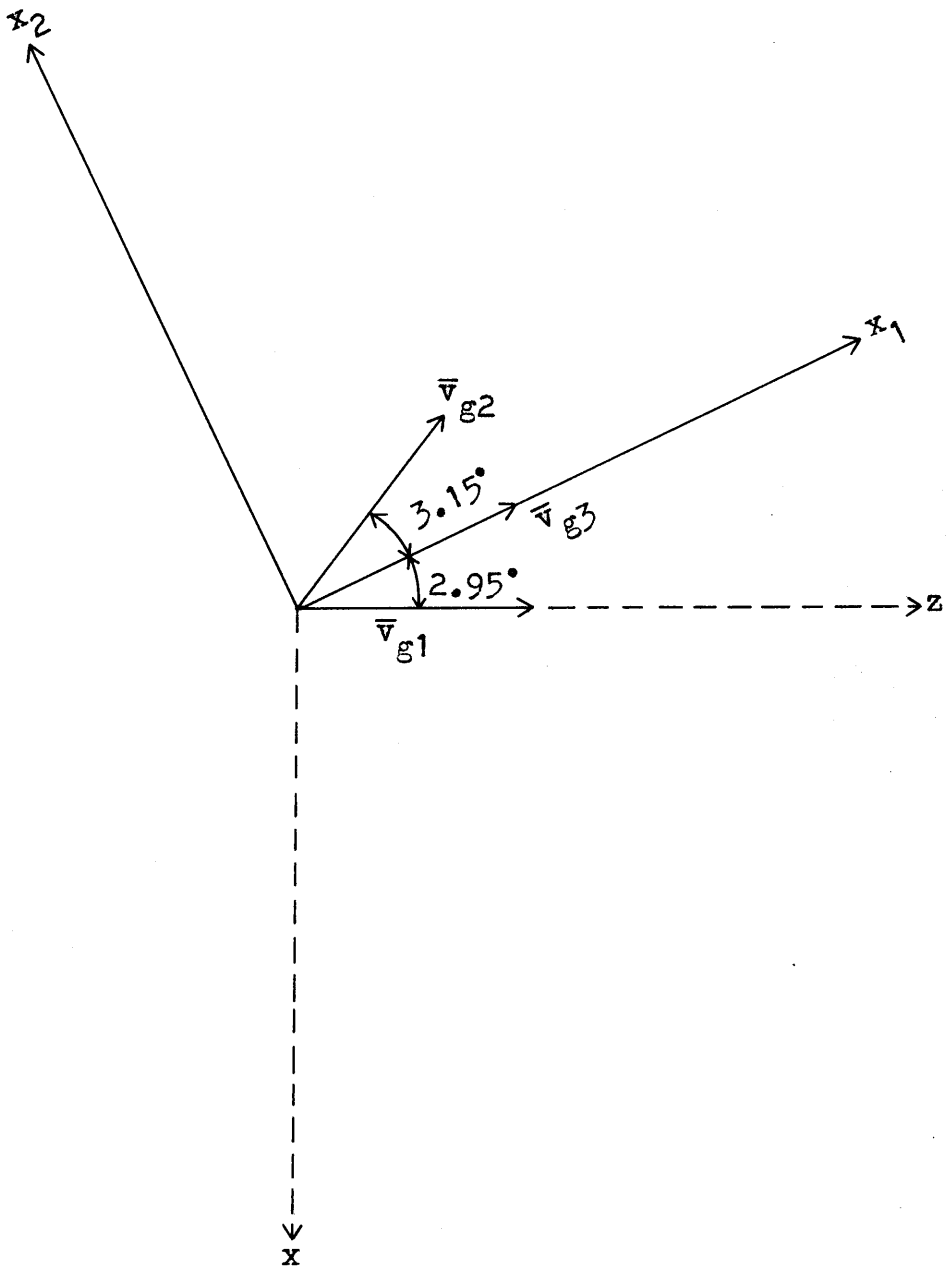

C. Pump Waves

The experiment was originally designed to examine an interaction of two pumps of rectangular cross-section. However, because of diffraction a specific region was chosen for data. This necessitated a reconsideration of the profiles of the pump waves.

During the course of the experiments, it was found that the input power to the transducers varied from one data run to the next. The input power to transducer A ranged from 19.7 dBm to 20.0 dBm and for transducer B from 22.3 dBm to 22.5 dBm. When the power-switch was turned on the power to transducer A went from 16.7 dBm to 17.1 dBm, and 19.5 dBm to 19.7 dBm for transducer B. Because of this span of input powers, the profiles were examined in terms of $|a_\alpha|$ instead of $|q_\alpha|$.

By using $|a_\alpha|$ ((2.B.7)-(2.B.13)) instead of $|q_\alpha|$ one can establish a profile from which one can determine $|q_\alpha|$ from any input power. Associating a specified power density $|\langle\bar{S}_\alpha\rangle|$ with $|a_\alpha| = 1$ for a given wave, one can find $|q_\alpha|$ by multiplying this power density by the varying values of $|a_\alpha|$ of the profile. As an example, let $|\langle\bar{S}\rangle|$ be a power density for $|a_\alpha(x_1,x_2)| = 1$, then $|q_\alpha(x_1,x_2)| = \frac{|\langle S\rangle|}{v_{g\alpha}\omega_\alpha}$. When $|a_\alpha(x_1,x_2)| = \frac{1}{2}$, the $|q_\alpha(x_1,x_2)| = \frac{1}{2}\frac{|\langle S\rangle|}{v_{g\alpha}\omega_\alpha}$, and $|\langle S\rangle|$ is a constant for the wave in question.

The profiles revealed that Fresnel ripples had developed on the pump waves and that the beams had spread. To specify $|a_\alpha|$, the values of the peaks and valleys of the ripples were averaged. The average values was associated with $|a_\alpha| = 1$, and the rest of the profile

normalized with respect to this average value. This produced a profile of $|a_\alpha|$ for each pump wave and these profiles are shown in Fig. 5.5 and Fig. 5.6. These profiles are the shape of the wave as one looks towards the transducers. With this average over the Fresnel ripples, the profiles can be approximated by a trapezoid with the height of the trapezoid being $|a| = 1$. It was found from the data region discussed in the last section; the portion of the profiles interacting in this region was the ramp part of the profile.

The profiles shown in Figures 5.5 and 5.6 were taken a 4 μsec from the transducers, and it was assumed that the profiles did not change from 4 μsec to 6 μsec. Profiles were taken parallel to the phase fronts of their respective waves, and thus the profiles had to be examined in the x_1-x_2 coordinate system. Fig. 5.7 shows the x_1-x_2 coordinate system and the phase fronts of the 36 MHz and 214 MHz pump waves. From the geometry specified by the coordinate system and the phase fronts, one could find the point on the profile that corresponds to x_1 equal 4.5 μsec through 6 μsec, at a given value of x_2. The 4.4 μsec point of each profile is marked, and this corresponds to the intersection point of the hypothetical rectangular pulses. In other words, if the profiles were rectangular with a width equal to the apeture width of the transducers, 4.4 μsec would be the propagation time at which the two waves first collide. Also marked on the profiles are the values of $|a|$ used to calculate $|q|$ for the case $x_2=0$, and the longitudinal positions given in parentheses (microseconds from the transducers). The marked part of the profiles correspond to the crossover points of the profiles at the longitudinal

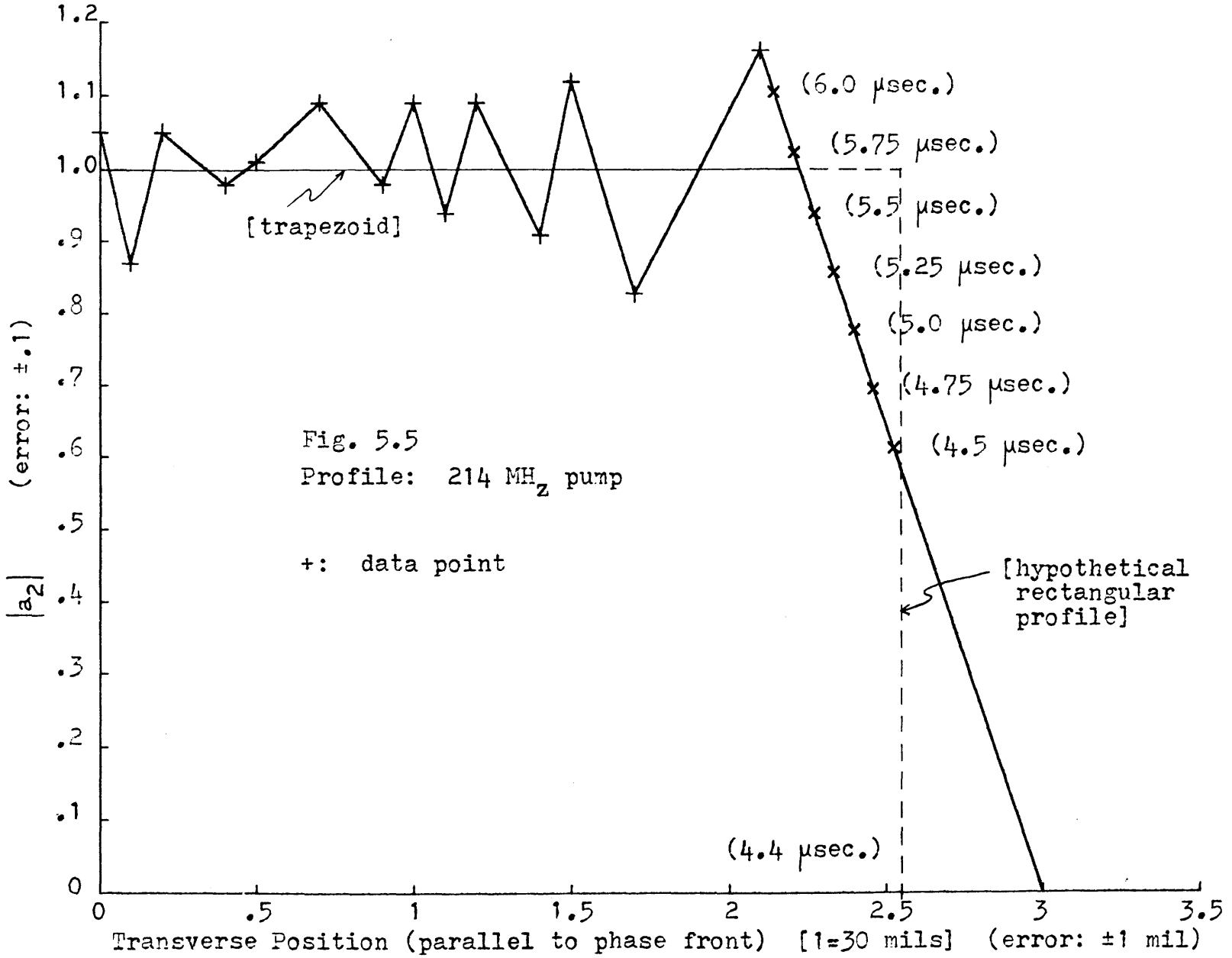

Fig. 5.5
Profile: 214 MH_z pump

+: data point

Fig. 5.6
Profile: 36 MH_z pump
+: data point

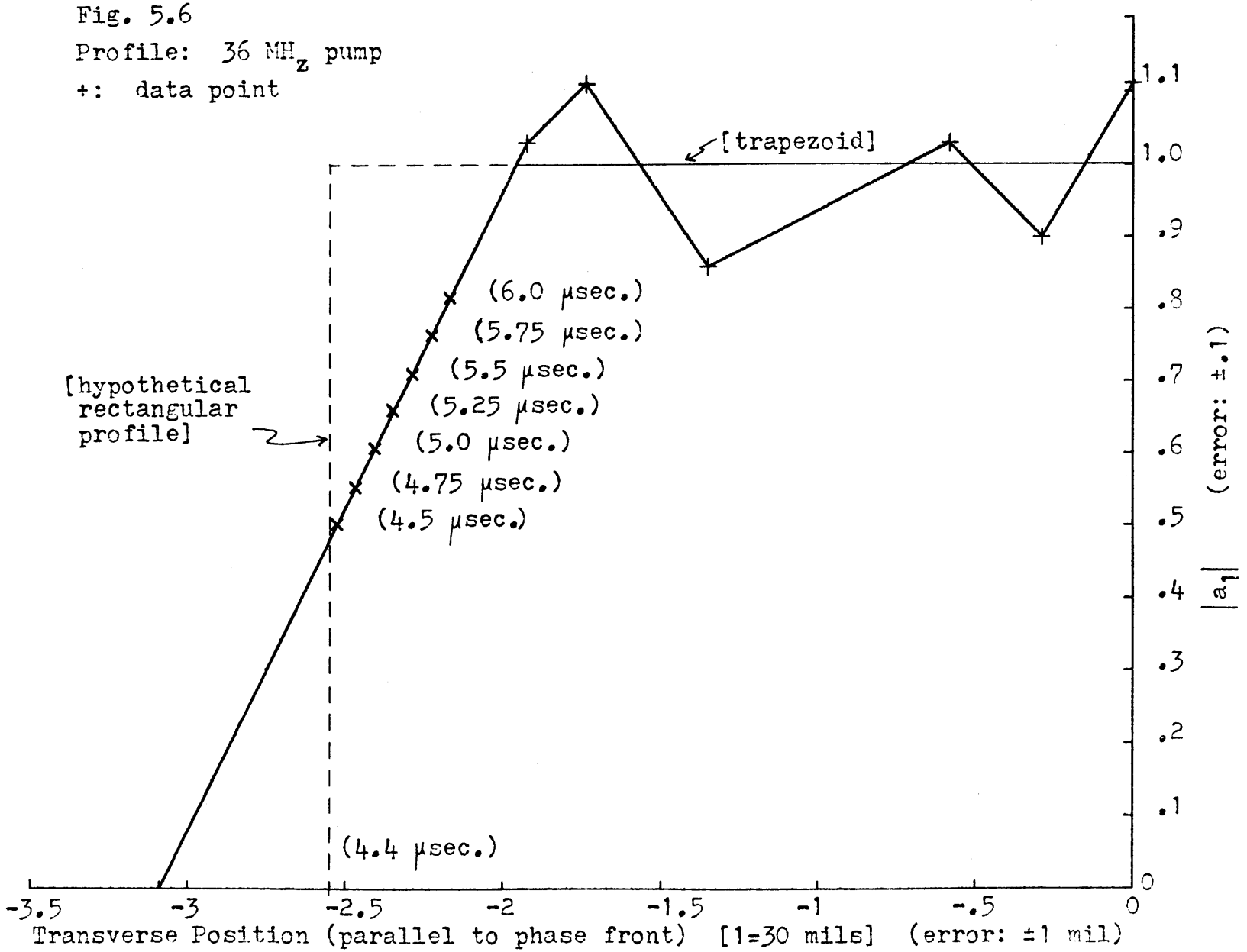

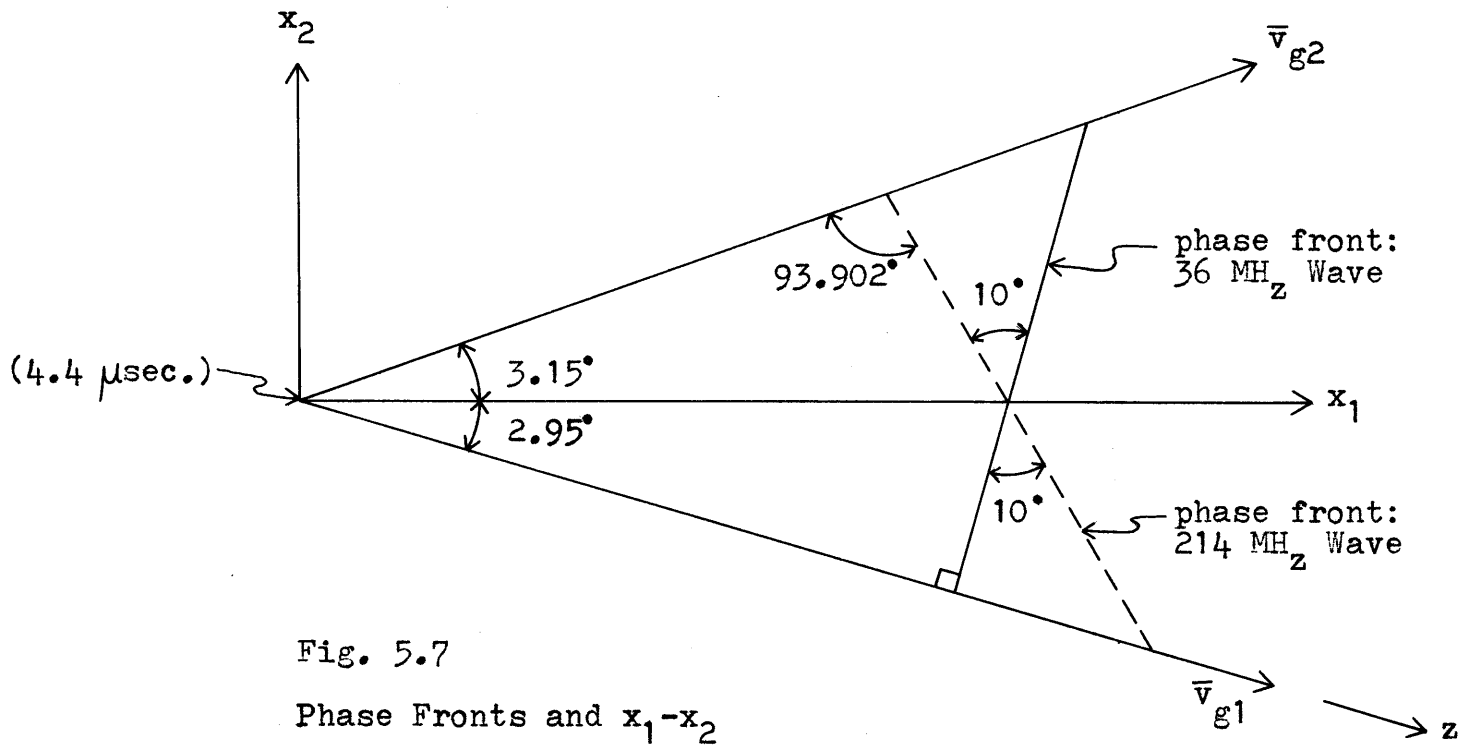

Fig. 5.7

Phase Fronts and x_1-x_2 Coordinate System

position. With $|a|$ found, one needs to determine $|\langle\bar{S}\rangle|$ so that $|q|$ can be calculated.

To find the power density $|\langle\bar{S}\rangle|$ that give $|a| = 1$, the diffraction loss [53] and propagation loss were analyzed [55]. It was found that 94 percent of the power launched from the transducers were contained in the transducer apeture width for each transducer at 4 μsec. Since so little power is contained outside of the original apeture width as marked by 4.4 μsec, the power of the SAW at 4.4 μsec was taken to be .94 times the power of the SAW at the transducers. Dividing .94 times initial SAW power the apeture width of the launching transducer gives the $|\langle\bar{S}_\alpha\rangle|$ for $|a_\alpha| = 1$, and thus $|q_\alpha|$ can be found from

$$|q_\alpha(x_1,x_2)| = \frac{|\langle\bar{S}_\alpha\rangle||a_\alpha(x_1,x_2)|}{\omega_\alpha v_{g\alpha}} \qquad (5.C.1)$$

where $|\langle\bar{S}_\alpha\rangle|$ = constant for a given wave.

This discussion gives the basic approach used in obtaining the values of $|q_1|$ and $|q_2|$ in computing $|K|$. However, because of the range of input powers encountered for the data-runs, an average $|\langle\bar{S}\rangle|$ was used in determining $|q|$ in computing $|K|$. This is discussed in the next section.

D. Detection Network Calibration Results

As discussed in Chapter 4, calibration of the detection network was necessary to find an output voltage to power density relation. This section examines the results of the calibration procedure.

Fig. 5.8 and Fig. 5.9 illustrates the reproducibility of the shape of the 250 MHz SAW launched from transducer A. Fig. 5.8 corresponds to the calibration data for experiment-A and Fig. 5.9 show the results for experiment-B. The graphs plot V as defined by equation (4.G.2) for the 11 transverse positions. The error is not plotted to avoid cluttering the diagrams, but a five percent error is estimated for each plotted point. The error is representative of power and phase drifts of the detection network and signal generators during data taking and the ±3° error of the 90°-hybrid of the cos/sin switch. The profiles shown are those used in analyzing the data runs and for experiment-B, only five of the calibration-runs are shown, but the graphs show the resproducibility of the profile.

The voltages shown are then averaged for each calibration-run to find V_{cal} for each run, and then the system response G. Fig. 5.10 and Fig. 5.11 are plots of G versus number of probe tip contacts with the crystal, for data-runs A and data-runs B respectively. The error encountered is due to the measurement of the input power, insertion-loss measurements of transducer A, and the error of each V. This gives a total error on G of ±15% of G for each calibration run.

Marked on the horizontal axis is the longitudinal position

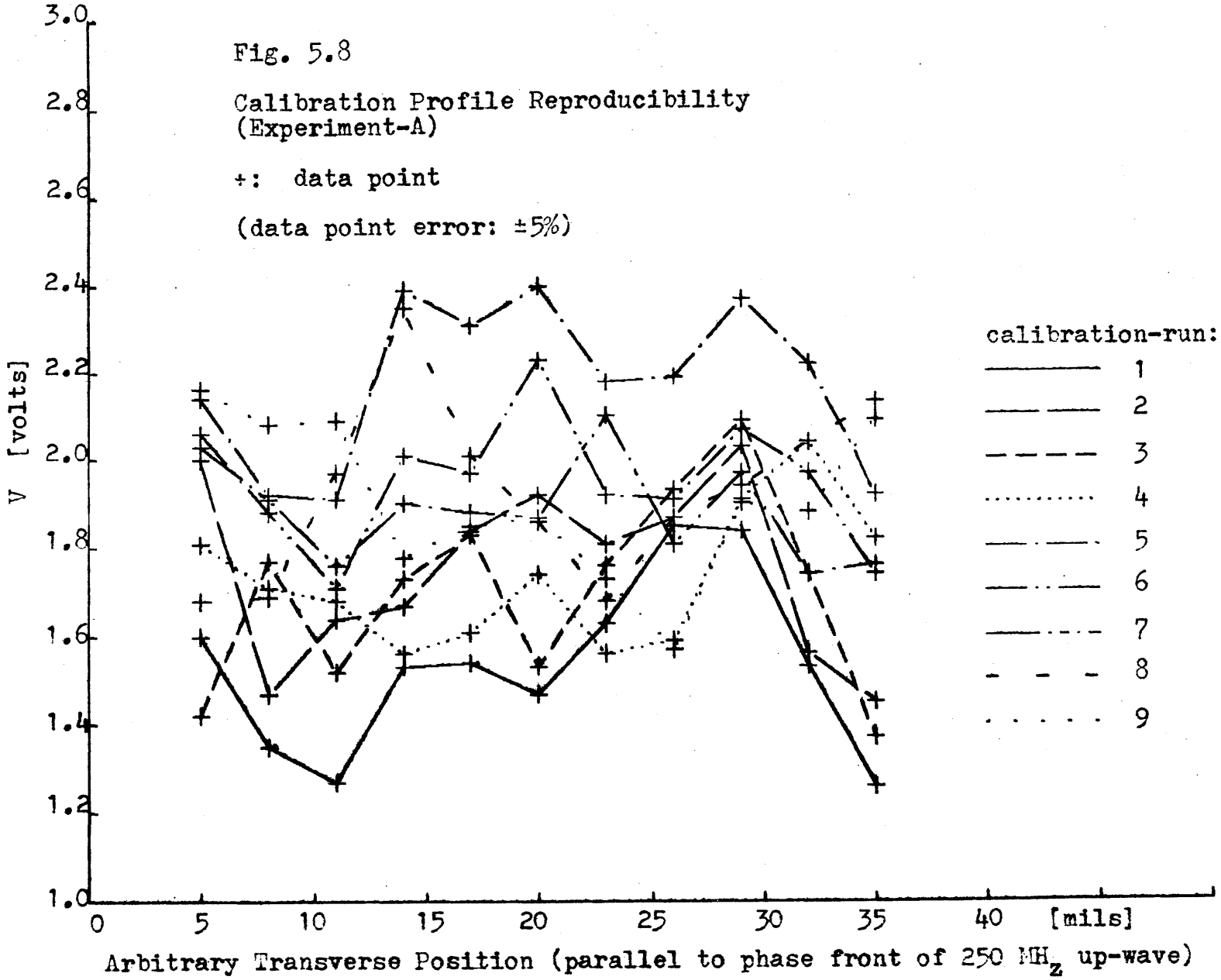

Fig. 5.8

Calibration Profile Reproducibility
(Experiment-A)

+: data point

(data point error: ±5%)

Fig. 5.9

Calibration Profile Reproducibility
(Experiment B)

+: data point

(data point error: ±5%)

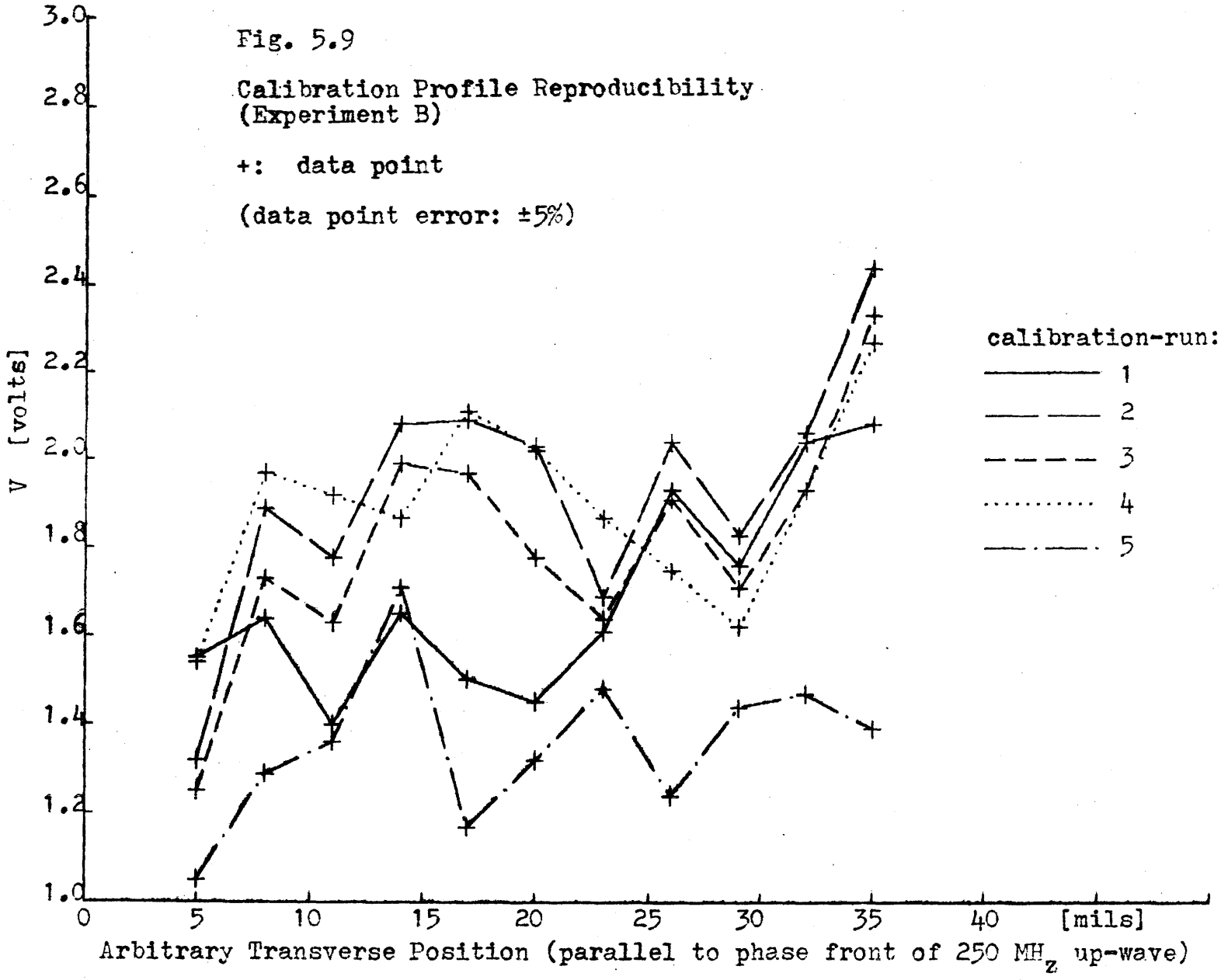

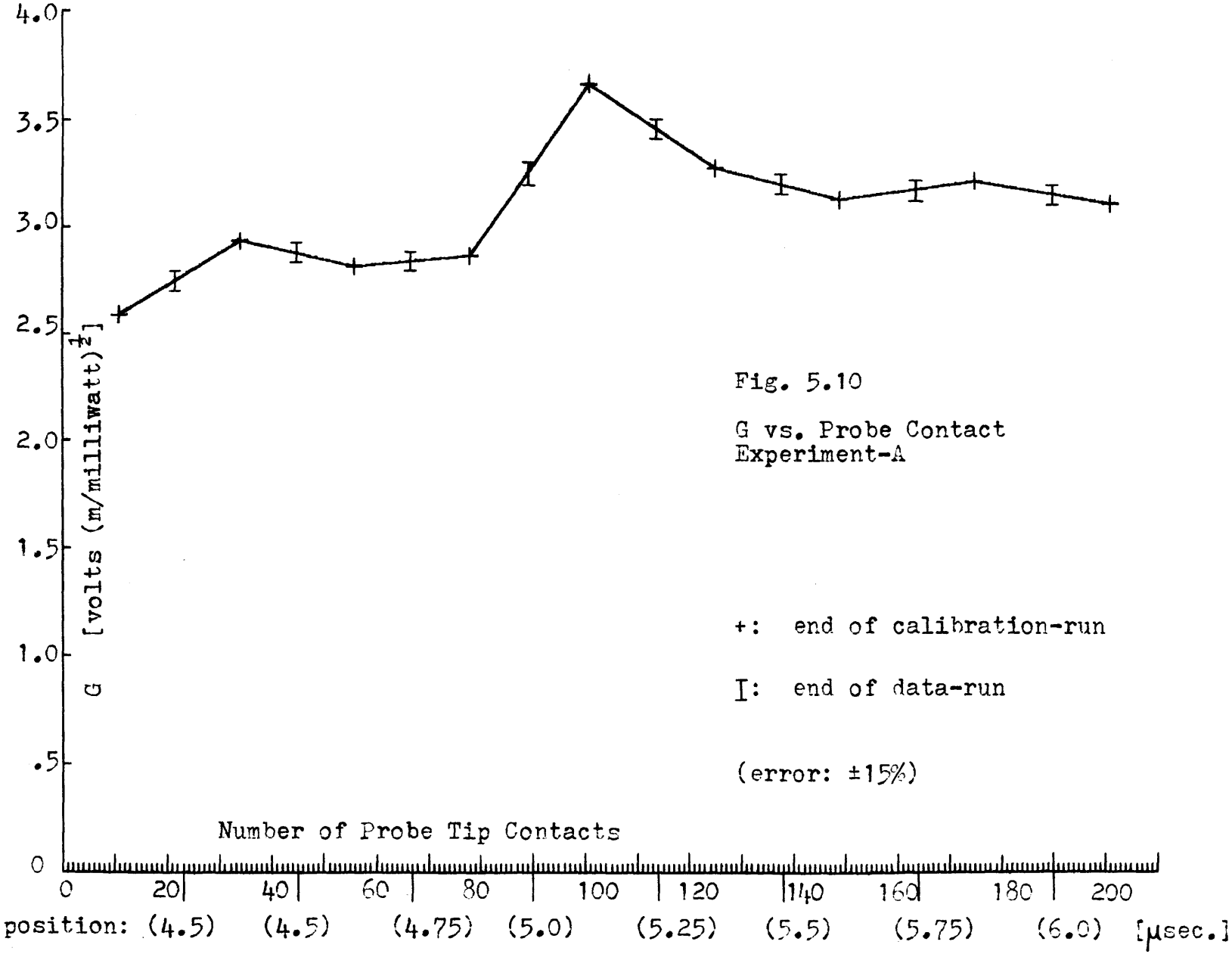

Fig. 5.10

G vs. Probe Contact
Experiment-A

+: end of calibration-run

I: end of data-run

(error: ±15%)

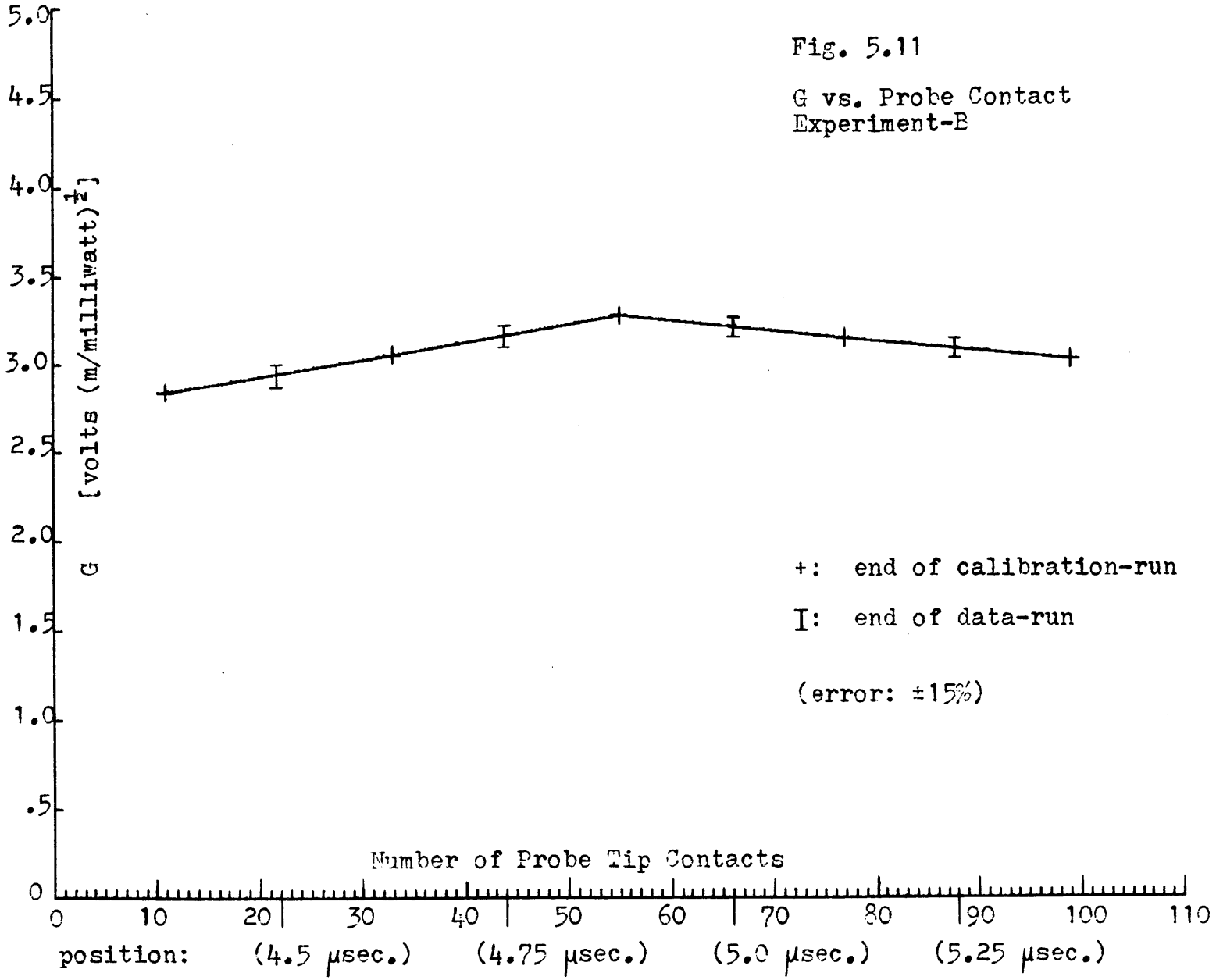

Fig. 5.11

G vs. Probe Contact
Experiment-B

+: end of calibration-run

I: end of data-run

(error: ±15%)

(in parentheses) that corresponds to the total number of contacts that have occurred up to the end of the data-run at the longitudinal position. The value of G for the data-run is the linear interpolation of the G's for the preceding and following calibration-run. The G for the data-run is marked with the small vertical bar. Thus G is determined for each data-run and the detection network is calibrated for a given data-run.

E. Magnitude of Coupling Constant

The magnitude of the coupling constant $|K|$ is found from the equation

$$\frac{v_{g3}}{|q_1||q_2|} \frac{d|q_3|}{dx_1} = |K| \qquad (5.E.1)$$

Because $|q_1|$ and $|q_2|$ are not constants, but are ramps as discussed in section C, $\frac{d|q_3|}{dx_1}$ must be determined from the $|q_3|$ for each longitudinal position. This can be done by fitting a curve that visually best approximates $|q_3|$ versus x_1. The slope of the curve gives $\frac{d|q_3|}{dx_1}$. Slope of the curve for each x_1 can be found by drawing a tangent line to the curve, and the slope of the tangent line is $\frac{d|q_3|}{dx_1}$.

As discussed in section C, the input power to each transducer varied between data-runs. Therefore the value of $|q_1(x_1,x_2)|$ and $|q_2(x_1,x_2)|$ varied between data-runs for the same x_1 and x_2. Thus

the measured $|q_3|$ would also not be the same for each data run at a given x_1, x_2. To compensate for this, the average value of the input power to transducer A, and the average value of the input to transducer B, were taken as a base input powers to each transducer respectively. This base was used in altering $|q_3|$ to give a set of data consistent to a single set of power densities. Equation (5.E.1) can be rewritten as:

$$v_{g3} \frac{d \frac{|\langle \bar{S}_3 \rangle||a_3|}{v_{g3}\omega_3}}{dx_1} = \frac{|K||\langle \bar{S}_1 \rangle||\langle \bar{S}_2 \rangle||a_1||a_2|}{v_{g1}v_{g2}\omega_1\omega_2} \qquad (5.E.3)$$

The values of $|\langle \bar{S}_1 \rangle|$ and $|\langle \bar{S}_2 \rangle|$ discussed in section C, found from the average input power can be written as S_1 and S_2. Whenever $|\langle \bar{S}_1 \rangle|$ and $|\langle \bar{S}_2 \rangle|$ differed from S_1 and S_2, $|q_3|$ was corrected to compensate. Therefore (5.E.3) becomes:

$$v_{g3} \frac{d}{dx_1}\left[\frac{|\langle \bar{S}_3 \rangle|S_1S_2}{|\langle \bar{S}_1 \rangle||\langle \bar{S}_2 \rangle|} \frac{|a_3|}{v_{g3}\omega_3}\right] = \frac{|K|S_1S_2|a_1||a_2|}{v_{g1}v_{g2}\omega_1\omega_2} \qquad (5.E.4)$$

The corrected value of $|q_3|$ is then

$$|q_3^c| = \frac{|\langle \bar{S}_3 \rangle|S_1S_2}{|\langle \bar{S}_1 \rangle||\langle \bar{S}_2 \rangle|} \frac{|a_3|}{v_{g3}\omega_3} \qquad (5.E.5)$$

or

$$|q_3^c| = \frac{|q_3|S_1S_2}{|\langle S_1\rangle||\langle S_2\rangle|} \qquad (5.E.6)$$

This establishes all the data to a given set of power densities for $|q_1|$ and $|q_2|$. With

$$|q_1| = \frac{S_1|a_1|}{v_{g1}\omega_1} \quad , \qquad (5.E.7)$$

and

$$|q_2| = \frac{S_2|a_2|}{v_{g2}\omega_2} \qquad (5.E.8)$$

and $|a_1|$ and $|a_2|$ are taken from Fig. 5.5 and Fig. 5.6 respectively. The (5.E.1) becomes

$$\frac{v_{g1}}{|q_1||q_2|}\ \frac{d|q_3^c|}{dx_1} = |K| \qquad (5.E.9)$$

Fig. 5.12 through 5.17 plot $|q_3^c|$ versus x_1 for experiments A and B. Fig. 5.12 through Fig. 5.15 show the results of experiment-A and Figures 5.16-5.17 illustrate experiment-B. Each graph has a curve visually fitted to the data. The lines tangent to each curve give the slope of the fitted curve to find $\frac{d|q_3^c|}{dx_1}$.

Experiment-A was conducted with the power-switch and thus $|K|$ could be evaluated with different power levels. When the power switch was turned on the input signals passed through a 3 dB pad prior to entering the transducers. The average power densities

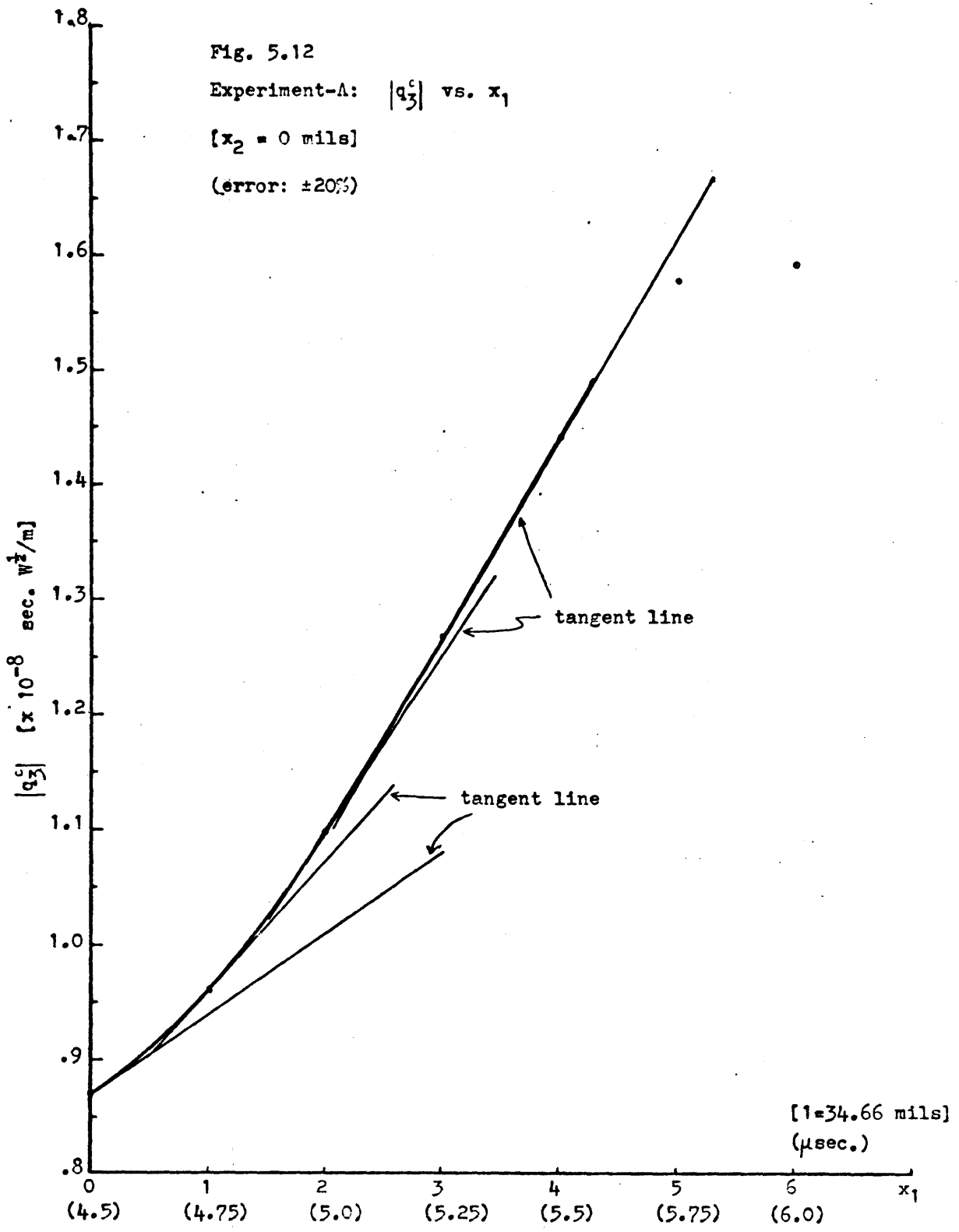
Fig. 5.12
Experiment-A: $|q_{3}^{c}|$ vs. x_1
[x_2 = 0 mils]
(error: ±20%)
1.8
1.7
1.6
1.5
1.4
1.3
1.2
1.1
1.0
.9
.8
$|q_{3}^{c}|$ [x 10^{-8} sec. $W^{\frac{1}{2}}$/m]
tangent line
tangent line
[1=34.66 mils]
(μsec.)
0 (4.5)
1 (4.75)
2 (5.0)
3 (5.25)
4 (5.5)
5 (5.75)
6 (6.0)
x_1

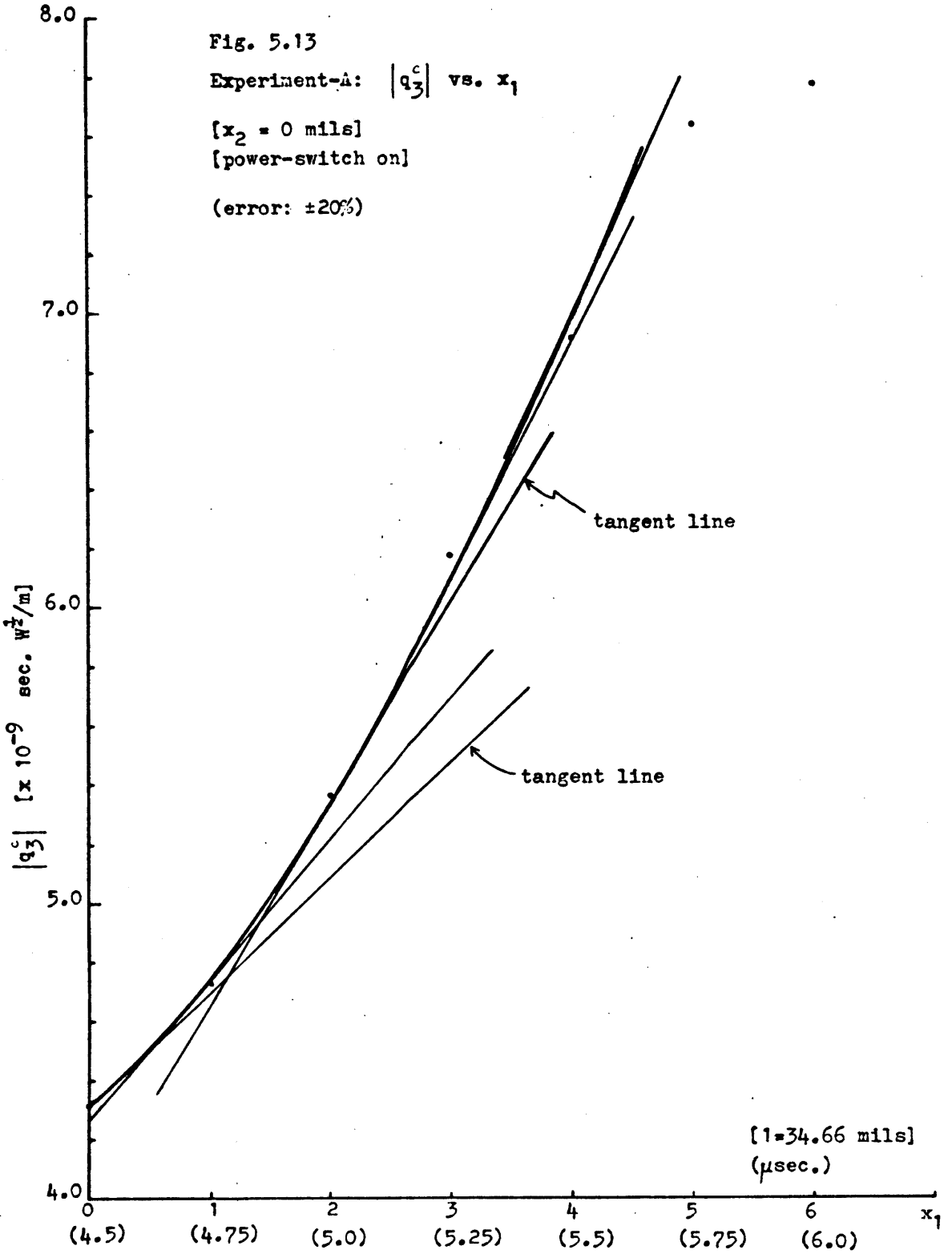

Fig. 5.13

Experiment-A: $|q_3^c|$ vs. x_1

[x_2 = 0 mils]
[power-switch on]

(error: ±20%)

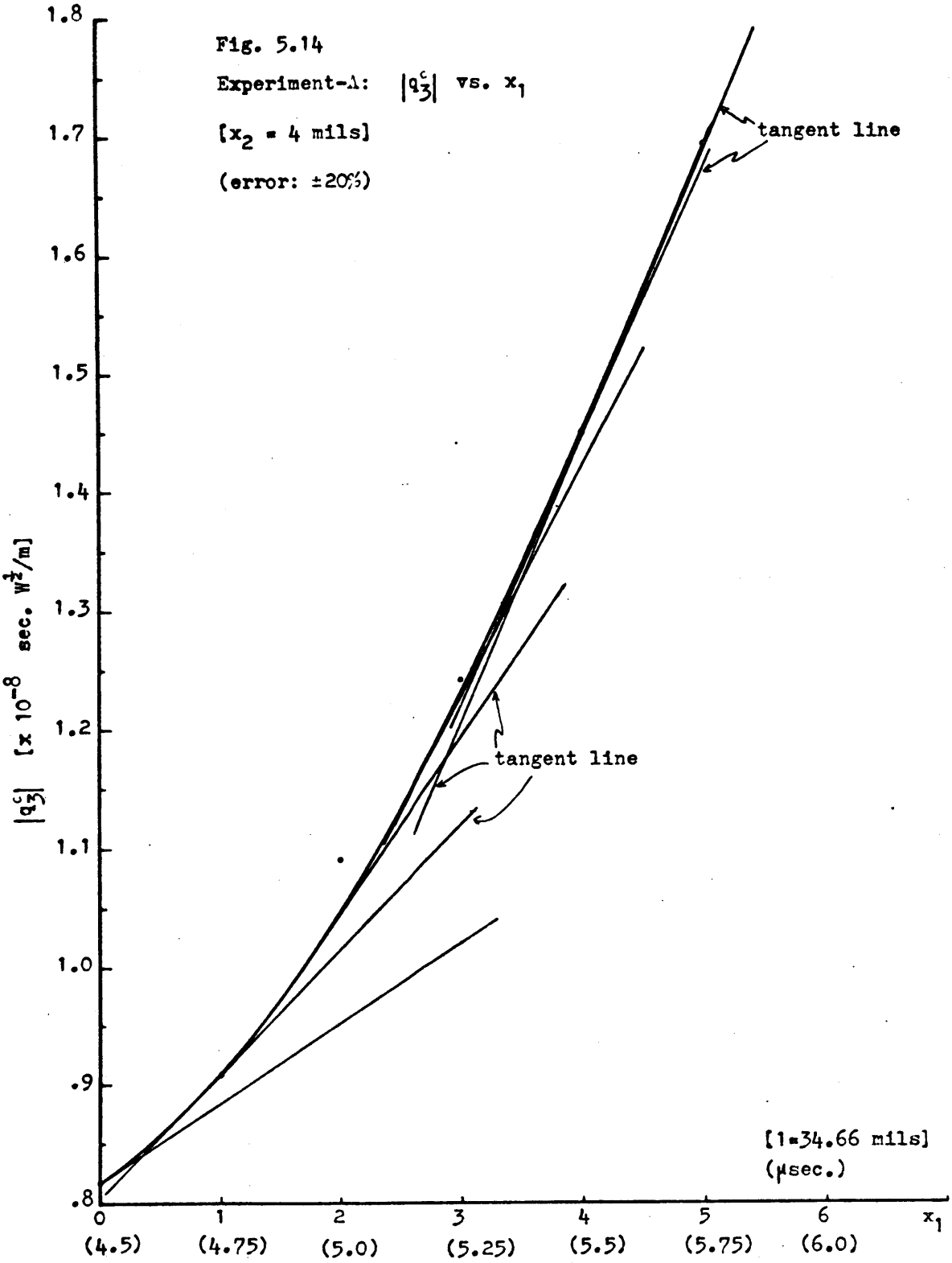
Fig. 5.14
Experiment-A: $|q_3^c|$ vs. x_1
[x_2 = 4 mils]
(error: ±20%)
tangent line
tangent line
$|q_3^c|$ [x 10^{-8} sec. $W^{\frac{1}{2}}$/m]
1.8
1.7
1.6
1.5
1.4
1.3
1.2
1.1
1.0
.9
.8
[1=34.66 mils]
(μsec.)
0 (4.5)
1 (4.75)
2 (5.0)
3 (5.25)
4 (5.5)
5 (5.75)
6 (6.0)
x_1

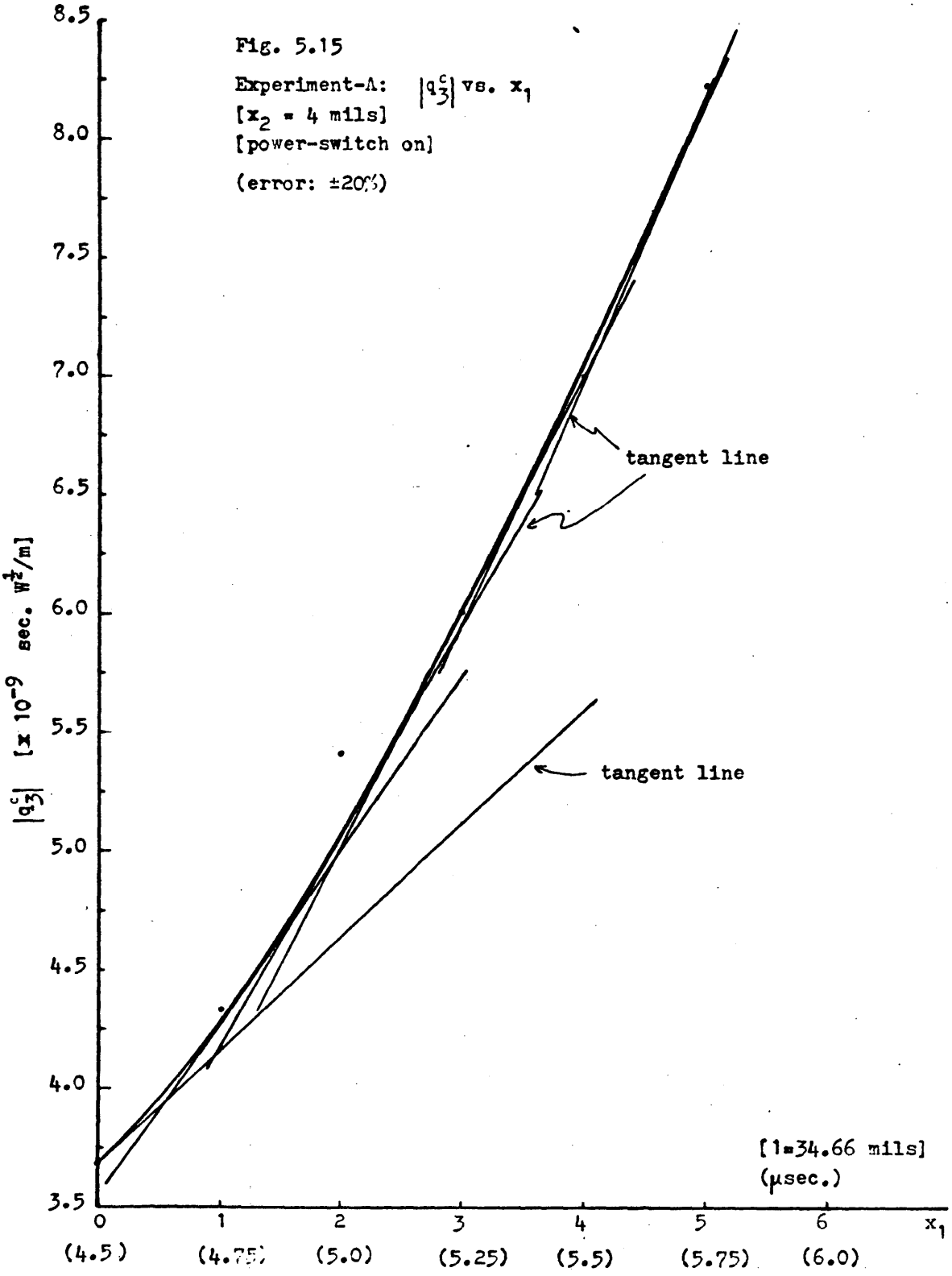

Fig. 5.15

Experiment-A: $|q_3^c|$ vs. x_1

[x_2 = 4 mils]

[power-switch on]

(error: ±20%)

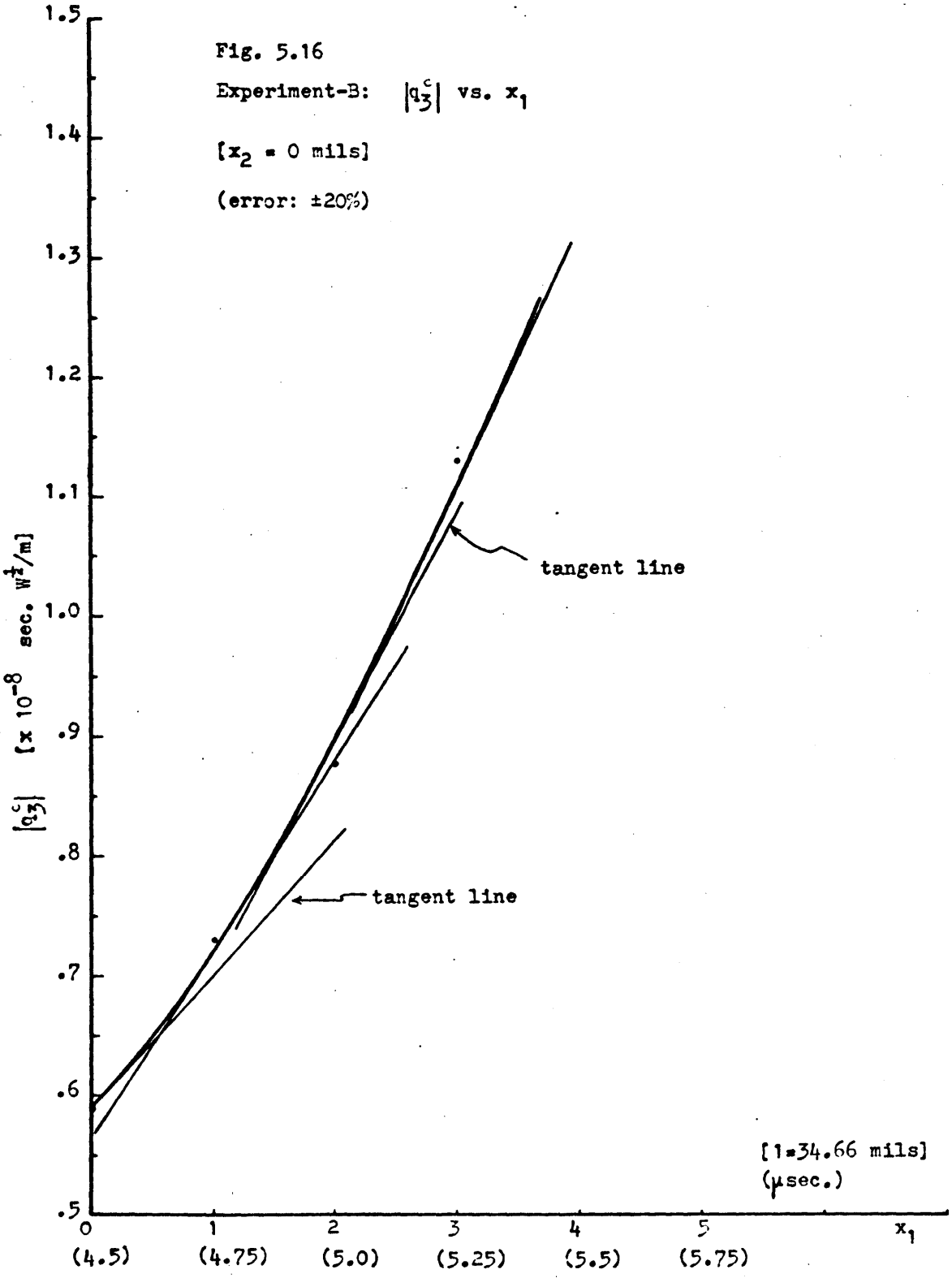

Fig. 5.16

Experiment-B: $|q_{3}^{c}|$ vs. x_1

[x_2 = 0 mils]

(error: ±20%)

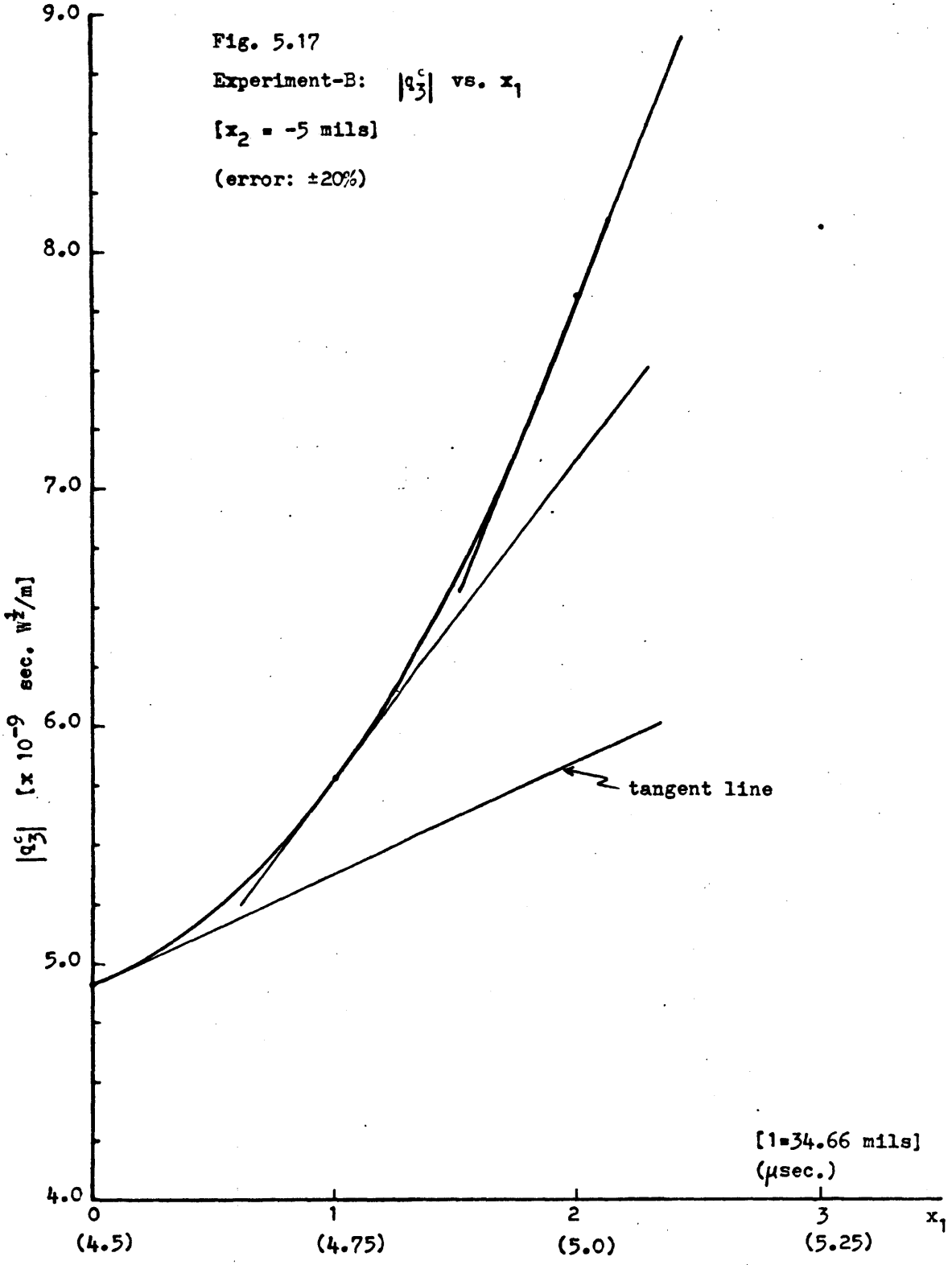

Fig. 5.17

Experiment-B: $|q_3^c|$ vs. x_1

[x_2 = -5 mils]

(error: ±20%)

found for experiment-A were:

1. power switch off: S_1 = 19.9 dBm
   S_2 = 22.4 dBm
2. power switch on: S_1 = 17.0 dBm
   S_2 = 19.6 dBm

Fig. 5.12 and Fig. 5.14 are plots of $|q_3^c|$ versus x_1 with the power-switch off, and Figures 5.13 and 5.15 are graphs for the power-switch on.

Only one set of input power levels were used for experiment-B. The average power densities were

S_1 = 19.9 dBm
S_2 = 22.3 dBm

In addition to calculating $|K|$ for x_2=0, calculations for $|K|$ for $x_2 \neq 0$ mils was also done. Figures 5.14, 5.15, and 5.17 show the graphs for off axis interactions. The data for experiment-A was x_2 = +4 mils, and for experiment-B, x_2 = -5 mils.

For all the graphs the zero for longitudinal position in length units was arbitrarily chosen. The propagation position from the transducers in time is given under the x_1 coordinate. Error on $|q_3|$ is ± 20 percent which is due to the estimated probe tip change between any two contact times and the error of the system response G for that data run as discussed in section C.

After calculating $|K|$ for each x_1 in Figures 5.12 through 5.17, a scatter plot of $|K|$ versus x_1 was made and is shown in Fig. 5.18. $|K|$ for each case determined from Fig. 5.12 through 5.17 is plotted. The horizontal line is the average value of all the $|K|$'s calculated, and the bar on the $|K|$ axis is ± one standard deviation.

The error for each $|K|$ calculated is estimated to be ±50 percent. This error includes a number of factors. Error exists in determining $|q_1|$ and $|q_2|$ as discussed in section C. Further as stated, the curves that are fitted to the results of Figs. 5.12-5.17 can have as much as a ten percent error with a five percent error in drawing the tangent curves, thus giving about ±20 percent error for the slope. These two sources of error plus the error of $|q_3|$ result in a total error on $|K|$ of approximately ±50 percent. This is a very large error for determining $|K|$ and making comparisons for power and position independence.

Rather than examining the $|K|$ based on the error for each $|K|$, one can examine the scattering of the values of $|K|$ statistically. As illustrated in Fig. 5.18, the average values of $|K|$ is $7.9\times10^8 \frac{m}{\sec^2 w^{1/2}}$ with one standard deviation of $2.5\times10^8 \frac{m}{\sec^2 w^{1/2}}$. Thus 23 of the 27 values of $|K|$ fall within ±32 percent of the average value, which is well within the error. Thus $|K|$ can be concluded to power and position independent with

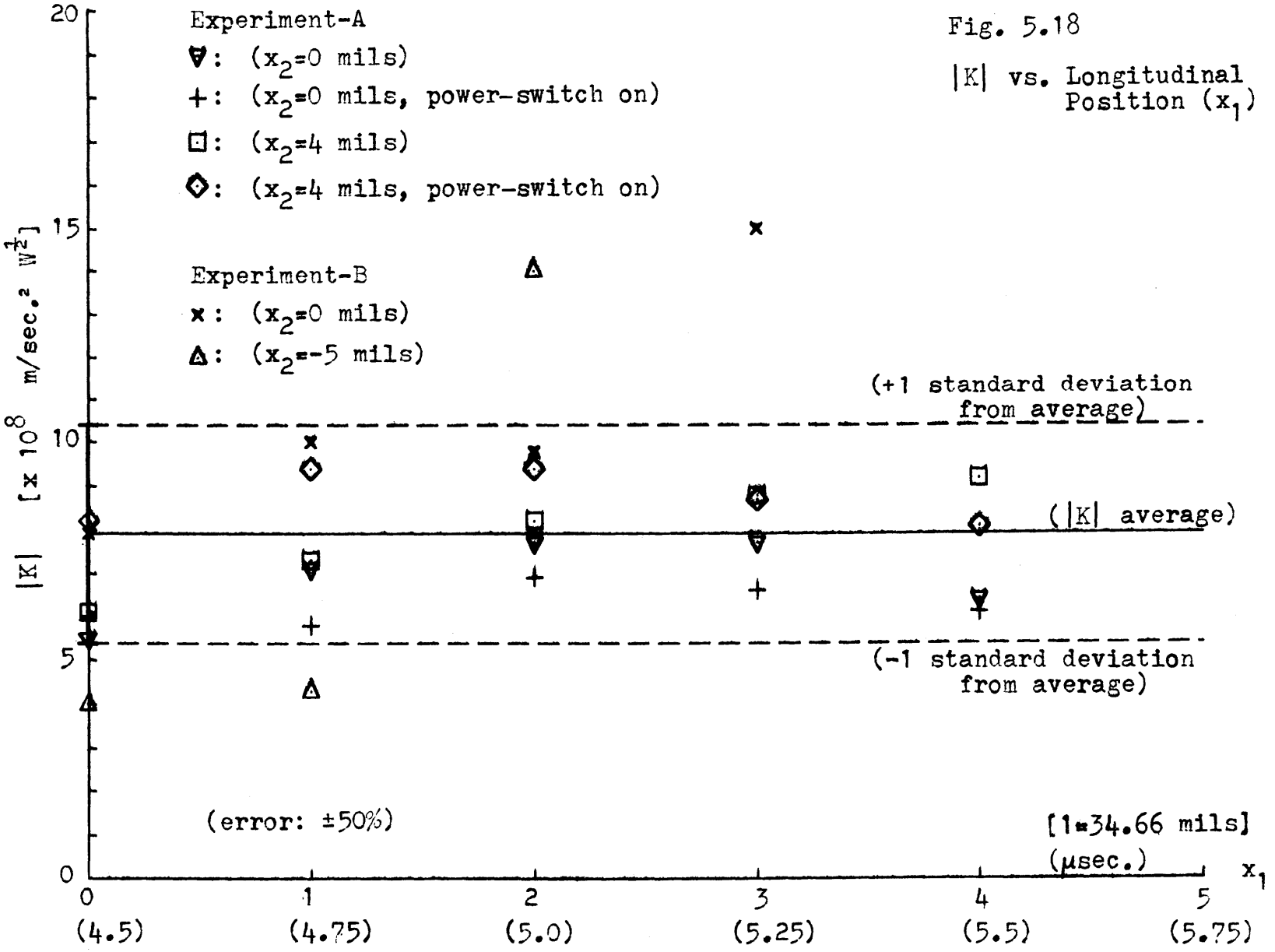

Fig. 5.18

|K| vs. Longitudinal Position (x_1)

$$|K| = 7.9\times10^{8} \frac{m}{sec^{2}w^{1/2}} \pm 4.0\times10^{8} \frac{m}{sec^{2}w^{1/2}} \qquad (5.E.10)$$

as a value for $|K|$ determined by the experiments.

F. Profiles of 250 MHz Wave

Figures 5.19 through 5.26 are normalized profiles of the 250 MHz up-converted wave at different longitudinal positions and are taken parallel to the phase fronts of the wave. The profiles are normalized so that the maximum voltage V is one, and the longitudinal positions are in microseconds starting with 4.5 μsec and ending at 25 μsec from the transducers. Power densities for the two pump waves are the same as those used for experiment-A with the power-switch off.

The horizontal scales of Figs. 5.19-5.21 have the same zero. Figs. 5.22-5.23 were made with data from a different probe tip than was used with the 4.5 μsec-6 μsec profiles, and thus the transverse zero for these figures are the same. An extension was added to the probe for the 15 μsec-25 μsec profiles, and Figs. 5.24-5.26 have the same zero, but different from the other figures.

The profiles are uncalibrated; however, data was randomly retaken at a few transverse positions. Extra data are marked with triangles on the graphs and are referred to a check points. The number in parentheses beside the triangle is the number of contact times between the data used for the profile and the check point. This gives an indication as to the consistency of the probe and thus accuracy

Fig. 5.19

Normalized Profile
250 MH_z Wave [4.5 μsec.]

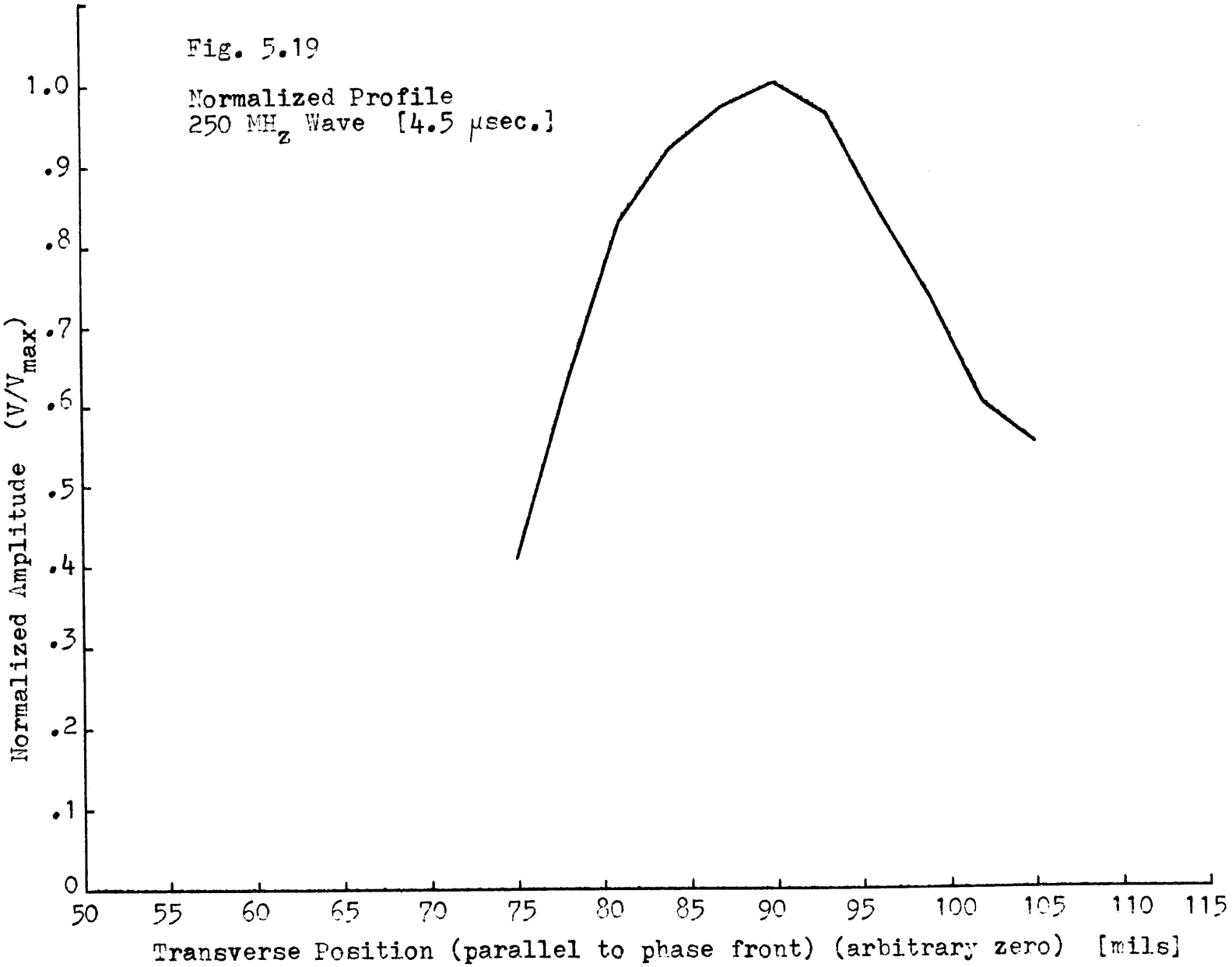

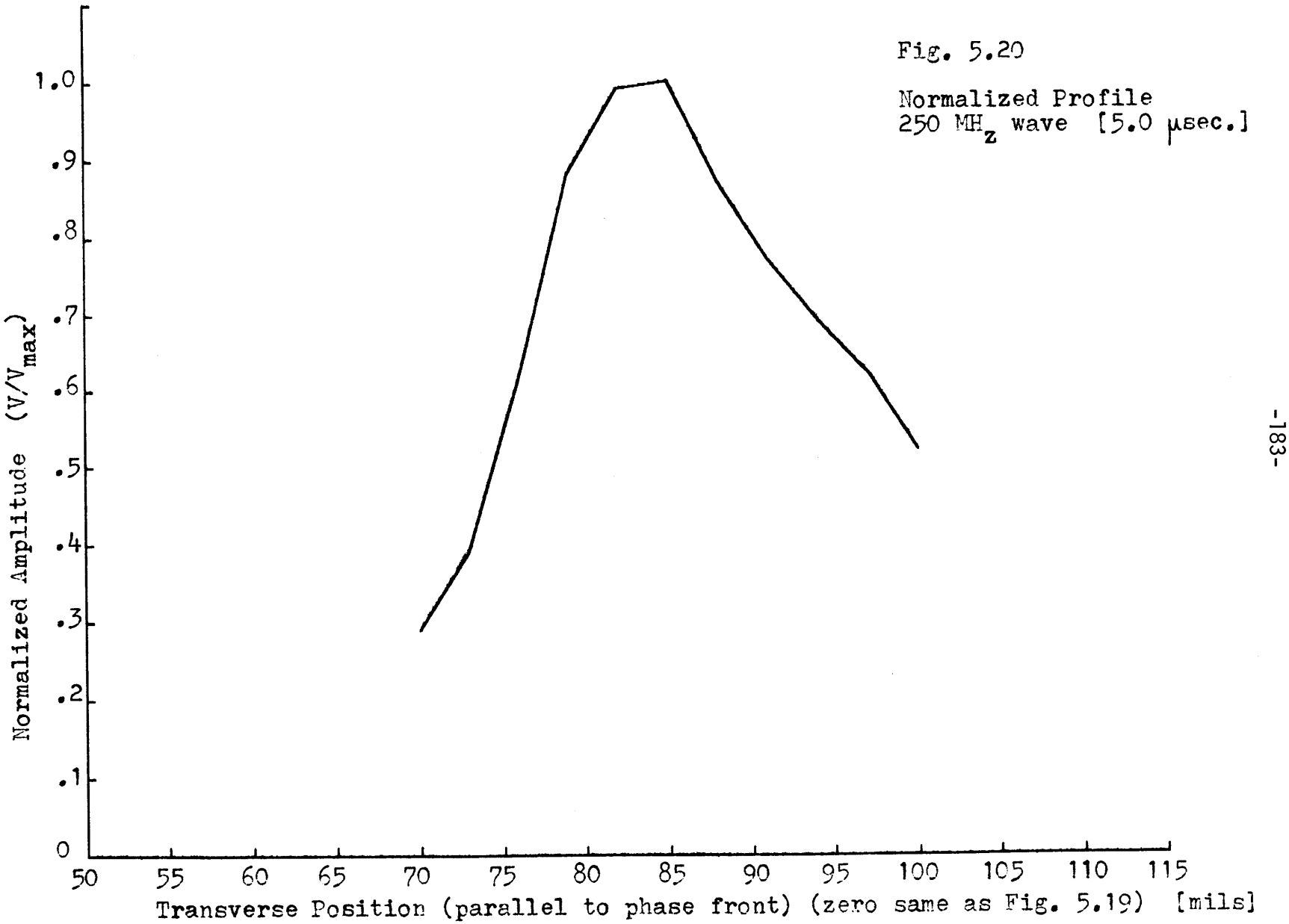

Fig. 5.20

Normalized Profile
250 MH$_z$ wave [5.0 μsec.]

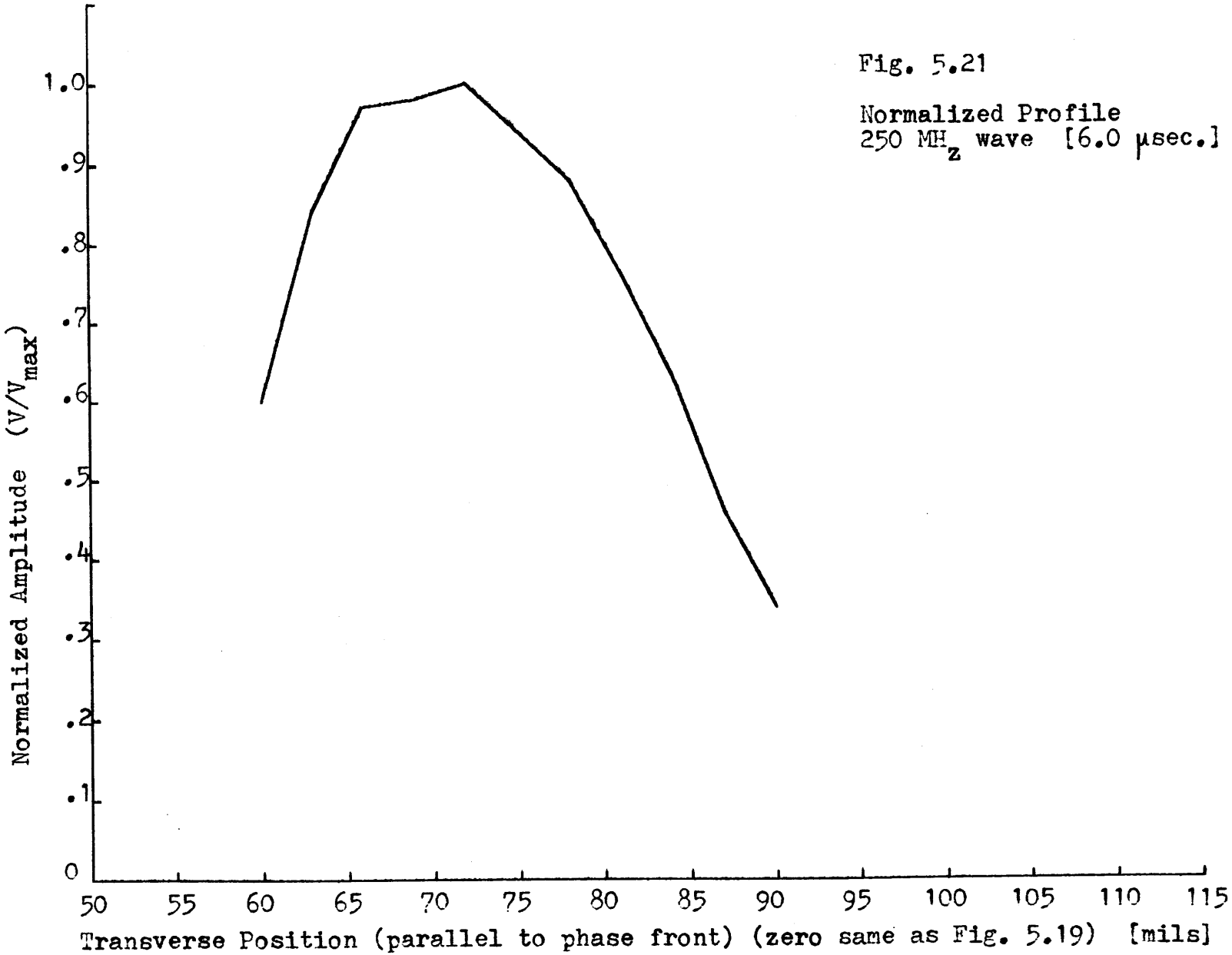

Fig. 5.21

Normalized Profile
250 MH$_z$ wave [6.0 μsec.]

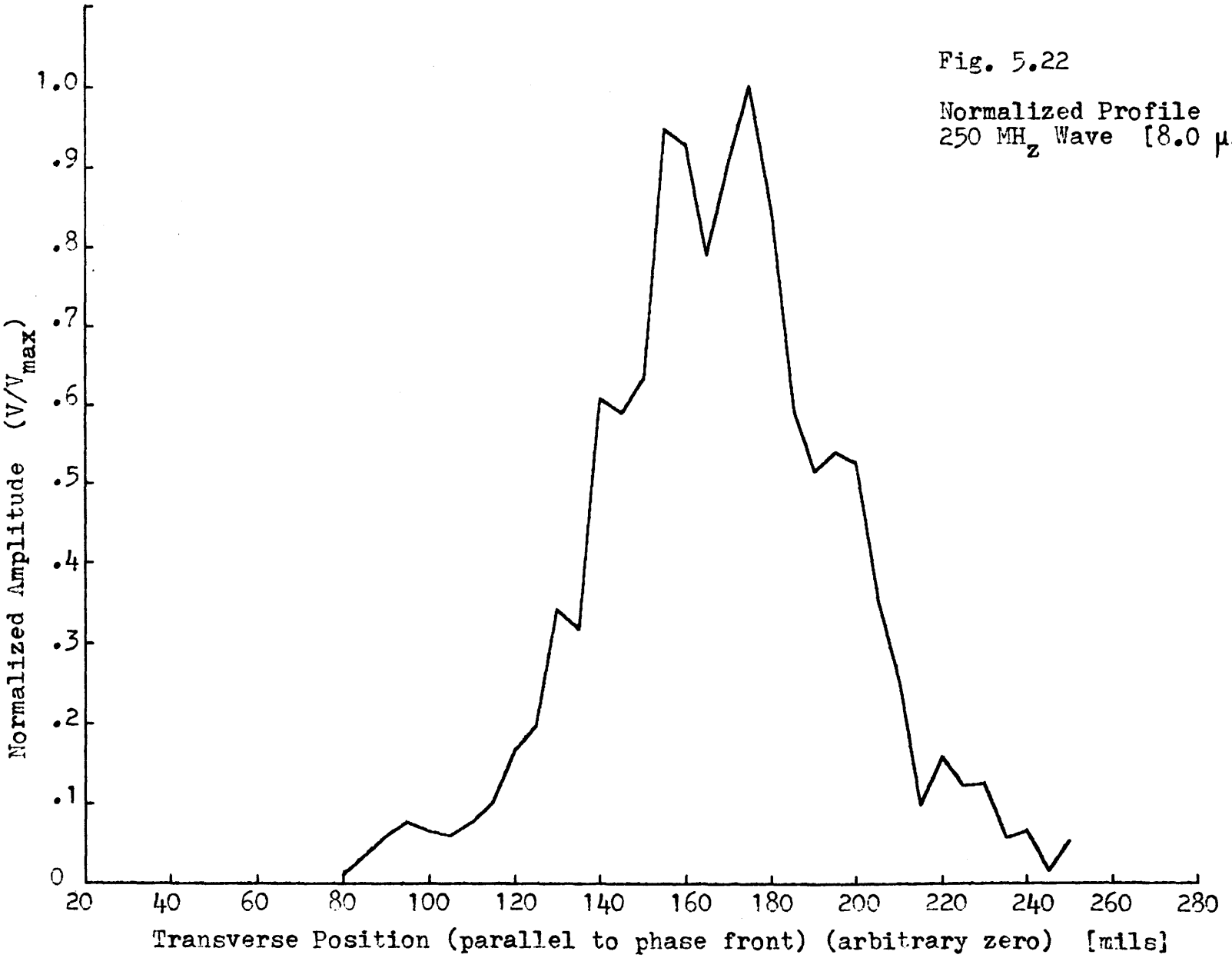

Fig. 5.22

Normalized Profile
250 MH$_z$ Wave [8.0 μsec.]

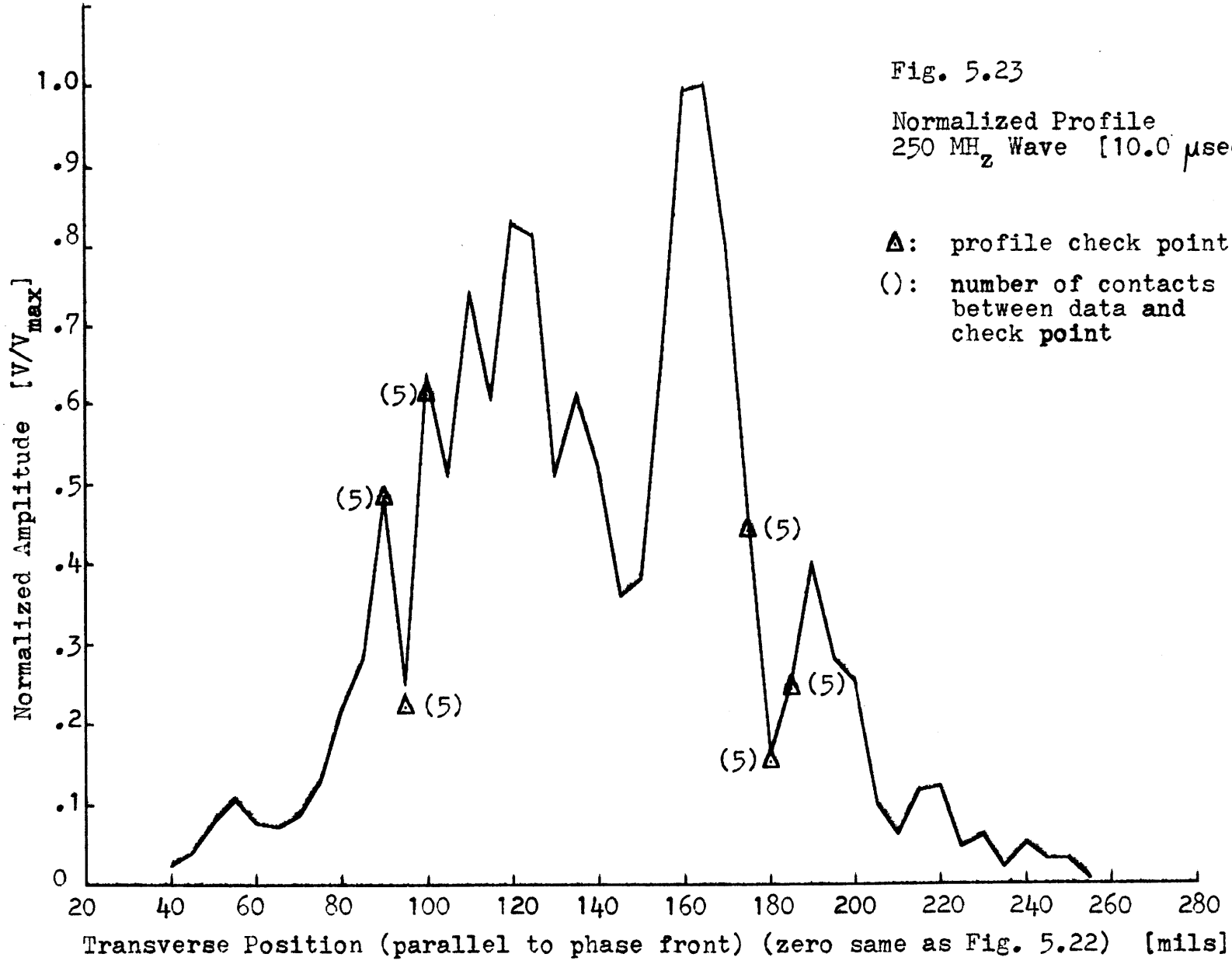

Fig. 5.23

Normalized Profile
250 MH_z Wave [10.0 μsec.]

Δ: profile check point

(): number of contacts between data and check point

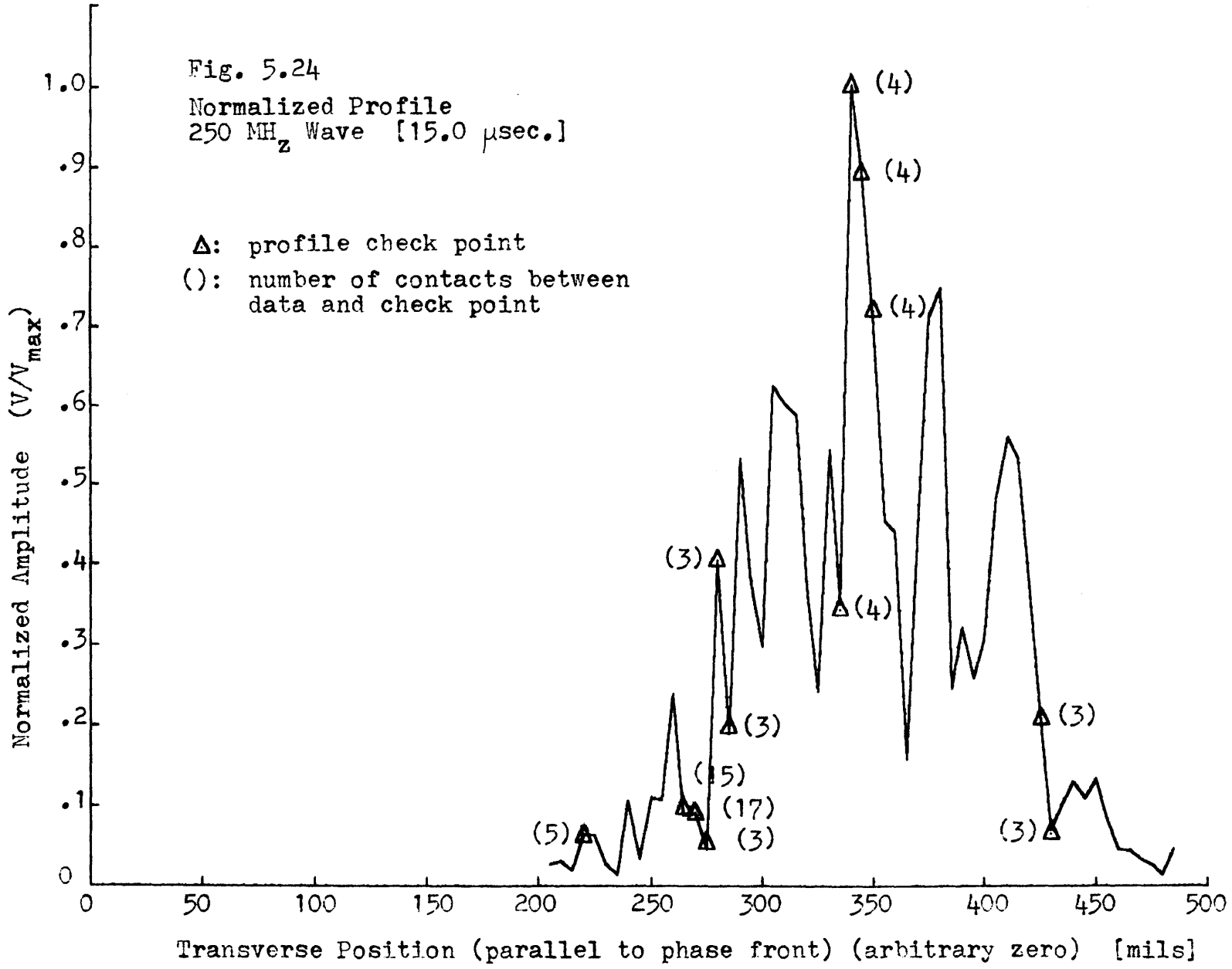
Fig. 5.24
Normalized Profile
250 MH$_z$ Wave [15.0 μsec.]
Δ: profile check point
(): number of contacts between data and check point
Normalized Amplitude (V/V$_{max}$)
1.0
.9
.8
.7
.6
.5
.4
.3
.2
.1
0
0
50
100
150
200
250
300
350
400
450
500
Transverse Position (parallel to phase front) (arbitrary zero) [mils]
(4)
(4)
(4)
(4)
(3)
(4)
(3)
(3)
(5)
(15)
(17)
(3)
(3)

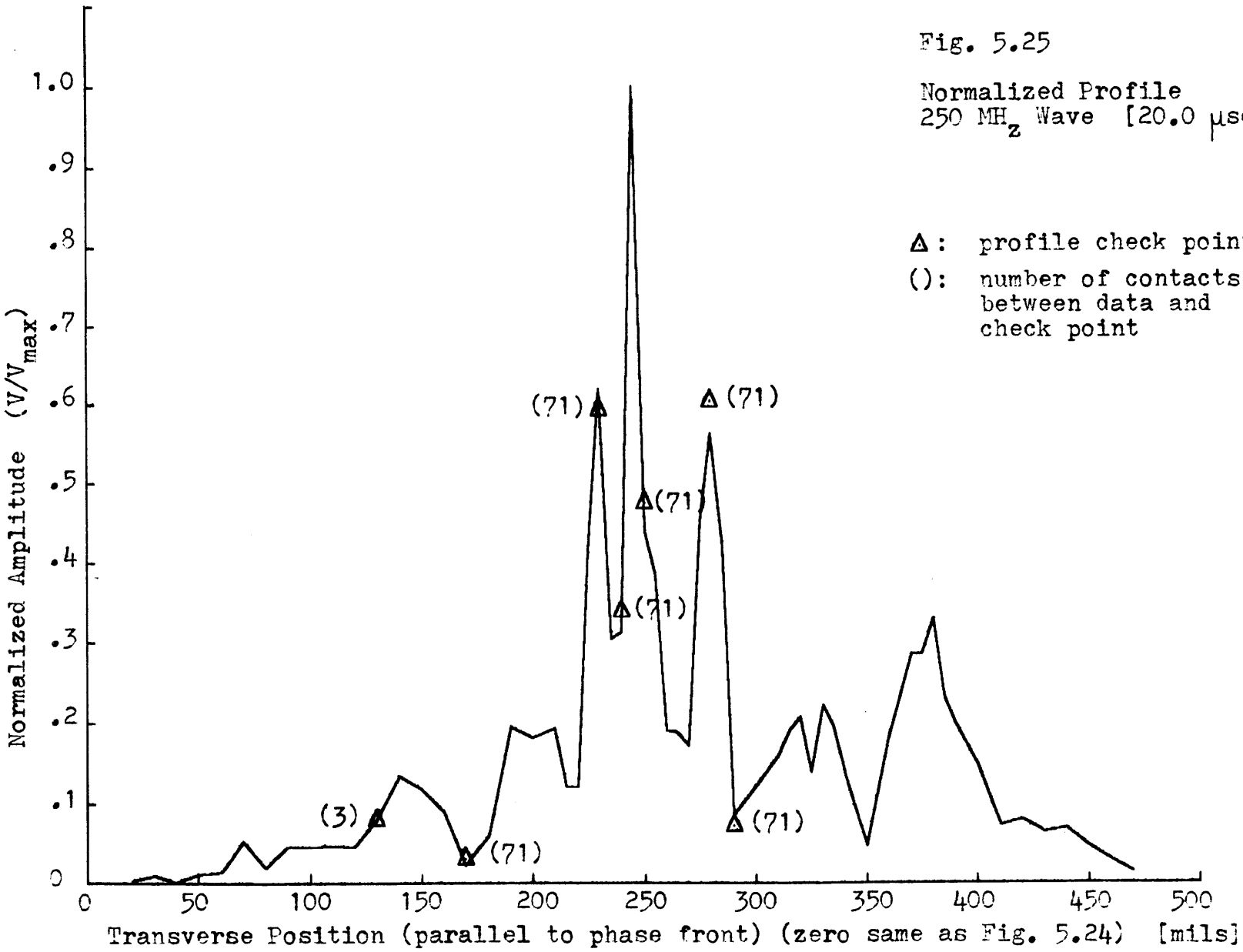

Fig. 5.25

Normalized Profile
250 MH$_z$ Wave [20.0 μsec.]

Δ: profile check point

(): number of contacts between data and check point

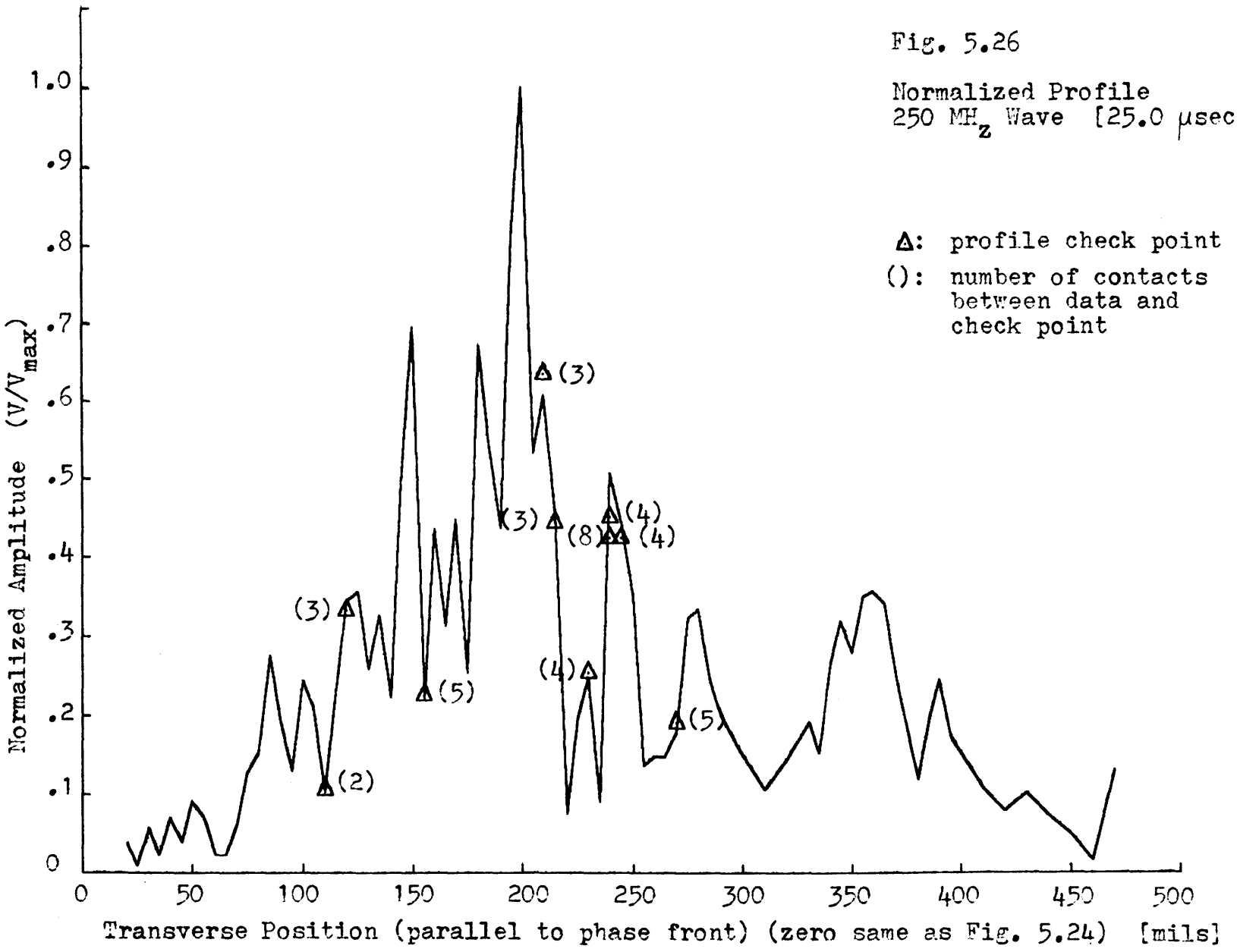

Fig. 5.26

Normalized Profile
250 MH_z Wave [25.0 μsec.]

Δ: profile check point

(): number of contacts between data and check point

of the profiles.

As can be seen from the figures, the nonlinear interaction plus diffraction result in a complicated profile that would be difficult to analyze theoretically. The primary significance of this section is to illustrate the complexity of the three-wave interaction of noncollinear surface acoustic waves.

As a comparison with the 250 MHz up-converted wave, Fig. 5.27 illustrates the profiles of the pump waves. Fig. 5.27a is the 214 MHz wave profile and Fig. 5.27b is the 36 MHz pump profile. Longitudinal positions are in microseconds from the transducers starting with 1 μsec and ending at 25 μsec. The profiles shown are the profile and its reflection in a mirror plane perpendicular to the plane of the paper and containing the horizontal axis of the oscilloscope graticule. The oscilloscope was used to display the profiles obtained as described in reference [51]. The profiles are amplitudes of arbitrary units and no amplitude relationship exists among them. For the 36 MHz wave profiles, the horizontal axes have the same zero, but there is no common zero for the 214 MHz wave profiles.

Fig. 5.27

PROFILES OF 214 MHz AND 36 MHz WAVES

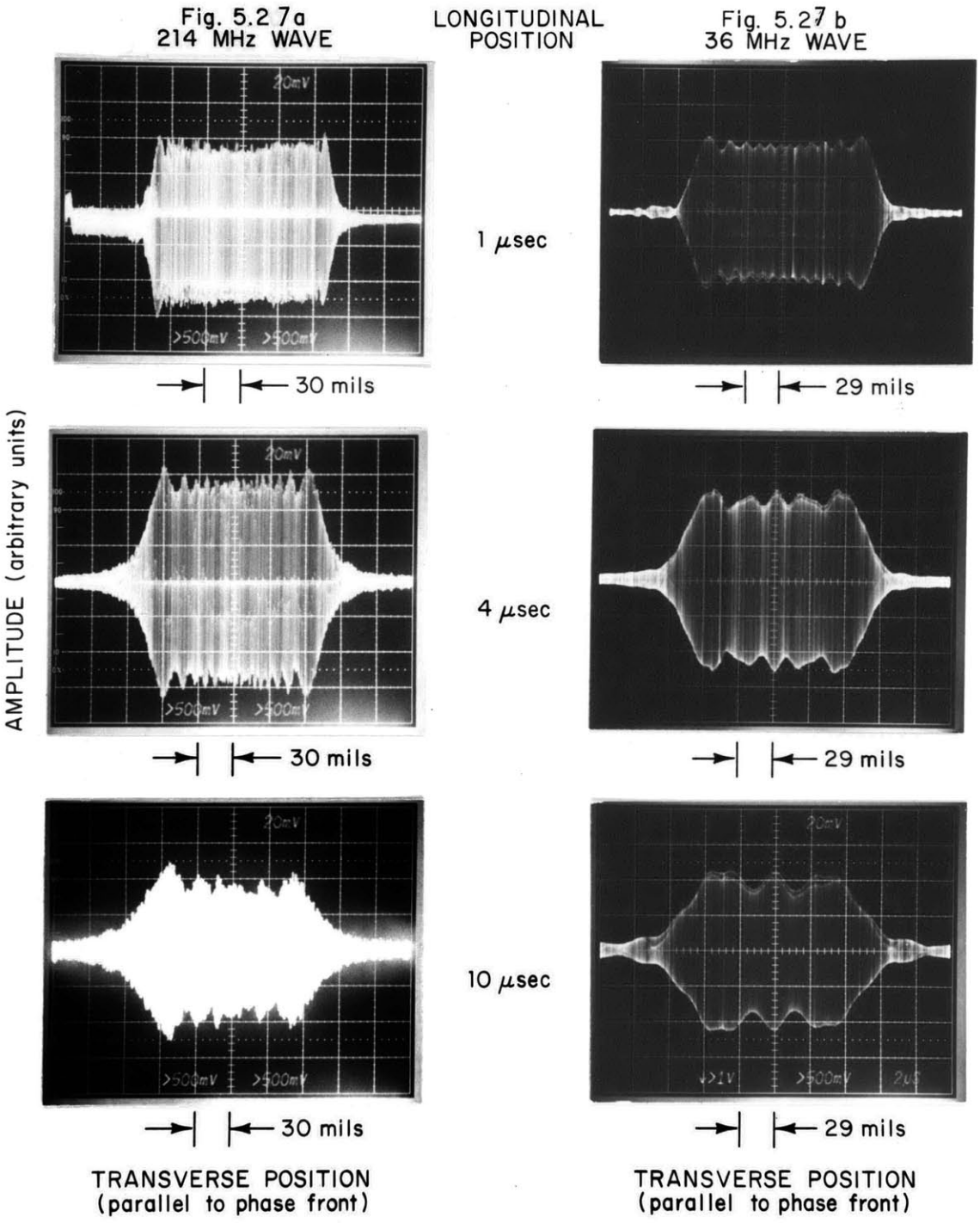

Fig. 5.27a (cont.)
214 MHz WAVE

LONGITUDINAL POSITION

Fig. 5.27b (cont.)
36 MHz WAVE

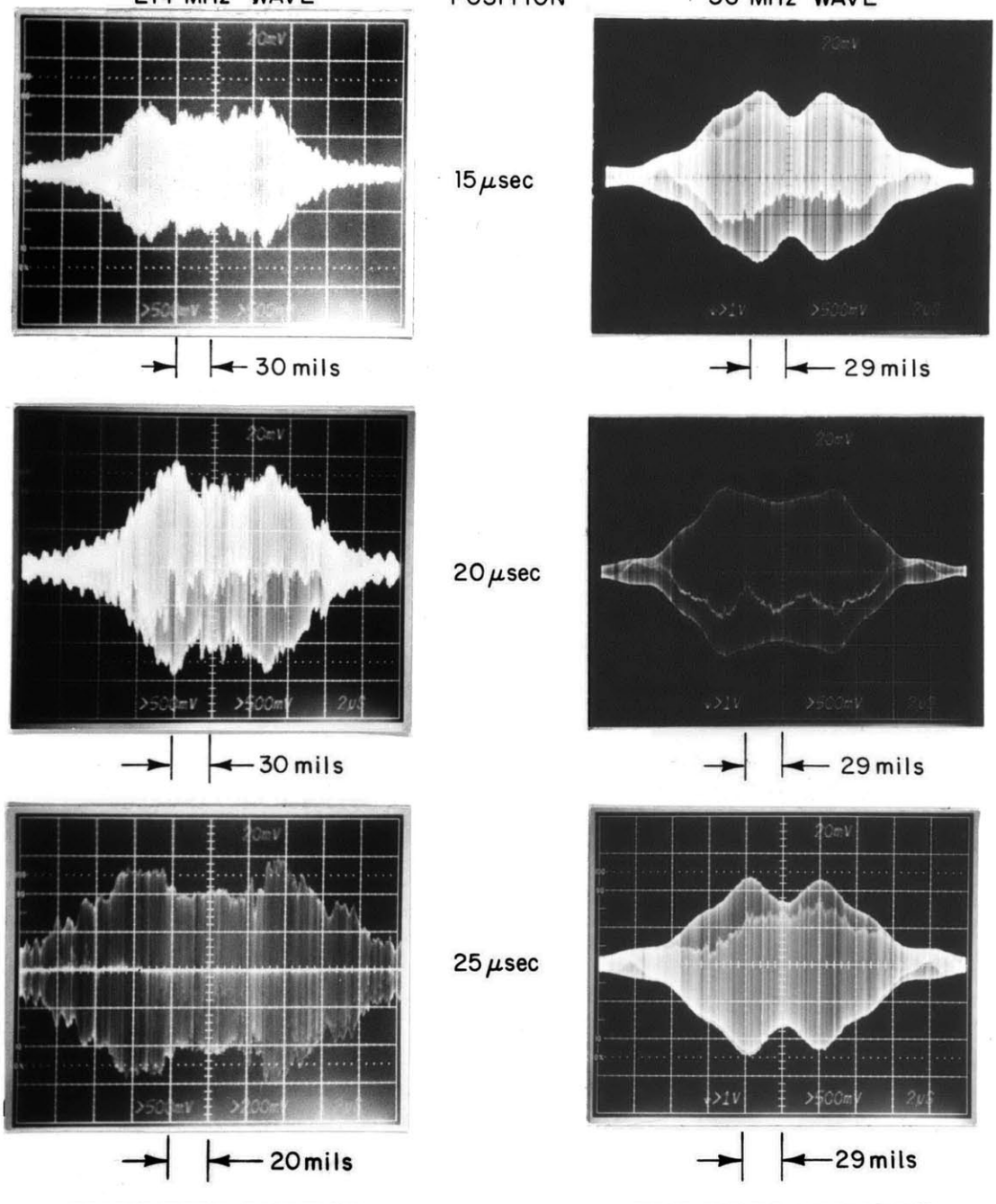

CHAPTER 6

CONCLUDING DISCUSSION

A. Review

Coupled mode theory has been used to model nonlinear interactions of surface acoustic waves, and the results have shown that this approach is successful in describing the interactions. Early theory was inconsistent, incomplete, or incorrect in developing the coupled amplitude equations for coupled mode theory. The theoretical results were accurate partly because the experiments conformed to the assumptions of the derivations of the coupled amplitude equations. However, understanding of the results of experiments and models is unsatisfactory as previously discussed.

Because of the problems associated with past work, a general coupled amplitude equation was developed from coupled mode theory. The derivation of the equation is consistent with the assumptions of coupled mode theory and the characteristics of surface acoustic waves. Further, it is useful in describing both linear and nonlinear interactions of surface waves. With the development of the general equation, a specific application was made to nonlinear interactions.

The nonlinear material constants, as defined from the electric Gibbs function, provide the nonlinearities that generate the external current and force densities that perturb normal mode propagation. Complex forms of these external sources provide the mathematical description used by the coupled amplitude equation. As a result of

normalization to action density, the coupling constants of the normalized amplitude equations are found to be independent of power and frequency dependent. The coupling constants can be computed from normalized field quantities that are universal for a given material cut and propagation direction of the interacting waves. Further, relations among the coupling constants can be found for resonant or near resonant conditions.

Upon applying the nonlinear coupled mode theory to experimental results of harmonic generation, several characteristics of the theory were validated and qualities of the experiment explained. Experiment showed the coupling constants were independent of power and dependent upon frequency as predicted. Because of phase-locking due to experimental procedure for harmonic generation, it was shown that the successful results of the energy cross-section approach was a fortunate consequence. With a slightly nonresonant, phase-mismatched case for $LiNbO_3$, the experimental and theoretical results could be explained from the nonlinear coupled mode theory developed here. The attempt at calculating the coupling constant resulted only in order of magnitude agreement with

a. $|K|$ experimental: $1.1 \times 10^9 \frac{m}{sec^2 W^{1/2}}$

b. $|K|$ theoretical: $5.5 \times 10^8 \frac{m}{sec^2 W^{1/2}}$

the difference between the two magnitudes is most likely due to the

use of only one source of nonlinearity and incomplete knowledge of the nonlinear material constants.

The wealth of information on collinear interactions, and the lack of measurements for find the coupling constants for noncollinear interactions, led to an experiment to find the coupling constants. The experiment gave a value for the magnitude of the coupling constant and indicated that it was power and position independent. However, the result had a ±50 percent error due to the electrostatic probe used in the experiment and the experimental technique.

The above discussion is a synopsis of the past four chapters. The conclusion is that coupled mode theory as developed here is an accurate description of weak nonlinear interaction due to the nonlinear properties of the materials that support surface acoustic waves.

B. Future Work

Theoretical predictions of coupling constants for piezoelectric materials need to be pursued. However, work in this direction is stymied until better measurements of the nonlinear material constants have been made. Thus the accurate calculation of the coupling constants must wait until the experimental work in determining nonlinear material constants is done. Therefore rather than continuing to pursue experiments of harmonic generation and noncollinear interactions on piezoelectric materials, the coupled mode description would be enhanced if the nonlinear material constants were known. Hence experimental work in determining these material constants should

have priority.

In regard to noncollinear interactions, improved experimental procedures need to be developed for measuring the interaction. Because of the varying sensitivity of the electrostatic probe as it presently exists data will continue to have large error. Therefore a new probe designed to be calibrated and constant in sensitivity needs to be built. Suggestions to accomplish this are replacing the tungsten tip with a minute transducer, or enclosing the tip in a protective coating that would not wear or scratch a crystal's surface. Another possibility is to extend the use of the laser optical probe applied to collinear work. This would require understanding the scattering of light from a surface distorted in two dimensions. With an improved probe the errors associated with the present electrostatic probe will be reduced and the statistical calibration procedure eliminated.

With respect to the use of surface wave profiles in calculating coupling constants several improvements can be made. Profiles of the pump waves should be made at each longitudinal position so that $|q_1|$ and $|q_2|$ are more closely determined than assuming a constant trapezoidal shape. These profiles could be taken with an optical probe thus increasing the accuracy over the electrostatic probe. If a sufficient number of profiles are taken, a point by point numerical integration of coupled mode equations could be performed to determine the extent diffraction modifies the nonlinear interactions.

This discussion gives a few of the most obvious improvements that

could be made to experiments to increase accuracy and reliability. The single most important change is an improved probe. Varying tungsten tips are a constant and the largest source of error. Because of the point-by-point technique for data taking and at times rapid changes of probe sensitivity, many hours of work for a few data-runs were needed and the experiments could be a frustrating experience.

Tests on the coupled mode theory should be extended for non-collinear interactions. Only one set of frequencies and propagation directions were explored, and this was done only with y-cut $LiNbO_3$. Thus further work is needed to determine frequency dependence of the coupling constant, the variation of the coupling constant with different propagation directions of the interacting SAW and with other materials to examine the properties of $|K|$ in these media.

Nonlinear interactions as performed here were weak, to which the approximation of constant pumps could be applied. The experiments should be extended so that pumps deplete during the interaction. This would entail considering all possible surface waves generated by the nonlinearities including collinear harmonic generation and the mixing of harmonics of one pump wave with another. Another possibility is to launch three waves of comparable power densities and examine the interaction which implies that phase-locking does not occur.

An interesting variation on the noncollinear experiments would be to add a thin film to the surface of the crystal. This would cause dephasing of the harmonic generation interactions, and a resonant parametric noncollinear interaction could be sought. With the

harmonic interactions nonresonant, the resonant noncollinear interaction would be the dominant nonlinear interaction and strong noncollinear interactions could be investigated.

REFERENCES

1. R.N. Thurston and K. Brugger, "Third-Order Elastic Constants and the Velocity of Small Amplitude Elastic Waves in Homogeneously Stressed Media", Physical Review, Vol. 133, No. 6A, 16 March 1964, pp. A1604-A1610.

2. K. Brugger, "Determination of Third-Order Elastic Coefficients in Crystals," Jour. of Appl. Phys., Vol. 36, No. 3, March 1965, pp. 768-773.

3. B.E. Powell and M.J. Skove, "Relation Between Isothermal and Mixed Third-Order Elastic Constants," Jour. of Appl. Phys., Vol. 38, No. 1, Jan. 1966, pp. 404-405.

4. M.J. Skove and B.E. Powell, "Symmetry of Mixed Third-Order Elastic Constants," Jour. of Appl. Phys., Vol. 38, Jan. 1966, p. 404.

5. S.S. Sekoyan, "Calculation of the Third-Order Elastic Constants from the Results of Ultrasonic Measurements," Sov. Phys.-Acoust., Vol. 16, No. 3, Jan.-March 1971, pp. 377-380.

6. S.S. Sekoyan, "Thurston-Brugger Equations for Cubic Crystals," Sov. Phys.-Acoust., Vol. 21, No. 2, March-April 1975, pp. 163-165.

7. E.A. Kraut, T.C. Lim, B.R. Tittman, "Application of Nonlinear Interactions in Ferroelectric Ceramics to Microwave Signal Processing," IEEE Trans. on Sonics and Ultrasonics, SU-19, No. 2, April 1972, pp. 247-255.

8. V.E. Ljamov, "Nonlinear Acoustical Parameters of Piezoelectric Crystals," Jour. Acous. Soc. of Amer., Vol. 52, No. 1 (part 2), 1972, pp. 199-202.

9. Y. Nakagawa, K. Yamanouchi, and K. Shibayama, "Third-Order Elastic Constants of Lithium Niobate," Jour. of Appl. Phys., Vol. 44, No. 9, Sept. 1973, pp. 3969-3973.

10. A.I. Korobov and V.E. Lyamov, "Nonlinear Piezoelectric Coefficients of $LiNbO_3$," Sov. Phys. Solid State, Vol. 17, No. 5, pp. 932-933.

11. R.A. Graham, "Linear and Nonlinear Piezoelectric Constants of Quartz, Lithium Niobate, and Lithium Tantalate," Satellite Symposium of the 8th International Congress on Acoustics on Microwave Acoustics, 31 July-2 Aug. 1974, European Phys.

Soc., Inst. Phys., Inst. Acoustics, Royal Soc., Lancaster England, Univ. Lancaster, 1974, pp. 124-129.

12. R.A. Graham, "Second- and Third-Order Piezoelectric Stress Constants of Lithium Niobate as Determined by the Impact-Loading Technique," Jour. of Appl. Phys., Vol. 48, No. 6, June 1977, pp. 2153-2163.

13. N.S. Shiren, "Ultrasonic Traveling-Wave Parametric Amplification," Proceedings of IEEE, Vol. 53, No. 10, Oct. 1965, pp. 1540-1546.

14. C.F. Quate and R.B. Thompson, "Convolution and Correlation in Real-Time with Nonlinear Acoustics," Appl. Phys. Lett., Vol. 16, No. 12, 16 June 1970, pp. 494-496.

15. R.B. Thompson and C.F. Quate, "Nonlinear Interactions of Microwave Electric Fields and Sound in $LiNbO_3$," Jour. of Appl. Phys., Vol. 42, No. 3, 1 March 1971, pp. 907-919.

16. L.O. Svaasand, "Interaction Between Elastic Surface Waves in Piezoelectric Materials," Appl. Phys. Lett., Vol. 15, No. 9, 1 Nov. 1969, pp. 300-302.

17. L.O. Svaasand, Interaction Between Elastic Waves and Electric Fields in Dielectrics, The University of Trondheim - The Norwegian Institute of Technology, ELAB report STF44 A7415.

18. M. Luukkala and G.S. Kino, "Convolution and Time Inversion Using Parametric Interactions of Acoustic Surface Waves," Appl. Phys. Lett., Vol. 18, No. 9, 1 May 1971, pp. 393-394.

19. M. Luukkala and J. Surakka, "Acoustic Convolution and Correlation and the Associated Nonlinearity Parameters in $LiNbO_3$," Jour. of Appl. Phys., Vol. 43, No. 6, June 1972, pp. 2510-2518.

20. W.C. Wang, "Convolution of Waves in a Structure of Semiconductor on $LiNbO_3$," Appl. Phys. Lett., Vol. 20, No. 10, 15 May 1972, pp. 389-392.

21. A. Bers and J.H. Cafarella, "Surface Wave Correlator Convolver with Memory," 1974 Ultrasonics Symposium Proceedings, IEEE Cat #74 CHO 896-1SU, pp. 778-786.

22. Ph.Defranould and C. Maerfeld, "Acoustic Convolver Using Multistrip Beamwidth Compressors", 1974 Ultrasonics Symposium Proceedings, IEEE Cat. #74 CHO 896-1SU, pp. 224-227.

23. T.C. Lim, E.A. Kraut, and R.B. Thompson, "Nonlinear Materials for Acoustic-Surface-Wave Convolver," Appl. Phys. Lett., Vol. 20, No. 3, 1 February 1972, pp. 127-129.

24. P.O. Lopen, "Second-Harmonic Generation in an Elastic Surface Wave in α-Quartz," Jour. of Appl. Phys., Vol. 39, No. 12, Nov. 1968, pp. 5400-5404.

25. E.G. Lean, C.C. Tsang, and C.G. Powell, "Optical Probing of Acoustic-Surface-Wave Harmonic Generation," Appl. Phys. Lett., Vol. 16, No. 1, 1 Jan. 1970, pp. 32-35.

26. A.J. Slobodnik, Jr., "Nonlinear Effects in Microwave Acoustic $LiNbO_3$ Surface-Wave Delay Lines", Jour. Acous. Soc. of Amer., Vol. 48, No. 1 (part 2), 1970, pp. 203-210.

27. Y. Nakagawa, K. Yamanouchi, and K. Shibayama, "Nonlinear Effects in Acoustic Surface Waves," Electronics and Communications in Japan, Vol. 55-A, No. 10, 1972, pp. 1-7.

28. E.L. Adler, E. Bridoux, G. Coussot, and E. Dieulesaint, "Harmonic Generation of Acoustic Surface Waves in $Bi_{12}GeO_3$ and $LiNbO_3$," IEEE Trans. on Sonics and Ultrasonics, Vol. SU-20, No. 1, Jan. 1973, pp. 13-16.

29. E.L. Adler and A.A. Nasser, "Effect of Dispersion on Harmonic Generation of Acoustic Surface Waves," 1973 Ultrasonics Symposium Proceedings, IEEE Cat. #74 CHO 807-8SU, pp. 268-270.

30. E.G. Lean and C.C. Tsang, "Nonlinear Effects in Surface Acoustic Waves," Jour. of Appl. Phys., Vol. 41, No. 10, Sept. 1970, pp. 3912-3917.

31. E.G. Lean, Surface Waves in Solids, D.D.C. Defense Supply Agency, Accession number U106302A.

32. P.J. Vella, T.C. Padmore, G.I. Stegeman, and V.M. Ristic, "Nonlinear Surface-Wave Interactions: Parametric Mixing and Harmonic Generation," Jour. of Appl. Phys., Vol. 45, No. 5, May 1974, pp. 1993-2006.

33. P.J. Vella, G.I. Stegeman, and V.M. Ristic, "Surface-Wave Harmonic Generation on Y-Z, X-Z, and 41$\frac{1}{2}$-X Lithium Niobate," Jour. of Appl. Phys., Vol. 48, No. 1, Jan. 1977, pp. 82-85.

34. A. Alippi, A. Palma, L. Palmieri, and G. Socino, "Determination of Coupling Coefficient in Second Harmonic Generation of Acoustic Surface Waves," Jour. of Appl. Phys., Vol. 45, No. 10, Oct. 1974, pp. 4347-4349.

35. A. Alippi, A. Palma, L. Palmieri, and G. Socino, "Phase and Amplitude Relations Between Fundamental and Second Harmonic Acoustic Surface Waves on SiO_2 and $LiNbO_3$," Jour. of Appl. Phys., Vol. 48, No. 6, June 1977, pp. 2182-2190.

36. P.H. Carr, "Mixing of Noncollinear Elastic Surface Waves," Jour. of Appl. Phys., Vol. 42, No. 13, Dec. 1971, pp. 5330-5332.

37. K.L. Davis and V.L. Newhouse, "Mixing Between Noncollinear Surface Elastic Waves," IEEE Trans. on Sonics and Ultrasonics, SU-22, No. 1, Jan. 1975, pp. 33-38.

38. V.L. Newhouse, C.L. Chen, and K.L. Davis, "Possibility of Switching and Stearing Surface Waves by Nonlinear Mixing in Anisotropic Media," Jour. of Appl. Phys.

39. K.L. Davis, Mixing Between Non-Collinear Surface Waves, TR-EE 73-78, Nov. 1973, School of Electrical Engineering, Purdue University.

40. K.L. Davis and V.L. Newhouse, "Steering Acoustic Waves by Nonlinear Mixing," Appl. Phys. Lett., Vol. 21, No. 7, Oct. 1972, pp. 323-325.

41. R.C. Ho and C.L. Chen, "Nonlinear Interaction Between Noncollinear Saw Beams," 1974 Ultrasonics Symposium Proceedings, IEEE Cat. #74 CHO 896-1SU, pp. 232-235.

42. T.C. Padmore and G.I. Stegeman, "Surface-Wave Nonlinearities: Nonlinear Bulk-Wave Generation by Two Oppositely Directed Collinear Surface Waves," Jour. of Appl. Phys., Vol. 47, No. 4, April 1976, pp. 1209-1228.

43. J.M. Rouvaen, R. Torguet, E. Bredoux, and C. Bruneel, "Nonlinear Elastic Interactions Between Acoustic Bulk and Surface Waves," Jour. of Appl. Phys., Vol. 48, No. 3, March 1977, pp. 934-939.

44. A. Bers, D.J. Kaup, and A.H. Reiman, "Nonlinear Interactions of Three Wave Packets in a Homogeneous Medium," Phys. Rev. Lett., Vol. 37, No. 4, 26 July 1976, pp. 182-185.

45. A.H. Reiman, Space-Time Evolution of Nonlinear Three-Wave

Interactions, Thesis submitted to Department of Physics, Princeton University, June 1977, pp. 34-35.

46. A. Bers, Linear Waves and Instabilities, M.I.T. PRR-7210, Cambridge, Mass., 1972, Section V.

47. B.A. Auld, Acoustic Fields and Waves in Solids, (John Wiley & Sons, Inc., New York, New York, 1973), Vol. I-II.

48. R.N. Thurston, Physical Acoustics, ed. by W.P. Mason, (Academic Press, New York, 1968), Vol. 1A., p. 92.

49. W.R. Jones, J.L. Campbell, S.L. Veilleux, Theoretical Investigation of Acoustic Surface Waves on Piezoelectric Crystals. Hughes Aircraft Co., Ground Systems Group, USAF Contract No.: F19628-69-C-1032, AFCRL-70-0020, 4 Dec. 1969.

50. A.L. Slobodnik, Jr., E.D. Conway, and R.T. Delmonico, Microwave Acoustics Handbook, Volume 1A, Surface Wave Velocities Air Force Cambridge Research Labs, AFCRL-TR-73-0597, Oct. 1, 1973.

51. R.C. Williamson, "Improved Electrostatic Probe for Measurement of Elastic Surface Waves," IEEE Trans. on Sonics and Ultrasonics, Vol. SU-19, No. 4, Oct. 1972, pp. 436-441.

52. A.J. Slobodnik, Jr., R.T. Delmonico, E.D. Conway, Microwave Acoustics Handbook, Volume 2, Surface Wave Velocities - Numerical Data, Air Force Cambridge Research Labs, AFCRL-TR-74-0536, 23 Oct. 1974.

53. T.L. Szabo and A.J. Slobodnik, Jr., "The Effect of Diffraction on the Design of Acoustic Surface Wave Devices," IEEE Trans. on Sonics and Ultrasonics, Vol. SU-20, No. 3, July 1973, pp. 240-251.

54. R.C. Williamson, "Problems Encountered in High-Frequency Surface-Wave Devices," 1974 Ultrasonics Symposium Proceedings, IEEE Cat. #74 CHO 896-1SU, pp. 321-328.

55. A.J. Slobodnik, Jr., "A Review of Material Tradeoffs in the Design of Acoustic Surface Wave Devices at VHF and Microwave Frequencies," IEEE Trans. on Sonics and Ultrasonics, Vol. SU-20, No. 4, Oct. 1973, pp. 315-323.

APPENDIX I

DERIVATION OF COUPLED AMPLITUDE EQUATION

The Cartesian coordinate system referenced in this discussion is given in Fig. I.1. The acoustic field equations and Maxwell's equation for a lossless, charge-free medium can be written [47] as,

$$\bar{\nabla} \times \bar{\bar{T}} = \rho \frac{\partial \bar{v}}{\partial t} - \bar{F}_e \tag{I.1}$$

$$\frac{\partial}{\partial t} \bar{\bar{S}} = \nabla_s \bar{v} \tag{I.2}$$

$$\bar{\nabla} \times \bar{E} = - \frac{\partial \bar{B}}{\partial t} \tag{I.3}$$

$$\bar{\nabla} \times \bar{H} = \frac{\partial \bar{D}}{\partial t} + \bar{J}_e \tag{I.4}$$

$$\bar{\nabla} \times \bar{B} = 0 \tag{I.5}$$

$$\bar{\nabla} \times \bar{D} = \rho_e \tag{I.6}$$

where $\bar{J}_e$, $\bar{F}_e$, and ρ_e are external perturbations of current density, force density, and charge density respectively. The other variables can be identified as stress ($\bar{\bar{T}}$), strain ($\bar{\bar{S}}$), particle velocity ($\bar{v}$), electric field ($\bar{E}$), magnetic flux ($\bar{B}$), magnetic field ($\bar{H}$), electric displacement ($\bar{D}$), and mass density (ρ). The expression $\nabla_s \bar{v}$ is the matrix form of the tensor

Fig. I.1

Cartesian Coordinate System

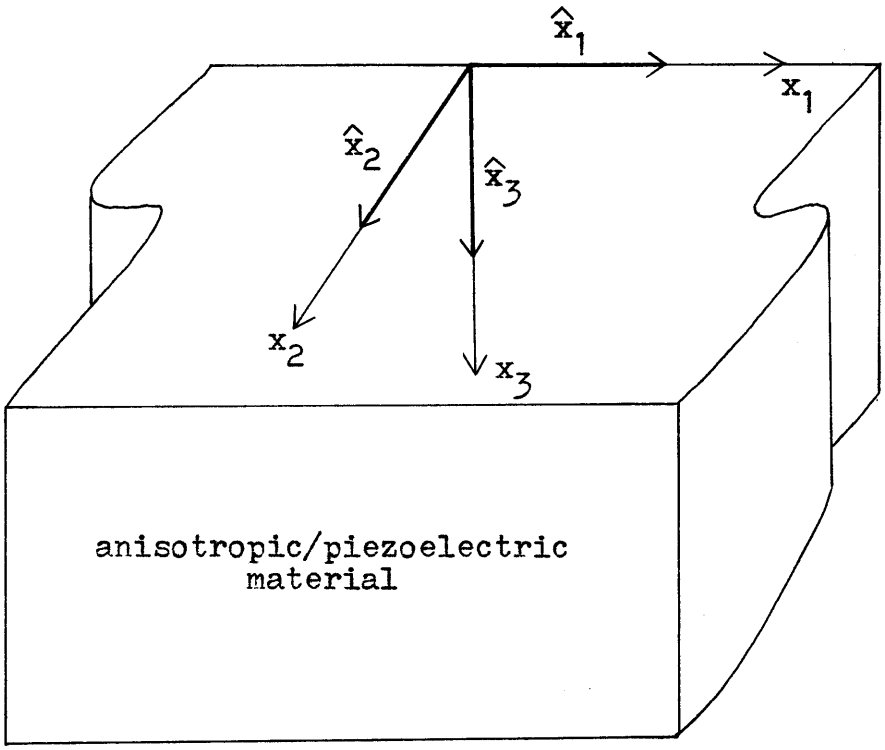

$\hat{x}_i$: unit vector in i^{th} direction

$$\frac{\partial S_{ij}}{\partial t} = \frac{1}{2}\left[\frac{\partial v_i}{\partial x_j} + \frac{\partial v_j}{\partial x_i}\right]$$

The total of each field quantity is the sum of the contribution from each mode that is propagating. The total of each field is given by the following expressions:

$$\bar{v} = \sum_{\beta=1}^{\infty}\left[\underline{v}_\beta(x_3)a_\beta(t,x_1,x_2)e^{i(\omega_\beta t-\bar{k}_\beta\cdot\bar{r}')}\right] \tag{I.7}$$

$$\bar{\bar{T}} = \sum_{\beta=1}^{\infty}\left[\underline{\underline{t}}_\beta(x_3)a_\beta(t,x_1,x_2)e^{i(\omega_\beta t-\bar{k}_\beta\cdot\bar{r}')}\right] \tag{I.8}$$

$$\bar{\bar{S}} = \sum_{\beta=1}^{\infty}\left[\underline{\underline{s}}_\beta(x_3)a_\beta(t,x_1,x_2)e^{i(\omega_\beta t-\bar{k}_\beta\cdot\bar{r}')}\right] \tag{I.9}$$

$$\bar{E} = \sum_{\beta=1}^{\infty}\left[\underline{e}_\beta(x_3)a_\beta(t,x_1,x_2)e^{i(\omega_\beta t-\bar{k}_\beta\cdot\bar{r}')}\right] \tag{I.10}$$

$$\bar{B} = \sum_{\beta=1}^{\infty}\left[\underline{b}_\beta(x_3)a_\beta(t,x_1,x_2)e^{i(\omega_\beta t-\bar{k}_\beta\cdot\bar{r}')}\right] \tag{I.11}$$

$$\bar{H} = \sum_{\beta=1}^{\infty}\left[\underline{h}_\beta(x_3)a_\beta(t,x_1,x_2)e^{i(\omega_\beta t-\bar{k}_\beta\cdot\bar{r}')}\right] \tag{I.12}$$

$$\bar{D} = \sum_{\beta=1}^{\infty}\left[\underline{d}_\beta(x_3)a_\beta(t,x_1,x_2)e^{i(\omega_\beta t-\bar{k}_\beta\cdot\bar{r}')}\right] \tag{I.13}$$

where

$$\bar{k}_\beta = k_1^{(\beta)}\hat{x}_1 + k_2^{(\beta)}\hat{x}_2,$$

$$\bar{r}' = x_1\hat{x}_1 + x_2\hat{x}_2,$$

the subscript β indicates the β^{th} mode. The terms $\underline{v}_\beta(x_3)$, $\underline{\underline{t}}_\beta(x_3)$, $\underline{\underline{s}}_\beta(x_3)$, $\underline{e}_\beta(x_3)$, $\underline{b}_\beta(x_3)$, $\underline{h}_\beta(x_3)$ and $\underline{d}_\beta(x_3)$ are unperturbed polarization amplitudes of the field quantities of the β^{th} mode. $\underline{v}_\beta(x_3)$, $\underline{e}_\beta(x_3)$ $\underline{d}_\beta(x_3)$, $\underline{h}_\beta(x_3)$ and $\underline{b}_\beta(x_3)$ are vector quantities and functions of x_3 only. $\underline{\underline{t}}_\beta(x_3)$ and $\underline{\underline{s}}_\beta(x_3)$ are tensors and also functions of x_3 only. The amplitude terms $a_\beta(t,x_1,x_2)$ are dimensionless, slowly varying functions of position and time. By slowly varying, one has:

$$\left|\frac{\partial a_\beta(t,x_1,x_2)}{\partial t}\right| << \left|\omega_\beta a_\beta(t,x_1,x_2)\right| \tag{I.14}$$

$$\left|\frac{\partial a_\beta(t,x_1,x_2)}{\partial x_1}\right| << \left|k_1^{(\beta)} a_\beta(t,x_1,x_2)\right| \tag{I.15}$$

$$\left|\frac{\partial a_\beta(t,x_1,x_2)}{\partial x_2}\right| << \left|k_2^{(\beta)} a_\beta(t,x_1,x_2)\right| \tag{I.16}$$

To facilitate the derivation of the coupled amplitude equation, the following identities are made:

$$a_\beta = a_\beta(t,x_1,x_2) \qquad \underline{v}_\beta = \underline{v}_\beta(x_3) \qquad \underline{\underline{t}}_\beta = \underline{\underline{t}}_\beta(x_3)$$

$$\underline{\underline{s}}_\beta = \underline{\underline{s}}_\beta(x_3) \qquad \underline{e}_\beta = \underline{e}_\beta(x_3) \qquad \underline{b}_\beta = \underline{b}_\beta(x_3)$$

$$\underline{h}_\beta = \underline{h}_\beta(x_3) \qquad \underline{d}_\beta = \underline{d}_\beta(x_3)$$

With the definitions of the fields given in (I.7)-(I.13), $\overline{F}_e$, $\overline{J}_e$, and ρ_e are the complex external perturbations.

Placing the expressions for the total fields given in (I.7)-(I.13), into equations (I.1)-(I.6), and expanding, one obtains:

$$\sum_\beta \left(\left[\underline{\underline{t}}_\beta \cdot (-i\overline{k}_\beta) a_\beta + (\overline{\nabla} \cdot \underline{\underline{t}}_\beta) a_\beta + \underline{\underline{t}}_\beta \cdot \overline{\nabla} a_\beta \right] e^{i(\omega_\beta t - \overline{k}_\beta \cdot \overline{r}')} \right) =$$

$$\rho \left(\sum_\beta \left[i\omega_\beta \underline{v}_\beta a_\beta + \underline{v}_\beta \frac{\partial a_\beta}{\partial t} \right] e^{i(\omega_\beta t - \overline{k}_\beta \cdot \overline{r}')} \right) - \overline{F}_e \qquad \text{(I.17)}$$

$$\sum_\beta \left(\left[i\omega_\beta \underline{\underline{s}}_\beta a_\beta + \underline{\underline{s}}_\beta \frac{\partial a_\beta}{\partial t} \right] e^{i(\omega_\beta t - \overline{k}_\beta \cdot \overline{r}')} \right) =$$

$$\sum_\beta \left(\left[\frac{-i}{2} \left(\underline{v}_\beta \overline{k}_\beta + \overline{k}_\beta \underline{v}_\beta + i\nabla_s \underline{v}_\beta \right) a_\beta + \frac{1}{2} \left(\underline{v}_\beta \overline{\nabla} a_\beta + (\overline{\nabla} a_\beta) \underline{v}_\beta \right) \right] e^{i(\omega_\beta t - \overline{k}_\beta \cdot \overline{r}')} \right) \qquad \text{(I.18)}$$

$$\sum_\beta \left(\left[-i\overline{k}_\beta \times \underline{e}_\beta + \overline{\nabla} \times \underline{e}_\beta \; a_\beta + (\overline{\nabla} a_\beta \times \underline{e}_\beta) \right] e^{i(\omega_\beta t - \overline{k}_\beta \cdot \overline{r}')} \right) =$$

$$-\sum_\beta \left(\left[i\omega_\beta \underline{b}_\beta a_\beta + \underline{b}_\beta \frac{\partial a_\beta}{\partial t} \right] e^{i(\omega_\beta t - \overline{k}_\beta \cdot \overline{r}')} \right) \qquad \text{(I.19)}$$

$$\sum_{\beta}\left\{\left[\left[-i\bar{k}_{\beta}x\underline{h}_{\beta}+\bar{\nabla}x\underline{h}_{\beta}\right]a_{\beta}+(\bar{\nabla}a_{\beta}x\underline{h}_{\beta})\right]e^{i(\omega_{\beta}t-\bar{k}_{\beta}\cdot\bar{r}')}\right\} =$$

$$\sum_{\beta}\left\{\left[i\omega_{\beta}\underline{d}_{\beta}a_{\beta}+\underline{d}_{\beta}\frac{\partial a_{\beta}}{\partial t}\right]e^{i(\omega_{\beta}t-\bar{k}\cdot\bar{r}')}\right\}+\bar{J}_{e} \qquad (I.20)$$

$$\sum_{\beta}\left\{\left[(-i\bar{k}_{\beta}\cdot\underline{b}_{\beta}+\bar{\nabla}\cdot\underline{b}_{\beta})a_{\beta}+\underline{b}_{\beta}\cdot\bar{\nabla}a_{\beta}\right]e^{i(\omega_{\beta}t-\bar{k}_{\beta}\cdot\bar{r}')}\right\} = 0 \qquad (I.21)$$

$$\sum_{\beta}\left\{\left[(-i\bar{k}_{\beta}\cdot\underline{d}_{\beta}+\bar{\nabla}\cdot\underline{d}_{\beta})a_{\beta}+\underline{d}_{\beta}\cdot\bar{\nabla}a_{\beta}\right]e^{i(\omega_{\beta}t-\bar{k}_{\beta}\cdot\bar{r}')}\right\} = \rho_{e} \qquad (I.22)$$

The terms $\underline{v}_{\beta}\bar{k}_{\beta}$, $\bar{k}_{\beta}\underline{v}_{\beta}$, $\underline{v}_{\beta}\bar{\nabla}a_{\beta}$, $(\bar{\nabla}a_{\beta})\underline{v}_{\beta}$ are diadic products.

Equations (I.17)-(I.22) contain slowly varying and rapidly varying terms as specified by (I.14)-(I.16), and the perturbations $\bar{F}_{e}$, $\bar{J}_{e}$, and ρ_{e} are assumed slowly varying. Following coupled mode formalism, the slow and fast terms can be separated. The rapidly varying terms are:

$$\sum_{\beta}\left\{\left[(-i\underline{t}_{=\beta}\cdot\bar{k}_{\beta}+\nabla\cdot\underline{t}_{=\beta})a_{\beta}\right]e^{i(\omega_{\beta}t-\bar{k}_{\beta}\cdot\bar{r}')}\right\} =$$

$$\rho\sum_{\beta}\left\{i\omega_{\beta}\underline{v}_{\beta}a_{\beta}e^{i(\omega_{\beta}t-\bar{k}_{\beta}\cdot\bar{r}')}\right\} \qquad (I.23)$$

$$\sum_{\beta}\left(i\omega_{\beta}\underline{\underline{s}}_{\beta}a_{\beta}e^{i(\omega_{\beta}t-\bar{k}_{\beta}\cdot\bar{r}')}\right) = \sum_{\beta}\left(\frac{-i}{2}\left[\underline{v}_{\beta}\bar{k}_{\beta}+\bar{k}_{\beta}\underline{v}_{\beta}+i\nabla s\ \underline{v}_{\beta}\right]a_{\beta}e^{i(\omega_{\beta}t-\bar{k}_{\beta}\cdot\bar{r}')}\right) \tag{I.24}$$

$$\sum_{\beta}\left([-i\bar{k}_{\beta}x\underline{e}_{\beta}+\bar{\nabla}x\underline{e}_{\beta}]a_{\beta}e^{i(\omega_{\beta}t-\bar{k}_{\beta}\cdot\bar{r}')}\right) = -\sum_{\beta}\left(i\omega_{\beta}\underline{b}_{\beta}a_{\beta}e^{i(\omega_{\beta}t-\bar{k}_{\beta}\cdot\bar{r}')}\right) \tag{I.25}$$

$$\sum_{\beta}\left((-i\bar{k}_{\beta}x\underline{h}_{\beta}+\bar{\nabla}x\underline{h}_{\beta})a_{\beta}e^{i(\omega_{\beta}t-\bar{k}_{\beta}\cdot\bar{r}')}\right) = \sum_{\beta}\left(i\omega_{\beta}\underline{d}_{\beta}a_{\beta}e^{i(\omega_{\beta}t-\bar{k}_{\beta}\cdot\bar{r}')}\right) \tag{I.26}$$

$$\sum_{\beta}\left((-i\bar{k}_{\beta}\cdot\underline{b}_{\beta}+\bar{\nabla}\cdot\underline{b}_{\beta})a_{\beta}e^{i(\omega_{\beta}t-\bar{k}_{\beta}\cdot\bar{r}')}\right) = 0 \tag{I.27}$$

$$\sum_{\beta}\left((-i\bar{k}_{\beta}\cdot\underline{d}_{\beta}+\bar{\nabla}\cdot\underline{d}_{\beta})a_{\beta}e^{i(\omega_{\beta}t-\bar{k}_{\beta}\cdot\bar{r})}\right) = 0 \tag{I.28}$$

The slowly varying terms are:

$$\sum_{\beta}\left((\underline{\underline{t}}_{\beta}\cdot\bar{\nabla}a_{\beta})e^{i(\omega_{\beta}t-\bar{k}_{\beta}\cdot\bar{r}')}\right) = \rho\sum_{\beta}\left(\left(\underline{v}_{\beta}\frac{\partial a_{\beta}}{\partial t}\right)e^{i(\omega_{\beta}t-\bar{k}_{\beta}\cdot\bar{r}')}\right) - \bar{F}_{e} \tag{I.29}$$

$$\sum_{\beta}\left(\left(\underline{\underline{s}}_{\beta}\frac{\partial a_{\beta}}{\partial t}\right)e^{i(\omega_{\beta}t-\bar{k}_{\beta}\cdot\bar{r}')}\right) = \sum_{\beta}\left(\frac{1}{2}(\underline{v}_{\beta}\bar{\nabla}a_{\beta}+(\bar{\nabla}a_{\beta})\underline{v}_{\beta})e^{i(\omega_{\beta}t-\bar{k}_{\beta}\cdot\bar{r}')}\right) \tag{I.30}$$

$$\sum_{\beta}\left((\bar{\nabla}a_{\beta}x\underline{e}_{\beta})e^{i(\omega_{\beta}t-\bar{k}_{\beta}\cdot\bar{r}')}\right) = -\sum_{\beta}\left(\underline{b}_{\beta}\frac{\partial a_{\beta}}{\partial t}e^{i(\omega_{\beta}t-\bar{k}_{\beta}\cdot\bar{r}')}\right) \tag{I.31}$$

$$\sum_{\beta}\left[(\bar{\nabla}a_{\beta}x\underline{h}_{\beta})e^{i(\omega_{\beta}t-\bar{k}_{\beta}\cdot\bar{r}')}\right] = \sum_{\beta}\left[\underline{d}_{\beta}\frac{\partial a_{\beta}}{\partial t}e^{i(\omega_{\beta}t-\bar{k}_{\beta}\cdot\bar{r}')}\right] + \bar{J}_{e} \qquad (I.32)$$

$$\sum_{\beta}\left[(\underline{b}_{\beta}\cdot\bar{\nabla}a_{\beta})e^{i(\omega_{\beta}t-\bar{k}_{\beta}\cdot\bar{r}')}\right] = 0 \qquad (I.33)$$

$$\sum_{\beta}\left[(\underline{d}_{\beta}\cdot\bar{\nabla}a_{\beta})e^{i(\omega_{\beta}t-\bar{k}_{\beta}\cdot\bar{r}')}\right] = 0 \qquad (I.34)$$

The rapidly varying terms of equations (I.23)-(I.28) and the boundary conditions give the normal mode characteristics of surface acoustic waves. The slow terms contained in equations (I.29)-(I.32) describe the coupled mode interaction as a sum over all the modes. However, one is interested in examining the effects of the coupling on each mode alone, and what contributes to the evolution of each mode. To obtain the equations that give the behavior of each mode, one works through the orthogonality relation of surface waves. The orthogonality relation is derived in Appendix II, and is applied here.

The coupled amplitude equation is developed after performing the operations on equations (I.29)-(I.32) with field quantities of mode α:

$$\frac{\underline{v}^{*}_{\alpha}}{4}e^{-i(\omega_{\alpha}t-\bar{k}_{\alpha}\cdot\bar{r}')}\cdot \qquad (I.29)$$

$$\frac{\underline{\underline{t}}_\alpha}{4} e^{-i(\omega_\alpha t - \bar{k}_\alpha \cdot \bar{r}')} : \text{(I.30)}$$

$$\frac{\underline{h}^*_\alpha}{4} e^{-i(\omega_\alpha t - \bar{k}_\alpha \cdot \bar{r}')} \cdot \text{(I.31)}$$

$$\frac{-\underline{e}^*_\alpha}{4} e^{-i(\omega_\alpha t - \bar{k}_\alpha \cdot \bar{r})} \cdot \text{(I.32)}$$

and letting $\Delta\omega = \omega_\beta - \omega_\alpha$, $\Delta\bar{k} = \bar{k}_\beta - \bar{k}_\alpha$. The results are

$$\frac{1}{4}\sum_\beta \left((\underline{v}^*_\alpha \cdot \underline{\underline{t}}_\beta \cdot \bar{\nabla} a_\beta) e^{i(\Delta\omega t - \Delta\bar{k}\cdot\bar{r}')} \right) = \frac{1}{4}\sum_\beta \left(\left(\rho \underline{v}^*_\alpha \cdot \underline{v}_\beta \frac{\partial a_\beta}{\partial t} \right) e^{i(\Delta\omega t - \Delta\bar{k}\cdot\bar{r})} \right) - \frac{1}{4} \underline{v}^*_\alpha \cdot \bar{F}_e \, e^{-i(\omega_\alpha t - \bar{k}_\alpha \cdot \bar{r}')} \quad \text{(I.35)}$$

$$\frac{1}{4}\sum_\beta \left(\left(\underline{\underline{t}}^*_\alpha : \underline{\underline{s}}_\beta \frac{\partial a_\beta}{\partial t} \right) e^{i(\Delta\omega t - \Delta\bar{k}\cdot\bar{r}')} \right) = \frac{1}{4}\sum_\beta \left(\frac{1}{2} \underline{\underline{t}}^*_\alpha : (\underline{v}_\beta \bar{\nabla} a_\beta + (\bar{\nabla} a_\beta)\underline{v}_\beta) e^{i(\Delta\omega t - \Delta\bar{k}\cdot\bar{r}')} \right) \quad \text{(I.36)}$$

$$\frac{1}{4}\sum_\beta \left(\underline{h}^*_\alpha \cdot (\bar{\nabla} a_\beta \times \underline{e}_\beta) e^{i(\Delta\omega t - \Delta\bar{k}\cdot\bar{r}')} \right) = \frac{1}{4}\sum_\beta \left(\left(\underline{h}^*_\alpha \cdot \underline{b}_\beta \frac{\partial a_\beta}{\partial t} \right) e^{i(\Delta\omega t - \Delta\bar{k}\cdot\bar{r}')} \right) \quad \text{(I.37)}$$

$$\frac{1}{4}\sum_\beta \left(-\underline{e}^*_\alpha \cdot (\bar{\nabla} a_\beta \times \underline{h}_\beta) e^{i(\Delta\omega t - \Delta\bar{k}\cdot\bar{r}')} \right) = -\frac{1}{4}\sum_\beta \left(\left(\underline{e}^*_\alpha \cdot \underline{d}_\beta \frac{\partial a_\beta}{\partial t} \right) e^{i(\Delta\omega t - \Delta\bar{k}\cdot\bar{r}')} \right) - \frac{1}{4} \underline{e}^*_\alpha \cdot \bar{J}_e \, e^{i(\omega_\alpha t - \bar{k}_\alpha \cdot \bar{r}')} \quad \text{(I.38)}$$

The expression

$$\frac{1}{2}\,\underline{\underline{t}}^{*}_{\alpha}:(\underline{v}_{\beta}\bar{\nabla}a_{\beta}+(\bar{\nabla}a_{\beta})\underline{v}_{\beta})$$

appears in equation (I.36). Appendix III shows

$$\frac{1}{2}\,\underline{\underline{t}}^{*}_{\alpha}:(\underline{v}_{\beta}\bar{\nabla}a_{\beta}+(\bar{\nabla}a_{\beta})\underline{v}_{\beta})=\underline{v}_{\beta}\cdot\underline{\underline{t}}^{*}_{\alpha}\cdot\bar{\nabla}a_{\beta} \tag{I.39}$$

With (I.39), the vector identity A·(BxC) = B·(CxA) = C·(AxB), and regrouping terms, (I.35)-(I.38) can be written as

$$\frac{1}{4}\sum_{\beta}\left[\left(\rho\underline{v}^{*}_{\alpha}\cdot\underline{v}_{\beta}\,\frac{\partial a_{\beta}}{\partial t}-\underline{v}^{*}_{\alpha}\cdot\underline{\underline{t}}_{\beta}\cdot\bar{\nabla}a_{\beta}\right)e^{i(\Delta\omega t-\Delta\bar{k}\cdot\bar{r}')}\right]=\frac{1}{4}\underline{v}^{*}_{\alpha}\cdot\bar{F}_{e}\,e^{-i(\omega_{\alpha}t-\bar{k}_{\alpha}\cdot\bar{r}')} \tag{I.40}$$

$$\frac{1}{4}\sum_{\beta}\left[\left(\underline{\underline{t}}^{*}_{\alpha}:\underline{\underline{s}}_{\beta}\,\frac{\partial a_{\beta}}{\partial t}-\underline{v}_{\beta}\cdot\underline{\underline{t}}^{*}_{\alpha}\cdot\bar{\nabla}a_{\beta}\right)e^{i(\Delta\omega t-\Delta\bar{k}\cdot\bar{r}')}\right]=0 \tag{I.41}$$

$$\frac{1}{4}\sum_{\beta}\left[\left(\underline{h}^{*}_{\alpha}\cdot\underline{b}_{\beta}\,\frac{\partial a_{\beta}}{\partial t}+(\underline{e}_{\beta}x\underline{h}^{*}_{\alpha})\cdot\bar{\nabla}a_{\beta}\right)e^{i(\Delta\omega t-\Delta\bar{k}\cdot\bar{r}')}\right]=0 \tag{I.42}$$

$$\frac{1}{4}\sum_{\beta}\left[\left(\underline{e}^{*}_{\alpha}\cdot\underline{d}_{\beta}\,\frac{\partial a_{\beta}}{\partial t}+(\underline{e}^{*}_{\alpha}x\underline{h}_{\beta})\cdot\bar{\nabla}a_{\beta}\right)e^{i(\Delta\omega t-\Delta\bar{k}\cdot\bar{r}')}\right]=-\frac{1}{4}\underline{e}^{*}_{\alpha}\cdot\bar{J}_{e}e^{-i(\omega_{\alpha}t-\bar{k}_{\alpha}\cdot\bar{r}')} \tag{I.43}$$

Adding (I.40)-(I.43), one finds:

$$\sum_{\beta}\left[\left[\frac{1}{4}(\rho\underline{v}_{\alpha}^{*}\cdot\underline{v}_{\beta}+\underline{\underline{t}}_{\alpha}^{*}:\underline{\underline{s}}_{\beta}+\underline{h}_{\alpha}^{*}\cdot\underline{b}_{\beta}+\underline{e}_{\alpha}^{*}\cdot\underline{d}_{\beta})\frac{\partial a_{\beta}}{\partial t}+\frac{1}{4}(-\underline{v}_{\alpha}^{*}\cdot\underline{\underline{t}}_{\beta}-\underline{v}_{\beta}\cdot\underline{\underline{t}}_{\alpha}^{*}+(\underline{e}_{\beta}\times\underline{h}_{\alpha}^{*})+(\underline{e}_{\alpha}^{*}\times\underline{h}_{\beta}))\cdot\nabla a_{\beta}\right]\right.$$

$$\left.e^{i(\Delta\omega t-\Delta\bar{k}\cdot\bar{r}')}\right] = \frac{1}{4}[\underline{v}_{\alpha}^{*}\cdot\bar{F}_{e}-\underline{e}_{\alpha}^{*}\cdot\bar{J}_{e}]e^{-i(\omega_{\alpha}t-\bar{k}_{\alpha}\cdot\bar{r}')} \qquad (I.44)$$

Equation (I.44) is still a sum over all modes of terms that are products of operators on the unperturbed amplitudes, $\underline{v}_{\beta}^{\alpha}$, $\underline{\underline{t}}_{\beta}^{\alpha}$, $\underline{h}_{\beta}^{\alpha}$, $\underline{e}_{\beta}^{\alpha}$, $\underline{\underline{s}}_{\beta}^{\alpha}$, $\underline{d}_{\beta}^{\alpha}$, $\underline{h}_{\beta}^{\alpha}$, $\underline{b}_{\beta}^{\alpha}$, and slowly varying amplitudes a_{β}. However, this equation is in a form from which an equation for a specific mode can be found. Integrating equation (I.44) with respect to x_3, $-\infty \leq x_3 \leq \infty$,

$$\sum_{\beta}\left[\left[\left(\frac{1}{4}\int_{-\infty}^{\infty}(\rho\underline{v}_{\alpha}^{*}\cdot\underline{v}_{\beta}+\underline{\underline{t}}_{\alpha}^{*}:\underline{\underline{s}}_{\beta}+\underline{h}_{\alpha}^{*}\cdot\underline{b}_{\beta}+\underline{e}_{\alpha}^{*}\cdot\underline{d}_{\beta})dx_3\right)\frac{\partial a_{\beta}}{\partial t}\right.\right.$$

$$\left.\left.+\left(\frac{1}{4}\int_{-\infty}^{\infty}(-\underline{v}_{\alpha}^{*}\cdot\underline{\underline{t}}_{\beta}-\underline{v}_{\beta}\cdot\underline{\underline{t}}_{\alpha}^{*}+(\underline{e}_{\beta}\times\underline{h}_{\alpha}^{*})+(\underline{e}_{\alpha}^{*}\times\underline{h}_{\beta}))dx_3\right)\cdot\nabla a_{\beta}\right]e^{i(\Delta\omega t-\Delta\bar{k}\cdot\bar{r}')}\right]$$

$$=\int_{-\infty}^{\infty}\frac{1}{4}[\underline{v}_{\alpha}^{*}\cdot\bar{F}_{e}-\underline{e}_{\alpha}^{*}\cdot\bar{J}_{e}]\,e^{-i(\omega_{\alpha}t-\bar{k}_{\alpha}\cdot\bar{r}')}\,dx_3 \qquad (I.45)$$

One can define the following identities:

$$\langle W_{\alpha\beta} \rangle = \frac{1}{4} \int_{\infty}^{\infty} (\rho \underline{v}^*_{\alpha} \cdot \underline{v}_{\beta} + \underline{\underline{t}}^*_{\alpha} : \underline{\underline{s}}_{\beta} + \underline{h}^*_{\alpha} \cdot \underline{b}_{\beta} + \underline{e}^*_{\alpha} \cdot \underline{d}_{\beta}) dx_3 \tag{I.46}$$

$$\langle \overline{S}_{\alpha\beta} \rangle = \frac{1}{4} \int_{\infty}^{\infty} (-\underline{v}^*_{\alpha} \cdot \underline{\underline{t}}_{\beta} - \underline{v}_{\alpha} \cdot \underline{\underline{t}}_{\beta} + (\underline{e}_{\beta} \times \underline{h}^*_{\alpha}) + (\underline{e}^*_{\alpha} \times \underline{h}_{\beta})) dx_3 \tag{I.47}$$

Rewriting equation (I.45) by using the above identities,

$$\sum_{\beta} \left(\left[\langle W_{\alpha\beta} \rangle \frac{\partial a_{\beta}}{\partial t} + \langle \overline{S}_{\alpha\beta} \rangle \cdot \overline{\nabla} a_{\beta} \right] e^{i(\Delta\omega t - \Delta\overline{k} \cdot \overline{r}')} \right) =$$

$$\int_{\infty}^{\infty} \frac{1}{4} [\underline{v}^*_{\alpha} \cdot \overline{F}_e - \underline{e}^*_{\alpha} \cdot \overline{J}_e] e^{-i(\omega_{\alpha} t - \overline{k}_{\alpha} \cdot \overline{r}')} dx_3 \tag{I.48}$$

From the orthogonality relations for surface acoustic waves derived in Appendix II, one has:

$$(\overline{k}_{\alpha} - \overline{k}_{\beta}) \cdot \langle \overline{S}_{\alpha\beta} \rangle = 0$$

$$(\omega_{\alpha} - \omega_{\beta}) \langle W_{\alpha\beta} \rangle = 0$$

If $\alpha \neq \beta$, then $\langle \overline{S}_{\alpha\beta} \rangle = 0$ and $\langle W_{\alpha\beta} \rangle = 0$, and thus the only non-zero term of the $\sum_{\beta}$ expression in (I.48) is $\beta = \alpha$, and (I.48) becomes

$$\langle W_{\alpha\alpha} \rangle \frac{\partial a_{\alpha}}{\partial t} + \langle \overline{S}_{\alpha\alpha} \rangle \cdot \overline{\nabla} a_{\alpha} = \int_{-\infty}^{\infty} \frac{1}{4} [\underline{v}^*_{\alpha} \cdot \overline{F}_e - \underline{e}^*_{\alpha} \cdot \overline{J}_e] e^{-i(\omega_{\alpha} t - \overline{k}_{\alpha} \cdot \overline{r}')} dx_3 \tag{I.49}$$

$\langle W_{\alpha\alpha} \rangle$ and $\langle \bar{S}_{\alpha\alpha} \rangle$ are the time-average energy density and power density respectively of mode α. The ratio

$$\frac{\langle \bar{S}_{\alpha\alpha} \rangle}{\langle W_{\alpha\alpha} \rangle} = \bar{v}_{g\alpha} \tag{I.50}$$

is the group velocity of that mode. For notation, let

$$\langle W_{\alpha\alpha} \rangle = \langle W_{\alpha} \rangle$$

$$\langle \bar{S}_{\alpha\alpha} \rangle = \langle \bar{S}_{\alpha} \rangle$$

Dividing equation (I.49) by $\langle W_{\alpha} \rangle$ and using (I.50), the coupled amplitude equation for mode α can be written as:

$$\frac{\partial a_{\alpha}}{\partial t} + \bar{v}_{g\alpha} \cdot \bar{\nabla} a_{\alpha} = \frac{\int_{-\infty}^{\infty} \frac{1}{4} [\underline{v}^*_{\alpha} \cdot \bar{F}_e - \underline{e}^*_{\alpha} \cdot \bar{J}_e] e^{-i(\omega_{\alpha} t - \bar{k}_{\alpha} \cdot \bar{r}')} dx_3}{\langle W_{\alpha} \rangle} \tag{I.51}$$

APPENDIX II

ORTHOGONALITY RELATION FOR SURFACE ACOUSTIC WAVES IN ANISOTROPIC/PIEZOELECTRIC MATERIALS

The Cartesian coordinate system used in Appendix I, and given in Fig. I.1, is used for this discussion.

From the complex reciprocity relation [47], one has

$$\bar{\nabla}\cdot\{-\bar{v}^*_\alpha\cdot\bar{\bar{T}}_\beta - \bar{v}_\beta\cdot\bar{\bar{T}}^*_\alpha + \bar{E}^*_\alpha x\bar{H}_\beta + \bar{E}_\beta x\bar{H}^*_\alpha\} =$$

$$-\frac{\partial}{\partial t}\left(\begin{bmatrix}\bar{V}^*_\alpha\cdot & \bar{\bar{T}}^*_\alpha: & \bar{H}^*_\alpha\cdot & \bar{E}^*_\alpha\cdot\end{bmatrix}\begin{bmatrix}\rho & 0 & 0 & 0\\ 0 & \bar{\bar{s}}^E & 0 & \bar{\bar{d}}\cdot\\ 0 & 0 & \bar{\bar{\mu}}\cdot & 0\\ 0 & \bar{\bar{d}}: & 0 & \bar{\bar{\varepsilon}}^T\cdot\end{bmatrix}\begin{bmatrix}\bar{v}_\beta\\ \bar{\bar{T}}_\beta\\ \bar{H}_\beta\\ \bar{E}_\beta\end{bmatrix}\right) \qquad \text{(II.1)}$$

with

$\bar{V}_\alpha$ = particle velocity of $\{^\alpha_\beta\}$ mode

$\bar{\bar{T}}^\beta_\alpha$ = stress of $\{^\alpha_\beta\}$ mode

$\bar{E}^\beta_\alpha$ = electric field of $\{^\alpha_\beta\}$ mode

$\bar{H}^\beta_\alpha$ = magnetic field of $\{^\alpha_\beta\}$ mode

$\bar{\bar{s}}^E$ = compliance constants

$\bar{\bar{d}}$ = piezoelectric strain constants

$\bar{\bar{\mu}}$ = magnetic permeability constants

$\bar{\bar{\varepsilon}}^T$ = dielectric constants

Equation (II.1) can be rewritten as:

$$\bar{\nabla}\cdot\{-\bar{v}^*_\alpha\cdot\bar{\bar{T}}_\beta - \bar{v}_\beta\cdot\bar{\bar{T}}^*_\alpha + \bar{E}^*_\alpha x\bar{H}_\beta + \bar{E}_\beta x\bar{H}^*_\alpha\} =$$

$$-\frac{\partial}{\partial t}\{[\bar{v}^*_\alpha\cdot\ \bar{\bar{T}}^*_\alpha:\ \bar{H}^*_\alpha\cdot\ \bar{E}^*_\alpha][\rho\bar{v}_\beta\ \bar{\bar{s}}^E:\bar{T}_\beta+\bar{\bar{d}}\cdot\bar{E}_\alpha\quad\bar{\bar{\mu}}\cdot\bar{H}_\alpha\ \bar{\bar{d}}:\bar{\bar{T}}_\alpha+\bar{\bar{\varepsilon}}^T\cdot\bar{E}_\alpha]\} \tag{II.2}$$

However,

$\bar{\bar{S}}_\beta = \bar{\bar{s}}^E:\bar{T}_\beta + \bar{\bar{d}}\cdot\bar{E}_\alpha$ = strain of mode β,

$\bar{D}_\beta = \bar{\bar{d}}:T_\beta + \bar{\bar{\varepsilon}}^T\cdot\bar{E}_\beta$ = dielectric displacement of mode β,

$\bar{B}_\beta = \bar{\bar{\mu}}\cdot\bar{H}_\beta$ = magnetic flux of mode β

and equation (II.2) becomes:

$$\bar{\nabla}\cdot\{-\bar{v}^*_\alpha\cdot\bar{\bar{T}}_\beta - \bar{v}_\beta\cdot\bar{\bar{T}}^*_\alpha + \bar{E}^*_\alpha x\bar{H}_\beta + \bar{E}_\beta x\bar{H}^*_\alpha\} =$$

$$-\frac{\partial}{\partial t}\{[\bar{v}^*_\alpha\cdot\ \bar{\bar{T}}^*_\alpha:\ H^*_\alpha\cdot\ \bar{E}^*_\alpha\cdot][\rho\bar{v}_\beta\ \bar{\bar{S}}_\beta\ \bar{B}_\beta\ \bar{D}_\beta]\} =$$

$$-\frac{\partial}{\partial t}\{\rho\bar{v}^*_\alpha\cdot\bar{v}_\beta + \bar{\bar{T}}^*_\alpha:\bar{\bar{S}}_\beta + \bar{H}^*_\alpha\cdot\bar{B}_\beta + \bar{E}^*_\alpha\cdot\bar{D}_\beta\} \tag{II.3}$$

let

$$\overline{v}_{\substack{\alpha\\\beta}} = \underline{v}_{\substack{\alpha\\\beta}}(x_3)\, e^{i(\omega_{\substack{\alpha\\\beta}} t - \overline{k}_{\substack{\alpha\\\beta}} \cdot \overline{r}')} \tag{II.4}$$

$$\overline{\overline{T}}_{\substack{\alpha\\\beta}} = \underline{\underline{t}}_{\substack{\alpha\\\beta}}(x_3)\, e^{i(\omega_{\substack{\alpha\\\beta}} t - \overline{k}_{\substack{\alpha\\\beta}} \cdot \overline{r}')} \tag{II.5}$$

$$\overline{\overline{S}}_{\substack{\alpha\\\beta}} = \underline{\underline{s}}_{\substack{\alpha\\\beta}}(x_3)\, e^{i(\omega_{\substack{\alpha\\\beta}} t - \overline{k}_{\substack{\alpha\\\beta}} \cdot \overline{r}')} \tag{II.6}$$

$$\overline{E}_{\substack{\alpha\\\beta}} = \underline{e}_{\substack{\alpha\\\beta}}(x_3)\, e^{i(\omega_{\substack{\alpha\\\beta}} t - \overline{k}_{\substack{\alpha\\\beta}} \cdot \overline{r}')} \tag{II.7}$$

$$\overline{H}_{\substack{\alpha\\\beta}} = \underline{h}_{\substack{\alpha\\\beta}}(x_3)\, e^{i(\omega_{\substack{\alpha\\\beta}} t - \overline{k}_{\substack{\alpha\\\beta}} \cdot \overline{r}')} \tag{II.8}$$

$$\overline{B}_{\substack{\alpha\\\beta}} = \underline{b}_{\substack{\alpha\\\beta}}(x_3)\, e^{i(\omega_{\substack{\alpha\\\beta}} t - \overline{k}_{\substack{\alpha\\\beta}} \cdot \overline{r}')} \tag{II.9}$$

$$\overline{D}_{\substack{\alpha\\\beta}} = \underline{d}_{\substack{\alpha\\\beta}}(x_3)\, e^{i(\omega_{\substack{\alpha\\\beta}} t - \overline{k}_{\substack{\alpha\\\beta}} \cdot \overline{r}')} \tag{II.10}$$

The terms $\underline{v}_{\substack{\alpha\\\beta}}(x_3)$, $\underline{\underline{t}}_{\substack{\alpha\\\beta}}(x_3)$, $\underline{\underline{s}}_{\substack{\alpha\\\beta}}(x_3)$, $\underline{e}_{\substack{\alpha\\\beta}}(x_3)$, $h_{\substack{\alpha\\\beta}}(x_3)$, $\underline{d}_{\substack{\alpha\\\beta}}(x_3)$, $\underline{b}_{\substack{\alpha\\\beta}}(x_3)$ are functions of x_3 only; and

$$\overline{k}_{\substack{\alpha\\\beta}} = k_1^{(\substack{\alpha\\\beta})} \hat{x}_1 + k_2^{(\substack{\alpha\\\beta})} \hat{x}_2$$

with $k_1^{(\substack{\alpha\\\beta})}$ and $k_2^{(\substack{\alpha\\\beta})}$ real and constant

$$\overline{r}' = x_1 \hat{x}_1 + x_2 \hat{x}_2$$

Substituting (II.4)-(II.10) into equation (II.3), one has

$$-i(\bar{k}_\beta-\bar{k}_\alpha)\cdot\{-\underline{v}^*_\alpha(x_3)\cdot\underline{\underline{t}}_\beta(x_3)-\underline{v}_\beta(x_3)\cdot\underline{\underline{t}}^*_\alpha(x_3)+\underline{e}^*_\alpha(x_3)\times\underline{h}_\beta(x_3)+\underline{e}_\beta(x_3)\times\underline{h}^*_\alpha(x_3)\}$$

$$+x_3\cdot\frac{\partial}{\partial x_3}\{-\underline{v}^*_\alpha(x_3)\cdot\underline{\underline{t}}_\beta(x_3)-\underline{v}_\beta(x_3)\cdot\underline{\underline{t}}^*_\alpha(x_3)+\underline{e}^*_\alpha(x_3)\times\underline{h}_\beta(x_3)+\underline{e}_\beta(x_3)\times\underline{h}^*_\alpha(x_3)\} =$$

$$-i(\omega_\beta-\omega_\alpha)\{\rho\underline{v}^*_\alpha(x_3)\cdot\underline{v}_\beta(x_3)+\underline{\underline{t}}^*_\alpha(x_3):\underline{\underline{s}}_\beta(x_3)+\underline{h}^*_\alpha(x_3)\cdot\underline{b}_\beta(x_3)+\underline{e}^*_\alpha(x_3)\cdot\underline{d}_\beta(x_3)\}.$$

Integrating this result over x_3, $-\infty \leq x_3 \leq \infty$; and dividing by four,

$$-i(\bar{k}_\beta-\bar{k}_\alpha)\cdot\frac{1}{4}\int_{-\infty}^{\infty}\{-\underline{v}^*_\alpha(x_3)\cdot\underline{\underline{t}}_\beta(x_3)-\underline{v}_\beta(x_3)\cdot\underline{\underline{t}}^*_\alpha(x_3)+\underline{e}^*_\alpha(x_3)\times\underline{h}_\beta(x_3)+\underline{e}_\beta(x_3)\times\underline{h}^*_\alpha(x_3)\}$$

$$+\frac{1}{4}\int_{\infty}^{\infty}\hat{x}_3\cdot\frac{\partial}{\partial x_3}\{-\underline{v}^*_\alpha(x_3)\cdot\underline{\underline{t}}_\beta(x_3)-\underline{v}_\beta(x_3)\cdot\underline{\underline{t}}^*_\alpha(x_3)+\underline{e}^*_\alpha(x_3)\times\underline{h}_\beta(x_3)$$

$$+\underline{e}_\beta(x_3)\times\underline{h}^*_\alpha(x_3)\}\,dx_3 =$$

$$-i(\omega_\beta-\omega_\alpha)\,\frac{1}{4}\int_{\infty}^{\infty}\{\rho\underline{v}^*_\alpha(x_3)\cdot\underline{v}_\beta(x_3)+\underline{\underline{t}}^*_\alpha(x_3):\underline{\underline{s}}_\beta(x_3)+\underline{h}^*_\alpha(x_3)\cdot\underline{b}_\beta(x_3)+\underline{e}^*_\alpha(x_3)\cdot\underline{d}_\beta(x_3)\}dx_3$$

(II.12)

At this point the discussion shall digress to define two identities, and examine an integral expression in (II.12).

The definitions are

$$\langle \overline{S}_{\alpha\beta} \rangle = \frac{1}{4} \int_{\infty}^{\infty} \{-\underline{v}^*_{\alpha}(x_3)\cdot\underline{\underline{t}}_{\beta}(x_3)-\underline{v}_{\beta}(x_3)\cdot\underline{\underline{t}}^*_{\alpha}(x_3)+\underline{e}^*_{\alpha}(x_3)x\underline{h}_{\beta}(x_3)+\underline{e}_{\beta}(x_3)x\underline{h}^*_{\alpha}(x_3)\}dx_3, \tag{II.13}$$

a vector quantity, and a scalar term

$$\langle W_{\alpha\beta} \rangle = \frac{1}{4} \int_{\infty}^{\infty} \{\rho\underline{v}^*_{\alpha}(x_3)\cdot\underline{v}_{\beta}(x_3)+\underline{\underline{t}}^*_{\alpha}(x_3):\underline{\underline{s}}_{\beta}(x_3)+\underline{h}^*_{\alpha}(x_3)\cdot\underline{b}_{\beta}(x_3)+\underline{e}^*_{\alpha}(x_3)\cdot\underline{d}_{\beta}(x_3)\}dx_3. \tag{II.14}$$

The integral to be examined is

$$\int_{-\infty}^{\infty} \hat{x}_3\cdot\frac{\partial}{\partial x_3}\{-\underline{v}^*_{\alpha}(x_3)\cdot\underline{\underline{t}}_{\beta}(x_3)-\underline{v}_{\beta}(x_3)\cdot\underline{\underline{t}}^*_{\alpha}(x_3)+\underline{e}^*_{\alpha}(x_3)x\underline{h}_{\beta}(x_3)+\underline{e}_{\beta}(x_3)x\underline{h}^*_{\alpha}(x_3)\}dx_3. \tag{II.15}$$

Because of the different media for $x_3 \leq 0$ and $x_3 \geq 0$, (II.15) must be written as integrals over each medium. Therefore,

$$\int_{-\infty}^{\infty} \hat{x}_3\cdot\frac{\partial}{\partial x_3}\{-\underline{v}^*_{\alpha}(x_3)\cdot\underline{\underline{t}}_{\beta}(x_3)-\underline{v}_{\beta}(x_3)\cdot\underline{\underline{t}}^*_{\alpha}(x_3)+\underline{e}^*_{\alpha}(x_3)x\underline{h}_{\beta}(x_3)+\underline{e}_{\beta}(x_3)x\underline{h}^*_{\alpha}(x_3)\}dx_3 =$$

$$x_3\cdot\int_{-\infty}^{0} \frac{\partial}{\partial x_3}\{-\underline{v}^*_{\alpha}(x_3)\cdot\underline{\underline{t}}_{\beta}(x_3)-\underline{v}_{\beta}(x_3)\cdot\underline{\underline{t}}^*_{\alpha}(x_3)\}dx_3 +$$

$$x_3\cdot\int_{0}^{\infty} \frac{\partial}{\partial x_3}\{-\underline{v}^*_{\alpha}(x_3)\cdot\underline{\underline{t}}_{\beta}(x_3)-\underline{v}_{\beta}(x_3)\cdot\underline{\underline{t}}^*_{\alpha}(x_3)\}dx_3 +$$

$$\int_{-\infty}^{0} \frac{\partial}{\partial x_3}[\hat{x}_3\cdot(\underline{e}^*_{\alpha}(x_3)x\underline{h}_{\beta}(x_3)+\underline{e}_{\beta}(x_3)x\underline{h}^*_{\alpha}(x_3))]dx_3 +$$

$$\int_0^{\infty} \frac{\partial}{\partial x_3}[\hat{x}_3 \cdot (\underline{e}^*_\alpha(x_3) x \underline{h}_\beta(x_3) + \underline{e}_\beta(x_3) x \underline{h}^*_\alpha(x_3))]dx_3 \qquad \text{(II.16)}$$

For $x_3 < 0$,

$$\underline{v}_\beta(x_3) = v^*_\alpha(x_3) = 0$$

$$\underline{\underline{t}}_\beta(x_3) = \underline{\underline{t}}^*_\alpha(x_3) = 0$$

Further,

$$\underline{e}^*_\alpha(x_3) x \underline{h}_\beta(x_3) = [e^*_{\alpha 2}(x_3) h_{\beta 3}(x_3) - e^*_{\alpha 3}(x_3) h_{\beta 2}(x_3)]\hat{x}_1 +$$

$$[e^*_{\alpha 3}(x_3) h_{\beta 1}(x_3) - e^*_{\alpha 1}(x_3) h_{\beta 3}(x_3)]\hat{x}_2 +$$

$$[e^*_{\alpha 1}(x_3) h_{\beta 2}(x_3) - e^*_{\alpha 2}(x_3) h_{\beta 1}(x_3)]\hat{x}_3;$$

$$\underline{e}_\beta(x_3) x \underline{h}^*_\alpha(x_3) = [e_{\beta 2}(x_3) h^*_{\alpha 3}(x_3) - e_{\beta 3}(x_3) h^*_{\alpha 2}(x_3)]\hat{x}_1 +$$

$$[e_{\beta 3}(x_3) h^*_{\alpha 1}(x_3) - e_{\beta 1}(x_3) h^*_{\alpha 3}(x_3)]\hat{x}_2 +$$

$$[e_{\beta 1}(x_3) h^*_{\alpha 2}(x_3) - e_{\beta 2}(x_3) h^*_{\alpha 1}(x_3)]\hat{x}_3$$

With these results, (II.16) reduces to

$$\hat{x}_3 \cdot \int_0^{\infty} \frac{\partial}{\partial x_3}\{-\underline{v}^*_{\alpha}(x_3)\cdot\underline{\underline{t}}_{\beta}(x_3)-\underline{v}_{\beta}(x_3)\cdot\underline{\underline{t}}^*_{\alpha}(x_3)\}dx_3 +$$

$$\int_{-\infty}^{0} \frac{\partial}{\partial x_3}\{[e^*_{\alpha 1}(x_3)h_{\beta 2}(x_3)-e^*_{\alpha 2}(x_3)h_{\beta 1}(x_3)] +$$

$$[e_{\beta 1}(x_3)h^*_{\alpha 2}(x_3)-e_{\beta 2}(x_3)h^*_{\alpha 1}(x_3)]\}dx_3 +$$

$$\int_0^{\infty} \frac{\partial}{\partial x_3} [e^*_{\alpha 1}(x_3)h_{\beta 2}(x_3)-e^*_{\alpha 2}(x_3)h_{\beta 1}(x_3)] +$$

$$[e_{\beta 1}(x_3)h^*_{\alpha 2}(x_3)-e_{\beta 2}(x_3)h_{\alpha 1}(x_3)]\}dx_3 \qquad \text{(II.17)}$$

Performing the integrations, and regrouping, one has

$$[-\underline{v}^*_{\alpha}(x_3)\cdot\underline{\underline{t}}_{\beta}(x_3)\cdot\hat{x}_3-\underline{v}_{\beta}(x_3)\cdot\underline{\underline{t}}^*_{\alpha}(x_3)\cdot\hat{x}_3]\Big|_0^{\infty} +$$

$$\{[e^*_{\alpha 1}(x_3)h_{\beta 2}(x_3)-e^*_{\alpha 2}(x_3)h_{\beta 1}(x_3)]+[e_{\beta 1}(x_3)h^*_{\alpha 2}(x_3)-e_{\beta 2}(x_3)h^*_{\alpha 1}(x_3)]\}\Big|_{-\infty}^{0} +$$

$$\{[e^*_{\alpha 1}(x_3)h_{\beta 2}(x_3)-e^*_{\alpha 2}(x_3)h_{\beta 1}(x_3)]+[e_{\beta 1}(x_3)h^*_{\alpha 2}(x_3)-e_{\beta 2}(x_3)h^*_{\alpha 1}(x_3)]\}\Big|_0^{\infty} \qquad \text{(II.18)}$$

The components of $\overline{E}_{\substack{\alpha \\ \beta}}$ and $\overline{H}_{\substack{\alpha \\ \beta}}$ parallel to the boundary between the anisotropic/piezoelectric medium and its adjacent medium (vacuum) are continuous. These components are $e_{\alpha 1}$, $e_{\beta 1}$, $e_{\alpha 2}$, $e_{\beta 2}$, $h_{\alpha 1}$, $h_{\beta 1}$, $h_{\alpha 2}$, and $h_{\beta 2}$. Hence II.18 reduces to

$$[-\underline{v}^*_\alpha(x_3)\cdot\underline{\underline{t}}_\beta(x_3)\cdot\hat{x}_3-\underline{v}_\beta(x_3)\cdot\underline{\underline{t}}^*_\alpha(x_3)\cdot\hat{x}_3]\Big|_0^\infty +$$

$$\{[e^*_{\alpha 1}(x_3)h_{\beta 2}(x_3)-e^*_{\alpha 2}(x_3)h_{\beta 1}(x_3)]+[e_{\beta 1}(x_3)h^*_{\alpha 2}(x_3)-e_{\beta 2}(x_3)h^*_{\alpha 1}(x_3)]\}\Big|_{-\infty}^{\infty} \qquad \text{(II.19)}$$

at

$x_3 = 0$; $\quad \underline{\underline{t}}_{\substack{\alpha\\ \beta}}(x_3)\cdot\hat{x}_3 = 0$

$x_3 = -\infty$; $\quad \underline{e}_{\substack{\alpha\\ \beta}}(x_3) = 0$ and $\underline{h}_{\substack{\alpha\\ \beta}}(x_3) = 0$; and

$x_3 = \infty$: $\quad \underline{\underline{t}}_{\substack{\alpha\\ \beta}}(x_3) = 0$, $\underline{v}_{\substack{\alpha\\ \beta}}(x_3) = 0$, $\underline{e}_{\substack{\alpha\\ \beta}}(x_3) = 0$, $\underline{h}_{\substack{\alpha\\ \beta}}(x_3) = 0$

hence, (II.19) becomes zero. Therefore

$$\int_{-\infty}^{\infty} x_3\cdot\frac{\partial}{\partial x_3}\{-\underline{v}^*_\alpha(x_3)\cdot\underline{\underline{t}}_\beta(x_3)-\underline{v}_\beta(x_3)\cdot\underline{\underline{t}}^*_\alpha(x_3)+\underline{e}^*_\alpha(x_3)x\underline{h}_\beta(x_3)+\underline{e}_\beta(x_3)x\underline{h}^*_\alpha(x_3)\}dx_3=0 \qquad \text{(II.20)}$$

Returning to equation (II.12), the definitions (II.13) and (II.14) and the result (II.20), reduce equations (II.12) to:

$$i(\bar{k}_\beta-\bar{k}_\alpha)\cdot\langle\bar{S}_{\alpha\beta}\rangle = i(\omega_\beta-\omega_\alpha)\langle W_{\alpha\beta}\rangle \qquad \text{(II.21)}$$

Repeating the derivation, with the substitution in (II.4)-(II-10) of $\bar{k}_\alpha \to \bar{k}_\alpha$, and $\bar{k}_\beta \to -\bar{k}_\beta$, one obtains:

$$-i(\bar{k}_\beta-\bar{k}_\alpha)\cdot\langle\bar{S}_{\alpha\beta}\rangle = i(\omega_\beta-\omega_\alpha)\langle W_{\alpha\beta}\rangle \qquad \text{(II.22)}$$

Adding and substracting (II.21) and (II.22) to and from each other respectively, gives the orthogonality relation of two surface acoustic wave modes:

$$(\bar{k}_\alpha-\bar{k}_\beta)\cdot\langle\bar{S}_{\alpha\beta}\rangle = 0 \qquad \text{(II.23)}$$

$$(\omega_\alpha-\omega_\beta)\langle W_{\alpha\beta}\rangle = 0 \qquad \text{(II.24)}$$

Hence, if $\alpha\neq\beta$, then

$$\langle\bar{S}_{\alpha\beta}\rangle = 0$$

and

$$\langle W_{\alpha\beta}\rangle = 0$$

When $\beta=\alpha$, one can make the identification that

$\langle W_{\alpha\alpha}\rangle$ = time averge energy density of mode α,

$\langle\bar{S}_{\alpha\alpha}\rangle$ = time averge power density vector of mode α.

APPENDIX III

TENSOR IDENTITY

From Appendix I, the term

$$\frac{1}{2}\,\underline{\underline{t}}^*_\alpha : (\underline{v}_\beta \overline{\nabla} a_\beta + (\overline{\nabla} a_\beta)\underline{v}_\beta)$$

appears in equation (I.36)

$$\frac{1}{2}\,\underline{\underline{t}}^*_\alpha : (\underline{v}_\beta \overline{\nabla} a_\beta + (\overline{\nabla} a_\beta)\underline{v}_\beta) = \sum_{i=1}^{3}\sum_{j=1}^{3} \frac{1}{2}\, t^*_{\alpha ij}\left(v_{\beta i}\frac{\partial a_\beta}{\partial x_j} + v_{\beta j}\frac{\partial a_\beta}{\partial x_i}\right)$$

$$= \frac{1}{2}\Bigg[2t^*_{\alpha 11}v_{\beta 1}\frac{\partial a_\beta}{\partial x_1} + t^*_{\alpha 12}\left(v_{\beta 1}\frac{\partial a_\beta}{\partial x_2} + v_{\beta 2}\frac{\partial a_\beta}{\partial x_1}\right)$$

$$+ t^*_{\alpha 13}\left(v_{\beta 1}\frac{\partial a_\beta}{\partial x_3} + v_{\beta 3}\frac{\partial a_\beta}{\partial x_1}\right) + t^*_{\alpha 21}\left(v_{\beta 2}\frac{\partial a_\beta}{\partial x_1} + v_{\beta 1}\frac{\partial a_\beta}{\partial x_2}\right)$$

$$+ 2t^*_{\alpha 22}v_{\beta 2}\frac{\partial a_\beta}{\partial x_2} + t^*_{\alpha 23}\left(v_{\beta 2}\frac{\partial a_\beta}{\partial x_3} + v_{\beta 3}\frac{\partial a_\beta}{\partial x_2}\right)$$

$$+ t^*_{\alpha 31}\left(v_{\beta 3}\frac{\partial a_\beta}{\partial x_1} + v_{\beta 1}\frac{\partial a_\beta}{\partial x_3}\right) + t^*_{\alpha 32}\left(v_{\beta 3}\frac{\partial a_\beta}{\partial x_2} + v_{\beta 2}\frac{\partial a_\beta}{\partial x_3}\right)$$

$$+ 2t^*_{\alpha 33}\left(v_{\beta 3}\frac{\partial a_\beta}{\partial x_3}\right)\Bigg]$$

Regrouping terms and using the symmetry property of stress,

$t^*_{\alpha ij} = t^*_{\alpha ji}$,

$$\frac{1}{2}\,\underline{\underline{t}}^*_\alpha : (\underline{v}_\beta \overline{\nabla} a_\beta + (\overline{\nabla} a_\beta)\underline{v}_\beta) = v_{\beta 1}\left[t^*_{\alpha 11}\frac{\partial a_\beta}{\partial x_1} + t^*_{\alpha 12}\frac{\partial a_\beta}{\partial x_2} + t^*_{\alpha 13}\frac{\partial a_\beta}{\partial x_3}\right]$$

$$+ v_{\beta 2}\left[t^*_{\alpha 21}\frac{\partial a_\beta}{\partial x_1} + t^*_{\alpha 22}\frac{\partial a_\beta}{\partial x_2} + t^*_{\alpha 23}\frac{\partial a_\beta}{\partial x_3}\right]$$

$$+ v_{\beta 3}\left[t^*_{\alpha 31}\frac{\partial a_\beta}{\partial x_1} + t^*_{\alpha 32}\frac{\partial a_\beta}{\partial x_2} + t^*_{\alpha 33}\frac{\partial a_\beta}{\partial x_3}\right]$$

$$= \underline{v}_\beta \cdot \underline{\underline{t}}^*_\alpha \cdot \overline{\nabla} a_\beta$$

APPENDIX IV

DERIVATION OF NONLINEAR EQUATION

This discussion contains the derivation of the nonlinearly coupled amplitude equation. The Cartesian coordinate system used in this discussion is illustrated in Fig. I.1.

The nonlinearities of an anisotropic/piezoelectric material that contribute to nonlinear interactions are defined from the electric Gibbs function (G) [48], [9]:

$$G = \frac{1}{2}C_{ijk\ell}S_{ij}S_{k\ell} - e_{ijk}E_iS_{jk} - \frac{1}{2}\epsilon_{ij}E_iE_j + \frac{1}{6}\theta_{ijk\ell mn}S_{ij}S_{k\ell}S_{mn}$$

$$-\frac{1}{2}\eta_{ijk\ell m}E_iS_{jk}S_{\ell m} - \frac{1}{2}Q_{ijk\ell}E_iE_jS_{k\ell} - \frac{1}{6}O_{ijk}E_iE_jE_k - \sigma T \qquad \text{(IV.1)}$$

Sum over repeated indices is assumed, and magnetic effects are not considered. The terms in the above expression are:

S_{ij} = strain components

E_i = electric field components

$C_{ijk\ell}$ = elastic stiffness constants

e_{ijk} = piezoelectric constants

ϵ_{ij} = dielectric constants

$\theta_{ijk\ell mn}$ = nonlinear elastic constants

$\eta_{ijk\ell m}$ = nonlinear piezoelectric constants

$Q_{ijk\ell}$ = electrostriction constants

Q_{ijk} = electro-optic constants

σ = entropy

T = temperature

From the electric Gibbs function, the stress (T_{ij}) and electric displacement (D_i) can be determined:

$$T_{ij} = \left(\frac{\partial G}{\partial S_{ij}}\right)_{E_k, T} \tag{IV.2}$$

$$D_i = -\left(\frac{\partial E}{\partial G_i}\right)_{S_{k\ell}, T} \tag{IV.3}$$

Substituting for G the expression in equation (IV.1), equations (IV.2) and (IV.3) become

$$T_{ij} = C_{ijk\ell}S_{k\ell} - e_{kij}E_k - \eta_{kij\ell m}E_k S_{\ell m} + \frac{1}{2}\theta_{ijk\ell mn}S_{k\ell}S_{mn} - \frac{1}{2}Q_{k\ell ij}E_k E_\ell \tag{IV.4}$$

$$D_i = \epsilon_{ij}E_j + e_{ijk}S_{jk} + Q_{ijk\ell}E_j S_{k\ell} \frac{1}{2}\eta_{ijk\ell m}S_{jk}S_{\ell m} + \frac{1}{2}Q_{ijk}E_j E_k \tag{IV.5}$$

Equations (IV.4) and (IV.5) indicate the stress and electric displacement consist of a linear and nonlinear part. This is

represented as:

$$T_{ij} = T^{L}_{ij} + T^{NL}_{ij} \tag{IV.6}$$

$$D_{L} = D^{L}_{i} + D^{NL}_{L} \tag{IV.7}$$

where

$$T^{L}_{ij} = C_{ijk\ell}S_{k\ell} - e_{kij}E_{i} \tag{IV.8}$$

$$T^{NL}_{ij} = -\eta_{kij\ell m}E_{k}S_{\ell m} + \frac{1}{2}\theta_{ijk\ell mn}S_{k\ell}S_{mn} - \frac{1}{2}\eta_{k\ell ij}E_{k}E_{\ell} \tag{IV.9}$$

$$D^{L}_{i} = \epsilon_{ij}E_{j} + e_{ijk}S_{jk} \tag{IV.10}$$

$$D^{NL}_{i} = Q_{ijk\ell}E_{j}S_{k\ell} + \frac{1}{2}\eta_{ijk\ell m}S_{jk}S_{\ell m} + \frac{1}{2}O_{ijk}E_{j}E_{k} \tag{IV.11}$$

T^{NL}_{ij} and D^{NL}_{i} are assumed weak nonlinear perturbations on the linear stress (T^{L}_{ij}) and linear electric displacement (D^{L}_{i}). T^{NL}_{ij} and D^{NL}_{i} are responsible for the coupling of modes for this situation.

Following coupled mode theory, T^{NL}_{ij} and D^{NL}_{i} are determined from the unperturbed strain and electric field. The total unperturbed electric and strain fields are a sum of the contributions from each normal mode. Further, the field quantities in equation (IV.1) are real, and can be represented as a sum of a complex term and its complex conjugate:

$$E_i = \frac{1}{2}\left[\sum_{\beta=1}^{\infty} e_i^{(\beta)}(x_3)a_\beta(t,x_1,x_2)e^{i(\omega_\beta t - \bar{k}_\beta\cdot\bar{r}')} + c.c.\right] \quad (IV.12)$$

$$S_{ij} = \frac{1}{2}\left[\sum_{\beta=1}^{\infty} s_{ij}^{(\beta)}(x_3)a_\beta(t,x_1,x_2)e^{i(\omega_\beta t - \bar{k}_\beta\cdot\bar{r}')} + c.c.\right] \quad (IV.13)$$

Substituting the expanded expressions for E_i and S_{ij} into equations (IV.9) and (IV.11)

$$\begin{aligned}
D_i^{NL} = {} & Q_{ijk\ell}\left\{\frac{1}{4}\sum_{\beta\gamma\Sigma\Sigma} e_j^{(\beta)}s_{k\ell}^{(\gamma)}a_\beta a_\gamma e^{i[(\omega_\beta+\omega_\gamma)t-(\bar{k}_\beta+\bar{k}_\gamma)\cdot\bar{r}']}\right. \\
& \left. + \frac{1}{4}\sum_{\beta\gamma\Sigma\Sigma} e_j^{(\beta)}s_{k\ell}^{(\gamma)*}a_\beta a_\gamma^* e^{i[(\omega_\beta-\omega_\gamma)t-(\bar{k}_\beta-\bar{k}_\gamma)\cdot\bar{r}']} + c.c.\right\} \\
& + \frac{1}{2}\eta_{ijk\ell m}\left\{\frac{1}{4}\sum_{\beta\gamma\Sigma\Sigma} s_{jk}^{(\beta)}s_{\ell m}^{(\gamma)}a_\beta a_\gamma e^{i[(\omega_\beta+\omega_\gamma)t-(\bar{k}_\beta+\bar{k}_\gamma)\cdot\bar{r}']}\right. \\
& \left. + \frac{1}{4}\sum_{\beta\gamma\Sigma\Sigma} s_{jk}^{(\beta)}s_{\ell m}^{(\gamma)*}a_\beta a_\gamma^* e^{i[(\omega_\beta-\omega_\gamma)t-(\bar{k}_\beta-\bar{k}_\gamma)\cdot\bar{r}']} + c.c.\right\} \\
& + \frac{1}{2}O_{ijk}\left\{\frac{1}{4}\sum_{\beta\gamma\Sigma\Sigma} e_j^{(\beta)}e_k^{(\gamma)}a_\beta a_\gamma e^{i[(\omega_\beta+\omega_\gamma)t-(\bar{k}_\beta+\bar{k}_\gamma)\cdot\bar{r}']}\right. \\
& \left. + \frac{1}{4}\sum_{\beta\gamma\Sigma\Sigma} e_j^{(\beta)}e_k^{(\gamma)*}a_\beta a_\gamma^* e^{i[(\omega_\beta-\omega_\gamma)t-(\bar{k}_\beta-\bar{k}_\gamma)\cdot\bar{r}']} + c.c.\right\}
\end{aligned} \quad (IV.14)$$

$$T_{ij}^{NL} = -\eta_{kij\ell m}\left\{\frac{1}{4}\sum_{\beta\gamma} e_k^{(\beta)} s_{\ell m}^{(\gamma)} a_\beta a_\gamma e^{i[(\omega_\beta+\omega_\gamma)t-(\bar{k}_\beta+\bar{k}_\gamma)\cdot\bar{r}']}\right.$$

$$\left. + \frac{1}{4}\sum_{\beta\gamma} e_k^{(\beta)} s_{\ell m}^{(\gamma)*} a_\beta a_\gamma^* e^{i[(\omega_\beta-\omega_\gamma)t+(\bar{k}_\beta-\bar{k}_\gamma)\cdot\bar{r}']} + \text{c.c.}\right\}$$

$$+\frac{1}{2}\theta_{ijk\ell mn}\left\{\frac{1}{4}\sum_{\beta\gamma} s_{k\ell}^{(\beta)} s_{mn}^{(\gamma)} a_\beta a_\gamma e^{i[(\omega_\beta+\omega_\gamma)t-(\bar{k}_\beta+\bar{k}_\gamma)\cdot\bar{r}']}\right.$$

$$\left. + \frac{1}{4}\sum_{\beta\gamma} s_{k\ell}^{(\beta)} s_{mn}^{(\gamma)*} a_\beta a_\gamma^* e^{i[(\omega_\beta-\omega_\gamma)t-(\bar{k}_\beta-\bar{k}_\gamma)\cdot\bar{r}']} + \text{c.c.}\right\}$$

$$-\frac{1}{2}\zeta_{k\ell ij}\frac{1}{4}\sum_{\beta\gamma} e_k^{(\beta)} e^{(\gamma)} a_\beta a_\gamma e^{i[(\omega_\beta+\omega_\gamma)t-(\bar{k}_\beta+\bar{k}_\gamma)\cdot\bar{r}']}$$

$$\left. + \frac{1}{4}\sum_{\beta\gamma} e_k^{(\beta)} e_\ell^{(\gamma)*} a_\beta a_\gamma^* e^{i[(\omega_\beta-\omega_\gamma)t-(\bar{k}_\beta-\bar{k}_\gamma)\cdot\bar{r}']} + \text{c.c.}\right\} \tag{IV.15}$$

The real external current density ($\bar{J}_e^r$) and real external force density ($\bar{F}_e^r$) are found from $\bar{\bar{T}}^{NL}$ and $\bar{D}^{NL}$ through the relations

$$\bar{F}_e^r = \bar{\nabla}\cdot\bar{\bar{T}}^{NL} \tag{IV.16}$$

$$\bar{J}_e^r = \frac{\partial}{\partial t}\bar{D}^{NL} \tag{IV.17}$$

In tensor form, one has

$$F^r_{ei} = \frac{\partial T^{NL}_{ij}}{\partial x_j} \tag{IV.18}$$

$$J^r_{ei} = \frac{\partial D^{NL}_i}{\partial t} \tag{IV.19}$$

In terms of the electric field, strain, and nonlinear constants, and keeping only terms to first order, F^r_{ei} and J^r_{ei} are given by:

$$F^r_{ei} = -\eta_{kij\ell m}\left(\frac{1}{4}\sum_{\beta\gamma}\left[a_\beta a_\gamma\left[\frac{\partial}{\partial x_j}\left(e^{(\beta)}_k s^{(\gamma)}_{\ell m}\right) - i\left(k^{(\beta)}_j + k^{(\gamma)}_j\right)e^{(\beta)}_k s^{(\gamma)}_{\ell m}\right]\right.\right.$$
$$\left.\left.e^{i[(\omega_\beta+\omega_\gamma)t-(\bar{k}_\beta+\bar{k}_\gamma)\cdot\bar{r}']}\right] +$$

$$\frac{1}{4}\sum_{\beta\gamma}\left[a_\beta a^*_\gamma\left[\frac{\partial}{\partial x_j}\left(e^{(\beta)}_k s^{(\gamma)*}_{\ell m}\right) - i\left(k^{(\beta)}_j - k^{(\gamma)}_j\right)e^{(\beta)}_k s^{(\gamma)*}_{\ell m}\right]\right.$$
$$\left.\left.e^{i[(\omega_\beta-\omega_\gamma)t-(\bar{k}_\beta-\bar{k}_\gamma)\cdot\bar{r}']}\right] + c.c\right) +$$

$$\frac{1}{2}\theta_{ijk\ell mn}\left(\frac{1}{4}\sum_{\beta\gamma}\left[a_\beta a_\gamma\left[\frac{\partial}{\partial x_j}\left(s^{(\beta)}_{k\ell} s^{(\gamma)}_{mn}\right) - i\left(k^{(\beta)}_j + k^{(\gamma)}_j\right)s^{(\beta)}_{k\ell} s^{(\gamma)}_{mn}\right]\right.\right.$$
$$\left.\left.e^{i[(\omega_\beta+\omega_\gamma)t-(\bar{k}_\beta+\bar{k}_\gamma)\cdot\bar{r}']}\right] +$$

$$\frac{1}{4}\sum_{\beta\gamma}\Sigma\left[a_\beta a_\gamma^*\left[\frac{\partial}{\partial x_j}\left(s_{k\ell}^{(\beta)}s_{mn}^{(\gamma)*}\right)-i\left(k_j^{(\beta)}-k_j^{(\gamma)}\right)s_{k\ell}^{(\beta)}s_{mn}^{(\gamma)*}\right]\right.$$

$$\left.e^{i[(\omega_\beta-\omega_\gamma)t-(\bar{k}_\beta-\bar{k}_\gamma)\cdot\bar{r}']}\right]+\text{c.c.}\Bigg)+$$

$$-\frac{1}{2}Q_{k\ell ij}\left(\frac{1}{4}\sum_{\beta\gamma}\Sigma\left[a_\beta a_\gamma\left[\frac{\partial}{\partial x_j}\left(e_k^{(\beta)}e_\ell^{(\gamma)}\right)-i\left(k_j^{(\beta)}+k_j^{(\gamma)}\right)e_k^{(\beta)}e_\ell^{(\gamma)}\right]\right.\right.$$

$$\left.\left.e^{i[(\omega_\beta+\omega_\gamma)t-(\bar{k}_\beta+\bar{k}_\gamma)\cdot\bar{r}']}\right]+\right.$$

$$\frac{1}{4}\sum_{\beta\gamma}\Sigma\left[a_\beta a_\gamma^*\left[\frac{\partial}{\partial x_j}\left(e_k^{(\beta)}e_\ell^{(\gamma)*}\right)-i\left(k_j^{(\beta)}-k_j^{(\gamma)}\right)e_k^{(\beta)}e_\ell^{(\gamma)*}\right]\right.$$

$$\left.\left.e^{i[(\omega_\beta-\omega_\gamma)t-(\bar{k}_\beta-\bar{k}_\gamma)\cdot\bar{r}']}\right]+\text{c.c.}\right) \qquad \text{(IV.20)}$$

$$J_{ei}^r = Q_{ijk\ell}\left(\frac{1}{4}\sum_{\beta\gamma}\Sigma\left[i(\omega_\beta+\omega_\gamma)e_j^{(\beta)}s_{k\ell}^{(\gamma)}a_\beta a_\gamma e^{i[(\omega_\beta+\omega_\gamma)t-(\bar{k}_\beta+\bar{k}_\gamma)\cdot\bar{r}']}\right]+\right.$$

$$\left.\frac{1}{4}\sum_{\beta\gamma}\Sigma\left[i(\omega_\beta-\omega_\gamma)e_j^{(\beta)}s_{k\ell}^{(\gamma)*}a_\beta a_\gamma^* e^{i[(\omega_\beta-\omega_\gamma)t-(\bar{k}_\beta-\bar{k}_\gamma)\cdot\bar{r}']}\right]+\text{c.c}\right)+$$

$$\frac{1}{2}\eta_{ijk\ell mn}\left(\frac{1}{4}\sum_{\beta\gamma}\Sigma\left[i(\omega_\beta+\omega_\gamma)s_{jk}^{(\beta)}s_{\ell m}^{(\gamma)}a_\beta a_\gamma e^{i[(\omega_\beta+\omega_\gamma)t-(\bar{k}_\beta+\bar{k}_\gamma)\cdot\bar{r}']}\right]+\right.$$

$$\frac{1}{4}\sum_{\beta\gamma}\sum\left[i(\omega_\beta-\omega_\gamma)s_{jk}^{(\beta)}s_{\ell m}^{(\gamma)*}a_\beta a_\gamma^* e^{i[(\omega_\beta-\omega_\gamma)t-(\bar{k}_\beta-\bar{k}_\gamma)\cdot\bar{r}']}\right]+\text{c.c.}\Bigg)+$$

$$\frac{1}{2}O_{ijk}\Bigg(\frac{1}{4}\sum_{\beta\gamma}\sum\left[i(\omega_\beta+\omega_\gamma)e_j^{(\beta)}e_{k\ell}^{(\gamma)}a_\beta a_\gamma e^{i[(\omega_\beta+\omega_\gamma)t-(\bar{k}_\beta+\bar{k}_\gamma)\cdot\bar{r}']}\right]+$$

$$\frac{1}{4}\sum_{\beta\gamma}\sum\left[i(\omega_\beta-\omega_\gamma)e_j^{(\beta)}e_k^{(\gamma)*}a_\beta a_\gamma^* e^{i[(\omega_\beta-\omega_\gamma)t-(\bar{k}_\beta-\bar{k}_\gamma)\cdot\bar{r}']}\right]+\text{c.c.}\Bigg) \qquad \text{(IV.21)}$$

F_{ei}^r and J_{ei}^r consist of sums of complex terms and the complex conjugates of these terms. Therefore, F_{ei}^r and J_{ei}^r can be represented as

$$F_{ei}^r = \frac{F_{ei} + F_{ei}^*}{2} \qquad \text{(IV.22)}$$

$$J_{ei}^r = \frac{J_{ei} + J_{ei}^*}{2} \qquad \text{(IV.23)}$$

where F_{ei} and J_{ei} are components of $\bar{F}_e$ and $\bar{J}_e$ respectively. F_{ei} and J_{ei} can be found from (IV.20) and (IV.21) and are:

$$F_{ei} = -\eta_{kij\ell m}\left\{\frac{1}{2}\sum_{\beta\gamma}\sum\left[a_\beta a_\gamma\left[\frac{\partial}{\partial x_j}\left(e_k^{(\beta)}s_{\ell m}^{(\gamma)}+(1-\delta_{\beta\gamma})e_k^{(\beta)}s_{\ell m}^{(\gamma)}\right)-i\left(k_j^{(\beta)}+k_j^{(\gamma)}\right)\right.\right.\right.$$

$$\left.\left.\left.\left(e_k^{(\beta)}s_{\ell m}^{(\gamma)}+(1-\delta_{\beta\gamma})e_k^{(\gamma)}s_{\ell m}^{(\beta)}\right)\right]e^{i[(\omega_\beta+\omega_\gamma)t-(\bar{k}_\beta+\bar{k}_\gamma)\cdot\bar{r}']}\right]\right.$$

$$+\frac{1}{2}\sum_{\beta\gamma}\sum\left[a_\beta a_\gamma^*\left[\frac{\partial}{\partial x_j}\left(e_k^{(\beta)}s_{\ell m}^{(\gamma)*}+(1-\delta_{\beta\gamma})e_k^{(\gamma)*}s_{\ell m}^{(\beta)}\right)-i\left(k_j^{(\beta)}-k_j^{(\gamma)}\right)\right.\right.$$

$$\left.\left.\left.\left(e_k^{(\beta)}s_{\ell m}^{(\gamma)*}+(1-\delta_{\beta\gamma})e_k^{(\gamma)*}s_{\ell m}^{(\beta)}\right)\right]e^{i[(\omega_\beta-\omega_\gamma)t-(\bar{k}_\beta-\bar{k}_\gamma)\cdot\bar{r}']}\right]\right\}$$

$$+\frac{1}{2}\theta_{ijk\ell mn}\left\{\frac{1}{2}\sum_{\beta\gamma}\sum\left[a_\beta a_\gamma\left[\frac{\partial}{\partial x_j}\left(s_{k\ell}^{(\gamma)}s_{mn}^{(\beta)}+(1-\delta_{\beta\gamma})s_{k\ell}^{(\gamma)}s_{mn}^{(\beta)}\right)-i\left(k_j^{(\beta)}+k_j^{(\gamma)}\right)\right.\right.\right.$$

$$\left.\left.\left.\left(s_{k\ell}^{(\beta)}s_{mn}^{(\gamma)}+(1-\delta_{\beta\gamma})s_{k\ell}^{(\gamma)}s_{mn}^{(\beta)}\right)\right]e^{i[(\omega_\beta+\omega_\gamma)t-(\bar{k}_\beta+\bar{k}_\gamma)\cdot\bar{r}']}\right]\right.$$

$$+\frac{1}{2}\sum_{\beta\gamma}\sum\left[a_\beta a_\gamma^*\left[\frac{\partial}{\partial x_j}\left(s_{k\ell}^{(\beta)}s_{mn}^{(\gamma)*}+(1-\delta_{\beta\gamma})s_{k\ell}^{(\gamma)*}s_{mn}^{(\beta)}\right)-i\left(k_j^{(\beta)}-k_j^{(\gamma)}\right)\right.\right.$$

$$\left.\left.\left.\left(s_{k\ell}^{(\beta)}s_{mn}^{(\gamma)*}+(1-\delta_{\beta\gamma})s_{k\ell}^{(\gamma)*}s_{mn}^{(\beta)}\right)\right]e^{i[(\omega_\beta-\omega_\gamma)t-(\bar{k}_\beta-\bar{k}_\gamma)\cdot\bar{r}']}\right]\right\}$$

$$-\frac{1}{2}Q_{k\ell ij}\left\{\frac{1}{2}\sum_{\beta\gamma}\sum\left[a_\beta a_\gamma\left[\frac{\partial}{\partial x_j}\left(e_k^{(\beta)}e_\ell^{(\gamma)}+(1-\delta_{\beta\gamma})e_k^{(\gamma)}e_\ell^{(\beta)}\right)-i\left(k_j^{(\gamma)}+k_j^{(\beta)}\right)\right.\right.\right.$$

$$\left(e_k^{(\beta)}e_\ell^{(\gamma)}+(1-\delta_{\beta\gamma})e_k^{(\gamma)}e_\ell^{(\beta)}\right)\Bigg]e^{i[(\omega_\beta+\omega_\gamma)t-(\bar{k}_\beta+\bar{k}_\gamma)\cdot\bar{r}']}\Bigg]$$

$$+\frac{1}{2}\sum_{\beta\gamma}\sum\Bigg[a_\beta a_\gamma\Bigg[\frac{\partial}{\partial x_j}\left(e_k^{(\beta)}e_\ell^{(\gamma)*}+(1-\delta_{\beta\gamma})e_k^{(\gamma)*}e_\ell^{(\beta)}\right)-i\left(k_j^{(\beta)}-k_j^{(\gamma)}\right)$$

$$\left(e_k^{(\gamma)*}e_\ell^{(\beta)}+(1-\delta_{\beta\gamma})e_k^{(\gamma)*}e_\ell^{(\beta)}\right)\Bigg]e^{i[(\omega_\beta-\omega_\gamma)t-(\bar{k}_\beta-\bar{k}_\gamma)\cdot\bar{r}']}\Bigg]\Bigg) \tag{IV.24}$$

$$J_{ei}=Q_{ijk\ell}\Bigg(\frac{1}{2}\sum_{\beta\gamma}\sum\Bigg[i\,a_\beta a_\gamma(\omega_\beta+\omega_\gamma)\left(e_j^{(\beta)}s_{k\ell}^{(\gamma)}+(1-\delta_{\beta\gamma})e_j^{(\gamma)}s_{k\ell}^{(\beta)}\right)$$

$$e^{i[(\omega_\beta+\omega_\gamma)t-(\bar{k}_\beta+\bar{k}_\gamma)\cdot\bar{r}']}\Bigg]$$

$$+\frac{1}{2}\sum_{\beta\gamma}\sum\Bigg[i\,a_\beta a_\gamma^*(\omega_\beta-\omega_\gamma)\left(e_j^{(\beta)}s_{k\ell}^{(\gamma)*}+(1-\delta_{\beta\gamma})e_j^{(\gamma)*}s_{k\ell}^{(\beta)}\right)$$

$$e^{i[(\omega_\beta-\omega_\gamma)t-(\bar{k}_\beta-\bar{k}_\gamma)\cdot\bar{r}']}\Bigg]\Bigg)$$

$$+\frac{1}{2}\eta_{ijk\ell m}\Bigg(\frac{1}{2}\sum_{\beta\gamma}\sum\Bigg[i\,a_\beta a_\gamma(\omega_\beta+\omega_\gamma)\left(s_{k\ell}^{(\beta)}s_{mn}^{(\gamma)}+(1-\delta_{\beta\gamma})s_{k\ell}^{(\gamma)}s_{mn}^{(\beta)}\right)$$

$$e^{i[(\omega_\beta+\omega_\gamma)t-(\bar{k}_\beta+\bar{k}_\gamma)\cdot\bar{r}']}\Bigg]$$

$$+\frac{1}{2}\sum_{\beta\gamma}\Bigg[i\, a_\beta a^*_\gamma(\omega_\beta-\omega_\gamma)\left(s^{(\beta)}_{k\ell}s^{(\gamma)*}_{mn}+(1-\delta_{\beta\gamma})s^{(\gamma)*}_{k\ell}s^{(\beta)}_{mn}\right) e^{\,i[(\omega_\beta-\omega_\gamma)t-(\bar{k}_\beta-\bar{k}_\gamma)\cdot\bar{r}']}\Bigg]$$

$$+\frac{1}{2}O_{ijk}\Bigg\{\frac{1}{2}\sum_{\beta\gamma}\Bigg[i\, a_\beta a_\gamma(\omega_\beta+\omega_\gamma)\left(e^{(\beta)}_j e^{(\gamma)}_k+(1-\delta_{\beta\gamma})e^{(\gamma)}_j e^{(\beta)}_k\right) e^{\,i[(\omega_\beta+\omega_\gamma)t-(\bar{k}_\beta+\bar{k}_\gamma)\cdot\bar{r}']}\Bigg]$$

$$+\frac{1}{2}\sum_{\beta\gamma}\Bigg[i\, a_\beta a^*_\gamma(\omega_\beta-\omega_\gamma)\left(e^{(\beta)}_j e^{(\gamma)*}_k+(1-\delta_{\beta\gamma})e^{(\gamma)*}_j e^{(\beta)}_k\right) e^{\,i[(\omega_\beta-\omega_\gamma)t-(\bar{k}_\beta-\bar{k}_\gamma)\cdot\bar{r}']}\Bigg]\Bigg\} \qquad \text{(IV.25)}$$

with $\beta \geq \gamma$, and

$$\delta_{\beta\gamma} = \begin{cases} 1, & \beta=\gamma \\ 0, & \beta\neq\gamma \end{cases}$$

The complex external perturbations $\bar{F}_e$ and $\bar{J}_e$ are then specified by:

$$\bar{J}_e = J_{ei}\,\hat{x}_i \qquad \text{(IV.26)}$$

$$\bar{F}_e = F_{ei}\,\hat{x}_i \qquad \text{(IV.27)}$$

Substituting the results of (IV.24)-(IV.27) into equation (2.C.33) and regrouping terms one has:

$$\frac{\partial a_\alpha}{\partial t} + \bar{v}_{g\alpha}\cdot\bar{\nabla}a_\alpha + \nu_\alpha a_\alpha = \frac{1}{8<W_\alpha>}\int^{\infty} dx_3 \left\{ \sum_{\beta\gamma}\sum \left\{ a_\beta a_\gamma e^{i(\delta\omega^+ t - \delta\bar{k}^+\cdot\bar{r}')} \right.\right.$$

$$\left\{ v_i^{(\alpha)*}\left[-i\left(k_j^{(\beta)} + k_j^{(\gamma)} \right) + \frac{\partial}{\partial x_j} \right]\right.$$

$$\left[-\eta_{kij\ell m}\left(e_k^{(\beta)} s_m^{(\gamma)} + (1-\delta_{\beta\gamma}) e_k^{(\gamma)} s_{\ell m}^{(\beta)} \right)\right.$$

$$+\tfrac{1}{2}\theta_{ijk\ell mn}\left(s_{k\ell}^{(\beta)} s_{mn}^{(\gamma)} + (1-\delta_{\beta\gamma}) s_{k\ell}^{(\gamma)} s_{mn}^{(\beta)} \right)$$

$$\left.\left.-\tfrac{1}{2}Q_{k\ell ij}\left(e_k^{(\beta)} e_\ell^{(\gamma)} + (1-\delta_{\beta\gamma}) e_k^{(\gamma)} e_\ell^{(\beta)} \right)\right]\right.$$

$$-ie_i^{(\alpha)*}(\omega_\beta + \omega_\gamma)\left[Q_{ijk\ell}\left(e_j^{(\beta)} s_{k\ell}^{(\gamma)} + (1-\delta_{\beta\gamma}) e_j^{(\gamma)} s_{k\ell}^{(\beta)} \right)\right.$$

$$+\tfrac{1}{2}\eta_{ijk\ell m}\left(s_{jk}^{(\beta)} s_{\ell m}^{(\gamma)} + (1-\delta_{\beta\gamma}) s_{jk}^{(\gamma)} s_{\ell m}^{(\beta)} \right)$$

$$\left.\left.\left.+\tfrac{1}{2}O_{ijk}\left(e_j^{(\beta)} e_k^{(\gamma)} + (1-\delta_{\beta\gamma}) e_j^{(\gamma)} e_k^{(\beta)} \right)\right]\right]\right)$$

$$+a_\beta a_\gamma^* e^{i(\delta\omega^- t - \delta\bar{k}^- \cdot \bar{r}')}$$

$$\left\{ v_i^{(\alpha)*} \left[-i\left(k_j^{(\beta)} - k_j^{(\gamma)}\right) + \frac{\partial}{\partial x_j} \right] \right.$$

$$\left[-\eta_{kij\ell m}\left(e_k^{(\beta)} s_{\ell m}^{(\gamma)*} + (1-\delta_{\beta\gamma}) e_k^{(\gamma)*} s_{\ell m}^{(\beta)} \right) \right.$$

$$+\frac{1}{2}\theta_{ijk\ell mn}\left(s_{k\ell}^{(\beta)} s_{mn}^{(\gamma)*} + (1-\delta_{\beta\gamma}) s_{k\ell}^{(\gamma)*} s_{mn}^{(\beta)} \right)$$

$$\left. -\frac{1}{2}Q_{k\ell ij}\left(e_k^{(\beta)} e_\ell^{(\gamma)*} + (1-\delta_{\beta\gamma}) e_k^{(\gamma)*} e_\ell^{(\beta)} \right) \right]$$

$$-ie_i^{(\alpha)*}(\omega_\beta - \omega_\gamma)\left[Q_{ijk\ell}\left(e_j^{(\beta)} s_{k\ell}^{(\gamma)*} + (1-\delta_{\beta\gamma}) e_j^{(\gamma)*} s_{k\ell}^{(\beta)} \right) \right.$$

$$+\frac{1}{2}\eta_{ijk\ell m}\left(s_{jk}^{(\beta)} s_{\ell m}^{(\gamma)*} + (1-\delta_{\beta\gamma}) s_{jk}^{(\gamma)*} s_{\ell m}^{(\beta)} \right)$$

$$\left. \left. +\frac{1}{2}\theta_{ijk}\left(e_j^{(\beta)} e_k^{(\gamma)*} + (1-\delta_{\beta\gamma}) e_j^{(\gamma)*} e_k^{(\beta)} \right) \right] \right\} \qquad \text{(IV.28)}$$

with

$$\delta\omega^+ = \omega_\beta + \omega_\gamma - \omega_\alpha, \qquad \delta\bar{k}^+ = \bar{k}_\beta + \bar{k}_\gamma - \bar{k}_\alpha,$$

$$\delta\omega^- = \omega_\beta - \omega_\gamma - \omega_\alpha, \qquad \delta\bar{k}^- = \bar{k}_\beta - \bar{k}_\gamma - \bar{k}_\alpha,$$

and

$$\left[-i\left(k_j^{(\beta)}+k_j^{(\gamma)}\right) + \frac{\partial}{\partial x_j}\right] ;$$

$$\left[-i\left(k_j^{(\beta)}-k_j^{(\gamma)}\right) + \frac{\partial}{\partial x_j}\right]$$

are operators applied prior to intergration over x_3. The integration is from $0 \leq x_3 \leq \infty$ because the nonlinearities exist only in this region.

Equation (IV.28) is the nonlinearly coupled amplitude equation.

APPENDIX V

FIELD QUANTITY NORMALIZATION

The discussion given here explains the procedure to obtain normalized terms independent of power and frequency, and characteristic only of the material cut and propagation direction. An example is given in which field quantities are calculated for a specified frequency and power density.

The components of $\bar{u}(x_1,x_3,t)$ the mechanical displacement for a normal mode and $\phi(x_1,x_3,t)$ the electric potential for a quasistatic approximation, can be represented as [49],[50]

$$u_i(x_1,x_3,t) = \left[\sum_{\ell=1}^{4} B^{(\ell)}\beta_i^{(\ell)} e^{-\alpha^{(\ell)}\omega x_3/v_s}\right] e^{i(\omega t-kx_1)} \qquad (V.1)$$

$$\phi(x_1,x_3,t) = \left[\sum_{\ell=1}^{4} B^{(\ell)}\beta_4^{(\ell)} e^{-\alpha^{(\ell)}\omega x_3/v_s}\right] e^{i(\omega t-kx_1)} \qquad (V.2)$$

where

$\alpha^{(\ell)}$ = exponential decay constant into the material,

$B^{(\ell)}$ = partial field amplitude associated with each $\alpha^{(\ell)}$,

$\beta_i^{(\ell)}$ = i^{th} sub-amplitude (i=1,2,3,4) of a given $\alpha^{(\ell)}$,

x_1 = phase propagation direction,

x_3 = decay direction [Fig. I.1],

v_s = phase velocity.

The unperturbed polarization amplitudes are:

$$u_i = u_i(x_3) = \sum_{\ell=1}^{4} B^{(\ell)} \beta_i^{(\ell)} e^{-\alpha^{(\ell)} \omega x_3 / v_s} \qquad (V.3)$$

$$\phi = \phi(x_3) = \sum_{\ell=1}^{4} B^{(\ell)} \beta_4^{(\ell)} e^{-\alpha^{(\ell)} \omega x_3 / v_s} \qquad (V.4)$$

Reference [49] and [50] give a procedure for finding the $\alpha^{(\ell)}$'s and ratios of β's and B's. The $\alpha^{(\ell)}$'s are derived from the dispersion relation for the exponentially decaying surface waves. When $\alpha^{(\ell)}$'s are found, ratios of $\beta_i^{(\ell)}$'s can be determined as eigenvectors of the matrix derived from the equations of motion and used to compute $\alpha^{(\ell)}$'s and the ratios of the partial field amplitudes can be found from boundary conditions. Because one can only determine ratios of β's and B's, a normalization procedure must be determined to compute actual field amplitudes.

The normalization of the field quantities is derived from the fact that every surface acoustic wave carries mechanical power and a component of this power can always be taken in the phase velocity direction. From [49], the ratio of the complex mechanical power density flowing in the phase velocity direction (P_{1m}) to the radial frequency is given by [49]:

$$\frac{P_{lm}}{\omega} = \frac{1}{2} \sum_{\ell=1}^{4} \sum_{k=1}^{4} \frac{B^{(k)*}B^{(\ell)}}{\alpha^{(\ell)}+\alpha^{(k)*}} \Bigg\{ \beta_1^{(k)*} \Big[\beta_1^{(\ell)} \left(C_{11}-i\alpha^{(\ell)}C_{15}\right)+\beta_2^{(\ell)} \left(C_{16}-i\alpha^{(\ell)}C_{14}\right) +\beta_3^{(\ell)} \left(C_{15}-i\alpha^{(\ell)}C_{13}\right)+\beta_4^{(\ell)} \left(e_{11}-i\alpha^{(\ell)}e_{31}\right) \Big]$$

$$\beta_2^{(k)*} \Big[\beta_1^{(\ell)} \left(C_{16}-i\alpha^{(\ell)}e_{36}\right)+\beta_2^{(\ell)} \left(C_{66}-i\alpha^{(\ell)}C_{46}\right) +\beta_3^{(\ell)} \left(C_{56}-i\alpha^{(\ell)}C_{36}\right)+\beta_4^{(\ell)} \left(e_{16}-i\alpha^{(\ell)}C_{45}\right) \Big]$$

$$\beta_3^{(k)*} \Big[\beta_1^{(\ell)} \left(C_{15}-i\alpha^{(\ell)}C_{55}\right)+\beta_2^{(\ell)} \left(C_{56}-i\alpha^{(\ell)}C_{45}\right) +\beta_3^{(\ell)} \left(C_{55}-i\alpha^{(\ell)}C_{35}\right)+\beta_4^{(\ell)} \left(e_{15}-i\alpha^{(\ell)}e_{35}\right) \Big] \Bigg\} \tag{V.5}$$

with

C_{ij} = elastic constants

e_{ij} = piezoelectric constants

in Voight notation. (V.3) can be rewritten as:

$$\frac{P_{lm}}{\omega} = \frac{1}{2} \sum_{\ell=1}^{4} \sum_{k=1}^{4} \sum_{i=1}^{3} \sum_{j=1}^{4} \frac{B^{(k)*}B^{(\ell)}\beta_i^{(k)*}\beta_j^{(\ell)}M_{ij}^{(\ell)}}{(\alpha^{(\ell)}+\alpha^{(k)*})} \tag{V.6}$$

where $M_{ij}^{(\ell)}$ are composed of the C_{ij}, e_{ij}, and $\alpha^{(\ell)}$ from (V.5).

Since only ratios of β's and B's can be determined from the matrix that gives the dispersion relation, and the boundary conditions, (V.5) can be case as:

$$\frac{P_{1m}}{\omega} = |B^{(4)}\beta_4^{(4)}|^2 \left\{ \sum_{\ell=1}^{4} \sum_{k=1}^{4} \sum_{i=1}^{3} \sum_{j=1}^{4} \left[\frac{1}{2(\alpha^{(\ell)}+\alpha^{(k)*})} \right] \left[\frac{B^{(k)*}\beta_4^{(k)*}}{B^{(4)*}\beta_4^{(4)*}} \right] \left[\frac{B^{(\ell)}\beta_4^{(\ell)}}{B^{(4)}\beta_4^{(4)}} \right] \left[\frac{\beta_i^{(k)*}\beta_j^{(\ell)}}{\beta_4^{(k)*}\beta_1^{(\ell)}} \right] M_{ij}^{(\ell)} \right\} \qquad (V.7)$$

For a given material cut and propagation direction $M_{ij}^{(\ell)}$ is known. The ratios $\frac{B^{(\ell)}\beta_4^{(\ell)}}{B^{(4)}\beta_4^{(4)}}$ and its complex conjugate are found from the boundary conditions, and $\frac{\beta_i^{(\ell)}}{\beta_4^{(\ell)}}$ and its complex conjugate are determined from the matrix whose determinant gives the dispersion relation to find $\alpha^{(\ell)}$. Thus the only unknown term is $|B^{(4)}\beta_4^{(4)}|^2$. Since one only works with real powers,

$$\frac{R_e P_{1m}}{\omega} = |B^{(4)}\beta_4^{(4)}|^2 R_e \hat{P}_{1m}, \qquad (V.8)$$

where $\hat{P}_{1m}$ is the term within the braces of (V.7). Therefore

$$|B^{(4)}\beta_4^{(4)}| = \left[\frac{R_e P_{1m}}{\omega \, R_e \hat{P}_{1m}} \right]^{1/2} \qquad (V.9)$$

By arbitrarily choosing the phase of the complex numbers $B^{(4)}$ and $\beta_4^{(4)}$ to be zero, one sets the phase of the other B's and β's, and thus

$$B^{(4)}\beta_4^{(4)} = |B^{(4)}\beta_4^{(4)}|. \tag{V.10}$$

Given the above discussion, one can rewrite (V.3) as:

$$u_i = B^4\beta_4^4 \sum_{\ell=1}^{4} \left[\frac{B^{(\ell)}\beta_4^{(\ell)}}{B^{(4)}\beta_4^{(4)}}\right]\left[\frac{\beta_i^{(\ell)}}{\beta_4^{(\ell)}}\right] e^{-\alpha^{(\ell)}\omega x_3/v_s} \tag{V.11}$$

$$u_i = \left[\frac{R_e P_{1m}}{\omega\ R_e P_{1m}}\right]^{1/2} \sum_{\ell=1}^{4} \left[\frac{B^{(\ell)}\beta_4^{(\ell)}}{B^{(4)}\beta_4^{(4)}}\right]\left[\frac{\beta_i^{(\ell)}}{\beta_4^{(\ell)}}\right] e^{-\alpha^{(\ell)}\omega x_3/v_s} \tag{V.12}$$

Dividing (V.11) by $\left(\frac{R_e P_{1m}}{\omega}\right)^{1/2}$;

$$\hat{u}_i = \frac{u_i}{\left(R_e \frac{P_{1m}}{\omega}\right)^{1/2}} = \sum_{\ell=1}^{4} \left[\frac{1}{R_e \hat{P}_{1m}}\right]^{1/2}\left[\frac{B^{(\ell)}\beta_4^{(\ell)}}{B^{(4)}\beta_4^{(4)}}\right]\left[\frac{\beta_i^{(\ell)}}{\beta_4^{(\ell)}}\right] e^{-\alpha^{(\ell)}\frac{\omega x_3}{v_s}} \tag{V.13}$$

let

$$\hat{U}_i^{(\ell)} = \left[\frac{1}{R_e \hat{P}_{1m}}\right]^{1/2}\left[\frac{B^{(\ell)}\beta_4^{(\ell)}}{B^{(4)}\beta_4^{(4)}}\right]\left[\frac{\beta_i^{(\ell)}}{\beta_4^{(\ell)}}\right] \tag{V.14}$$

and

$$\hat{u}_i = \sum_{\ell=1}^{4} \hat{U}_i^{(\ell)} \, e^{-\alpha^{(\ell)} \omega x_3 / v_s} \tag{V.15}$$

The $\hat{U}_i^{(\ell)}$ are independent of power and frequency and are composed of terms that are constant for a given material cut. One can find $\hat{\phi}$ in the same manner, with the result:

$$\hat{\phi} = \frac{\phi}{\left(R_e \frac{P_{1m}}{\omega} \right)^{1/2}} = \sum_{\ell=1}^{4} \hat{\Phi}^{(\ell)} \, e^{-\alpha^{(\ell)} \omega x_3 / v_s} \tag{V.16}$$

where

$$\hat{\Phi}^{(\ell)} = \frac{1}{(R_e \hat{P}_{1m})^{1/2}} \, \frac{B^{(\ell)} \beta_4^{(\ell)}}{B^{(4)} \beta_4^{(4)}} \tag{V.17}$$

Computer programs have been written [49], [50] to calculated the ratios $\frac{\beta_i^{(\ell)}}{\beta_4^{(\ell)}}$ and $\frac{B^{(\ell)} \beta_4^{(\ell)}}{B^{(4)} \beta_4^{(4)}}$. The last ratios are listed as the partial field amplitudes as given in [49] and [50] where $\beta_4^{(\ell)}$ and $\beta_4^{(4)}$ have been absorbed in $B^{(\ell)}$ and $B^{(4)}$ respectively; however, the result is still the ratio $\frac{B^{(\ell)} \beta_4^{(\ell)}}{B^{(4)} \beta_4^{(4)}}$. Therefore the partial field amplitudes $[\hat{B}^{(\ell)}]$ defined from [49] and [50] are

$$\hat{B}^{(\ell)} = \frac{B^{(\ell)} \beta_4^{(\ell)}}{B^{(4)} \beta_4^{(4)}} \, , \tag{V.18}$$

let

$$\hat{\beta}_i^{(\ell)} = \frac{\beta_i^{(\ell)}}{\beta_4^{(\ell)}} \tag{V.19}$$

Once the ratios are computed, $\hat{P}_{1m}$ is then calculated.

The field quantities of particular interest are e_i, $s_{k\ell}$, and v_i. These terms are found from $e_i(x_1,x_3,t)$, $s_{k\ell}(x_1,x_3,t)$, and $v_i(x_1,x_3,t)$ which are in turn found from (V.1) and (V.2)

$$e_i(x_1,x_3,t) = \frac{-\partial\phi(x_1,x_3,t)}{\partial x_i} \tag{V.20}$$

$$v_i(x_1,x_3,t) = \frac{\partial}{\partial t} u_i(x_1,x_3,t) \tag{V.21}$$

$$s_{k\ell}(x_1,x_3,t) = \frac{1}{2}\left[\frac{\partial u_k}{\partial x_\ell} + \frac{\partial u_\ell}{\partial x_k}\right] \tag{V.22}$$

e_i, $s_{k\ell}$, v_i are the unperturbed polarization amplitudes found from (V.20)-(V.22) as is done in (V.3)-(V.4). They are functions of x_3, ω, B's and β's. However, e_i/ω, v_i/ω, and $s_{k\ell}/\omega$ are functions only of x_3, B's and β's. By dividing these ratios of the field quantities to ω, by $(R_e P_{1m}/\omega)$, one is left with B's and β's and exponential decay terms. The normalized field quantities are then:

$$\hat{e}_i = \frac{e_i}{\omega\left(\frac{R_e P_{1m}}{\omega}\right)^{1/2}} = \sum_{\ell=1}^{4} \hat{E}_i^{(\ell)} e^{-\alpha^{(\ell)}\omega x_3/v_s} \tag{V.23}$$

$$\hat{v}_i = \frac{v_i}{\omega\left(\frac{R_e P_{1m}}{\omega}\right)^{1/2}} = \sum_{\ell=1}^{4} \hat{V}_i^{(\ell)} e^{-\alpha^{(\ell)}\omega x_3/v_s} \tag{V.24}$$

$$\hat{s}_{k\ell} = \frac{s_{k\ell}}{\omega\left(\frac{R_e P_{1m}}{\omega}\right)^{1/2}} = \sum_{\ell=1}^{4} \hat{S}_k^{(\ell)} \, e^{-\alpha^{(\ell)}\omega x_3/v_s} \tag{V.25}$$

with $\hat{E}_i^{(\ell)}$, $\hat{V}_i^{(\ell)}$, $\hat{S}_{k\ell}^{(\ell)}$ given in terms of the results for the computer programs [49]:

$$\hat{E}_1^{(\ell)} = \frac{i \, \hat{B}^{(\ell)} \hat{\beta}_4^{(\ell)}}{v_s[R_e(\hat{P}_{1m})]^{1/2}} \tag{V.26}$$

$$\hat{E}_2^{(\ell)} = 0 \tag{V.27}$$

$$\hat{E}_3^{(\ell)} = \frac{\alpha^{(\ell)} \hat{B}^{(\ell)} \hat{\beta}_4^{(\ell)}}{v_s[R_e(\hat{P}_{1m})]^{1/2}} \tag{V.28}$$

$$\hat{V}_i = \frac{i \, \hat{B}^{(\ell)} \hat{\beta}_i^{(\ell)}}{[R_e(\hat{P}_{1m})]^{1/2}} \tag{V.29}$$

$$\hat{S}_{11} = \frac{-i \, \hat{B}^{(\ell)} \hat{\beta}_1^{(\ell)}}{v_s[R_e(\hat{P}_{1m})]^{1/2}} \tag{V.30}$$

$$\hat{S}_{22} = 0 \tag{V.31}$$

$$\hat{S}_{33} = \frac{-\alpha^{(\ell)}\hat{B}^{(\ell)}\hat{\beta}_3^{(\ell)}}{v_s[R_e(\hat{P}_{1m})]^{1/2}} \tag{V.32}$$

$$\hat{S}_{12} = \hat{S}_{21} = \frac{-i\,\hat{B}^{(\ell)}\hat{\beta}_2^{(\ell)}}{2v_s[R_e(\hat{P}_{1m})]^{1/2}} \tag{V.33}$$

$$\hat{S}_{13} = \hat{S}_{31} = \frac{\hat{B}^{(\ell)}}{2[R_e(\hat{P}_{1m})]^{1/2}}\left[\frac{-\alpha^{(\ell)}\hat{\beta}_1^{(\ell)}}{v_s} - \frac{i\,\hat{\beta}_3^{(\ell)}}{v_s}\right] \tag{V.34}$$

$$\hat{S}_{23} = \hat{S}_{32} = \frac{-\alpha^{(\ell)}\hat{B}^{(\ell)}\hat{\beta}_2^{(\ell)}}{2v_s[R_e(\hat{P}_{1m})]^{1/2}} \tag{V.35}$$

(V.26)-(V.35) are all constants independent of power and frequency. It is these terms that appear in $C^{\pm}_{\alpha\beta\gamma}$ after operations of differentiation and integration are carried through.

To see how the normalize field quantities are used in calculating the actual field quantities, the perpendicular component of displacement $u_3(x_3=0)$ shall be calculated for YZ-$LiNbO_3$ with a free surface. Reference [49] calculates $\hat{B}^{(\ell)}$, $\hat{\beta}_i^{(\ell)}$, $\alpha^{(\ell)}$ and $R_e(\hat{P}_{1m})$ for YZ-$LiNbO_3$. From (V.13), (V.18) and (V.19)

$$\hat{u}_3(x_3) = \sum_{\ell=1}^{4} \frac{1}{[R_e P_{1m}]^{1/2}}\,\hat{B}^{(\ell)}\hat{\beta}_3^{(\ell)}\; e^{-\alpha^{(\ell)}\omega x_3/v_s} \tag{V.36}$$

and from [49]

$$\hat{B}^{(1)} = 0.00$$

$$\hat{B}^{(2)} = 7.20\text{x}10^{-1} + 8.09\text{x}10^{-1}\,i$$

$$\hat{B}^{(3)} = -1.5.\text{x}10^{-1} - 1.38\text{x}10^{-1}\,i$$

$$\hat{B}^{(4)} = 1.00$$

$$\hat{\beta}_3^{(1)} = -6.58\text{x}10^{-11} + 4.09\text{x}10^{-12}\,i \left[\frac{\text{meters}}{\text{volt}}\right]$$

$$\hat{\beta}_3^{(2)} = 0.00 \left[\frac{\text{meters}}{\text{volt}}\right]$$

$$\hat{\beta}_3^{(3)} = -2.48\text{x}10^{-10} + 5.44\text{x}10^{-10}\,i \left[\frac{\text{meters}}{\text{volt}}\right]$$

$$\hat{\beta}_3^{(4)} = 1.00 \left[\frac{\text{meters}}{\text{volt}}\right]$$

$$R_e(\hat{P}_{1m}) = 2.22\text{x}10^{-9} [\text{Watt-seconds/meter-Volts}^2]$$

$$v_s = 3487.689 \text{ meters/second}$$

$$\alpha^{(1)} = 1.53\text{x}10^{-1} + 1.20\text{x}10^{-1}\,i$$

$$\alpha^{(2)} = 7.74\text{x}10^{-1} + 3.96\text{x}10^{-1}\,i$$

$$\alpha^{(3)} = 1.22\text{x}10^{-1} - 6.46\text{x}10^{-2}\text{i}$$

$$\alpha^{(4)} = 1.04 - 3.80\text{x}10^{-1}\text{i}$$

Substituting these values into (V.36) gives the numerical expressions for $\hat{u}_3(x_3)$. Fig. V.1 is a graphical representation of $|\hat{u}(x_3)|$ vs. ωx_3 [50]. Reference [50] specifies the phase of $B_4^{(4)}$ and $\beta_4^{(4)}$ so that the phase of $\hat{u}_1(x_3=0)$ is zero.

The result of the calculations as done from [49] gives for $\hat{u}_3(x_3=0)$:

$$\hat{u}_3(x_3=0) = 2.62\text{x}10^{-6}\ e^{(-15.145\pi/180)\text{meter}}\left[\frac{\text{meter}}{\text{Watt-seconds}}\right]^{1/2} \qquad \text{(V.37)}$$

In addition to calculating $R_e\hat{P}_{1m}$; $R_e\hat{P}_{1E}$, $R_e\hat{P}_{2E}$ and $R_e\hat{P}_{2m}$ are also calculated. The ratios

$$\frac{R_eP_{1E}/\omega}{R_eP_{1m}/\omega} = \frac{R_e\hat{P}_{1E}}{R_e\hat{P}_{1m}} = -4.09\text{x}10^{-2}$$

$$\frac{R_eP_{2E}/\omega}{R_eP_{1m}/\omega} = \frac{R_e\hat{P}_{2E}}{R_e\hat{P}_{1m}} = 0$$

$$\frac{R_eP_{2m}/\omega}{R_eP_{1m}/\omega} = \frac{R_e\hat{P}_{2m}}{R_e\hat{P}_{1m}} = 0.$$

Fig. V.1

Normalized Verticle Displacement
vs. Normalized Decay Depth

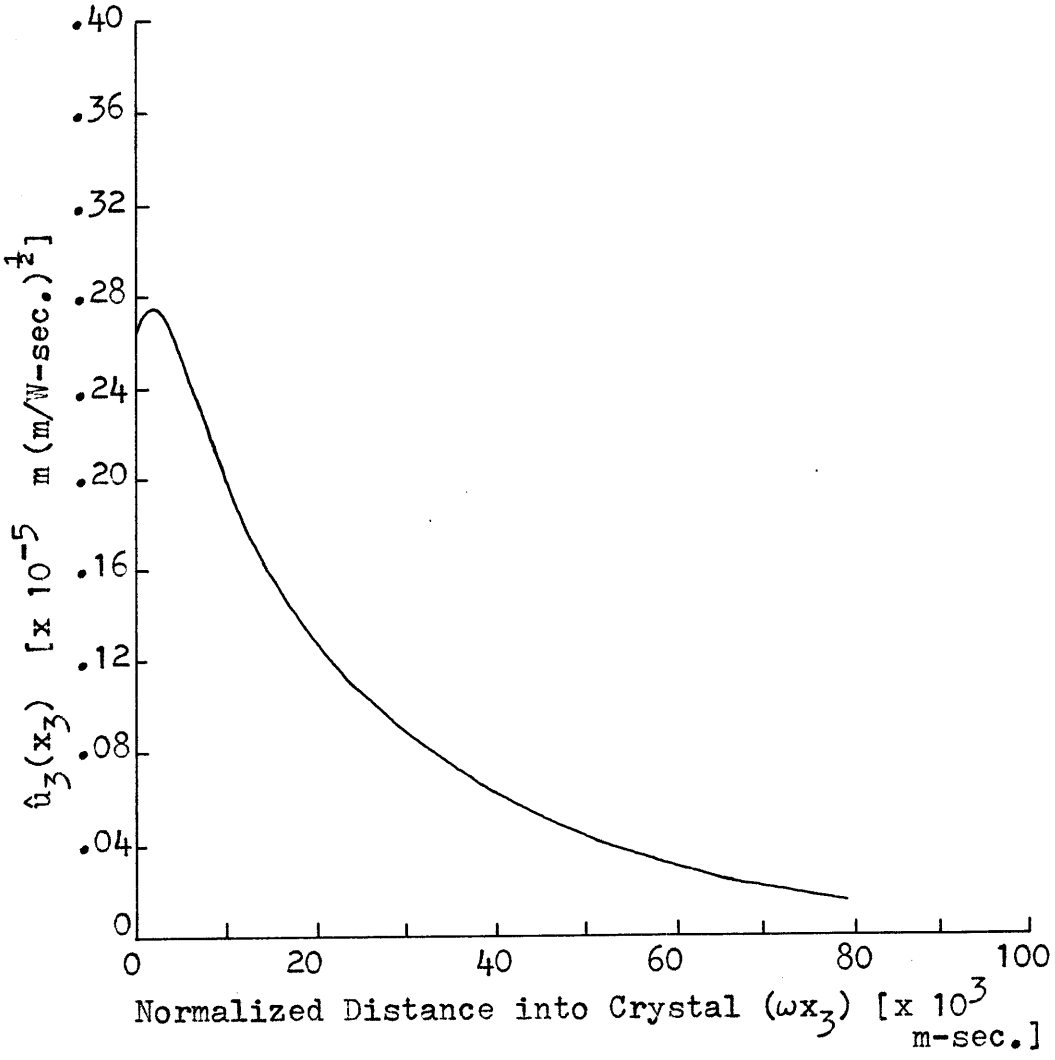

Therefore P_{1m} can be approximated as the total power density of a SAW.

To calculate $u_3(x_3=0)$ from $\hat{u}_3(x_3=0)$ for a specific example, consider

$$P_{ac}(\text{Total Power of SAW}) = 10^{-2} \text{ Watt}$$
$$b(\text{beam width}) = 2\text{x}10^{-3} \text{ meters}$$
$$\omega = 2\pi\text{x}100 \text{ Megahertz}$$

therefore

$$\frac{R_e P_{1m}}{\omega} = \frac{10^{-2} \text{ Watt}}{2\text{x}10^{-3}\text{m} \cdot \frac{2\pi\text{x}10^8}{\text{sec}}}$$

$$\left[\frac{R_e P_{1m}}{\omega}\right]^{1/2} = \left[\frac{10^{-7}}{2\pi} \frac{\text{Watt-sec}}{\text{m}}\right]^{1/2} \qquad \text{(V.38)}$$

Multiplying (V.37) by (V.38)

$$u_3(x_3=0) = 2.3\text{x}10^{-10} \text{ meters } e^{-.264i} \qquad \text{(V.39)}$$

Reference [50] would give a slightly different result. In this case $B_4^{(4)}$ and $\beta_i^{(4)}$ are chosen so that the phase of $\hat{u}_1$ is zero at $x_3=0$. Hence for [50]

$$u_3^s(x_3=0) = 2.3\text{x}10^{-10} \text{ meters } e^{1.576i} \tag{V.40}$$

In calculating a field quantity such as strain, or electric field, one multiplies $\hat{s}_{k\ell}$, $\hat{e}_i$ by $\omega\left(\frac{R_e P_{1m}}{\omega}\right)^{1/2}$. For this example $\hat{e}_1(x_3=0)$ and $\hat{s}_{11}(x_3=0)$, one has

$$\hat{e}_1(x_3=0) = 4.17e^{(-200.27\cdot\pi/180)i}\left[\frac{\text{Volts}}{\text{m}} \sec\left(\frac{\text{meters-Volts}^2}{\text{Watt-sec}}\right)^{1/2}\right] \tag{V.41}$$

$$\hat{s}_{11}(x_3=0) = 5.09\text{x}10^{-10}e^{(-195.44\cdot\pi/180)i}\left[\sec\left(\frac{\text{meters}}{\text{Watt-sec}}\right)^{1/2}\right] \tag{V.42}$$

Multiplying (V.41) and (V.42) by $\omega\left[\frac{R_e P_{1m}}{\omega}\right]^{1/2}$ and using the same values for ω and $\left[\frac{R_e P_{1m}}{\omega}\right]^{1/2}$ from the $u_3(x_3=0)$ example, gives:

$$e_1(x_3=0) = 3.31\text{x}10^5 \; e^{-3.495i} \text{ Volts/m} \tag{V.43}$$

$$s_{11}(x_3=0) = 4.03\text{x}10^{-5} \; e^{-3.411i} \tag{V.44}$$

From [50] (V.43) and (V.44) are:

$$e_1^s(x_3=0) = 3.31\times10^5\ e^{-1.491i}\ \text{Volts/m} \qquad \text{(V.45)}$$

$$s_{11}^s(x_3=0) = 4.03\times10^{-5}\ e^{-1.571i}$$

APPENDIX VI

CALCULATION OF K^{+}_{211} FOR YZ-$LiNbO_3$

For resonant collinear second harmonic generation, $\hat{C}^{+}_{211}$ is found from (2.E.26). Considering only elastic nonlinearities one has

$$\hat{C}^{+}_{211} = -i\theta_{il k\ell mn}\hat{V}_i^{(r)}\hat{S}_{k\ell}^{(t)}\hat{S}_{mn}^{(w)}[\alpha^{(t)} + \alpha^{(w)} + 2\alpha^{(r)*}]^{-1}$$

$$- \frac{1}{2}\theta_{i3k\ell mn}\hat{V}_i^{(r)}\hat{S}_{k\ell}^{(t)}\hat{S}_{mn}^{(w)}\left[\frac{\alpha^{(t)} + \alpha^{(w)}}{\alpha^{(t)} + \alpha^{(w)} + 2\alpha^{(r)*}}\right] \qquad \text{(VI.1)}$$

The superscripts for each mode have been dropped since the terms $\hat{V}_i^{(r)}$, $\hat{S}_k^{(t)}$, $\hat{S}_{mn}^{(w)}$ and $\alpha^{(t)}$, $\alpha^{(w)}$, $\alpha^{(r)}$ are constants for all modes propagating collinearly. Because the group and phase velocity vectors are identical for YZ-$LiNbO_3$, and choosing x_1 in the phase propagation direction, there is no contribution for j=2. Sum over repeated indices is assumed with

$i,k,\ell,m,n = 1,2,3;$

$t,w,r = 1,2,3,4.$

Appendix V discusses how $\hat{V}_i^{(r)}$, $\hat{S}_{k\ell}^{(t)}$, $\hat{S}_{mn}^{(w)}$ are calculated from [49], and the numerical values of the terms that contribute to $\hat{V}_i^{(r)}$, $\hat{S}_{k\ell}^{(t)}$, $\hat{S}_{mn}^{(w)}$ are listed for YZ-$LiNbO_3$. The four α's for YZ-$LiNbO_3$ are also given in Appendix V.

Because of the degeneracies of YZ-$LiNbO_3$ whenever i,k,ℓ,m or n equals two, $\hat{S}_{k\ell} = \hat{S}_{mn} = 0$, and $\hat{V}_i = 0$. Therefore the only terms that effect the harmonic generation are those without a subscript of two. This reduces the number of nonlinear elastic constants contributing from 729 to 64. These 64 are listed below:

Θ_{111111};

$\theta_{111113} = \theta_{111131} = \theta_{111311} = \theta_{113111} = \theta_{131111} = \theta_{311111}$;

$\theta_{111133} = \theta_{113311} = \theta_{331111}$;

$\theta_{111313} = \theta_{111331} = \theta_{113113} = \theta_{113131} =$
$\theta_{131113} = \theta_{131131} = \theta_{311113} = \theta_{311131} =$
$\theta_{131311} = \theta_{133111} = \theta_{311311} = \theta_{313111}$;

$\theta_{131313} = \theta_{131331} = \theta_{133113} = \theta_{133131} =$
$\theta_{311313} = \theta_{311331} = \theta_{313113} = \theta_{313131}$;

$\theta_{111333} = \theta_{113133} = \theta_{113313} = \theta_{113331} =$
$\theta_{331311} = \theta_{333111} = \theta_{331113} = \theta_{331131} =$
$\theta_{131133} = \theta_{133311} = \theta_{311133} = \theta_{313311}$;

$\theta_{131333} = \theta_{133133} = \theta_{133313} = \theta_{133331} =$

$\theta_{311333} = \theta_{313133} = \theta_{313313} = \theta_{313331} =$
$\theta_{331313} = \theta_{331331} = \theta_{333113} = \theta_{333131}$;

$\theta_{113333} = \theta_{331133} = \theta_{333311}$;

$\theta_{133333} = \theta_{313333} = \theta_{331333} = \theta_{333133} = \theta_{333313} = \theta_{333331}$;

θ_{33333}.

As is indicated, many of the 64 constants are equal. This is due to the symmetries introduced from the thermodynamic definitions of $\theta_{ijk\ell mn}$ [8],[9]. Further, $LiNbO_3$ is a trigonal 3m material, and from crystallographic symmetries only 14 of the 729 constants are independent.

Reference [9] lists the independent constants in the crystallographic XYZ coordinate system for $LiNbO_3$, but the $\theta_{ijk\ell mn}$ listed here are for the Euler angle rotated coordinate system of 0°, 90°, 90° [49]. Hence the $C_{ijk\ell mn}$ nonlinear elastic constants of the XYZ coordinate system listed in [9], must be related to $\theta_{ijk\ell mn}$ by appropriate tensor transformation. With numerical values from [9], and the use of Voight notation, the tensor transformation gives;

$\theta_{111111} = C_{333333} = C_{333} = -3.63\times10^{11}\ N/m^2$

$$\theta_{111113} = -C_{333332} = -C_{334} = 0 \text{ N/m}^2$$

$$\theta_{111133} = C_{333322} = C_{332} = C_{133} = -0.34\text{x}10^{\text{"}} \text{ N/m}^2$$

$$\theta_{111313} = C_{333232} = C_{344} = -5.4\text{x}10^{\text{"}} \text{ N/m}^2$$

$$\theta_{131313} = -C_{323232} = -C_{444} = .41\text{x}10^{\text{"}} \text{ N/m}^2$$

$$\theta_{111333} = C_{333222} = -C_{342} = C_{134} = -.01\text{x}10^{11} \text{ N/m}^2$$

$$\theta_{131333} = C_{323222} = C_{244} = C_{155} = -5.99\text{x}10^{\text{"}} \text{ N/m}^2$$

$$\theta_{113333} = C_{332222} = C_{233} = C_{113} = 7.28\text{x}10^{\text{"}} \text{ N/m}^2$$

$$\theta_{133333} = -C_{322222} = -C_{224} = C_{114} + 2C_{214} = -3.00\text{x}10^{\text{"}} \text{ N/m}^2$$

$$\theta_{333333} = C_{222222} = C_{222} = -4.78\text{x}10^{\text{"}} \text{ N/m}^2$$

Let

$$L_{i1k\ell mn} = -i\hat{V}_i^{(r)}\hat{S}_{k\ell}^{(t)}\hat{S}_{mn}^{(w)}[\alpha^{(t)} + \alpha^{(w)} + 2\alpha^{(r)*}]^{-1} \qquad \text{(VI.2)}$$

$$L_{i3k\ell mn} = -\frac{1}{2}\hat{V}_i^{(r)}\hat{S}_{k\ell}^{(t)}\hat{S}_{mn}^{(w)}\left[\frac{\alpha^{(t)} + \alpha^{(w)}}{(\alpha^{(t)} + \alpha^{(w)} + 2\alpha^{(r)}{}_*)}\right] \qquad \text{(VI.3)}$$

Substituting (VI.2) and (VI.3) into (VI.1) gives

$$\hat{C}_{211} = \theta_{i1k\ell mn} L_{i1k\ell mn} + \theta_{i3k\ell mn} L_{i3k\ell mn} \qquad \text{(VI.4)}$$

$L_{i1k\ell mn}$ and $L_{i3k\ell mn}$ possess symmetry properties due to the symmetries of $\hat{S}^{(t)}_{k\ell}$ and $\hat{S}^{(w)}_{mn}$, and the sums over the superscripts t, w, and r. Because $\hat{S}^{(t)}_{k\ell} = \hat{S}^{(t)}_{\ell k}$ and $\hat{S}^{(w)}_{mn} = \hat{S}^{(w)}_{nm}$ (see, Appendix V) the subscripts k and ℓ, and m and n can be interchanged respectively for $L_{i1k\ell mn}$ and $L_{i3k\ell mn}$. Since this is a collinear interaction and $f_{\beta\gamma} = 1$, $\hat{S}^{(t)}_{k\ell}$ can be interchanged with $\hat{S}^{(w)}_{mn}$ in the summation over t and w. Thus $L_{i1k\ell mn} = L_{i1mnk\ell}$ and $L_{i3k\ell mn} = L_{i3mnk\ell}$. Hence $L_{i1k\ell mn}$ and $L_{i3k\ell mn}$ follow the same symmetry properties for k,ℓ,m,n as $\theta_{i1k\ell mn}$ and $\theta_{i3k\ell mn}$ for this nonlinear interaction.

Applying the qualities found for $\theta_{ijk\ell mn}$'s, one can expand (VI.4) as:

$$\begin{aligned}
\hat{C}_{211} = {} & \theta_{111111} L_{11111} + \\
& (4\theta_{111113} L_{111113} + \theta_{131111} L_{131111} + \theta_{311111} L_{311111}) + \\
& (2\theta_{111133} L_{111133} + \theta_{331111} L_{331111}) + \\
& (4\theta_{111313} L_{111313} + 4\theta_{131113} L_{131113} + 4\theta_{311113} L_{311113}) + \\
& (4\theta_{131313} L_{131313} + 4\theta_{311313} L_{311313}) + \\
& (4\theta_{111333} L_{111333} + 4\theta_{331311} L_{331311} + 2\theta_{131133} L_{131133} \\
& \quad + 2\theta_{311133} L_{311133}) +
\end{aligned}$$

$$(4\theta_{131333}L_{131333} + 4\theta_{311333}L_{311333} + 4\theta_{331313}L_{331313}) +$$
$$(2\theta_{331133}L_{331133} + \theta_{113333}L_{113333}) +$$
$$(4\theta_{331333}L_{331333} + \theta_{133333}L_{133333} + \theta_{313333}L_{313333}) +$$
$$\theta_{333333}L_{333333}. \qquad \text{(VI.5)}$$

Because $\theta_{111113} = \theta_{131111} = \theta_{311111} = 0$, L_{111113}, L_{131111}, and L_{311111} do not contribut to $\hat{C}_{211}$. Given below are the values of $L_{ilk\ell mn}$ and $L_{i3k\ell mn}$ that were calculated for YZ-$LiNbO_3$. The units are $\frac{(sec\text{-}m)^{3/2}}{N\text{-}W^{1/2}}$

$$L_{111111} = 1.76\times10^{-26} + 6.45\times10^{-26}\ i$$
$$L_{111133} = -3.34\times10^{-26} - 1.54\times10^{-26}\ i$$
$$L_{331111} = -2.39\times10^{-25} + 2.16\times10^{-25}\ i$$
$$L_{111313} = -2.13\times10^{-27} + 5.99\times10^{-26}\ i$$
$$L_{131113} = -9.78\times10^{-27} - 2.85\times10^{-26}\ i$$
$$L_{311113} = 4.71\times10^{-26} + 4.19\times10^{-26}\ i$$
$$L_{131313} = 1.23\times10^{-26} - 4.46\times10^{-27}\ i$$
$$L_{311313} = 4.56\times10^{-25} + 2.79\times10^{-25}\ i$$
$$L_{111333} = 2.33\times10^{-26} - 4.47\times10^{-27}\ i$$
$$L_{331311} = 4.18\times10^{-27} - 8.27\times10^{-28}\ i$$
$$L_{131133} = -4.65\times10^{-26} - 1.32\times10^{-26}\ i$$
$$L_{131333} = 2.40\times10^{-27} + 4.25\times10^{-27}\ i$$

$$L_{311133} = -4.65\times10^{-26} + 1.32\times10^{-26}\ i$$

$$L_{311333} = 4.17\times10^{-26} - 1.51\times10^{-25}\ i$$

$$L_{331313} = -7.46\times10^{-26} + 2.86\times10^{-26}\ i$$

$$L_{331133} = 8.51\times10^{-26} - 7.29\times10^{-26}\ i$$

$$L_{113333} = -1.26\times10^{-27} - 1.22\times10^{-27}\ i$$

$$L_{331333} = 8.94\times10^{-27} + 2.03\times10^{-26}\ i$$

$$L_{133333} = 1.74\times10^{-26} - 4.94\times10^{-26}\ i$$

$$L_{313333} = -5.97\times10^{-26} - 1.21\times10^{-26}\ i$$

$$L_{333333} = -2.46\times10^{-26} + 2.13\times10^{-26}\ i$$

These values for $L_{i1k\ell mn}$ and $L_{i3k\ell mn}$, and $\theta_{i1k\ell mn}$ and $\theta_{i3k\ell mn}$ are substituted into (VI.5) to find $\hat{C}_{211}$. The value of $\hat{C}_{211}$ found was

$$\hat{C}_{211} = 2.12\times10^{-13} + 4.39\times10^{-15}\ i\ \frac{sec^{3/2}}{m^{1/2}w^{1/2}} \qquad \text{(VI.6)}$$

This is then substituted into equation (3.B.13). With

$$\omega_1 = 2\pi\times50\ \text{MHz},$$

$$\langle\hat{S}\rangle \simeq 1,$$

$$v_g = 3488\ \text{m/sec}^2$$

K was found to be

$$K = 5.4 \times 10^{8} \, e^{.021 \, i} \, \frac{m}{sec^{2} w^{1/2}} \qquad \text{(VI.7)}$$

APPENDIX VII

FREQUENCY RATIO EQUATION

For resonant three-wave interactions, the three acoustic surface waves must be matched by the following conditions:

$$\omega_3 = \omega_1 + \omega_2 \tag{VII.1}$$

$$\bar{k}_3 = \bar{k}_1 + \bar{k}_2 \tag{VII.2}$$

with the subscript 3 indicating the highest frequency wave. Fig. VII.1 illustrates the phase matching on the y-cut $LiNbO_3$ coordinate system [50].

In the up-conversion interaction $\bar{k}_1$ and $\bar{k}_2$ collide to produce $\bar{k}_3$. The magnitude of the three wave vectors are related to each other by

$$|\bar{k}_3|^2 = |\bar{k}_1|^2 + |\bar{k}_2|^2 - 2|\bar{k}_1||\bar{k}_2| \cos \psi_3 \tag{VII.3}$$

with

$$|\bar{k}_i| = \frac{\omega_i}{v_{pi}}$$

where

ω_i = radial frequency

v_{pi} = phase velocity,

Fig. VII.1

$\bar{k}$-matching on
Y-Cut $LiNbO_3$ Coordinate System

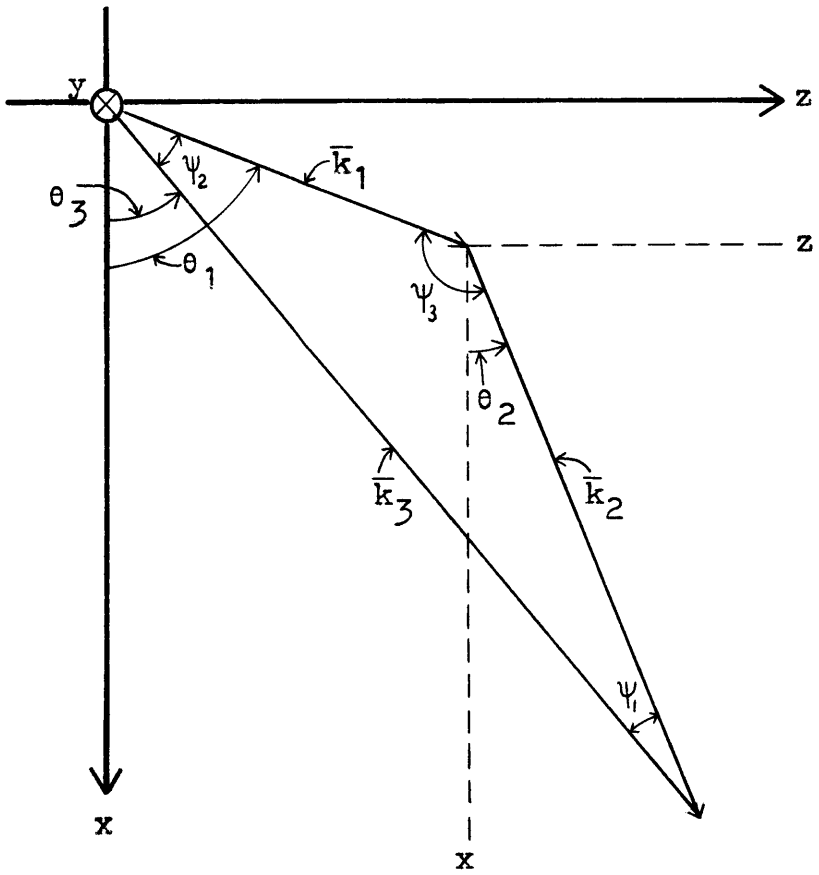

one has:

$$\left(\frac{\omega_3}{v_{p3}}\right)^2 = \left(\frac{\omega_1}{v_{p1}}\right)^2 + \left(\frac{\omega_2}{v_{p2}}\right)^2 - 2\left(\frac{\omega_1}{v_{p1}}\right)\left(\frac{\omega_2}{v_{p2}}\right)\cos\psi_3 \qquad \text{(VII.4)}$$

After substituting $\omega_1 + \omega_2$ into (VII.4) for ω_3, and some algebraic manipulation, the frequency ratio of f_1 to f_2 can be found:

$$\frac{f_2}{f_1} = \frac{\omega_2}{\omega_1} = \frac{-\left[\frac{\cos\psi_3}{v_{p1}v_{p2}} + \frac{1}{v_{p3}^2}\right] + \left[\left[\frac{\cos\psi_3}{v_{p1}v_{p2}} + \frac{1}{v_{p3}^2}\right]^2 - \left(\frac{1}{v_{p3}^2} - \frac{1}{v_{p1}^2}\right)\left(\frac{1}{v_{p3}^2} - \frac{1}{v_{p2}^2}\right)\right]^{1/2}}{\left(\frac{1}{v_{p3}^2} - \frac{1}{v_{p2}^2}\right)}$$

(VII.5)

Data from reference [52] can be used to find the frequency ratios for phase matching on y-cut $LiNbO_3$.